NORTHWESTERN UNIVERSITY

Hybrid 2D Halide Perovskite Materials for Optoelectronics

A DISSERTATION

SUBMITTED TO THE GRADUATE SCHOOL IN PARTIAL FULFILLMENT OF THE REQUIREMENTS

for the degree

DOCTOR OF PHILOSOPHY

Field of Chemistry

By

Lingling Mao

EVANSTON, ILLINOIS

December 2018

Abstract

Hybrid 2D Halide Perovskite Materials for Optoelectronics

Lingling Mao

Hybrid Organic-inorganic halide perovskites are emerging semiconducting materials that have shown over 23% in power conversion efficiency (PCE) for solar cells. The most prominent materials, three-dimensional (3D) perovskites, have limited scope for structural engineering and exhibit instability when encounter with moisture and heat. Here, we focus on studying the structure-property relationship in low-dimensional materials, where large organic cations can be inserted in the structure to increase the stability and structural diversity. We are interested in developing white-light emitting materials for solid-state lighting applications. Here we study the lead bromide-based and mixed bromide/chloride systems and have found a direct correlation between the distortion of the inorganic framework and the emission. Following this principle, we have synthesized and characterized a series of hybrid perovskite materials which emit white-light at room temperature. We have developed the first complete series of two-dimensional (2D) Dion-Jacobson (DJ) hybrid halide perovskites with the general formula $(A')(A)_{n-1}Pb_nI_{3n+1}$ (A' = 3-(aminomethyl)piperidinium (3AMP) or 4-(aminomethyl)piperidinium (4AMP), A = methylammonium (MA)). The higher layer member (n = 4) has demonstrated good performance, with the initial PCE of 7.3% and increased PCE of 12.0% with formamidinium incorporation.

Acknowledgements

First, I would like to thank my advisor Prof. Mercouri Kanatzidis, for the past four years of incredible guidance and generous support. Mercouri has been an inspiring role model, who is always curious, enthusiastic and rigorous about science. Mercouri's knowledge and intuition in solid state chemistry is truly admirable and I will always look up to him. I have benefited a lot from our discussion and constantly being encouraged by Mercouri, which is one of the most important driving forces in my doctoral study. I would also like to thank my committee members Prof. SonBinh Nguyen and Prof. Danna Freedman for their participation and contribution in my qualifying exam, original research proposal and finally the thesis defense.

Prof. Costas Stoumpos is one of the best chemist I have ever known. I am fortunately enough to work with him throughout my PhD and have him as my mentor during the years. The thinking process that works for us is highly intense, we had countless of arguments and debates revolving the projects we were working on, but managed to reach a common ground in the end. I cannot thank him enough for bringing these sparkling conversations and most importantly, the mutual share of love for chemistry makes us both better chemists. I wish him all the best for his future career in University of Crete as an independent PI and cannot wait to see his upcoming work.

Northwestern is a wonderful incubator for many talents. I have met many of them and fortunately have some of them as collaborators. Dr. Yilei Wu has contributed a lot in the white-light emitting perovskite projects, which he helped me with the photoluminescence measurements. Yilei is a truly remarkable chemist that does everything, the complicated organic synthesis and subsequent spectroscopy studies. I'm gratefully that Yilei has spent so much time on our collaboration and the results did not disappoint. Dr. Weijun Ke is a device expert in our lab. He

has fabricated the solar cell devices with the materials I made and further improved the efficiency. Weijun is also one of the most hard-working and humble people I have ever known. I believe he will go far with his high work ethics and unbelievably high level of execution. Dr. Peijun Guo has carried out lots of the spectroscopy work for our latest collaboration. I always send him a million samples and have him measure them. I truly appreciate his hard work and on-point suggestions.

Prof. Claudine Katan, Prof. Mikael Kepenekian, Prof. Jacky Even, Dr. Boubaca Traore and Dr. Laurent Pedesseau have provided theoretical support for most of my projects. I greatly acknowledge their input and enjoy our collaboration very much. I also thank Dave Tsai, Dr. Wanyi Nie and Prof. Aditya Mohite for their help in some device work.

The Kanatzidis group has been a solid team and I'm honored to be part of it. Thanks to all my great friends and colleagues here, previous members Dr. Dana Cao, Prof. Chengliang Xiao, Prof. Xianli Su, Jiangwei Li, current member Dr. Yihui He, Dr. Ido Hadar, Dr. Haijie Chen, Dr. Jim Hodges, Dr. Ioannis Spanopoulos, my fellow graduate students Xiaotong Li, Kyle McCall, Grant Alexander, Jason Khoury, Tyler Slade, Daniel Chica, Justin Hoffman, Becca McClain, Songting Cai, Craig Laing, Michael Quintero, Juncen Li and Eugenia Vasileiadou. Special thanks to Prof. Christos Malliakas, for all these years of tech support of a wide range of instruments in our lab and at IMSERC.

I would like to give special thanks to my roommate Tingting Liu, who is also a graduate student in the department of chemistry here at Northwestern. She has always been a dear friend to me. I have enjoyed her company and friendship ever since I got here in 2014.

There are so many beloved families and friends who helped me through all these years. I will keep on working hard to keep you guys proud. My parents are my rocks. Thanks for always be there for me!

Preface

This dissertation is original and includes both independent and collaborative work carried out by the author, Lingling Mao. The contributions from other researchers will be described at the beginning of each chapter.

The author acknowledges support from Department of Energy, Office of Science, Basic Energy Sciences, under Grant SC0012541.

Dedication

This thesis is dedicated to my parents Zongwan Mao and Li Long. I hope I have inherited my dad's brain and my mom's look. I love you so much.

Table of contents

List of Figures

List of Tables

Chapter 1. Introduction of Hybrid 2D Halide Perovskite Materials

1.1 Overview of Halide Perovskite Materials

Hybrid inorganic-organic halide perovskites have made their mark in their scientific world in the last decade, driven by the meteoric rise in the photovoltaic efficiency of the methylammonium lead iodide, $CH_3NH_3PbI_3$ (or $MAPbI_3$). The discovery of $CH_3NH_3PbI_3$, a three dimensional (3D) compound that shares similar structural features with the namesake mineral $CaTiO_3$ can be traced back to Weber's work in 1978,[1] yet the history of the halide perovskites dates long before that with the works of Wells (1893)[2] and Moller (1957-1959)[3-4] on $CsPbX_3$ and Auger and Karantassis ($CsSnX_3$, 1925; $CsGeX_3$, 1935).[5-6] Several breakthroughs, however, occurred in 2009 and 2012 where In 2009 Miyasaka and coworkers reported the liquid-based dye sensitized solar cells based on nanocrystals of $MAPbI_3$, attached to a TiO_2 surface.[7] The 2012 however was the watershed moment when a) the all-solid state dye sensitized cells based on a solid layer of $CsSnI_3$ perovskite acting as a hole transport layer and light absorber with ~10% efficiency were reported in 2012 by Kanatzidis and coworker;[8] b) demonstration of cells based on a solid layer of $MAPbI_3$ devices was reported in 2012 by Miyasaka, Snaith and coworkers;[9] c) independent confirmation of the solid layer perovskite of $MAPbI_3$ reported by Park and co-workers.[10] After that, the halide perovskite field really took off and perovskite solar cells (PSCs) have performed an epic march to >23% efficiencies that compare favorably with many established inorganic semiconductors.[9-24] Given this history it is fair to say that the current perovskite solar cell field is more of an intellectual child of the solution-processed dye-sensitized cell (Grätzel cell)[25] rather than a logical evolution of the more traditional Si, CdTe and $CuInSe_2$ cells. The field has also borrowed heavily from techniques utilized in the organic photovoltaics area. More importantly, the enormous success of PSCs firmly established the emergence of halide perovskites as the next generation of high-performance

semiconductors.[26-30] Indeed, halide perovskites match in optoelectronic performance benchmark inorganic semiconductors in a wide array of applications (LEDs,[31-33] FETs,[34-35] laser,[36-38] hard radiation detectors,[39-42] etc.), forecasting a great potential for commercialization. Mechanistically, however, the halide perovskites have distinctive properties that derive from their soft lattices and dynamically disordered crystal structure[43-44] which favorable modifies their charge-carrier recombination lifetimes and renders them nonclassical semiconductor characteristics.[45-48] A major obstacle in further development, exists in the form of limited composition accessible in the ABX_3 ($A = Cs^+$, $CH_3NH_3^+$, $[HC(NH_2)_2]^+$; $B = Pb^{2+}$, Ge^{2+}, Sn^{2+},; $X = Cl^-$, Br^-, I^-) perovskite structure with only three A-site cations being able to maintain the 3D corner-sharing inorganic framework,[49] in some cases only forming metastable compounds.[50] Whereas a solution in stabilizing some metastable phases was found in the form of perovskite nanocrystals, [51-53] an important relief form the narrow compositional diversity was found in the form of two-dimensional (2D) halide perovskites (Figure 1).

Through the chemically accomplished dimensional reduction of the 3D crystal lattice, 2D perovskites, $(A')_m(A)_{n-1}B_nX_{3n+1}$, adopt a new structural and compositional dimension, A', where

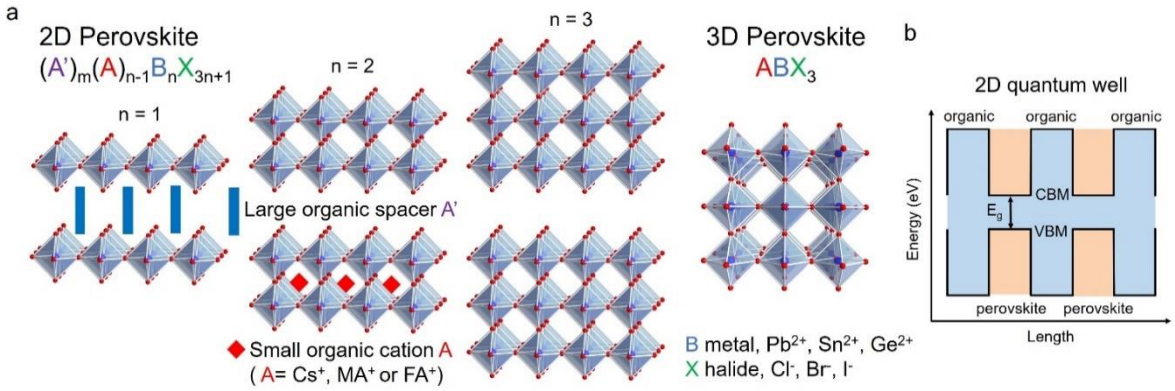

Figure 1. (a) Schematic illustration of the evolution from 2D perovskite to 3D perovskite with key components. (b) 2D quantum well structure illustration.

monovalent (m = 2) or divalent (m = 1) cations can intercalate between the anion 2D perovskite sheets. Besides its apparent simplicity, the concept of dimensional reduction not only grants access to a plethora of hybrid organic-inorganic materials with tailorable functionalities, but also gives rise to an unparalleled structural complexity[54] which allows for the fine-tuning of the optoelectronic properties. In the 2D hybrid halide perovskites, the organic cations act as insulating barriers that confine the charge carriers in two dimensions but they also serve as dielectric moderators that determine the electrostatic forces exerted on the photogenerated electron-hole pairs. The specific arrangement of alternating organic-inorganic layers generates a crystallographically-ordered 2D multiple quantum-well (MQW) electronic structure that forms naturally in a bottom-up fashion through self-assembly. The structural coherence of the halide perovskite MQWs resembles that of the artificially synthesized III-V films semiconductor heterostructures, and in addition, due to the high organic/inorganic dielectric contrast the perovskite materials generate huge electron-hole binding energies. 2D halide perovskite MQWs can stabilize excitons that can be readily observed even at ambient temperatures. The multitude of possibilities deriving from the MQW structures, already demonstrated in III-V semiconductors,[55-58] makes the 2D halide MQWs particularly interesting material for the discovery of new fundamental physics and efficient room temperature optoelectronic applications.

1.2 A Brief History of 2D Halide Perovskites

2D perovskites, especially the transition metal based structures $(RNH_3)_2BX_4$ with $B = Cd^{2+}$, Mn^{2+}, Fe^{2+}, Cu^{2+}, Hg^{2+} etc., $X = Cl^-$, Br^- have been investigated for dielectric and magnetic

properties.[59-62] The exploration in the multilayered 2D system was reported by Maruyama and co-workers for $(CH_3(CH_2)_8NH_3)_2PbI_4$ in 1986.[63]. However, it was mainly Ishihara et al.[61, 64-68], Papavassiliou[69-73] and Thorn *et al*. who systematically studied the optical properties of the materials. The latter introduced the concept of the "in-between phases" (i.e. between the $(RNH_3)PbI_4$ and $MAPbI_3$) which was the first conceptual relationship between the standard 2D oxide perovskites and the hybrid 2D halide perovskites.[74] Thorn demonstrated this hypothesis by the successful isolation of whole families of halide perovskites, which instead of a discrete compositions they could be collectively describes as homologous series (i.e. $((CH_3(CH_2)_8NH_3)_2(CH_3NH_3)_{n-1}Pb_nX_{3n+1}$, X = Br^-, I^-), or $(PEA)_2(MA)_{n-1}Pb_nI_{3n+1}$ (n= 1-2, PEA = phenylethylammonium).[74] Mitzi and co-workers combined the collective knowledge of that time into a well-defined research field and laid the foundation for the explosive growth of the 2D halide perovskite semiconductors. The report on the evolution of the $(C_4H_9NH_3)_2(CH_3NH_3)_{n-1}Sn_nI_{3n+1}$ (n = 1–5) homologous series for many n-members demonstrated how the electrical properties of the compounds may change as a function of n, from the nearly intrinsic n = 1 to the heavily doped, "metal-like" n =∞.[75] In addition to the so-called (100)-oriented (reflecting the cleavage plane relative to the ideal cubic 3D perovskite) $(C_4H_9NH_3)_2(CH_3NH_3)_{n-1}Sn_nI_{3n+1}$ multilayer series, the (110)-oriented $[NH_2\text{-}C(I)]NH_2]_2(CH_3NH_3)_mSn_mI_{3m+2}$ (m =1–4) series was also described[76]. Subsequently, Mitzi and coworkers developed the synthesis and characterization on the single-layered (n = 1) 2D perovskite with different organic cations,[77-94] and extended the choice of the metal ion to include Ge^{2+}[95], group 15[96] and rare earth elements.[97] However, his contributions related with the development of thin-film transistor devices, ,[34] based on 2D halide perovskites, demonstrating their potential as high-performance semiconductors.

In the current era 2D halide perovskites provide a new window with a synthetic handle towards material engineering customized to the needs of specific applications. They excel in all of the traditional research fields such as solar cells,[98-103] light-emitting diodes (LEDs)[104-106] and photodetectors.[107-109] More exotic forms have also emerge with the rise of 2D halide perovskites such as 2D nanocrystals,[110-111] single-component white-light emission[112-118] for solid-state lighting devices,[119] strong optical nonlinearity[120] and ferroelectricity.[121] 2D hybrid perovskite materials not only perform well by themselves, but also can be integrated into heterostructures,[122-123] enhancing the device functionalities and performance. Because of their fundamental importance it is therefore crucial to understand the structure property relationships at the molecular level that govern these materials and allowing for targeted device engineering and further optimization to take place.[124-127]

1.3 Structural Types and Connectivity Modes

Akin to their 3D congeners, 2D halide perovskites obey stereochemical rules that determine the growth of the perovskite sheets. Three octahedral connectivity modes have been

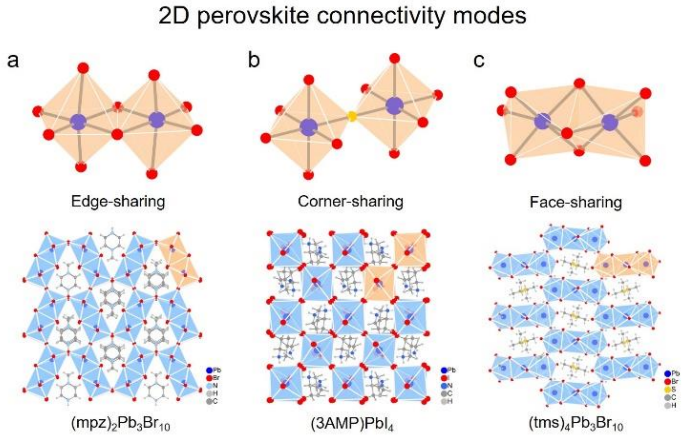

Figure 2. Connectivity modes in 2D perovskite and their representative example. (a) Edge-sharing, $(mpz)_2Pb_3Br_{10}$ from ref. 121. (b) Corner-sharing, $(3AMP)PbI_4$ from ref. 61. (c) Face-sharing, $(tms)_4Pb_3Br_{10}$ from ref. 133.

experimentally observed; corner-sharing, edge-sharing and face-sharing as seen in Figure 2. [128] Different from the 3D structures, where the connectivity depends primarily on the relative size of the A-si do not have far fewer size restrictions for the A'-site (A-site still follows the same rules as 3D perovskites) since cations must fit within the inter layer space. Instead what determines the suitability of the cation as a spacer is: i) its net positive charge at the perovskite anchoring position and degree of substitution, i.e. $RNH_3^+ > R_2NH_2^+ > R_3NH^+ > R_4N^+$ in ordered of decreased preference, ii) its hydrogen-bonding capacity (iii) its stereochemical configuration i.e. flexible aliphatic hydrocarbons > rigid aromatic hydrocarbons and (iv) its space-filling ability, i.e. linear interdigitating cations > branched irregular cations. Since there are many cations that fulfil these prerequisites, there are, in fact, many cations that can stabilize the regular (i.e. corner-sharing) 2D perovskite structure, which we have included in Figure 4's pool. However, in rare occasions the configurational strain that the cations impose to the 2D perovskite break the standard connectivity pattern and instead, stabilize edge-sharing or face-sharing networks.[129] These networks almost never form with exclusive edge-sharing or face-sharing connectivity, since area-filling in two dimensions is difficult with edge-sharing or altogether improbable with face-sharing to achieve and instead form in combination with partial corner-sharing contacts (Figure 2). For example, $(mpz)_2Pb_3Br_{10}$ (mpz = N-methylpiperazine) is comprised of repeating edge-sharing dimeric units (highlight in red), which are further connected in a corner-sharing fashion to complete a 2D layer.

Similarly, in $(tms)_4Pb_3Br_{10}$,[130] (tms = trimethylsulfonium) the triads of face-sharing units (highlight in red), share corners at both terminal apices to complete a 2D layer resembling the 9R perovskite polytype.[131] The way individual octahedra are linked determines the orbital overlap between the metal and the halide, which subsequently influences the band gap of the compound. As a general trend, determined experimentally and also theoretically confirmed, the band gap follows the increasing trend "corner-sharing < edge-sharing < face-sharing".[129, 132] This is perhaps expected within the special perovskite "inverted" band structure since corner sharing provides the strongest bonding between the metal and the halogen, which in turn gives rise to a "destabilization" of the ns^2 lone pair pushing it to the top of the valence band.[133] As the σ-bonding weakens through the interactions in the edge-sharing and face-sharing motifs, the lone pair is stabilized, localizing deep within the valence band, while the bottom of the conduction band increases in energy leading to an opening of the bandgap.[132] The structural diversity obtained in these 2D perovskites could be potentially be exploited to further adjust the optical properties of the hybrid perovskites.

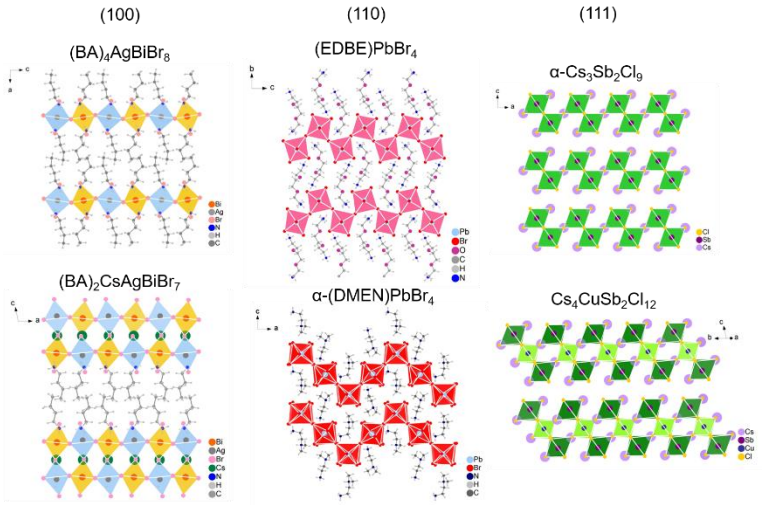

Figure 3. Examples of the double perovskite (100)-oriented structure (Ag^+ and Bi^{+3} are highlighted in blue and yellow, respectively), the (110)-oriented corrugated structure and the (111)-oriented perovskite structure (Cu^{2+} and Sb^{+3} are highlighted in light green and dark green, respectively)).

The main class of 2D halide perovskite compounds, therefore, consists of corner-sharing octahedra and these can be further classified into three categories: the (100)-oriented, the (110)-oriented and the (111)-oriented structures based on the crystallographic layer slicing direction cut along a specific (*hkl*) plane of the parent 3D structure. The general formula for the (100)-oriented and (110)-oriented 2D perovskite is $A'_2A_{n-1}B_nX_{3n+1}$ or $A'A_{n-1}B_nX_{3n+1}$ (A′ = 1+ or 2+, A = 1+ cation, B = Pb^{2+}, Sn^{2+}, Ge^{2+}, Cu^{2+}, Cd^{2+}, etc., X = Cl^-, Br^-, and I^-), while for the (111)-oriented 2D perovskite, the general formula is $A'_{n+1}B_nX_{3n+3}$ (n >1, where B valence is 3+, mixed-valence averaging 3+ or heterometallic, e.g. Cu^{2+} and Sb^{3+} in Figure 3).[134] Out of the three categories, the (100)-oriented 2D perovskites heavily dominate the classification tree and they are by far the most commonly obtained 2D perovskite structure. Besides the explosive development in the more standard 2D perovskites which will be discussed in the next section, remarkable progress has been achieved in the unconventional (100)-, (110)- and (111)-oriented perovskites. In this direction, many new compounds have been discovered, thus broadening the future scope of structural engineering in the halide perovskite family.

An interesting extension of the structural variation of the (100)-oriented perovskites comes from blending the dimensional reduction concept[135] with the ordered double perovskite structure.[136-137] The thus obtained single-layered and bi-layered bromide compounds $(BA)_4(AgBi)Br_8$ and $(BA)_2Cs(AgBi)Br_7$ represent a very special case of the (100) type arising from this combination with butylamine (BA^+) cation.[138] In these structures both Ag (1+) and Bi (3+) form alternating $(MBr_{6/2})^-$ octahedra, fulfilling both the charge and ionic size requirements of the 2D perovskite layer, while the butylammonium cation bilayer performs its usual role of separating the inorganic

layers (Figure 3).[75, 139] Another interesting 2D perovskite variation is found in the heteroleptic (100)-oriented layered perovskites.

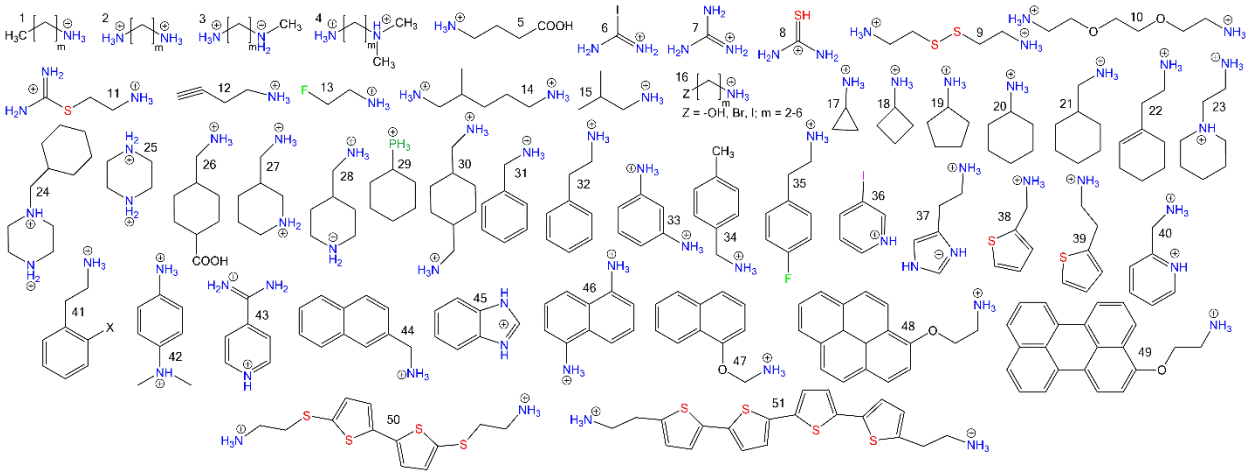

Figure 4. Reported organic cations that form corner-sharing (100)-oriented, (110)-oriented or (111)-oriented 2D halide perovskite structures (n = layer thickness number). 1. Primary-alkylammonium. m = 0-1, n = 1;[140] m = 1, n = 3;[117, 141] m = 2, n =1;[142-144] m =3, n = 1-5;[75, 139, 145-146] m = 4-5, n =1;[93] m = 6-9, n = 1;[147] m = 9-10, n = 1;[148] m = 11, 13, 15, 17, n = 1.[147, 149] 2. Primary-alkyldiammonium. m = 3, n = 1;[150] m = 4, n = 1;[114, 151-154] m = 4-9, n = 1-4;[155] m =5-6, n =1;[92, 154, 156] m = 8, 10, 12, n = 1.[84, 157] 3. m = 2, N^1 -methylethane-1,2-diammonium (N-MEDA); m = 3, N^1-methylpropane-1,3-diammonium (N-MPDA). All n = 1.[112]4. m = 2, 2-(dimethylamino)ethylammonium (DMEN); m = 3, 3-(dimethylamino)-1-propylammonium (DMAPA); m = 4, 4-(dimethylamino)butylammonium (DMABA). All n = 1.[116] 5. Ammonium 4-butyric acid, n = 2.[78] 6. Iodoformamidinium, n = 1-3.[76] 7. Guanidinium (GA), n = 1-3.[158-160] 8. Protonated thiourea cation, n =1.[161] 9. 2,2'-dithiodiethanammoniumn, n = 1.[162-163] 10. 2,2′-(ethylenedioxy)bis(ethylammonium) (EDBE), n = 1.[113] 11. Protonated 2-(aminoethyl)isothiourea, n = 1.[164] 12. but-3-yn-1-ammonium (BYA), n = 1. [165] 13. 2-fluoroethylammonium, n = 1.[166] 14. 2-Methylpentane-1,5-diammonium, n = 1.[150] 15. isobutyl-ammonium (IBA), n = 1.[167] 16. Heteroatom substituted alkylammonium, n = 1.[162] 17-20. Cyclopropylammonium, cyclobutylammonium, cyclopentylammonium and cyclohexylammonium, n = 1.[87, 168] 21. Cyclohexylmethylammonium, n = 1.[169] 22. 2-(1-Cyclohexenyl)ethylammonium, n = 1.[170-171] 23. N-(aminoethyl)piperidinium, n = 1.[92] 24. N-benzylpiperazinium, n = 1.[172] 25. Piperazinium, n = 1.[172] 26. (carboxy)cyclohexylmethylammonium, n = 1.[92] 27. 3-(aminomethyl)piperidinium. (3AMP), n = 1-4.[102] 28. 4-(aminomethyl)piperidinium (4AMP), n = 1-4.[102] 29. Cyclohexylphosphonium, n = 1.[173] 30. 1,4-bis(aminomethyl)cyclohexane, n = 1.[174] 31. Benzylammonium (BZA), n = 1.[90, 129, 175-178] 32. Phenylethylammonium (PEA), n = 1-3.[74, 92, 99, 179-180] 33. m-Phenylenediammonium, n = 1. 34. 4-methylbenzylammonium, n = 1-2.[77] 35. 4-fluorophenylethylammonium, n = 1.[181] 36. 3-iodopyridinium, n = 1.[92] 37. Histammonium, n = 1.[90] 38. 2-Thienylmethyl)ammonium, n = 2.[79] 39. 2-(2-thienyl)ethanaminium, n = 1.[182] 40. 2-(ammoniomethyl)pyridinium, n = 1.[183] 41. 2-substituted phenethylammonium (X = F, Cl, Br), n = 1.[184] 42. N,N-Dimethyl-p-phenylenediammonium, n = 1.[185-186] 43. 4-Amidinopyridinium, n = 1.[89] 44. 2-Naphthylmethyl)ammonium, n = 1.[94] 45. Benzimidazolium, n = 1.[187] 46. 1,5-diammoniumnaphthalene, n = 1.[84] 47-49. naphthalene-O-ethylammonium, pyrene-O-ethylammonium, perylene-O-ethylammonium. All n =1.[188] 50. 5-ammoniumethylsulfanyl)-2,2'-bithiophene (BAESBT), n = 1.[189] 51. 5,5‘ ‘‘-bis(aminoethyl)-2,2‘:5‘,2‘ ‘:5‘ ‘,2‘ ‘‘-quaterthiophene (AEQT), n = 1.[190]

So much the hybrid compound $(MA)_2PbI_2(SCN)_2$[191] as much as the all-inorganic compound $Cs_2SnI_2Cl_2$[192] and $Cs_2PbI_2Cl_2$[193] represent distinctive derivatives of the K_2NiF_4[194] prototype where the lattice positions along the perovskite plane and vertically to it are occupied by different chemical species. In these chemically ordered structures the larger heteroatoms (SCN^- in the former, I^- in the latter) decorate the surfaces of the layers, whereas the smaller heteroatom is responsible for the corner-sharing expansion of the perovskite along the layer. These three compounds differ significantly from the rest of the hybrid inorganic-organic perovskites as the separation between the layers occurs "naturally", without the use of bulky organic spacers and seems to be realized because of the ionic-size mismatch of the two heteroatoms.

The corrugated (110)-oriented structures are far less common since there are very few cations that can stabilize it, typically small, highly-symmetric ones[76, 195] or flexible ditopic ones.[113, 116] Until recently, the only building unit known was the most common "2×2" corrugation variation. Nevertheless, new results revealed that the corrugation "length" could be increased to "3×3"[116] and even to a "4×4"[90, 196] undulated structure. The (110)-oriented perovskite layers are intrinsically highly-distorted, often stabilized by site-specific hydrogen bonding or other secondary bonding interactions. Because of this, (110)-oriented perovskites often exhibit white-light emission at room temperature believed to be caused by the formation of self-trapped excitons (STE),[197] as for example (EDBE)$PbBr_4$ ("2×2")[113] and α-(DMEN)$PbBr_4$ ("3×3").[116] Very recently, the asymmetric "3×2"undulated structure was realized,[160] in $[CH(NH_2)_2][C(NH_2)_3]PbI_4$[160] which is the first member of the wider class of (210)-oriented 2D perovskites.[161]

The (111)-oriented 2D perovskites, with a general formula $A'_{n+1}B_nX_{3n+3}$, are in fact a class of defective perovskites.[198] Unlike the rest of the layered perovskite configurations, (111)-oriented

perovskites are M-site deficient since cleavage along the body diagonal of the 3D cubic cell selectively "eliminates" the metal sites, in contrast to other cleavage planes which eliminate neutral BX_2 fragments. As a result, B^{2+}-only halide (111)-oriented 2D perovskites cannot form, with the structures cleaved along the body diagonal preferring alternative 3D polytype configurations that maintain charge parity.[131] Thus, the only homo-valent p-block compounds in this class of materials are composed of group 15 B^{3+} ions (B = Bi, Sb, As) belonging either to the pseudo-layered $Cs_3Cr_2Cl_9$-type[199] 0D $[B_2X_9]^{3-}$ dimers or the $Cs_3Bi_2Br_9$-type[200] 2D $(B_2X_9)^{3-}$ defective perovskite layers.[201-205] Very recently, Solis-Ibarra and co-workers have managed to bypass the charge mismatch obstacle by synthesizing the heterometallic compound $Cs_4(CuSb_2)Cl_{12}$ which is the only known example for $n > 2$.[134] In this heterobimetallic perovskite, the Cu^{2+} (or Mn^{2+})[206] ions can be inserted between the Sb^{3+} sheets, forming the first example of the n = 3 structure of the general formula.

The recent progress in the generally unexplored, "exotic", 2D perovskite structural types has clearly shown that there is plenty of room for new material discovery. By further elucidation of the synthetic parameters we can rapidly move from the graphical cartoons of the general formulae to the isolation of useful materials on the bench with detailed structural characterization, thus pushing the boundaries of material understanding and exploitation.

1.4 (100)-oriented 2D Perovskites: Structure Directing Effects of Spacers

The (100)-oriented 2D perovskites are by far the most abundant class and it has been explored for a wide variety of cation templates. The geometrically planar inorganic-organic interface of the (100)-oriented layers not only allows the incorporation of a plethora of "spacer" cations between

the 2D perovskites, but it also allows for the templated "build-up" of the perovskite itself, which self-assembles in a layer-by-layer fashion between the spacers. These modular multilayered structures were first discovered in the oxide perovskites, where they were used to expand extended homologous series.[54, 207] Following the oxide perovskite nomenclature, the (100)-oriented oxide perovskites can be further categorized as the Ruddlesden-Popper (RP) phases,[208-209] the Dion-Jacobson (DJ) phases,[210-211] and the Aurivillius phases,[212-214] where their general formulae can be written as $A'_2A_{n-1}B_nO_{3n+1}$, $A'A_{n-1}B_nO_{3n+1}$ and $(Bi_2O_2)(A_{n-1}B_nO_{3n+1})$, respectively.

In the case of halide perovskites, most of these structure types have been realized, with the exception of the Aurivillius phases, which haven't yet been reported, possibly due to the reactivity of $(Bi_2O_2)^{2+}$ towards the formation of halides. It is entirely possible, however, that such layers can be formed using less reactive rock-salt type layers, such as $(Ba_2F_2)^{2+}$. As in the case of oxide perovskites, also in the case of halide perovskites, the nature of the spacer cation is important. Already from the expression of the chemical formula it is evident that the charge of the spacer cation defines the structural types of 2D perovskites. Nevertheless, both the RP and DJ classes exist for the halide family, having the general formula $A'_2A_{n-1}B_nX_{3n+1}$ and $A'A_{n-1}B_nX_{3n+1}$ (A' = interlayer "spacer" cation), respectively.

A new structural type, that is unique to the halide perovskites, is the alternating cation in the interlayer space (ACI)-type, where different cations order along the interlayer space.[158-159] The difference of ACI with the RP and DJ perovskites reflects directly on the formula $A'A_nB_nX_{3n+1}$, as the A-site "perovskitizer" cation (MA^+, FA^+ or Cs^+) does not only reside in the perovskite slab, but also fills in the interlayer along with the designated spacing cation A. Interestingly, guanidinium (GA^+) is the only reported A' cation that can form the ACI type structure, which suggests the

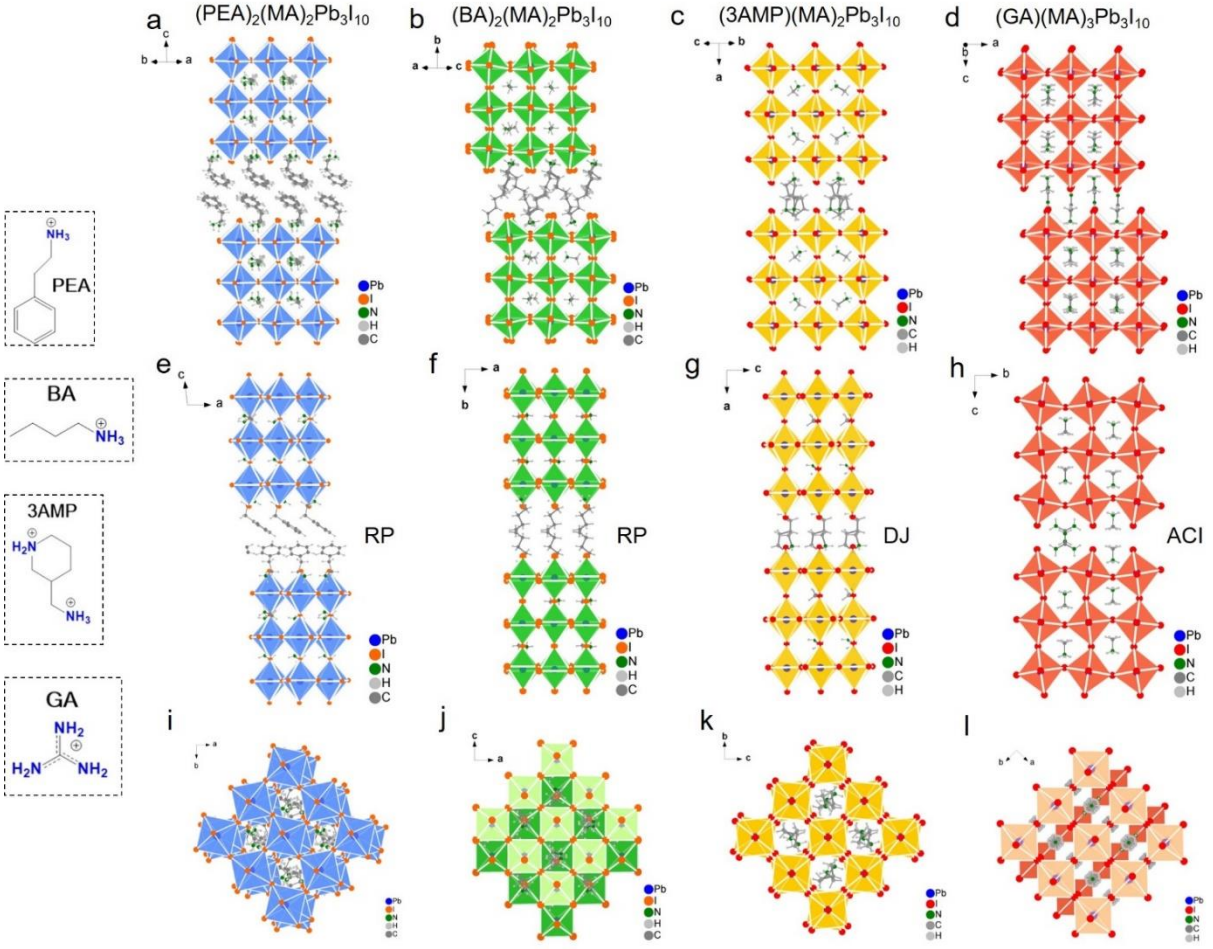

Figure 5. Structural comparison between the n = 3 crystal structure of RP phases, DJ phase and ACI phase: (a, e, i) $(PEA)_2(MA)_2Pb_3I_{10}$; (b, f, j) $(BA)_2(MA)_2Pb_3I_{10;}$ (c, g, k) $(3AMP)_2(MA)_2Pb_3I_{10}$; (d, h, i) $(GA)(MA)_3Pb_3I_{10}$.

preference of small cations that have similar size with the "perovskitizer" cations (MA^+, FA^+ or Cs^+) to form the ACI phases.

The crystal structure of all known structural types is shown in Figure 5. The side-by-side comparison of the n = 3 members of each of the RP, DJ and ACI homologous series, thus illustrating their structural differences and similarities across the three crystallographic directions. For the RP phases $(BA)_2(MA)_2Pb_3I_{10}$[100, 139] and $(PEA)_2(MA)_2Pb_3I_{10}$,[99] the layers are offset by one octahedral unit, showing a (½, ½) in-plane displacement. On the other extreme, the layers in the DJ phases $(3AMP)(MA)_2Pb_3I_{10}$[102] do exhibit any shift and are stacked perfectly on top of each

other (Figure 5k), without any (0,0) displacement. The ACI-type structure lies in between and combines the layer stacking characteristics from both RP and DJ structural types (Figure 5l), showing a (½, 0) displacement.

Obviously, the interlayer distance varies with the choice of spacing cation A' and this turns out to be one of the crucial factors that decide the excitonic PL emission from these quantum-well structures (Figure 5). Typically, the RP phases have larger interlayer distance due to the fact that they require a bi-layer of spacer organic cations, which inevitably will increase the layer separation from approximately 1.5 times the length of the cation in case of interdigitation (as in BA case) to more than double the cation's length in cases there is no overlap (like in the case of PEA). Thus, in the case of the RP phases the layers are well "isolated", showing no perovskite-perovskite interactions, thereby producing an excitonic emission that results directly from the spatial electronic confinement (n) of the individual layers.

Conversely, the ACI phases, and more so the DJ phases, require the organic cations to snugly fit in the perovskite "pockets" created in the interlayer space by the eclipsed stacking conformation of the perovskite layers. The close proximity of the layers generates a weak perovskite-perovskite interaction which can be readily observed in the position of the exciton which shows a pronounced

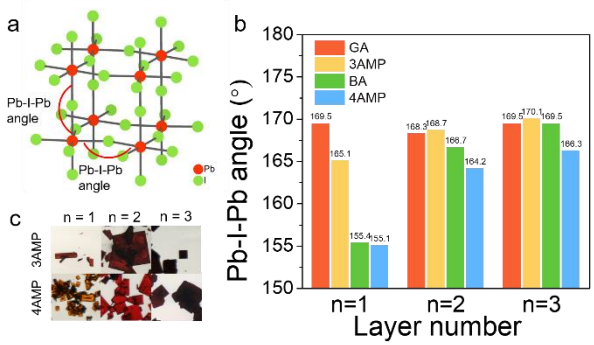

Figure 6. (a) Definition of the Pb-I-Pb angles. (b) Averaged Pb-I-Pb angles from the n = 1 to 3 structures of the $(GA)(MA)_nPb_nI_{3n+1}$, $(3AMP)(MA)_{n-1}Pb_nI_{3n+1}$, $(BA)_2(MA)_{n-1}Pb_nI_{3n+1}$ and $(4AMP)(MA)_{n-1}Pb_nI_{3n+1}$. Panel c reproduced from ref. 61 with permission. Copyright 2018.

redshift. The representative interlayer distances for the RP, DJ and ACI phases shown in Figure 5 are ~7 Å, ~4 Å and ~3 Å, respectively. Nevertheless, particularly for the RP phases, the value for BA represents a lower limit, as longer interlayer distances of up to ~26 Å have been reported, as for example in $(C_{18}H_{40}N)_2PbI_4$,[215] where the massive alkyl ammonium cation $CH_3(CH_2)_{17}NH_3^+$ was employed.

While the exciton emission trend largely depends on the quantum confinement, there are structural subtleties within a given n member that can also have a significant impact on it. These relate to the distortion of the 2D perovskites lattice, which has the least distorted lattices (in terms of B-X-B angle, see Figure 6a) to have the smallest exciton emission energy, in complete correspondence with the band gap trends of the 3D perovskites.[49] This can be readily observed from the photochromic change in the crystals, moving from a low symmetry structure at low temperature to a high symmetry structure at high temperature in the n = 1 RP series[93, 215-216] or by changes in the structure induced by cation templating effects at a given temperature in the DJ series (Figure 6c).[102]

In selected cases, where the synthesis and characterization of the completed homologous series

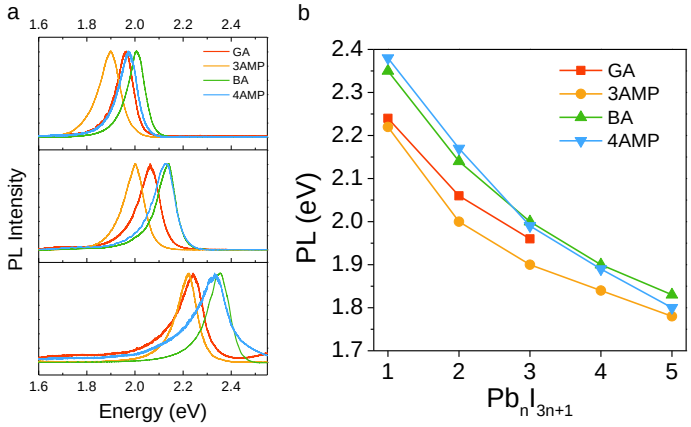

Figure 7. (a) Comparison between the PL emission of the n = 1-3 members of $(BA)_2(MA)_{n-1}Pb_nI_{3n+1}$, $(3AMP)(MA)_{n-1}Pb_nI_{3n+1}$ and $(GA)(MA)_nPb_nI_{3n+1}$. (b) PL emission energy versus layer thickness (n). (c) Averaged Pb-I-Pb angles versus layer thickness (n).

of the RP, DJ and ACI has been achieved, it is possible to analyze their structure-property correlations. Comparing between n = 1 to 3 for all families, the energy of the excitonic emission (as this is determined by the PL emission at room temperature) decreases for all the series. However, the relative emission energies are markedly different following a systematic trend with the emission energy decreasing in the "3AMP (DJ) < GA (ACI) < 4AMP (DJ) < BA (RP)" order (Figure 7a). The origin of this particular trend correlates well both with the structural distortion defined by the octahedron-linking Pb-I-Pb angles and with the interlayer spacing in the crystal structure. The larger angle represents less distortion, generally leading to a relative narrowing of the PL emission energy among the series. However, the n = 1 is an exception in the trend, with (GA)(MA)PbI_4 having a larger average Pb-I-Pb angle, but still slightly higher PL emission energy than the (3AMP)PbI_4, possibly due to the large out-of-plane distortion of (GA)(MA)PbI_4. This deviation indicates that there are other factors such as the anisotropy of the lattice[114] or the bond length variations also play a role in determining the optical properties of the quantum well structures.

It is important to point out that the difference of the Pb-I-Pb angle becomes very small as the layers get thicker (higher n members) for all structure types as seen in Figure 6b, suggesting that the distortion of the lattice stops being the determining factor and that the interlayer spacing starts becoming the dominant factor. However, in systems where all other thing are equal, structural distortion is still important, as in the case of 3AMP and 4AMP DJ perovskites (Figure 6b, c), where the Pb-I-Pb angles are consistently larger for the latter, thus leading to the systematically lower excitonic emission.[102]

1.5 (100)-Oriented 2D Perovskites: Tuning the layer thickness

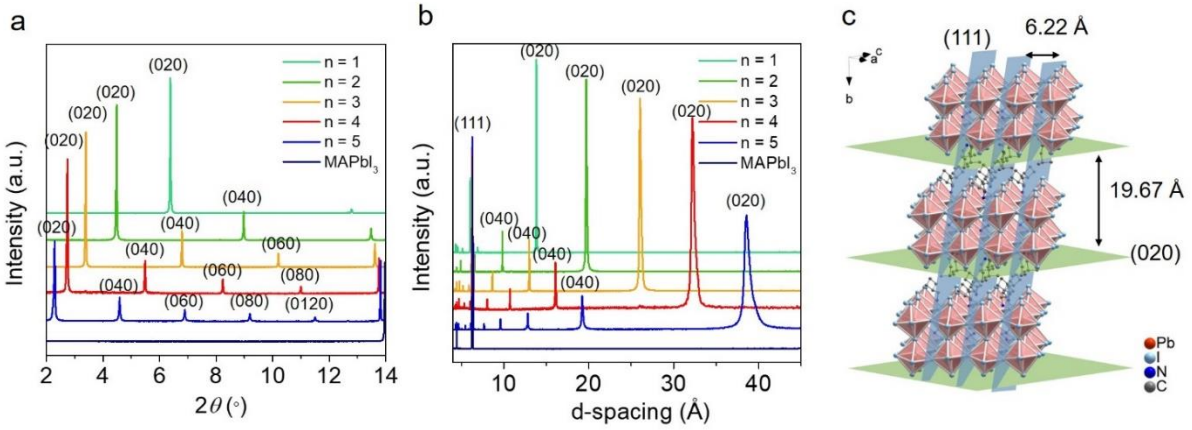

Figure 8. (a) High resolution PXRD of $(BA)_2(MA)_{n-1}Pb_nI_{3n+1}$ (n = 1-5). (b)PXRD plotted in d-spacing. (c) structure of $(BA)_2(MA)Pb_2I_7$ with the illustration of respective diffraction planes.

One of the most attractive properties of the 2D halide perovskites is that they can be tailored to the exact n-layer thickness using simple synthetic chemistry, thus allowing for the fine-tuning of the quantum well electronic structure. The (100)-oriented 2D perovskites are ideal for this "digital" growth due to their favorable geometry that guarantees the "high-fidelity" of the layer thickness. Indeed, careful composition control can generate all the "quantized" RP perovskites up to n = 7 for the $(BA)_2(MA)_{n-1}Pb_nI_{3n+1}$ series (Figure 9a), which is the thickest 2D perovskite with long-range crystallographic ordered known to date. Note that higher n-members have been observed for oxide based RP perovskites,[217-219] yet morphological effects preclude the formation of the ordered high-n members (n > 5) since these compounds do not have sufficient thermodynamic stabilization.[220] The mechanism for this instability is the disproportionation reaction (1):

$$(RNH_3)_2(MA)_{n-1}Pb_nI_{3n+1} \xrightarrow{disproportionation} (RNH_3)_2(MA)_2Pb_3I_{10} + (n\text{-}3)\ MAPbI_3 \qquad (1)$$

where large perovskite slabs tend to break down into more thermodynamically stable phases such as the thinner 2D perovskite slabs and the 3D perovskite. For instance, the n = 5 member of the

BA series undergoes a very slow disproportionation reaction and decomposes into the hydrated form of $MAPbI_3$ ($MAPbI_3 \cdot H_2O$)[221] and the n = 3 2D member over the course of several weeks.[145]

As the thickness of the perovskite layers increases, the dimensions of the stacking axis also increase, progressively moving from the atomic scale (few Å for n = 1) to the nanoscale (few nm for n = 7). The dimensions of the layers can be even roughly predicted following the general equation (2):

$$d_{(00l)} = a^*n + x \quad (2)$$

where the complete inorganic-organic layer thickness $d_{(001)}$ is determined by the lattice parameter (a*) of the 3D perovskite (~6.3Å for $MAPbI_3$), the thickness (x) of a complete organic layer (~7Å for the $(BA)_2^{2+}$ bilayer, ~3Å for the $(3AMP)^{2+}$ monolayer) and the number (n) of inorganic layers.[120] Because of their long range crystallographic ordering, the phase purity of the bulk material can be tracked down from their "fingerprint" reflections in X-ray diffraction patterns. Thus, the number so-called basal low angle Bragg (00*l*) peaks (when c is the stacking axis) reflections (or (*h*00) or (0*k*0) depending on the stacking axis lattice parameter) below the characteristic 3D perovskite reflections ($d_{(110)}$ = 6.26 Å and $d_{(001)}$ = 6.34 Å for tetragonal $MAPbI_3$), precisely define the number of perovskite layers (Figure 8c).

The change in the dimensionality can readily be seen in the evolution of the optical absorption spectra of the quantum wells. As the 3D perovskite is dimensionally reduced to form the 2D layers, so do the optical absorption edges of the multilayered 2D series which increase in energy with decreasing n value. Using the $(BA)_2(MA)_{n-1}Pb_nI_{3n+1}$ series as a representative example, the absorption edge blue shifts from 1.52 eV (n = ∞) to 2.43 eV (n = 1) (Figure 9b). Meanwhile, in addition to the characteristic halide perovskite sharp absorption edge, an exciton-like peak starts emerging for the n < 5 members, becoming more pronounced as n decreases further. The PL emission follows the same trend, with the pronounced difference that emission peak maxima now coincide with the cross section of the exciton-like feature and the absorption edge, ranging from1.6 eV (n = ∞) to 2.35 eV (n = 1) (Figure 9c). The difference in between emission and absorption in 2D perovskites is not well understood, but it is no different than the corresponding absorption and emission spectra of the 3D perovskites.[222-223]

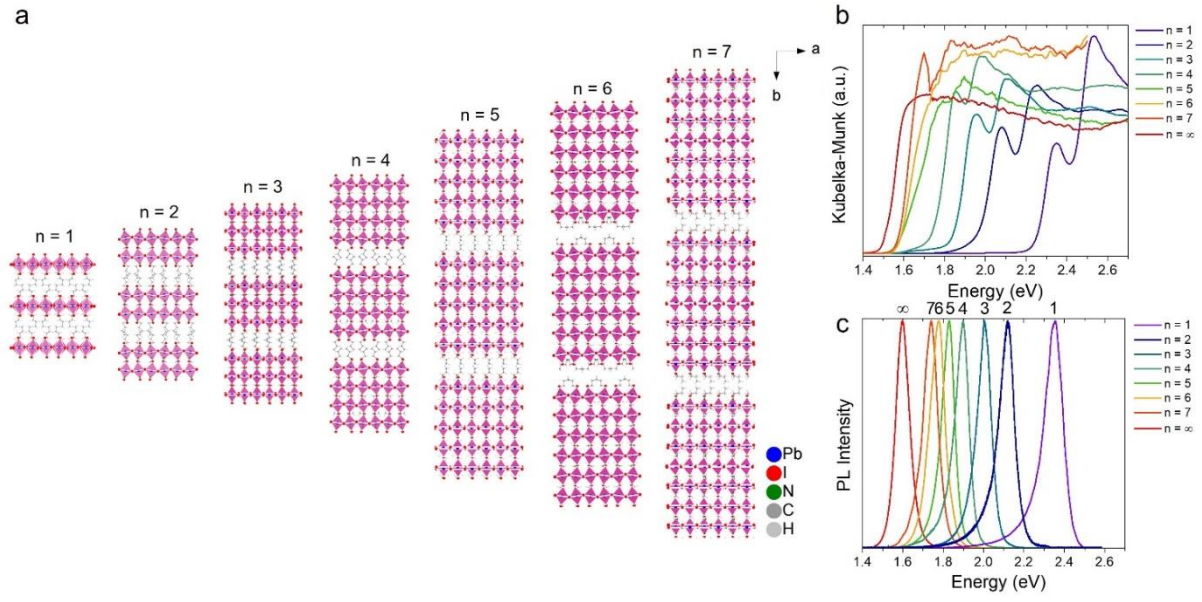

Figure 9. (a) Crystal structures of the RP phase $(BA)_2(MA)_{n-1}Pb_nI_{3n+1}$ (n = 1-7). Optical absorption spectra (b) and steady-state PL spectra (c) of the series.

The complexity, however, of the 2D perovskites increases even more, when one considers the magnitude of the exciton binding energy in 2D halide perovskites, which can be as high as E_b ~500 meV for the n = 1 member[224] at low temperatures. In order to reconcile the huge exciton binding energies with the observed spectra, alternative electronic structure models have been proposed that include the reduction of the effective dimensionality of the halide perovskites from to 2D to quasi-1D models.[127, 225] Even though theoretical investigations in this direction are still ongoing, it is clear that the wide range of tunability offered by the 2D halide provides an excellent playground for designing new materials with unexplored photo-physical properties that could be exploited for advanced optoelectronic applications.

1.6 (100)-Oriented 2D Perovskites: Effect of the Perovskitizer and Solid Solutions

Despite the rapid development of the 2D perovskites in the past five years, it has been remarkably difficult to isolate homologous series of perovskites that contain A-site cations different than MA^+ as "perovskitizers".[131] With the exceptions of the ethylammonium (EA^+) and isopropylammonium (IPA^+) which can produce the line (i.e. not part of a homologous series) 2D compounds $(EA)_2(EA)_2Pb_3X_{10}$[117] (X = Cl, Br) and the metastable $(IPA)_2(IPA)Sn_2I_7$[131], in which the organic cations occupies both A'- and A-site positions in the same compounds, it has not be possible to expand 2D perovskite homologies using the common Cs^+ and/or FA^+ perovskitizers. While on paper this would appear to be possible, the intrinsic instability of Cs^+ and FA^+ towards the formation of the $CsPbI_3$ and $FAPbI_3$ perovskites (both metastable)[50] is apparently transferable to the 2D perovskites as well. In contrast to the 3D perovskites where the thermodynamic phase is a non-perovskitic phase, in 2D perovskites the thermodynamic product appears to be the n = 2

member of the homologous series instead. This has been demonstrated in a number of 2D perovskite families, from RP[121] to ACI[158] and to double perovskites,[138] so that it one could tentatively conclude that it is the perovskitizer itself that inhibits the formation of the homologous series, and in spite the fact that the higher n-members may be possible to form, it is clear that they are not the thermodynamic products of these systems. In order to bypass this obstacle, several researchers have turned to the familiar remedy employed in 3D perovskites:[226] the mixing of cations in the A-site in order to tune the tolerance factor.[227] Although this approach paid some dividends in terms of improved devices when the mixed-compositions were employed to cast thin-films,[123, 228-229] the complete lack of structural characterization leaves the exact composition of the films in question. Nevertheless, in few cases structural characterization has been achieved, showing that incorporation of FA is possible as in the n = 4 DJ perovskite $(3AMP)(MA)_{2.25}(FA)_{0.75}Pb_4I_{13}$ (unpublished results in our lab).

The mixed cation, solid solution approach in 2D perovskites is not limited to the A-site cations but it has been also explored with respect to metal alloying, and halide mixing. These mixing metals or halides in very appealing since they can substantially change the energy band levels in the perovskite. Conceptually, they can also be envisioned to substitute selectively into different layers. These systems, however, have not yet drawn much attention compared to the 3D perovskite analogues[230-232] and they are limited to a handful of examples. The metal alloying has so far been explored in the single-layered mixed Pb and Sn systems of $(HA)Pb_{1-x}Sn_xI_4$[90] and $(BZA)_2Pb_{1-x}Sn_xI_4$[90] (HA = histammonium, BZA = benzylammonium) and in the mixed Sn and Ge system $(PEA)_2Ge_{1-x}Sn_xI_4$.[233] In the former case, the Pb/Sn mixing produces the "typical" for the 3D perovskites anomalous band gap trend, not following the Vegard's law between the two parent

compounds.[234-235] Particularly in the case of $(BZA)_2Pb_{1-x}Sn_xI_4$, all the intermediate (x = 0.25, 0.5, 0.75) compositions have lower band gaps (1.86 eV, 1.84 eV and 1.82 eV) than the pure Sn compound (1.89 eV).

As expected from the 3D perovskite precedence,[236] in the mixed Sn/Ge system the band gap decreases linearly with increasing Sn content, from 2.13 eV for x = 0 to 1.95 eV for x = 0.5. The halide mixing has also seen very little practical study in 2D perovskites (contrary to their extensive exploration in 3D materials[237] and 0D nanocrystals[31]), and it has been mainly employed in Cl/Br systems for the optimization of the quantum yield of white-light emission, such as in (EDBE)$[PbBr_{4-x}Cl_x]$,[113] $EA_4Pb_3Br_{10-x}Cl_x$ and $(PEA)_2PbBr_xCl_{4-x}$,[238] where a small addition of Cl can significantly broaden the PL emission bandwidth. Mixing Br with I in the $(PEA)_2SnI_xBr_{4-x}$ series causesshifts of the excitonic emission from 2.66 eV (x = 0) to 1.97 eV (x = 4), [239] while in the complete series $(PEA)_2PbY_xZ_{4-x}$ the whole spectrum between 2.4eV (Y = I, x = 4) and 3.8eV (Z = Cl, x = 0) can be accessed by adjusting the halide content between Cl, Br and I binary mixtures.[240]

1.7 2D Perovskites in Optoelectronics: Solar Cells, Light-emitting Diodes and Beyond

Several 2D perovskites have been deployed in actual devices showing superb performance. The unique advantages, derive from their nanostructured template and the increased organic component content. Their hybrid inorganic-organic nature allows for the development of multifunctional materials having the added advantage over the 3D perovskites of having enhanced environmental stability,[99] reduced ionic migration,[241] and their easily tunable electrical properties.[100] On the antipode, the increased organic content, slightly dilutes the functionally active

perovskite layers and as a result it decreases somewhat the maximum theoretical light-to-current conversion. The high exciton binding energy limits the diffusion length of the 2D perovskite, where the diffusion length increases with decreasing organic spacer content.[20] Though not as high as the 3D counterpart, the carrier mobility can reach about 10 $cm^2V^{-1}s^{-1}$ for 50% PEA in $MA_{n-1}PEA_2Pb_nI_{3n+1}$ system.[20] Despite starting the race with a small disadvantage, 2D perovskites have proven their worth, as the initial successful demonstration of $(PEA)_2(MA)_2Pb_3I_{10}$,[99] that yielded a 4% power-conversion efficiency (PCE), was superseded from $(BA)_2(MA)_2Pb_3I_{10}$ that exhibited a similar PCE.[100] However, the massive breakthrough came in the form of $(BA)_2(MA)_3Pb_4I_{13}$ which exhibited a PCE of 12.52%[242] using the hot-casting method,[243] showing impressive long-term stability against both light and moisture.

Since the initial demonstration of 2D perovskite solar cells, small improvements were achieved in the BA systems by the mixed A-cation (FA/MA)[228] and (Cs/MA)[229] strategies. Interestingly, higher n-members do not improve the efficiency leading to an optimized PCE ~ 10% for the n = 5 member.[244] The PCE could be further improved by employing the so-called "quasi-2D perovskites", targeting nominal compositions with high layer number (e.g. "n = 10, 50, 60"). This common strategy afforded solar cells with higher efficiency (~15%) for various cations and in different 2D systems (n = 60, PEA;[98] n = 10, ALA (allylammonium)[101]). The work by Sargent et al. illustrated the effect of incorporating different organic spacer (BA, PEA and ALA), where they found the ALA system with the highest lifetime, diffusion length and mobility reached the highest efficiency compared with BA and PEA.[101] This approach was successfully extended to lead bromide based systems, yielding a PCE~10% for "$(BZA)_2(MA)_{49}Pb_{50}Br_{151}$",[245] and also in the Sn-based 2D systems, leading to an improved efficiency and stability for the

"$(PEA)_2(FA)_8Sn_9I_{28}$" (5.94%).[246] Noted that the nominal stoichiometry does not equal to the actual layer thickness, where no evidence was found for the existence of "n = 50". The resulting material of the experimental input needs to be validated by XRD, NMR or other characterization methods. The lack of identification of the material leads to confusion of its corresponding properties and difficulty of comparing materials of the same layer thickness.

2D halide perovskites also perform excellently in the arena of LEDs, in this case displaying an even better performance than the 3D perovskites in certain cases.[247] In the $(PEA)_2(MA)_{n-1}Pb_nX_{3n+1}$ systems,[248] with the n = 5 member demonstrates a significantly higher external quantum efficiency (EQE) at 8.4% for red light emission for x = I, comparing to $MAPbI_3$. For the bromide analogue $(PEA)_2(MA)_4Pb_5Br_{16}$ (nominal composition), it also exhibits a high EQE (7.4%) for green light emission and luminescence (8400 cd/m^2) at low threshold voltage.[105] Interestingly, the BA systems also deliver high quantum yields in the higher "quasi-2D" regime,[249] but the efficiency is much lower for registered low n-members.[250] The high mobility of the Sn-based 2D halide perovskites have also been utilized in field-effect transistor (FET) devices.[251] Early work has clearly showed that FET could be realized for the n = 1 $(PEA)_2SnI_4$ perovskite derivatives[34, 181, 252] producing FET mobilities in the order of up to $\mu \sim 1.4\ cm^2\ V^{-1}\ s^{-1}$ and it has been recently revisited, showing an impressive enhancement to $\mu \sim 15\ cm^2\ V^{-1}\ s^{-1}$.[253]

The above qualities of the 2D perovskites make them obviously very promising for implementation in optoelectronic devices, yet a serious setback in this aspect arises from the fact that, in thin-film form, the 2D perovskites lose one of their main advantage, that of the controlled tunability of the layer number. This loss of synthetic control affects both the excitonic emission wavelength (mostly relevant for Pb-based perovskites) and potentially the loss of FET mobility

(mostly relevant for the Sn-based perovskites). In most cases, a targeted layer thickness in thin film yield a combination of different layer numbers, as seen in the absorption spectra (several slopes) and sometimes low angle peaks in PXRD.[101, 103, 244] Despite the loss of structural integrity, the superior performance of the 2D perovskites persists, and this is likely attributed to the engineered of mixtures of 2D phases that funnel their energy from high band gap to lower band gap phases, in a process which surprisingly reduces nonradiative recombination pathways.

Among the emerging applications that 2D perovskites hold great promise due to their strong excitonic emission at room temperature are in the fields of lasing and photodetectors. These device structures are still in their initial steps of development since they require careful engineering of the device and successful mechanical exfoliation of the 2D materials. Nevertheless, the initial results are very promising as this was demonstrated for the n = 1 $(PEA)_2PbI_4$ polariton laser[254] and the $(BA)_2(MA)_3Pb_4I_{13}$ engineered photodetectors.[107, 255] Such new device design principles may even allow for fast hard radiation scintillation detectors for medical applications since the intrinsic excitonic emission in these systems lies in the order of few picoseconds.[256-257]

The nonlinear optical responses of the 2D halide perovskites, which tend to amplify upon reduction of dimensionality in excitonic systems,[258-259] also been the focus of the early work. The main focus was given to the n = 1 system $(C_6H_{13}NH_3)_2PbI_4$,[260] producing a massive large third-harmonic generation coefficient $\chi^{(3)}$ = 1.6 x 10^{-6} esu at cryogenic temperatures. The successful isolation of higher n-members in $(BA)_2(MA)_{n-1}Pb_nI_{3n+1}$ system allowed for the determination of the $\chi^{(3)}$ coefficients for higher n-members as well, [120] which for the mid-infrared region, room temperature, range between 4.6-5.6 x 10^{-11} esu and could be utilized for medical applications.[32]

Provided that the 2D perovskites could be integrated in suitable device structures, they should have a bright future in the field of optoelectronics.

1.8 Thesis Outline

This thesis will primarily focus on new 2D hybrid halide perovskite materials, from structural characterization, optical properties to optoelectronic applications. Chapter 2-4 are dedicated to the discovery of a series of white-light emitting hybrid perovskite materials, where we have attempted to illustrate the structure-PL relationship by studying their structural distortions and the broadband emission arising from self-trapped excitons states (STEs) at excited states. First, we start with the 2D system (Chapter 2, 3) and laterwards extend to all sorts of structural types ranging from 1D to 3D (Chapter 4).

The second part of the thesis will be focused on the Dion-Jacobson phase 2D perovskites, which we have synthesized the first complete series from single-layer (n = 1) to as high as seven-layer (n = 7). We have resolved the crystal structures and studied their trend in particular, how the Pb-I-Pb affect the optical properties. Following this rule, we have selected a series of compounds to try for solar cell devices. Chapter 5 will be based on the two series of A'$A_{n-1}Pb_nI_{3n+1}$ (A' = 3-(aminomethyl)piperidinium (3AMP) or 4-(aminomethyl)piperidinium (4AMP), A = methylammonium (MA), n = 1-5). Chapter 6 is all about comparison between the seven-layered DJ and RP phases. From iodide-based system to bromide-based system, we compare the effect of the organic spacers 3AMP and 4AMP versus the perovskitizer cations (MA and FA), which will be discussed in Chapter 7. Conclusions and insights will be offered in the end of the thesis, providing our perspectives for future hybrid perovskite material design.

Chapter 2. White-light Emission and Structural Distortion in New Corrugated 2D Lead Bromide Perovskites

Author contributions

Wu, Y.: performed the photoluminescence studies (steady-state and time-resolved).

Stoumpos, C. C and Kanatzidis, M. G.: discussed the results and directed this research.

All authors discussed the results and contributed to revising the manuscript

2.1 Abstract

Hybrid inorganic-organic perovskites are developing rapidly as high-performance semiconductors. Recently, two-dimensional (2D) perovskites were found to have white-light, broadband emission in the visible range and was attributed mainly to the role of self-trapped excitons (STEs). Here, we describe three new 2D lead bromide perovskites incorporating a series of bifunctional ammonium di-cations as templates which also emit white light: 1) α-(DMEN)$PbBr_4$ (DMEN = 2-(Dimethylamino)ethylamine), which adopts a unique corrugated layered structure in space group *Pbca* with unit cell a =18.901(4) Å, b = 11.782(2) Å and c = 23.680(5) Å; 2) (DMAPA)$PbBr_4$ which crystalizes in $P2_1/c$ with a = 10.717(2) Å, b = 11.735(2) Å, c = 12.127(2) Å, β = 111.53(3)°and 3) (DMABA)$PbBr_4$ (DMAPA = 3-(Dimethylamino)-1-propylamine, DMABA = 4-dimethylaminobutylamine) which adopts *Aba*2 with a = 41.685(8) Å, b = 23.962(5) Å, c = 12.000(2) Å. Photoluminescence (PL) studies show a correlation between the distortion of the "$PbBr_6$" octahedron in the 2D layer and the broadening of PL emission, with the most distorted structure having the broadest emission (183 nm full width at half maximum) and longest lifetime (τ_{avg} = 1.39 ns). The most distorted member α-(DMEN)$PbBr_4$ exhibits white-light emission with a color rendering index (CRI) of 73 and correlated color temperature (CCT) of 7863K, producing "cold" white light similar to a fluorescent light source.

2.2 Introduction

Hybrid inorganic-organic halide perovskites exhibit exceptional performance in photovoltaic and optoelectronic device applications.[9, 17, 49, 261-265] In addition to the 3D perovskites, which are the most extensively investigated materials, the two-dimensional (2D) perovskites also show promising results for applications such as stable solar cells and light emitting diodes (LEDs).[242, 266-268] White-light emitting 2D perovskites are attracting strong interest for solid-state lighting applications.[269-270] Having the advantages of easy-processing, low cost, high tunability and color stability, white-light emitting 2D perovskites are promising as single-component light emitters.[271-272] The 2D perovskites derive from the 3D structure by slicing the inorganic lattice along different crystallographic planes, which can be categorized as the (100)-oriented, (110)-oriented and (111)-oriented.[81] The 2D materials have greater room for property tuning (than the 3D perovskites) by changing widely the functional organic cations or increasing the perovskite layer thickness.[139]

Different from the (100) -oriented 2D perovskites, which consist of flat perovskite sheets,

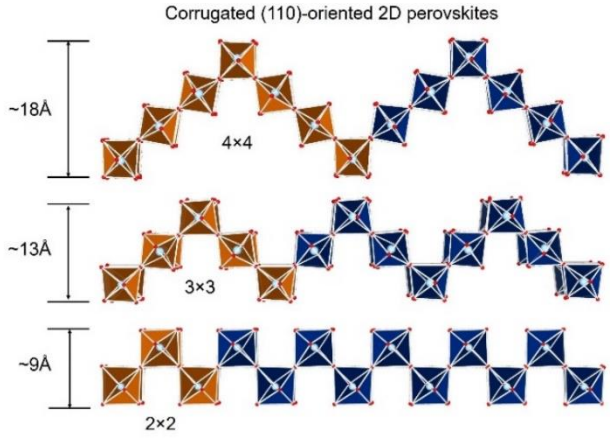

Figure 10. Schematic representation of different structural types of corrugated (110)-oriented members of the 2D perovskite family.

(110)-oriented perovskites have corrugated layers.[273] Depending on where the corrugation occurs in the layers these structures can be defined as 2×2, 3×3, 3×4, 4×4 etc. as shown in Figure 12. We name these "roof-like" (110)-oriented 2D perovskites as "n×n", which n stands for the number of the octahedra composing half of the roof as seen in Figure 1. Because of the more distorted nature of the (110)-oriented perovskites, a broadband photoluminescence (PL) emission presumably arises from self-trapped excitons (STEs) states. STEs are photo-generated transient defects formed by large lattice deformations associated with strong electron-phonon coupling.[274-275] The first (110)-oriented lead bromide perovskite with broad emission $(C_6H_{13}N_3)PbBr_4$ was reported in 2006.[276] Recently, (N-MEDA)[$PbBr_4$][269] (N-MEDA = N1-methylethane- 1,2-diammonium and (EDBE)[$PbBr_4$][270] (EDBE = 2,2′- (ethylenedioxy)bis(ethylammonium) were both reported to have "warm" white-light emission. A (100)-oriented 2D perovskite, $(C_6H_{11}NH_3)_2PbBr_4$, was also found to have white-light emission.[275] White-light emission has been observed in chloride systems such as (EDBE)$PbCl_4$,[270] $(FC_2H_4NH_3)_2PbCl_4$,[166] and 3D lead chloride clusters.[277]

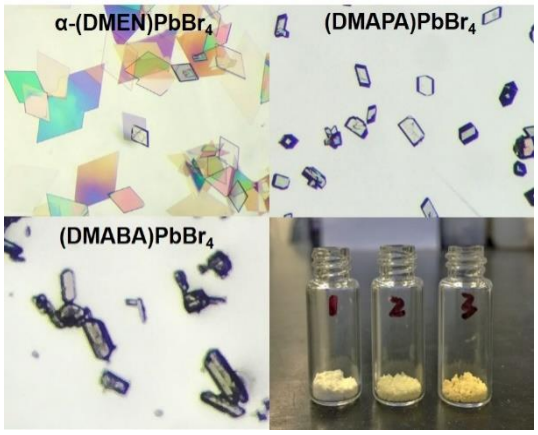

Figure 11. Optical images of α-(DMEN)$PbBr_4$, (DMAPA)$PbBr_4$, (DMABA)$PbBr_4$ and picture of the powdered samples (1 = α-(DMEN)$PbBr_4$, 2 = (DMAPA)$PbBr_4$ and 3 = (DMABA)$PbBr_4$).

Here, we report three new 2D lead bromide perovskites α-(DMEN)$PbBr_4$, (DMAPA)$PbBr_4$ and (DMABA)$PbBr_4$ (Table 1). The α-(DMEN)$PbBr_4$ features a new corrugated "3×3" layer and belongs to the (110)-oriented family (Figure 10), while (DMAPA)$PbBr_4$ and (DMABA)$PbBr_4$ belong to the conventional (100)-oriented type with flat layers as shown in Figure 12. The corrugated 2D perovskite α-(DMEN)$PbBr_4$ exhibits white light emission attributed to its highly distorted structure. The optical properties of the three 2D compounds described here exhibit a strong correlation between the PL emission bandwidth with the degree of distortion in the "$PbBr_6$" octahedra in the crystal structure.

2.3 Experimental Details

2.3.1 Synthesis.

All chemicals were purchased from Sigma-Aldrich and unless otherwise stated, were used as received.

α-(DMEN)$PbBr_4$ and β-(DMEN)$PbBr_4$. An amount of 0.669 g (3 mmol) PbO powder was dissolved in 6.0 ml of 48% hydrobromic acid and 1.0 ml of 50% aqueous H_3PO_2 by heating under stirring for 10 min at 122°C until all PbO dissolved. 0.264 g (5 mmol) of 2-(Dimethylamino)ethylamine was added drop-wise to the previous solution under heating and stirring. Pale yellow and colorless plate-like crystals formed during slow cooling. After leaving the pale yellow plates in mother solution for 10-14 days, all crystals transformed to colorless rhombic shaped crystals of α-(DMEN)$PbBr_4$ (Figure 11). Yield 0.632g (34.1% based on total Pb

content). Pale yellow crystals of β-(DMEN)$PbBr_4$ can be separated through immediate filtration. Though PXRD shows pure the β phase is pure at times, it is not guaranteed for every experiment.

(DMAPA)$PbBr_4$ and (DMABA)$PbBr_4$. An amount of 0.892 g (4 mmol) PbO powder was dissolved in 6.0 ml of 48% hydrobromic acid and 1.0 ml of 50% aqueous H_3PO_2 by heating under stirring for 10 min at 122°C until all PbO dissolved. 1.0 ml of 48% hydrobromic acid was added to protonate 0.408 g (4 mmol) of 3-(Dimethylamino)-1-propylamine. Combining both solution under heating at 122°C for 5 min, pale yellow plate-like crystals formed during slow cooling. Yield 0.973 g (38.5% based on total Pb content). The same method was used to prepare (DMABA)$PbBr_4$, using 0.500 g (4.3 mmol) 4-dimethylaminobutylamine instead. Yield 1.042 g (40.4% based on total Pb content).

2.3.2 Single Crystal X-ray Diffraction

Single crystals of appropriate size were selected for X-ray diffraction experiments. After screening a few diffracted frames to ensure crystal quality, full sphere data were collected using either a STOE IPDS 2 or IPDS 2T diffractometer with graphite-monochromatized Mo Kα radiation (λ = 0.71073 Å), operating at 50 kV and 40 mA under N_2 flow. Integration and numerical absorption corrections on the data were performed using the STOE X-AREA programs. Crystal structures were solved by direct methods and refined by full-matrix least-squares on F^2 using the OLEX2 program package.[278]

2.3.3 Powder X-ray Diffraction (PXRD)

PXRD analysis was performed using a Rigaku Miniflex600 or STOE's STADI MPpowder X-ray diffractometer (Cu Kα graphite, λ = 1.5406 Å) operating at 40 kV/15 mA with a Kβ foil filter.

2.3.4 Optical Absorption Spectroscopy

Optical diffuse reflectance measurements were performed using a Shimadzu UV-3600 UV-VIS-NIR spectrometer operating in the 200-1200 nm region at room temperature. $BaSO_4$ was used as the reference of 100% reflectance for all measurements. The reflectance versus wavelength data generated were used to estimate the band gap by converting reflectance to absorption according to the Kubelka–Munk equation[279]: $\alpha/S = (1-R)^2(2R)^{-1}$, where R is the reflectance, α and S are the absorption and scattering coefficients, respectively.

2.3.5 Steady state and Time-resolved Photoluminescence

Steady-state and time-resolved photoluminescence (TRPL) spectra were acquired using HORIBA Fluorolog-3 equipped with a 450-W xenon lamp and a TCSPC module (diode laser excitation at λ = 375 nm) and an integrating sphere (Horiba Quanta–φ) for absolute photoluminescence quantum yield determination. The spectra were corrected for the monochromator wavelength dependence and photomultiplier response functions provided by the manufacturer. The measurements were performed using dried, powdered polycrystalline samples. No filters were used during the TRPL measurements.

2.4 Results and Discussion

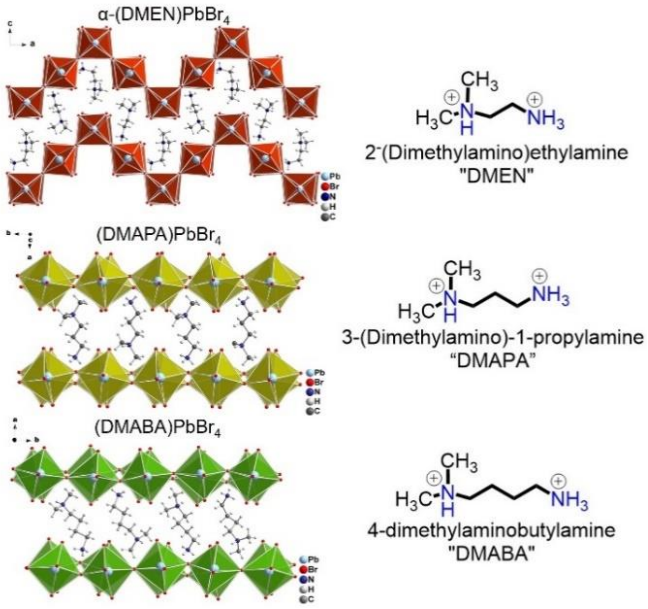

Figure 12. Crystal structures of α-(DMEN)$PbBr_4$, (DMAPA)$PbBr_4$ and (DMABA)$PbBr_4$ and the organic cations incorporated in each structure.

Unlike the relatively common "2×2" structural type,[269-270, 276] α-(DMEN)$PbBr_4$ represents the first example of the "3×3" type of roof-like corrugated structure. The "4×4" structural type is also very rare, as α -[NH_3 $(CH_2)_5NH_3$]SnI_4[280] and α-(HA)SnI_4,[281] are the only two other examples reported. In this work, in order to investigate the effect of the cation length on the inorganic layers, a set of di-cations with formula $[(CH_3)_2NH(CH_2)_nNH_3]^{2+}$ (n = 2, 3 and 4) were used as templates.

Table 1. Structural characteristics and bandgaps of the new compounds reported in this work.

Compound	***2D structural type***	***Space group***	***bandgap***
α-(DMEN)$PbBr_4$	"3×3" (110)	*Pbca*	3.00 eV
(DMAPA)$PbBr_4$	(100)	*$P2_1/c$*	2.88 eV
(DMABA)$PbBr_4$	(100)	*Aba2*	2.85 eV

Table 2. Crystal data and structure refinement for α-(DMEN)$PbBr_4$ and β-(DMEN)$PbBr_4$.

Empirical formula	α-$[(CH_3)_2NH(CH_2)_2NH_3]PbBr_4$	β-$[(CH_3)_2NH(CH_2)_2NH_3]PbBr_4$
Formula weight	617.00	617.00
Crystal system	Orthorhombic	Monoclinic
Space group	*Pbca*	*P2₁/c*
Unit cell dimensions	a = 18.901(4) Å, α = 90° b = 11.782(2) Å, β = 90° c = 23.680(5) Å, γ = 90°	a = 17.625(4) Å, α = 90° b = 11.982(2) Å, β = 90.44(3)° c = 18.724(4) Å, γ = 90°
Volume, Z	5273.3(18) $Å^3$, 16	3953.9(14) $Å^3$, 12
Density (calculated)	3.109 g/cm^3	3.110 g/cm^3
Absorption coefficient	24.878 mm^{-1}	24.885 mm^{-1}
F(000)	4384	3288
θ range for data collection	1.720 to 29.225°	2.761 to 29.182°
Index ranges	-25<=h<=25, -16<=k<=16, -32<=l<=32	-24<=h<=21, -16<=k<=16, -25<=l<=25
Reflections collected	48443	36919
Independent reflections	7132 [R_{int} = 0.1326]	10650 [R_{int} = 0.0596]
Data / restraints / parameters	7132 / 1 / 184	10650 / 0 / 303
Final R indices [I > 2σ(I)]	R_{obs} = 0.0789, wR_{obs} = 0.1415	R_{obs} = 0.0559, wR_{obs} = 0.1319
R indices [all data]	R_{all} = 0.1366, wR_{all} = 0.1628	R_{all} = 0.0889, wR_{all} = 0.1477

$R = \Sigma||F_o|-|F_c|| / \Sigma|F_o|$, $wR = \{\Sigma[w(|F_o|^2 - |F_c|^2)^2] / \Sigma[w(|F_o|^4)]\}^{1/2}$, $w=1/[\sigma^2(Fo^2)+(0.0540P)^2+53.6400P]$ (for α-$[(CH_3)_2NH(CH_2)_2NH_3]PbBr_4$) and $w=1/[\sigma^2(Fo^2)+(0.0850P)^2]$ (for β-$[(CH_3)_2NH(CH_2)_2NH_3]PbBr_4$) where $P=(Fo^2+2Fc^2)/3$. Temperature 293K. Wavelength Mo K*a* 0. 71073 Å.

Interestingly, the shortest cation, DMEN, forms two phases with lead bromide, namely β-(DMEN)$PbBr_4$ which is the kinetic product that upon standing in the mother liquor subsequently transforms to α-(DMEN)$PbBr_4$, the thermodynamic product (Figure 13). The stable phase α-(DMEN)$PbBr_4$ crystallizes in the orthorhombic space group *Pbca* (Table 2). It adopts a layered structure, where each layer is formed with corner-sharing octahedra forming a 3×3 corrugation (Figure 4d). (DMAPA)$PbBr_4$ and (DMABA)$PbBr_4$ crystalize in monoclinic space group *P*2_1*/c*

Table 3. Crystal data and structure refinement for (DMAPA)$PbBr_4$ and (DMABA)$PbBr_4$.

Empirical formula	$[(CH_3)_2NH(CH_2)_3NH_3]PbBr_4$	$[(CH_3)_2NH(CH_2)_4NH_3]PbBr_4$
Formula weight	631.03	645.05
Crystal system	Monoclinic	Orthorhombic
Space group	$P2_1/c$	*Aba2*
Unit cell dimensions	a = 10.717(2) Å, α = 90° b = 11.735(2) Å, β = 111.53(3)° c = 12.127(2) Å, γ = 90°	a = 41.685(8) Å, α = 90° b = 23.962(5) Å, β = 90° c = 12.000(2) Å, γ = 90°
Volume, Z	1418.7(6) $Å^3$, 4	11987(4) $Å^3$, 32
Density (calculated)	2.954 g/cm^3	2.860 g/cm^3
Absorption coefficient	23.122 mm^{-1}	21.896 mm^{-1}
F(000)	1088	9280
θ range for data collection	3.436 to 29.282°	2.590 to 29.186°
Index ranges	-14<=h<=14, -16<=k<=16, -16<=l<=16	-44<=h<=57, -32<=k<=32, -13<=l<=16
Reflections collected	13236	45002
Independent reflections	3822 [R_{int} = 0.0984]	13741 [R_{int} = 0.1118]
Data / restraints / parameters	3822 / 0 / 113	13741 / 7 / 412
Final R indices [I > 2σ(I)]	R_{obs} = 0.0354, wR_{obs} = 0.0599	R_{obs} = 0.0541, wR_{obs} = 0.0919
R indices [all data]	R_{all} = 0.0522, wR_{all} = 0.0641	R_{all} = 0.1250, wR_{all} = 0.1112

$R = \Sigma||F_o|-|F_c|| / \Sigma|F_o|$, $wR = \{\Sigma[w(|F_o|^2 - |F_c|^2)^2] / \Sigma[w(|F_o|^4)]\}^{1/2}$, $w=1/[\sigma^2(Fo^2)+(0.0250P)^2]$ (for $[(CH_3)_2NH(CH_2)_3NH_3]PbBr_4$) and $w=1/[\sigma^2(Fo^2)+(0.0350P)^2]$ (for $[(CH_3)_2NH(CH_2)_4NH_3]PbBr_4$) where $P=(Fo^2+2Fc^2)/3$. Temperature 293K. Wavelength Mo K*a* 0. 71073 Å.

and orthorhombic space group *Aba*2 respectively (Table 3). The layers in these (100)-oriented perovskites consist of corner-sharing octahedra formed along the *bc* crystallographic plane. As the cations become longer, by adding a $-CH_2-$ group (DMAPA) or two $-CH_2-$ groups (DMABA) (Figure 12), the corrugated layers no longer form. This suggests that the formation of the corrugated phase is cation-length dependent and it seems that is the length of the diamine should

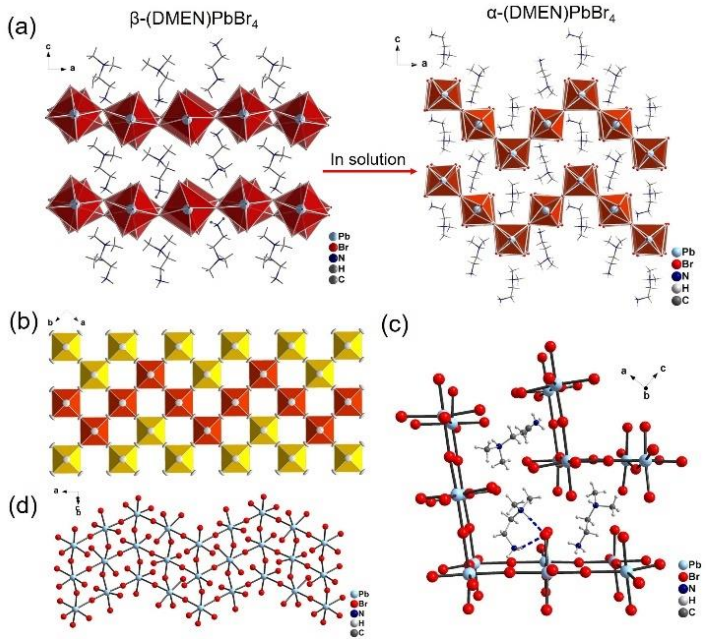

Figure 13. (a) Transformation of β-(DMEN)$PbBr_4$ to α-(DMEN)$PbBr_4$ in the mother liquor solution. (b) Inorganic layer of α-(DMEN)$PbBr_4$ as a fragment sliced out of the 3D framework. (c) Local hydrogen bonding of the "chelating" effect causes the unique bending of the inorganic layers. (d) Detailed representation viewing down the c-axis.

be about the same as the length of two consecutive corner-connected octahedra, see Figure A1. The driving force for the formation of the corrugated inorganic layers, is attributed to a form of "chelating" effect in which the cation chelates the Br atoms through hydrogen atoms. The secondary ammonium group and the primary ammonium group bond closely (Donor-Acceptor distances: 3.40 Å and 3.47 Å) to the bromide anion to form weak hydrogen bonds (Figure 13c, highlighted in blue),[282] resulting in the inorganic sheets folding at a ~90° angle giving rise to a strong corrugation.

The optical bandgaps of the (100)-oriented compounds, (DMAPA)$PbBr_4$ and (DMABA)$PbBr_4$, follow the expected trend,[49, 261] i.e. decreasing bandgaps with increasing Pb-Br-Pb angles.

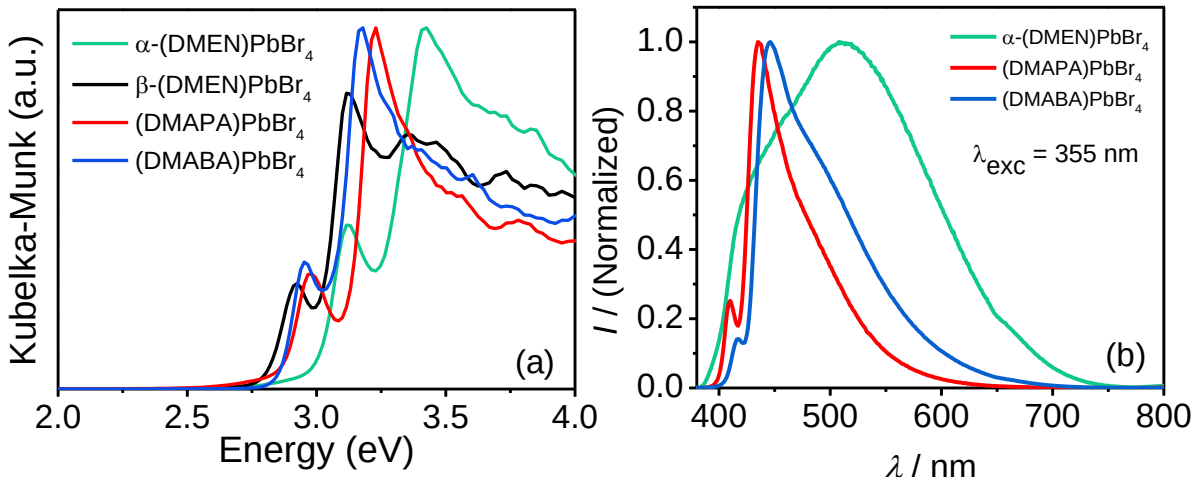

Figure 14. (a) Optical absorption spectra of α-(DMEN)$PbBr_4$ (3.00 eV), β-(DMEN)$PbBr_4$ (2.80 eV), (DMAPA)$PbBr_4$ (2.88 eV) and (DMAPA)$PbBr_4$ (2.85 eV). (b) Steady-state PL emission spectra of α-(DMEN)$PbBr_4$, (DMAPA)$PbBr_4$ and (DMABA)$PbBr_4$excited at 355 nm.

(DMAPA)$PbBr_4$ has a bandgap of 2.88 eV, with an average Pb-Br-Pb angle of 163.9º. (DMABA)$PbBr_4$ on the other hand, has a slightly smaller bandgap (2.85 eV), due to a larger averaged angle of 168.6º. α-(DMEN)$PbBr_4$ has a larger bandgap of 3.00 eV. β-(DMEN)$PbBr_4$ has the smallest bandgap and the largest Pb-Br-Pb angle among all, 2.80 eV and 169.0º respectively, making these two phases distinguishable by color . Excitonic features in all the optical absorption spectra are clearly observed in this series as in other 2D halide perovskites.[281] The nature of the higher energy emission peaks is excitonic. As seen in Figure 14b, the sharp peaks of (DMAPA)$PbBr_4$ (436 nm, 2.84 eV) and (DMABA)$PbBr_4$ (446 nm, 2.78 eV), are in agreement with the bandgap trend and the exciton position at the band edge. The overall broadness of the emission appears to be heavily influenced by the structural distortion, which is evaluated here by the level of the distortion of the "$PbBr_6$" octahedron. We quantitatively measure the magnitude of the

distortion of the octahedra (Δd) using the flowing equation: [283-284]

$$\Delta d = (\frac{1}{6})\sum\left[\frac{d_n - d}{d}\right]^2$$

Where d is the mean Pb-Br bond distance and d_n are the six individual Pb-Br bond distances. In Table 4, the average Δd of the entire structure and individual Δd of different "$PbBr_6$" octahedra are listed. Among the three new compounds, α-(DMEN)$PbBr_4$ has the largest distortion (Δd_{avg} = 17.4×10^{-4}), (where Δd_{avg} is the statistical average of Δd for each crystallographically independent Pb composed octahedron), and also has the broadest emission in this series. Pb1 in α-(DMEN)$PbBr_4$ refers to the "$PbBr_6$" located on the "corner" position, whereas Pb2 is the bridging "$PbBr_6$" linking both Pb1 as seen in Figure A2. Structurally, this Pb1 corresponds to the Pb1 in the reported "2×2" (110)-oriented structure $(C_6H_{13}N_3)PbBr_4$ in Table 4, which in both cases these

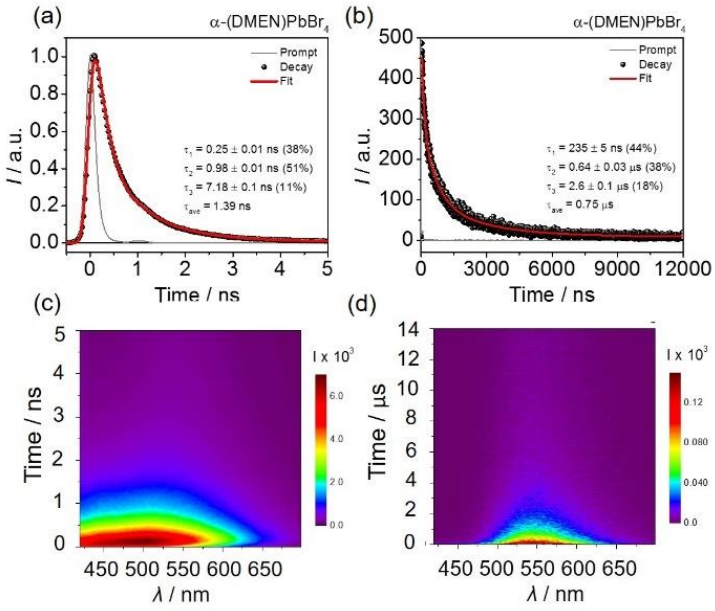

Figure 15. Time-resolved PL of α-(DMEN)$PbBr_4$. Fittings of the (a) emission A at ~ 500 nm (τ_{avg} = 1.39 ns) and (b) emission B at ~ 550 nm (τ_{avg} = 0.75 µs). Two-dimensional TRPL shows the (c) emission A (~ 500 nm) is much short-lived than the (d) emission B at (~ 550 nm).

Table 4. Summary of distortions of individual "$PbBr_6$" octahedra within each structure. Averaged distortions (Δd_{avg}) are given at the end for structures with more than one type of "$PbBr_6$" octahedra.

Compound	$\Delta d_{Pb}1$ ($\times 10^{-4}$)	$\Delta d_{Pb}2$ ($\times 10^{-4}$)	$\Delta d_{Pb}3$ ($\times 10^{-4}$)	$\Delta d_{Pb}4$ ($\times 10^{-4}$)	Δd_{avg} ($\times 10^{-4}$)
α-(DMEN)$PbBr_4$	30.8	4.0	-	-	17.4
(DMAPA)$PbBr_4$	1.1	-	-	-	1.1
(DMABA)$PbBr_4$	3.0	7.4	1.3	5.4	4.3
$(C_6H_{13}N_3)PbBr_4$ (ref.)	26.0	-	-	-	26.0

octahedra are extremely distorted, giving Δd of 30.8×10^{-4} and 26.0×10^{-4}, respectively. Since α-(DMEN)$PbBr_4$ is an extended "3×3" corrugated (110)-oriented perovskite, a second "$PbBr_6$" is present acting as the "bridge" (Figure A2), which is much less distorted ($\Delta d = 4.0\times10^{-4}$). Compared to the (110)-oriented structures, the (100)-oriented (DMAPA)$PbBr_4$ and (DMABA)$PbBr_4$ have much smaller distortion with more regular octahedra. However, the differences still reflect on the broadness of the PL emission, where (DMAPA)$PbBr_4$ has the sharpest emission but the smallest degree of distortion (Δd) of 1.1×10^{-4}. The full width at half maximum (FWHM) of the PL follows a linear trend with increasing octahedral distortion (Figure 16a).

From time-resolved PL experiments, we observed two emission bands (Figure 15, Figure A7-9) from all compounds with distinct decay constant and spectral feature. In Figure 15c-d, the lower wavelength emission band (A), having shorter lifetimes, can be assigned to the combination of band edge emission and STEs emissions. Comparing emission A, α-(DMEN)$PbBr_4$ has the longest lifetime among all (τ_{avg} = 1.39 ns). (DMAPA)$PbBr_4$ and (DMABA)$PbBr_4$ have shorter averaged lifetimes of 0.23 ns and 0.73 ns, respectively. The lifetime of the emission A (band edge

and STEs) is associated with the distortion level of the octahedral as more STEs states are populated for the more distorted structure thus is more long-lasting (Figure 16b). The longer wavelength emission (B) at ~ 550 nm is similar for all compounds with lifetimes in the microsecond time-range (τ = 0.8~1.0 μs). The latter emission (B) might be associated with carriers trapped at permanent defects. Its contribution to the overall steady-state emission, however, is small as compared to the band edge emission and STEs emissions. Further investigations are needed, and particularly magnetic-field effect and optically-detected electron spin resonance spectroscopies will be helpful.[285-288] We also compared the thin-films of α-(DMEN)$PbBr_4$ and the reported (N-MEDA)[$PbBr_4$][269] in time-resolved PL measurements (Figure A10-11). Film samples were prepared by dissolving 0.5 mmol powder sample of the above compounds in 1 ml dimethylformamide (DMF). Then the solution was spin-coated onto plain glass substrate at 2500 rpm for 20 s. α-(DMEN)$PbBr_4$ shows a slower decay curve than (N-MEDA)[$PbBr_4$], possibly because of the more corrugated structure. Similar to the polycrystalline powder samples, the PL emission of the thin films consist of band edge emission and STEs emission at shorter wavelength which decays much faster than the prolonged emission B (carriers trapped at permanent defects). Overall, the lifetime of the PL emission A (band edge and STEs) increases with the distortion level of the crystal structure (Figure 15b), while emission B is relatively constant for all compounds.

Different from the previously reported (110)-oriented perovskites (N-MEDA)$PbBr_4$[269] and (EDBE)$PbBr_4$,[270] which have “warm” white-light and CCT below 5000K, α-(DMEN)$PbBr_4$ has an intense emission at the bluer visible region, resulting in a “cold” white-light emission with CCT

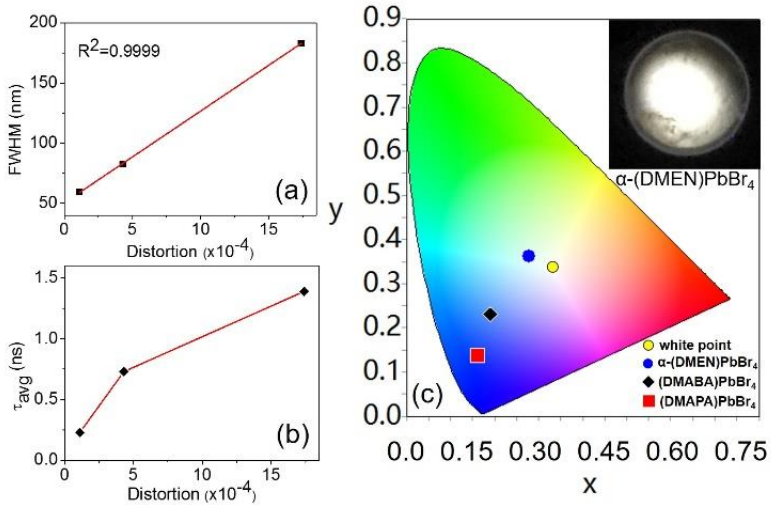

Figure 16. (a) Full width at half maximum (FWHM) of all compounds follows a linear trend with increasing octahedral distortion. (b) The τ_{avg} of emission A also increases with with increasing octahedral distortion. (c) Chromaticity coordinates of α-(DMEN)$PbBr_4$ (0.28, 0.36), (DMAPA)$PbBr_4$ (0.17, 0.16), (DMABA)$PbBr_4$ (0.20, 0.26) and white point (0.33, 0.33) in 1931 color space chromaticity diagram. Inserted: white light emission picture of polycrystalline α-(DMEN)$PbBr_4$ excited at 365nm.

of 7843K, more suitable for "cold" white-light LEDs. The chromaticity coordinates and CCT are calculated using the ColorCalculator by OSRAM Sylvania, Inc. In Figure 16c, α-(DMEN)$PbBr_4$ has a chromaticity coordinates of (0.28, 0.36). The deviation from the white point (0.33, 0.33) also results from the partial contribution of the blue emission. The color rendering index (CRI) reflects the accuracy of the light source compared to daylight. Most commercially available LEDs have CRI around 80. In this case, the CRI of α-(DMEN)$PbBr_4$ is slightly lower (CRI = 73), which is comparable to fluorescent light source (CRI ~ 72).[289]

2.5 Conclusions

In conclusion, we have identified three new 2D lead bromide perovskite compounds which exhibit strong effects of the organic cations that influence the templating of the inorganic layers

and their optical properties. We observe a structure-PL correlation which predicts that the larger the octahedral distortion of the inorganic layer, the broader the bandwidth of the PL emission. In addition, the averaged lifetime of the emission A (band edge and STEs) increases with the distortion level of the octahedral in the crystal structure. Among these three compounds, an intriguing new "3×3" type of corrugated (110)-oriented 2D perovskite, α-(DMEN)$PbBr_4$, is stabilized by a special "chelating effect" of hydrogen bonding interactions. Because of this effect, α-(DMEN)$PbBr_4$ has the most distorted structure, which leads to broad white-light emission and has CRI comparable to a fluorescent light source. This correlation can serve as a design tool of the PL emission properties in other 2D perovskite systems.

Chapter 3. Tunable White-light Emission in Single Cation Templated Three-layered 2D Perovskites $(CH_3CH_2NH_3)_4Pb_3Br_{10-x}Cl_x$

Reprinted with permission from Mao, L.; Wu, Y., Stoumpos, C. C.; Traore, B.; Katan, C.; Even, J.; Wasielewski, M. R.; Kanatzidis, M. G. "Tunable White-light Emission in Single Cation Templated Three-layered 2D Perovskites $(CH_3CH_2NH_3)_4Pb_3Br_{10-x}Cl_x$." *J. Am. Chem. Soc.*, **2017**, *139* (34), 11956–11963.

Author contributions

Wu, Y.: performed the photoluminescence studies (steady-state and time-resolved).

Traore, B.; Katan, C.; Even, J.: performed the DFT calculations.

Stoumpos, C. C and Kanatzidis, M. G.: discussed the results and directed this research.

All authors discussed the results and contributed to revising the manuscript.

3.1 Abstract

Two-dimensional (2D) hybrid halide perovskites come as a family $(B)(A)_nPb_nX_{3n+1}$ (B, A= cations; X= halide). These perovskites are promising semiconductors for solar cells and optoelectronic applications. Among the fascinating properties of these materials is white-light emission, which has been mostly observed in single-layered 2D lead bromide or chloride systems (n = 1), where the broad emission comes from the transient photoexcited states generated by self-trapped excitons (STEs) from structural distortion. Here we report a multi-layered 2D perovskite (n = 3) exhibiting a tunable white-light emission. Ethylammonium (EA^+) can stabilize the 2D perovskite structure in $EA_4Pb_3Br_{10-x}Cl_x$ (x = 0, 2, 4, 6, 8, 9.5, 10) with EA^+ being both the A and B cations in this system. Because of the larger size of EA, these materials show a high distortion level in their inorganic structures with $EA_4Pb_3Cl_{10}$ having a much larger distortion than $EA_4Pb_3Br_{10}$, which results in broadband white-light emission in $EA_4Pb_3Cl_{10}$, while $EA_4Pb_3Br_{10}$ has narrow blue emission. The averaged lifetime of the series decreases gradually from the Cl end to the Br end, indicating the larger distortion also prolongs the lifetime (more STE states). The band gap of $EA_4Pb_3Br_{10-x}Cl_x$ ranges from 3.45 eV (x = 10) to 2.75 eV (x = 0), following the Vegard's law. First-principles Density Functional Theory calculations (DFT) show both $EA_4Pb_3Cl_{10}$ and $EA_4Pb_3Br_{10}$ are direct band gap semiconductors. The color rendering index (CRI) of the series improves from 66 ($EA_4Pb_3Cl_{10}$) to 83 ($EA_4Pb_3Br_{0.5}Cl_{9.5}$), displaying high tunability and versatility of the title compounds.

3.2 Introduction

Halide perovskite materials with hybrid organic-inorganic structures have captured the broad interest of the scientific community because their promises high performance photovoltaic (PV) and optoelectronic devices.[290-298] Among the leading materials, the $APbX_3$ perovskites are singled-out because they deliver the highest PV performance. However, the further utilization of the materials is hampered by the limited options in varying the A^+ cation which is limited to Cs, MA^+($MA^+ = CH_3NH_3^+$) and FA^+($FA^+ = HC(NH_2)_2^+$) which is due to stereochemical restrictions. Attempts to find alternative cations typically lead to unfavorable structures which do not have desirable semiconducting properties. An exception to this trend is seen in the case of 2D perovskites. Decreasing the dimensionality from three-dimensional (3D) to two-dimensional (2D), more versatile organic cations can be incorporated as templates to produce new structural types.[299] Compared to the single-layered 2D perovskites,[83, 90] multi-layered 2D perovskites are less intensively investigated[34, 273, 300] but do promise superior properties in applications such as solar cells[242, 301-303] and LEDs.[106, 304] Multi-layered 2D systems also show better chemical stability than the 3D perovskite materials, as the longer organic cations are hydrophobic, making the devices moisture-stable.[242, 301-302] As the "in-betweens" of the 3D compounds and the single-layered 2D compounds, multi-layered 2D perovskites of the formula $(B)(A)_nPb_nX_{3n+1}$ (B, A= cations; X= halide) can be tuned through multiple pathways: (1) layer thickness (i.e. value of n);[303, 305-306] (2) halide anion;[307] (3) metal cation; (4) organic spacer cation. All of these tunable components can

be used to tailor the optical and electronic properties of the materials,[124, 306] to design materials for specific applications.

One of the emerging applications for perovskite materials comes in white light-emitting diodes (WLEDs) for solid state lighting. Single component white-light emitters have an easily controlled emission, better color rendering capability and reproducibility comparing to the multicomponent phosphors.[308-309] Unlike the doping strategy (rare earth ion into a host matrix), the energy transfer approach, white-light emitting nanocrystals[310-313] or other hybrid organic-inorganic white-light emitters,[309, 314] broad band emissions in perovskite materials are usually associated with structural distortions,[315-316] which gives rise to self-trapped excitons (STEs) due to strong electron-phonon coupling after photoexcitation.[317-318] Most of the reported white-light emitting perovskite materials up to date are single-layered 2D lead bromide or chloride perovskites, for instance $(C_6H_{13}N_3)PbBr_4$,[276] (N-MEDA) $PbBr_4$[269] (N-MEDA = N1-methylethane- 1,2-diammonium), (EDBE)$PbCl_4$, (EDBE)$PbBr_4$[270] (EDBE = 2,2′- (ethylenedioxy)bis(ethylammonium), $(C_6H_{11}NH_3)_2PbBr_4$[275], α-(DMEN)$PbBr_4$ (DMEN = 2-(dimethylamino)ethylamine)[315], $(C_6H_5C_2H_4NH_3)_2PbCl_4$[319] and (AEA)$PbBr_4$ (AEA = 3-(2-ammonioethyl)anilinium).[316]

In this work, we report the first example of multi-layered 2D perovskite with tunable white-light emission obtained from the use of ethylammonium ($CH_3CH_2NH_3^+$ = EA^+) cation. $EA_4Pb_3Cl_{10}$, $EA_4Pb_3Br_{10}$ and the $EA_4Pb_3Br_{10-x}Cl_x$ solid solution are synthesized, and they represent a very rare example of a multilayer perovskite made of a single cation acting both as the B and A-cation in

the structure of $(B)(A)_nPb_nX_{3n+1}$. The crystal structures of the $EA_4Pb_3Cl_{10}$ and $EA_4Pb_3Br_{10}$ perovskites are similar but the chloride analog is heavily distorted with respect to the bromide. The greater distortion is the result of the relatively large size of EA than the standard A-cations and smaller cage size of the chloride analog compared to the bromide. The PL emission reflects the structural distortion as $EA_4Pb_3Cl_{10}$ has a broadband white-light emission and $EA_4Pb_3Br_{10}$ has a narrow bandwidth of blue emission. To maximize the effect of STEs for broad emission, we further tune the compositions in the solid solutions, and find two of the intermediate compounds $EA_4Pb_3Br_{10-x}Cl_x$ (x = 8, 9.5) which have more optimized white-light emissions than $EA_4Pb_3Cl_{10}$. This provides a useful handle for controlling the photoluminescence (PL) properties in hybrid perovskite systems by utilizing the structure-PL relationship.

3.3 Experimental Details

3.3.1 Synthesis

Materials. PbO (99.9%), $PbCl_2$ (98%), $PbBr_2$ (98%), ethylamine hydrochloride (98%), hydrochloric acid (ACS reagent, 37%) and hydrobromic acid (ACS reagent, 48%) were purchased from Sigma-Aldrich and used as received.

Synthesis of $EA_4Pb_3Cl_{10}$. An amount of 1.338g (6 mmol) 99.9% PbO powder was dissolved in 20 ml of 37% hydrochloric acid by heating under stirring for 15 min at 110°C until solution turned colorless. 0.652g (8 mmol) of solid ethylamine hydrochloride was added directly to the above solution under heating and then kept under stirring until about 70% of the above solution

was evaporated. If the solution is not concentrated enough, then $PbCl_2$ co-precipitates. Transparent rectangular plate-like crystals precipitated during slow cooling to room temperature Yield 1.237g (53.3% based on total Pb content).

Synthesis of $EA_4Pb_3Br_{10}$. An amount of 1.338g (6 mmol) 99.9% PbO powder was dissolved in 10 ml of 48% hydrobromic acid by heating under stirring for 10 min at 122°C until solution turned colorless. 0.652g (8 mmol) of ethylamine hydrochloride was added directly to the above solution under heating. Yellow rectangular plate-like crystals precipitated during slow cooling. Yield 1.218g (37.9% based on total Pb content).

Synthesis of $EA_4Pb_3Br_{10-x}Cl_x$ (x = 9.5, 8, 6, 4, 2). Using solid-state grinding method, $EA_4Pb_3Br_{10-x}Cl_x$ (x = 9.5, 8, 6, 4, 2) were prepared with pre-synthesized EACl and EABr with $PbCl_2$ and $PbBr_2$. In a typical procedure for x = 8, 0.652g (8 mmol) of EACl with 1.112g (4 mmol) $PbCl_2$ and 0.734g (2 mmol) $PbBr_2$ was mixed and ground for 5 min. The homogenous mixture was annealed in the vacuum oven at 80°C for 2 hours. The rest of the series were synthesized using the same method with stoichiometric ratio of the cation source and anion source. Yield > 90%. The purity of the compounds was checked by Powder X-ray Diffraction (PXRD).

3.3.2 High-resolution Powder X-ray Diffraction and Single Crystal X-ray Diffraction

High resolution synchrotron powder diffraction data were collected using beamline 11-BM at the Advanced Photon Source (APS), Argonne National Laboratory using an average wavelength of 0.517040 Å. Discrete 9 detectors covering an angular range from 0 to 4º 2θ are scanned over a

26º 2θ range, with data points collected every 0.001º 2θ and scan speed of 0.1º/s. Le Bail analysis was performed with the Jana2006 package.

Full sphere data were collected after screening for a few frames using either a STOE IPDS 2 or IPDS 2T diffractometer with graphite-monochromatized Mo Kα radiation (λ = 0.71073 Å) (50 kV/40 mA) under N_2. The collected data was integrated and applied with numerical absorption corrections using the STOE X-AREA programs. Crystal structures were solved by charge flipping and refined by full-matrix least squares on F^2 with the Jana2006 package.

3.3.3 Optical Absorption Spectroscopy

Optical diffuse reflectance measurements were performed using a Shimadzu UV-3600 UV-VIS-NIR spectrometer operating in the 200–1000 nm region using $BaSO_4$ as the reference of 100% reflectance. The band gap of the material was estimated by converting reflectance to absorption according to the Kubelka–Munk equation[320]: $\alpha/S = (1–R)^2(2R)^{-1}$, where R is the reflectance and α and S are the absorption and scattering coefficients, respectively.

3.3.4 Steady State and Time-resolved Photoluminescence

Steady-state and time-resolved photoluminescence (TRPL) spectra were acquired using HORIBA Fluorolog-3 equipped with a 450-W xenon lamp and a TCSPC module (diode laser excitation at λ = 375 nm) and an integrating sphere (Horiba Quanta–φ) for absolute photoluminescence quantum yield determination. The spectra were corrected for the

monochromator wavelength dependence and photomultiplier response functions provided by the manufacturer.

3.3.5 Electronic Structure Calculations

The calculations were performed within the Density Functional Theory (DFT)[321-322] as implemented in SIESTA package[323] with a basis set of finite-range of numerical atomic orbitals. We used the van der Waals density functional with C09 exchange (VDWC09)[324] to describe the exchange-correlation term. This functional has proven to provide superior description of experimental lattice constants similar to those obtained with optimized GGA based PBEsol functional in solids.[325] Norm-conserving Troullier-Martins pseudopotentials were used for each atomic species to account for the core electrons.[326] $1s^1$, $2s^2 2p^2$, $2s^2 2p^3$, $3s^2 3p^5$, $4s^2 4p^5$ and $5d^{10} 6s^2 6p^2$ were used as valence electrons for H, C, N, Cl, Br and Pb respectively. Polarized Double-Zeta (DZP) basis set with an energy shift of 200 meV and a real space mesh grid energy cutoff of 200 Rydberg were used for the calculations. The Brillouin zone was sampled with 2×2×6 and 4×4×1 Monckhorst-Pack grids for the primitive cell and slab systems respectively. The electronic and dielectric properties were calculated with the experimental lattice parameters, and atomic coordinates were transformed to their primitive cells whenever applicable. Since the positions of H are not well resolved in these structures, they were optimized using VDW-C09 functional within the primitive cells while keeping the other atomic sites fixed. Spin-orbit coupling was taken into account in the calculation of the electronic band structures, although it was not

considered in the high-frequency dielectric constant computations. For spin-orbit coupling, the revised PBE (revPBE) functional[327] was used. For the high-frequency dielectric constant profiles, slabs based on the respective systems were constructed, and an electric field of 0.01 eV/Å was applied along the [001] direction with the relaxation of the sole electron density as described elsewhere.[328-329]

3.4 Results and Discussion

$EA_4Pb_3X_{10}$ (X = Br, Cl) belongs to the homologous series of layered perovskite phases $(B)(A)_nPb_nX_{3n+1}$ as defined above. In these structures B is the spacer cation that separates the inorganic layers, and A occupies the perovskite cages. In this case, EA acts as both the spacing A

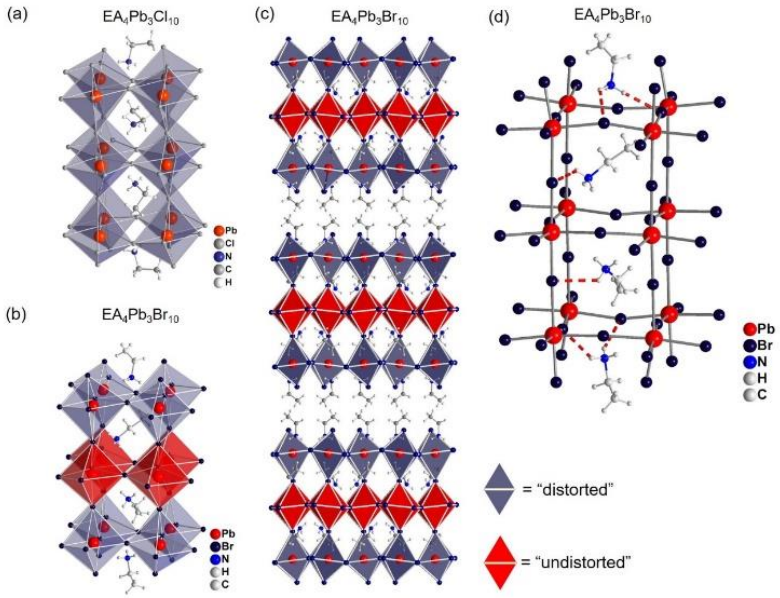

Figure 17. Structure fragment of the three-layered (a) $EA_4Pb_3Cl_{10}$ and (b) $EA_4Pb_3Br_{10}$. (c) Crystal structure of $EA_4Pb_3Br_{10}$, where the inner-layers compose of "undistorted" octahedra and outer-layers compose of "distorted" octahedra. (d) Hydrogen bonding network in $EA_4Pb_3Br_{10}$.

cation and the "perovskitizer" A' cation,[330] forming the three-layered (n = 3) structure. The $EA_4Pb_3Cl_{10}$ is the only known three-layered halide perovskite with a single kind of cation reported to date.[331] We have investigated this system with other halides (Br and I) and found that Br^- can also stabilize the three-layered structure, while I^- cannot form the analogue with EA^+. Instead it forms a one-dimensional (1D) perovskite featuring chains of face-sharing octahedra.[332] In 3D $APbX_3$ perovskites, MA^+, FA^+ and Cs^+ are the only known cations that can fit in the framework. Because of the larger size of EA^+ cation the n = 3 perovskite layers are highly distorted to accommodate the extra $-CH_2-$ group as seen in Figure 17a. Compared to the chloride structure, the bromide analogue has undistorted "inner-layer" and similarly very distorted "outer-layer" (Figure

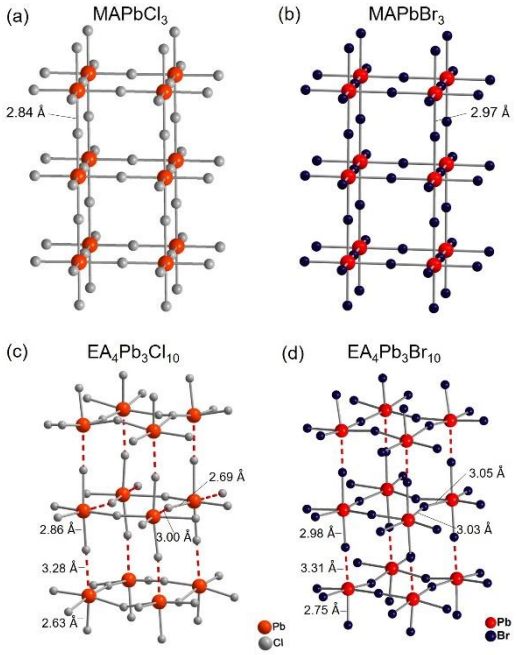

Figure 18. Pb-X (X = Cl or Br) bond lengths in (a) $MAPbCl_3$ (b) $MAPbBr_3$ (c) $EA_4Pb_3Cl_{10}$ and (d) $EA_4Pb_3Br_{10}$. The organic cations have been omitted for clarity.

Table 5. Crystal data and structure refinement for $EA_4Pb_3Cl_{10}$ and $EA_4Pb_3Br_{10}$ at 293 K.

Empirical formula	$(CH_3CH_2NH_3)_4Pb_3Cl_{10}$	$(CH_3CH_2NH_3)_4Pb_3Br_{10}$
Formula weight	1160.5	1609
Temperature	293 K	
Wavelength	0.71073 Å	
Crystal system	Orthorhombic	
Space group	$A2_1ma$	$C2cb$
Unit cell dimensions	a = 8.024(8) Å, α = 90° b = 45.498(7) Å, β = 90° c = 8.080(3) Å, γ = 90°	a = 8.4267(12) Å, α = 90° b = 46.351(5) Å, β = 90° c = 8.4298(10) Å, γ = 90°
Volume	2949(12) $Å^3$	3292.5(7) $Å^3$
Z	4	4
Density (calculated)	2.6136 g/cm^3	3.2459 g/cm^3
Absorption coefficient	17.994 mm^{-1}	27.443 mm^{-1}
F(000)	2096	2816
Crystal size	0.0224 x 0.0689 x 0.1045 mm^3	0.0337 x 0.0753 x 0.0860 mm^3
θ range for data collection	2.86 to 29.21°	3.45 to 29.15°
Index ranges	-10<=h<=5, -51<=k<=62, -11<=l<=10	-11<=h<=11, -62<=k<=63, -10<=l<=11
Reflections collected	6096	14688
Independent reflections	1920 [R_{int} = 0.1312]	5228 [R_{int} = 0.073]
Completeness to θ = 29.15°	95%	94%
Refinement method	Full-matrix least-squares on F^2	
Data / restraints / parameters	1920 / 6 / 86	5228 / 6 / 81
Goodness-of-fit	2.50	3.14
Final R indices [I>2σ(I)]	R_{obs} = 0.0762, wR_{obs} = 0.1384	R_{obs} = 0.0964, wR_{obs} = 0.1753
R indices [all data]	R_{all} = 0.1124, wR_{all} = 0.1441	R_{all} = 0.1496, wR_{all} = 0.1854
Largest diff. peak and hole	3.76 and -2.82 e·$Å^{-3}$	2.83 and -3.84 e·$Å^{-3}$

$R = \Sigma||F_o|-|F_c|| / \Sigma|F_o|$, $wR = \{\Sigma[w(|F_o|^2 - |F_c|^2)^2] / \Sigma[w(|F_o|^4)]\}^{1/2}$ and $w=1/(\sigma^2(I)+0.0004I^2)$

17c). Since the ionic radius[333] of Br^-(1.95 Å) is larger than Cl^- (1.81 Å),[333] it is reasonable that it

can better accommodate the EA^+ cation in the structure.

$EA_4Pb_3Cl_{10}$ crystallizes in the polar orthorhombic space group $A2_1ma$ (≡ $Cmc2_1$), while $EA_4Pb_3Br_{10}$ crystallizes in the polar orthorhombic space group $C2cb$ (≡ $Aba2$). Their detailed crystallographic parameters are given in Table 5. Both compounds consist of three layers of corner-connected $[PbX_6]^{4-}$octahedra separated from one another with bilayers of EA^+ cations as "spacers" as seen in Figure 17c. Within the three-layers, EA^+ cations which act as "perovskitizers" filling the voids of the perovskite cavities (Figure 17d). The three-layer configuration requires a middle layer (the "inner-layer") and two symmetry related exterior layers (the "outer-layer"). From the lead halide framework, we can see that the distortion results in one short Pb-X bond and one long Pb-X bond from the [Pb-X-Pb] unit. In the 3D structure $MAPbCl_3$ and $MAPbBr_3$ (Figure 18a and 18b), all Pb-X bonds have the same length of 2.84 Å and 2.97 Å, respectively. For $EA_4Pb_3Cl_{10}$ however, short and long bond length combinations are seen in all directions. For example, in Figure 18c, the vertical Pb-Cl bonds of the bottom-left octahedron have length of 3.28 Å and 2.63 Å, which are respectively much longer and shorter than the Pb-Cl bond length (2.84 Å) in the 3D structure. The same "short-long" combinations have been observed for the "inner-layer" octahedra, as the horizontal Pb-Cl bond length of the middle-left octahedron in Figure 2c are 2.69 Å and 3.00 Å. For $EA_4Pb_3Br_{10}$, the distortion of the [Pb-X-Pb] unit only happens in the "outer-layer", as the bond lengths (3.05 Å and 3.03 Å) of the "inner-layer" are more equal and close to the 3D structure bond length (2.97 Å). To quantify the degree of the distortion, we define the octahedral distortion based on Pb-X bond lengths,[334-335]

$$\Delta \boldsymbol{d} = \left(\frac{1}{6}\right)\sum\left[\frac{d_n - d}{d}\right]^2 \quad (1)$$

where d is the mean Pb-X bond distance and d_n are the six individual Pb-X bond distances (X = Br, Cl). In Figure 19, the "outer-layer" octahedra (layers next to the organic spacers, octahedra marked in purple in Figure 17c) of both $EA_4Pb_3Cl_{10}$ and $EA_4Pb_3Br_{10}$ have very high distortion level ($\Delta \boldsymbol{d}$) of 45.09×10^{-4} and 40.74×10^{-4}, respectively. As for the "inner-layer" octahedra, $EA_4Pb_3Cl_{10}$ still has a high distortion of 13.15×10^{-4} and $EA_4Pb_3Br_{10}$ has regular octahedra which are relatively undistorted ($\Delta \boldsymbol{d}$ = 0.96×10^{-4}). Structural distortions are further manifested in the octahedral tilting defined by two tilt-angles β and δ as illustrated in Figure 20. These angles are linked to the evolution of the band gap with respect to the structural deformation of the perovskite. For all the layers except the β of the inner layers, β and δ (reported in Figure 19b and Table B2)

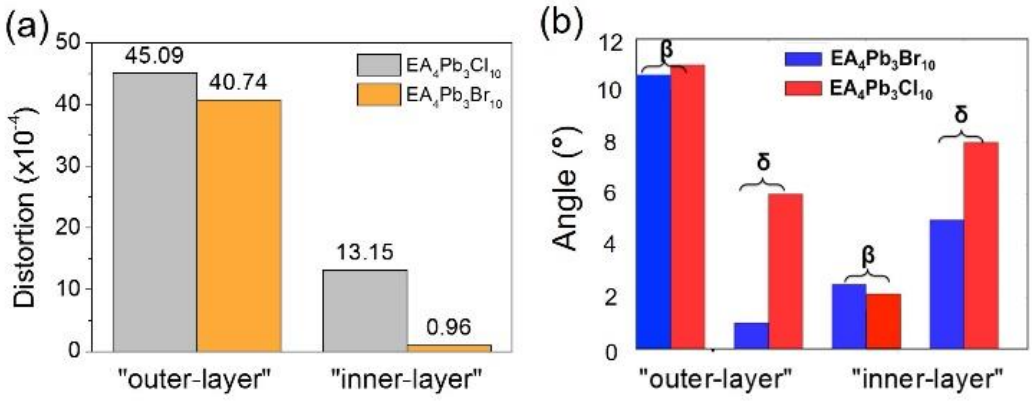

Figure 19. Comparison of the distortion level of "outer-layer" and "inner-layer" in $EA_4Pb_3Cl_{10}$ and $EA_4Pb_3Br_{10}$. From (a) Δ*d* defined by equation (1) and (b) distortion angles defined in Figure 4.

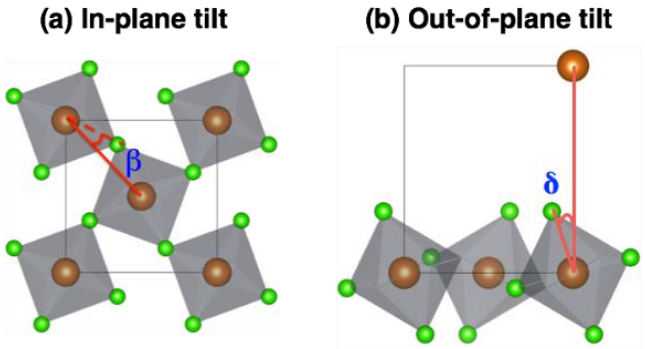

Figure 20. Definition of (a) the in-plane tilt angle β and (b) the out-of-plane tilt angle δ. β is the angle between the projected Pb1-X and Pb1-Pb2 to the plane perpendicular to the stacking axis. δ is the angle between Pb1'-X' and Pb1'-Pb2'. Note that Pb2' is the periodic image of Pb1'.

are larger for $EA_4Pb_3Cl_{10}$ as compared to $EA_4Pb_3Br_{10}$, which is consistent with the more distorted Cl-based structure.

The advantage of a single cation as both the A cage cation and the spacer is that phase purity is much improved comparing to other 2D systems as it does not form other neighboring phases (e.g. n = 2, 4) because they are presumably less stable. This allows for the $EA_4Pb_3Br_{10-x}Cl_x$ (x = 2, 4, 6,

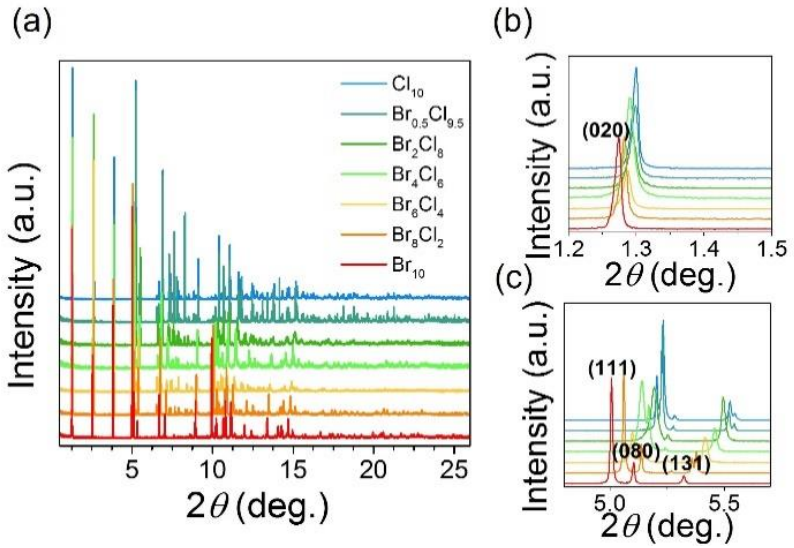

Figure 21. (a) High resolution PXRD of the $EA_4Pb_3Br_{10-x}Cl_x$ (x = 0, 2, 4, 6, 8, 9.5, 10) solid solution (synchrotron wavelength = 0.51704) (b) and (c) Peaks shift from higher angles to lower angles, suggesting increasing unit cell from x = 10 to x = 0.

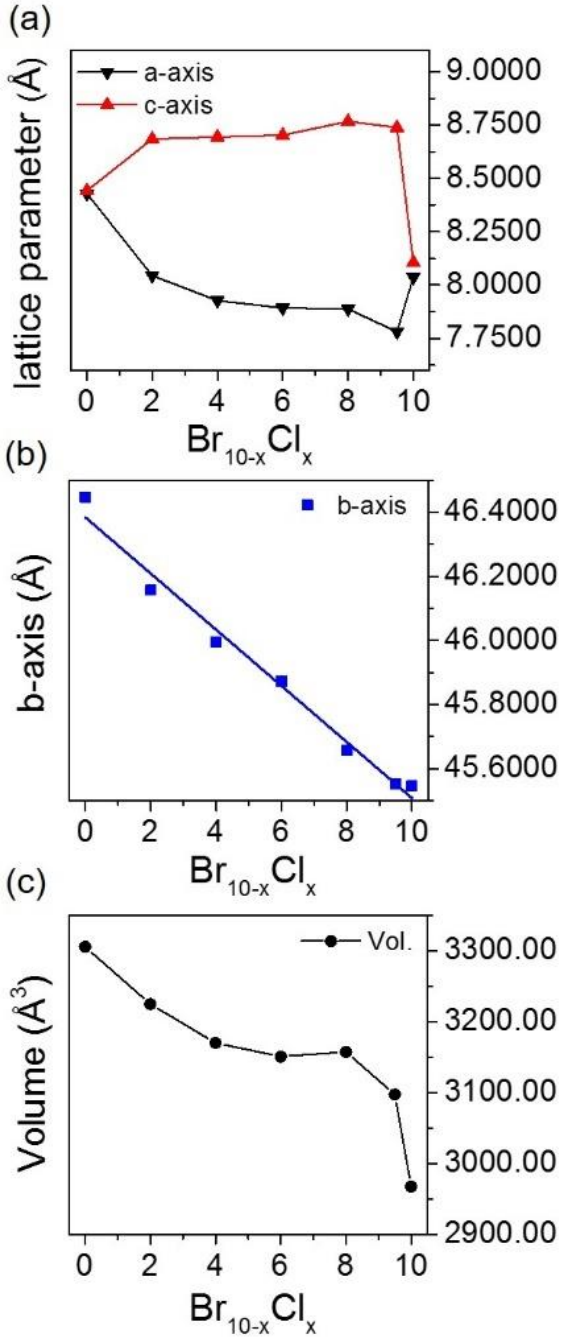

Figure 22. (a) (b) and (c) Unit cell parameters of the $EA_4Pb_3Br_{10-x}Cl_x$ (x = 0, 2, 4, 6, 8, 9.5, 10) solid solution.

8, 9.5) solid solutions to be readily synthesized as pure phases using solid-state grinding at ~80°C. High-resolution PXRD data of the entire $EA_4Pb_3Br_{10-x}Cl_x$ series were collected using the beamline 11-BM at the APS (Figure 21). The lattice parameters of the solid solutions were extracted using Le Bail refinement method. Interestingly, the a and c axes are very similar to each other for both

$EA_4Pb_3Br_{10}$ and $EA_4Pb_3Cl_{10}$. However, the intermediate compositions have a relatively large difference between a and c, for example $EA_4Pb_3Br_{0.5}Cl_{9.5}$ has the largest difference (a = 7.7807(2) (Å)) and c = 8.7393(2) (Å)), as seen in Figure 22a. The long axis, b, which runs perpendicular to the layers, decreases linearly from $EA_4Pb_3Br_{10}$ (b = 46.4483(3) Å) to $EA_4Pb_3Cl_{10}$ (b = 45.5452(6) Å). The unit cell volume also decreases from the Br end to the Cl end but not in a linear fashion as seen in Table 6 and Figure 22c. The anomaly in the evolution of the a and c axes for the intermediate compositions indicates that distortion occurs within the 2D inorganic layers which results in the amplification of the differences between the a and c axes. The difference between a and c axes gradually increases from x = 2 to x = 9.5, which suggest that the distortion increases when more Cl is incorporated in the structure.

The band gaps of the solid solution $EA_4Pb_3Br_{10-x}Cl_x$ (x = 0, 2, 4, 6, 8, 9.5, 10) exhibit a linear trend, following Vegard's law (Figure 23b). In this case the sharp absorption edge of the series is taken as the band gap, which ranges from 3.45 eV for $EA_4Pb_3Cl_{10}$ to 2.75 eV for $EA_4Pb_3Br_{10}$, and

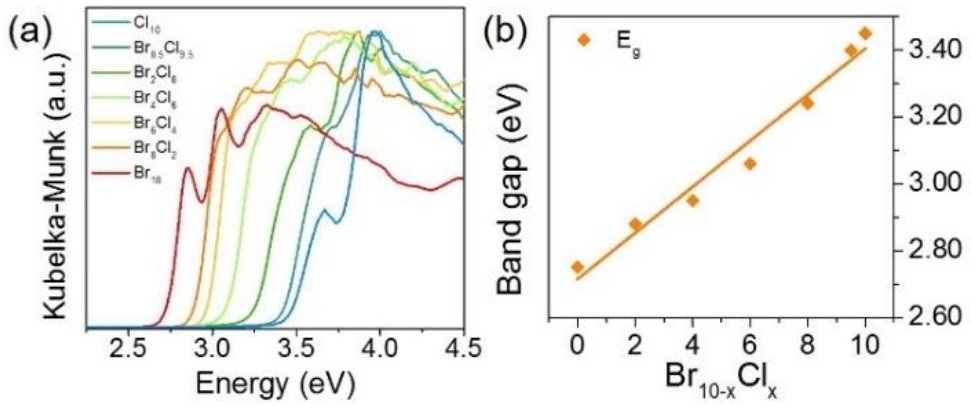

Figure 23. (a) Optical absorption spectra of $EA_4Pb_3Br_{10-x}Cl_x$ (x = 0, 2, 4, 6, 8, 9.5, 10). (b) Band gap of the solid solutions has a linear trend, which follows Vegard's law.

3.40, 3.24, 3.06, 2.95, 2.88 eV respectively for the intermediates (Figure 24a). $EA_4Pb_3Br_{10}$ and $EA_4Pb_3Cl_{10}$ have clear excitonic features near the absorption edge and at higher energy (3.04 eV and 3.96 eV) as seen in Figure 24a, which are characteristic for 2D perovskites.[90, 306]

The DFT calculations show that $EA_4Pb_3Br_{10}$ and $EA_4Pb_3Cl_{10}$ are direct bandgap semiconductors, as expected for the halide perovskites in general, although they exhibit a slightly indirect character owing to the symmetry breaking (Rashba effect) (Figure 25). For $EA_4Pb_3Br_{10}$ the gap is slightly shifted away from Γ. A similar but smaller shift was also seen in $EA_4Pb_3Cl_{10}$ along the Γ [010] direction in reciprocal space. This shift away from a high-symmetry point of the Brillouin zone is a signature of Rashba effect in the polar structure of $EA_4Pb_3Br_{10}$ related to the giant spin-orbit coupling of the Pb atom. The calculated band gaps are 1.5 eV and 2.0 eV, respectively, when including SOC, showing a significant deviation from the experimental band gaps (2.75eV and 3.45eV, respectively. The calculated band gap of $EA_4Pb_3Cl_{10}$ is ~ 0.5 eV larger

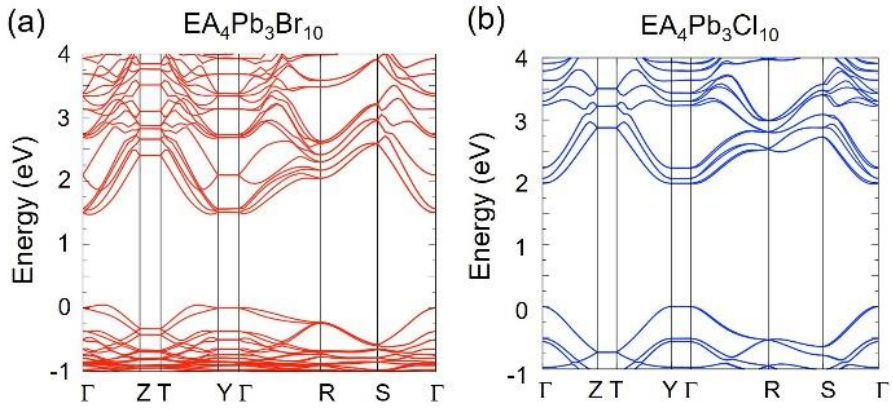

Figure 24. DFT calculations of electronic band structures for $EA_4Pb_3Br_{10}$ and $EA_4Pb_3Cl_{10}$, using the revPBE functional with SOC.

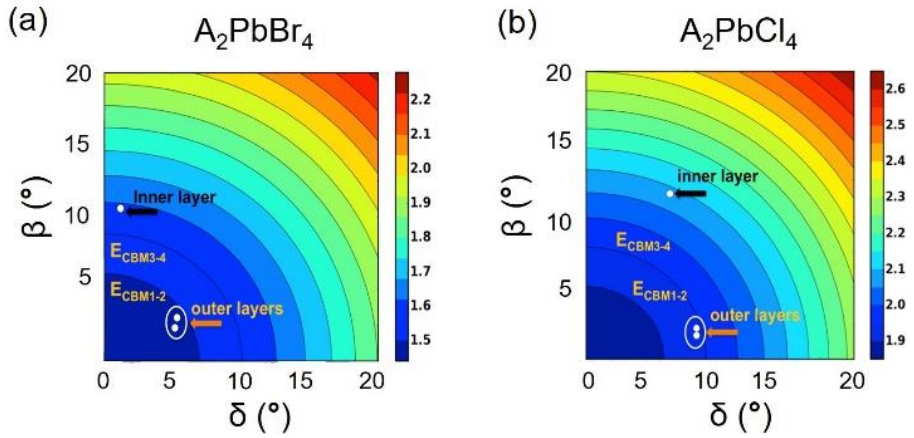

Figure 25. 2D color map of the electronic band gap variation including spin-orbit coupling with respect to octahedral distortions defined in Figure 4 for model systems A_2PbBr_4 and A_2PbCl_4 (A = Cs). Distortion angles of the inner and outer octahedral layers for $EA_4Pb_3Br_{10}$ and $EA_4Pb_3Cl_{10}$ are pointed to by the arrows in A_2PbBr_4 and A_2PbCl_4 respectively. ECBM1-2 and ECBM3-4 indicate the contour levels corresponding to their values from the band structure of Figure 7.

than that of $EA_4Pb_3Br_{10}$, which is comparable to the experimental band gap difference between the two compounds (~ 0.7 eV) but it also the difference between the corresponding 3D perovskites $MAPbCl_3$ and $MAPbBr_3$.[336]Unlike these 3D crystal structures, the electronic band structure in Figure 26 show flat dispersions between the Γ and Y k-points. This is indicative of little or vanishing electronic coupling along this direction, which coincides with the stacking axis.

The nature of the valence band maximum (VBM) and conduction band minimum (CBM) states can be captured by computing corresponding wave functions Ψ (without SOC) or local density of states (LDOS, with SOC). Ψ at Γ (Figure B8 and Figure B9) for both compounds show an anti-bonding hybridization between Pb 6s and p orbitals of the halides at the VBM while the CBM is mainly of Pb 6p type.[337] Consistent with the wave functions, the LDOS of VBM mostly localize on the inner octahedral layer, while those of CBM localize on the outer layers (Figure B10). For $EA_4Pb_3Cl_{10}$, both Ψ and LDOS are also partly present on the inner layer, indicative of a weaker

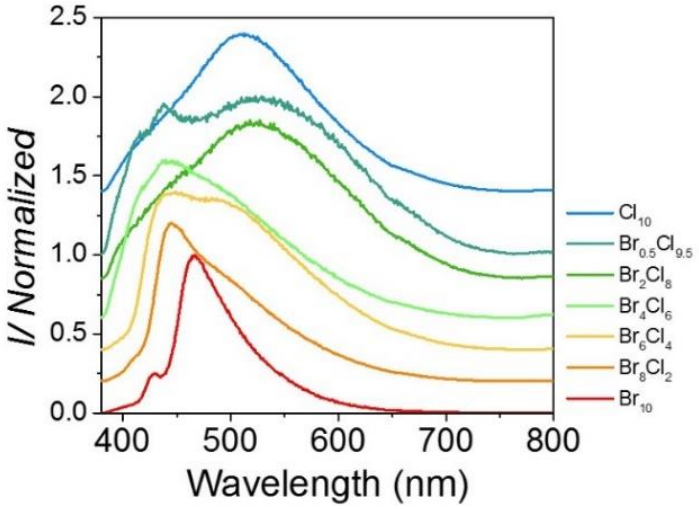

Figure 26. Steady-state PL of $EA_4Pb_3Br_{10-x}Cl_x$ (x = 0, 2, 4, 6, 8, 9.5, 10) (λ_{exc} = 315 nm).

charge separation across the layers. Hence, because of the spatial separation between VBM and CBM wave functions, we expect a more stable $EA_4Pb_3Cl_{10}$. The high-frequency dielectric constants are deduced from the computed dielectric profiles (Figure B12) and amount to 3.9 and 3.5 for $EA_4Pb_3Br_{10}$ and $EA_4Pb_3Cl_{10}$, respectively. Compared to the 3D compounds $MAPbBr_3$ (ε_∞ = 5.2) and $MAPbCl_3$ (ε_∞ = 4.2),[338] the EA system shows smaller dielectric confinement.

Previous studies have demonstrated that structural deformation has a significant effect on the band gap of hybrid perovskites which is directly linked to their optical properties.[91, 336, 339-340] To rationalize the interplay between octahedral distortions and band gap variation in $EA_4Pb_3Br_{10}$ and $EA_4Pb_3Cl_{10}$, we built model systems of A_2PbBr_4 and A_2PbCl_4 (A = Cs), similar to the A_2PbI_4 model (n = 1) proposed earlier.[124] Figure 25 shows the 2D color map of the electronic band gap variation with respect to the β and δ angles defined in Figure 20. The band gap increases with increasing structural deformation in agreement with previous works.[124, 341] Interestingly, for both $EA_4Pb_3Br_{10}$ and $EA_4Pb_3Cl_{10}$, the band gap predicted when considering the (β, δ) angles of the

"outer-layers" fit nicely to the calculated band gaps on the real crystal structures shown in Figure 25. This is consistent with the fact that band edge states (VBM and CBM) in hybrid halide perovskites are mainly determined by the inorganic framework and are produced by the hybridization of Pb and X atomic orbitals. Furthermore, the band gap variation obtained using (β, δ) of the inner and outer layers of $EA_4Pb_3Br_{10}$ and $EA_4Pb_3Cl_{10}$ reveal a sizeable difference. The variation in $EA_4Pb_3Br_{10}$ is half that of the $EA_4Pb_3Cl_{10}$ with two and three contour levels difference, respectively. This indicates that the electronic band gap fluctuations in $EA_4Pb_3Cl_{10}$ which derive from the structural distortion are larger than in $EA_4Pb_3Br_{10}$. As such, the spread in octahedral distortions is predicted to strongly broaden the emission spectra of $EA_4Pb_3Cl_{10}$.

Such a broadening is indeed observed by PL measurements. In fact, a broadband white-light emission is observed for $EA_4Pb_3Cl_{10}$ (peak centered at 500 nm, FWHM = 151 nm). The PL of the whole $EA_4Pb_3Br_{10-x}Cl_x$ series shows a different trend than that obtained for absorption as seen in

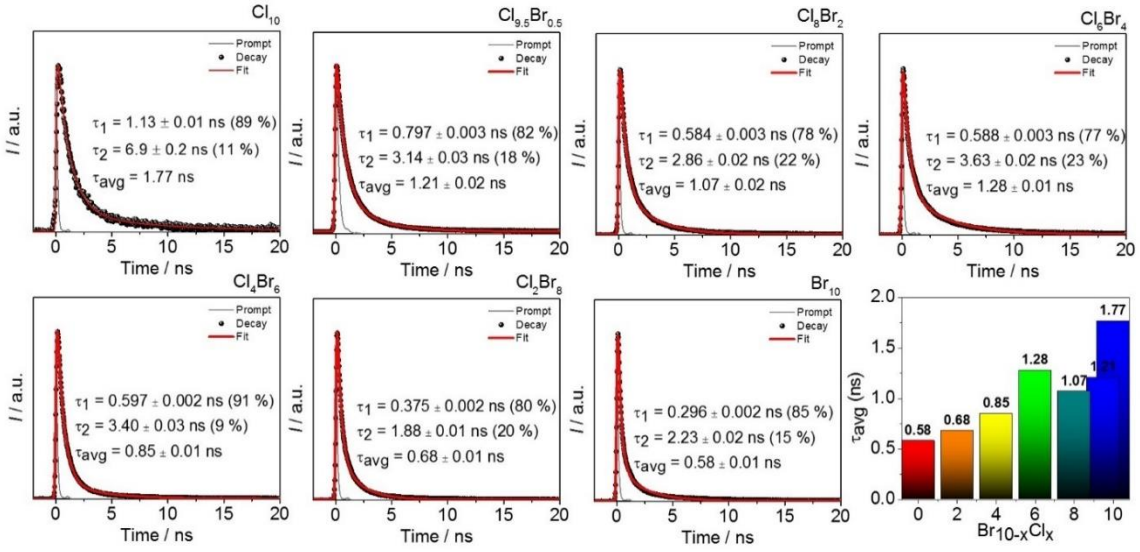

Figure 27. Time-resolved PL decays and fitting of $EA_4Pb_3Br_{10-x}Cl_x$ (x = 0, 2, 4, 6, 8, 9.5, 10). The averaged PL decay lifetime shows a decreasing trend from x = 10 to x = 0 (λ_{exc} = 375 nm).

Figure 26. It starts with. The intermediates x = 9.5 and 8 have even broader emission (FWHM = 228 nm and 187 nm), which could be due to the large difference in a and c axis caused by distortion along the layers as discussed in the previous paragraph. The bandwidth of the emission decreases from x = 9.5, becoming narrower all the way to the Br end member, which has an emission peak at 465 nm (2.67 eV). The bandwidth of the PL emission is anticipated since $EA_4Pb_3Cl_{10}$ has a much more distorted structure than $EA_4Pb_3Br_{10}$ and therefore it is expected to have more STEs

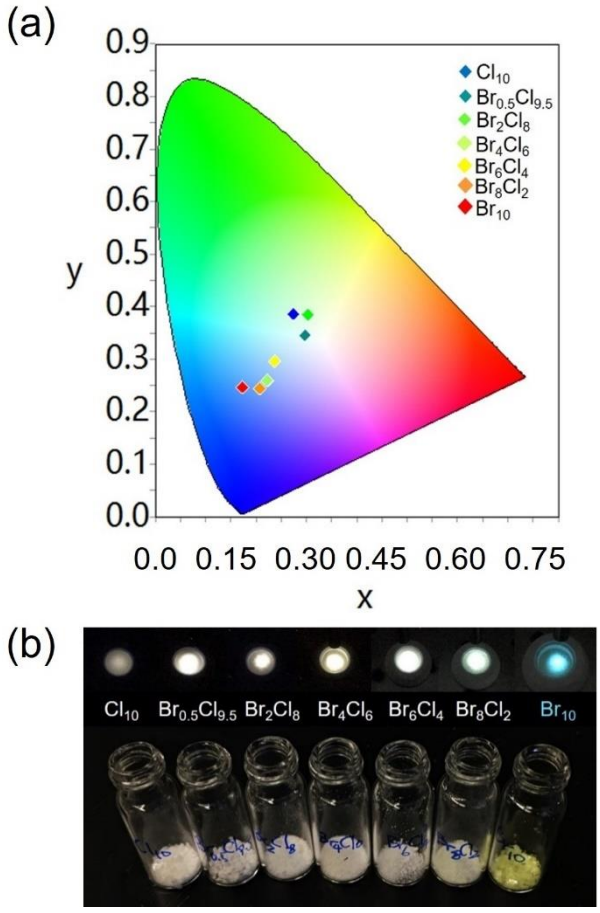

Figure 28. (a) CIE color coordinates of $EA_4Pb_3Br_{10-x}Cl_x$ (x = 0, 2, 4, 6, 8, 9.5, 10) in 1931 color space chromaticity diagram. Detailed values are given in Table 6. (b) White-light emissions from $EA_4Pb_3Br_{10-x}Cl_x$ (x = 2, 4, 6, 8, 9.5, 10) and blue-light emission from $EA_4Pb_3Br_{10}$ (excited at 315nm). Corresponding powered polycrystalline samples are shown on the bottom.

Table 6. Fitted lattice parameters from high-resolution PXRD (based on space group *C*2*cb*/*A*2$_1$*ma*), Commission International de I'Eclairage (CIE) color coordinates (x, y), Correlated Color Temperature (CCT), Color Rendering Index (CRI) and full-width at half-maximum (FWHM) of $EA_4Pb_3Br_{10-x}Cl_x$ (x = 0, 2, 4, 6, 8, 9.5, 10).

Compound	**a** (Å)	**b** (Å)	**c** (Å)	**Volume**	**x**	**y**	**CCT (K)**	**CRI**	**FWH (nm)**
Cl$_{10}$	8.0375(1)	45.5452(6)	8.1064(1)	2967.52(0)	0.27	0.39	7720	66	151
Br$_{0.5}$Cl$_{9.5}$	7.7807(2)	45.5530(12)	8.7393(2)	3097.51(0)	0.30	0.35	7132	83	228
Br$_2$Cl$_8$	7.8876(5)	45.6569(25)	8.7684(4)	3157.70(5)	0.30	0.38	6564	75	187
Br$_4$Cl$_6$	7.8921(4)	45.8723(18)	8.7038(4)	3151.05(3)	0.22	0.26	52126	N/A	147
Br$_6$Cl$_4$	7.9267(2)	45.9958(15)	8.6952(3)	3170.25(0)	0.24	0.30	15405	75	153
Br$_8$Cl$_2$	8.0443(1)	46.1571(5)	8.6860(2)	3225.12(0)	0.21	0.24	950000	N/A	98
Br$_{10}$	8.4297(1)	46.4483(3)	8.4432(1)	3305.90(0)	0.17	0.24	N/A	N/A	61

states and broader emission.[315] In Figure 27, time-resolved PL reveals that the average lifetime of the series decreases from being the longest in the Cl end member (τ_{avg} = 1.77 ns) to shortest in the Br end member (τ_{avg} = 0.58 ns), further confirming the correlation between structural distortion and PL (bandwidth and lifetime). Both the bond length variation in the octahedron and the angular (β, δ) distortion within the inorganic framework contributed to the overall broadening in the PL emission.

The light emission properties of the $EA_4Pb_3Br_{10-x}Cl_x$ (x = 0, 2, 4, 6, 8, 9.5, 10) are highly tunable, from cold white-light to relatively warm white-light as seen in Figure 27. The Commission International de I'Eclairage (CIE) color coordinates of these compounds shift from close to the center to the blue region in the 1931 color space chromaticity diagram in Figure 27a. Compared to $EA_4Pb_3Cl_{10}$ (0.27, 0.39), $EA_4Pb_3Br_{0.5}Cl_{9.5}$ and $EA_4Pb_3Br_2Cl_8$ have CIE coordinates closer to the white point (0.33, 0.33), which are (0.30, 0.35) and (0.30, 0.38), respectively. The Color Rendering

Indexes (CRI) are also significantly improved from 66 (Cl_{10}) to 83 ($Br_{0.5}Cl_{9.5}$) as seen in Table 6, giving much better quality of color rendering of the emission. Compared to our previous studied compound α-(DMEN)$PbBr_4$ (CRI = 73, CIE coordinates (0.28, 0.36)), the current system shows improved CRI with two compositions (x = 8, 9.5). The Correlated Color Temperatures (CCT) of the series are all above 6000K, suggesting these materials are emitting "cold" white-light.

3.5 Conclusions

The new series of 2D perovskites $EA_4Pb_3X_{10}$ (X = Cl, Br), is unique because it features a single A-cation acting both as a spacer and a "perovskitizer" cation. The large size of the EA cation (2.74 Å) relative to MA (2.17 Å)[342] introduces a severe structural distortion to the perovskite layers which becomes more prominent for the smaller Cl anions. The structural distortions lead to a white-light emission which can be understood in terms of an amplified STEs process. The highly distorted Pb-X framework helps to generate more transient photoexcited STEs states resulting from strong electron-phonon coupling, while also prolongs the process which is demonstrated in longer PL lifetime observed. The different distortion levels in $EA_4Pb_3Cl_{10}$ (large distortion) vs $EA_4Pb_3Br_{10}$ (small distortion) result in different PL emission bandwidth, where $EA_4Pb_3Cl_{10}$ has a broadband white-light emission while $EA_4Pb_3Br_{10}$ has a narrow blue emission. The emission properties can be conveniently tuned in the $EA_4Pb_3Br_{10-x}Cl_x$ (x = 0, 2, 4, 6, 8, 9.5, 10) solid solution. The band gap of the series follows the Vegard's law, increasing linearly from x = 0 to x = 10. Time-resolved PL measurements also show a gradual increase of average lifetimes from the Br end to

Cl end, showing the dependency of emissive STEs states on the structure composition. From DFT simulation, it is shown that the optoelectronic properties of $EA_4Pb_3Cl_{10}$ are more sensitive to the structural disorder leading to a dispersion of the electronic band gap and to exciton localization, which correlates well with longer average radiative lifetime. $EA_4Pb_3Br_{0.5}Cl_{9.5}$ has the highest CRI (CRI = 83) in the series, providing better color rendering than the pure Cl compound $EA_4Pb_3Cl_{10}$ (CRI = 66). This series of hybrid materials are promising candidates for solid state lighting as they demonstrate high tunability and have clear structure-PL relationships.

Chapter 4. Structural Diversity in White-light Emitting Hybrid Lead Bromide Perovskites

Author contributions

Guo, P.: performed the low-frequency Raman spectroscopy and photoluminescence studies (steady-state and time-resolved).

Kepenekian, M.: Katan, C.; Even, J.: performed the DFT calculations.

Hadar, I.: performed the photoemission spectroscopy.

Stoumpos, C. C and Kanatzidis, M. G.: discussed the results and directed this research.

All authors discussed the results and contributed to revising the manuscript.

4.1 Abstract

Hybrid organic-inorganic halide perovskites are under intense investigations because of their astounding physical properties and promises for optoelectronics. Lead bromide and chloride perovskites exhibit intrinsic white-light emission believed to arise from self-trap excitons (STEs). Here, we report a series of new structurally diverse hybrid lead bromide perovskites that have broadband emission at room temperature. They feature Pb/Br structures which vary from 1D face-sharing structures to 3D corner- and edge-sharing structures. Through single crystal X-ray diffraction and low frequency Raman spectroscopy, we have identified the local distortion level of the octahedral environments of Pb^{2+} within the structures. The band gaps of these compound range from 2.92 to 3.50 eV, following the trend of "corner-sharing < edge-sharing < face-sharing". Density functional theory (DFT) calculations suggest the electronic structure is highly dependent on the connectivity mode of the $PbBr_6$ octahedra, where the edge- and corner-sharing 1D structure of $(2,6\text{-dmpz})_3Pb_2Br_{10}$ exhibits more disperse bands and smaller band gap (2.49 eV) than the face-sharing 1D structure of $(hep)PbBr_3$ (3.10 eV). Using photoemission spectroscopy, we measured the energies of the valence band of these compounds and found them to remain almost constant, while the energy of conduction bands varies. Temperature dependent PL measurements reveal the 2D and 3D compounds have narrower PL emission at low temperature (~5K), whereas the 1D compounds have both free exciton emission and STEs emission. The 1D compound $(2,6\text{-dmpz})_3Pb_2Br_{10}$ has the highest photoluminescence quantum yield (PLQY) of 12%, owing to its unique structure that allows efficient charge carrier relaxation and light emission.

4.2 Introduction

Hybrid organic-inorganic perovskites are emerging semiconducting crystalline materials that are solution-processable, low-cost and can be easily synthesized.[81, 291, 343] The diverse nature of the organic cationic templates lend these materials to be highly tunable, which, in conjunction with the variable dimensionalities of these materials ranging from single crystals to nanocrystals and thin-films,[344] have provided a solid foundation of a wide range of optoelectronic devices such as photovoltaics[16, 345-346,24, 290, 347-348] and light-emitting diodes (LEDs). [248, 292, 349-350] Hybrid perovskites can be tuned "by design" for specific applications. The energy band gap is associated with choices of different metal ions (Pb^{2+}, Sn^{2+}, Ge^{2+}), halide anions (Cl^-, Br^- and I^-) and the dimensionality (0D to 3D) of the structure. For the three-dimensional (3D) structures, the general formula is ABX_3, where A is methylammonium (MA^+), formamidinium (FA^+) or Cs^+, B is Pb^{2+}, Sn^{2+} or Ge^{2+}, and X is halide (Cl^-, Br^- or I^-).[351] Lowering the dimensionality to two-dimensions (2D) with corner-sharing octahedral layers and bulky organic cations separating the perovskite layers, gives rise to increased structural diversity. The general perovskite formula then becomes $A'_2A_{n-1}B_nX_{3n+1}$ (A′ = 1+ cation, A = MA^+, FA^+ or Cs^+), in the Ruddlesden−Popper (RP) phases, $A'A_{n-1}M_nX_{3n+1}$,[139] in the Dion-Jacobson phases (A′ = 2+ cation, A = MA^+, FA^+ or Cs^+).[102] Further reducing the dimensionality to one-dimension (1D), the formula is then dictated by the connectivity modes of the $[BX_6]^{4-}$ octahedra, with the most common connectivity modes being face-sharing, followed by corner-sharing as well as rare edge-sharing connectivity. Notably, a single compound can have one connectivity mode or a combination of connectivity modes,[352] thus

producing extremely rich and diverse structural types. Zero-dimensional (0D) compounds composed of isolated $[BX_6]^{4-}$ octahedra have also been reported, with representative examples being Cs_2SnI_6 (Sn^{4+}),[353] Cs_4PbBr_6[354-355] and possibly the mixed-metal double perovskites.[356]

Broadband white-light emission at room temperature from hybrid perovskite materials is an attractive optical property and has received tremendous attention, given the poorly understood and apparently unique photo-physics that gives rise to this phenomenon.[357] It was discovered in various (110)-oriented 2D lead bromide perovskites, such as $(C_6H_{13}N_3)PbBr_4$,[358] (N-MEDA)[$PbBr_4$] (N-MEDA = N1- methylethane-1,2-diammonium)[359] and (EDBE)[$PbBr_4$] (EDBE = 2,2′-(ethylenedioxy)bis(ethylammonium)).[113] Subsequent studies have focused on the correlation between the lattice distortion in order to explain the origins of the broad emission.[197, 360-361] The currently debated broadband emission model has been connected to the highly deformed/deformable crystal lattice that induces electron-phonon coupling associated with excited states (i.e., polarons), generating the so-called self-trapped exciton (STE) states.[197] Interestingly, the broad-band emission does not only exist in layered structures, but also in lower dimensional structures, such as the recent report on 1D perovskite that exhibits bluish white-light emission and a higher photoluminescence quantum yield (PLQY) compared to the 2D perovskites.[362] Because of this, the concept of dimensional reduction[82, 363-364] provides a new materials' design principle to access a broader variety of white light-emitting materials.[108, 277, 365-367] In general, lower-dimensional structures possess more vibrational degrees of freedom and are more easily

polarizable under photo-excitation, thus leading to enhancements in the STE process and to the amplification of the broad-band emission.[368-369]

Exploring the above concepts, we report here a variety of new hybrid lead bromide perovskites, representative of each kind, focusing on their white-light emission properties. We investigate the templating effect[370] of asymmetric diammonium organic cations based on the piperazinium and piperidinium backbone as seen in Figure 29a in the lead bromide system, since these types of cations are known to interact strongly with the anionic perovskite lattice.[102, 371] The resulting compounds present a library that includes 1D face-sharing structures, 1D corner- and edge-sharing structure, 2D (100)-oriented and (110)-oriented corner-sharing structures, to 3D corner- and edge-sharing structures as summarized in Table 7. We find that all the compounds reported here have broad-band PL emission at room temperature with different emission characteristics. We investigate the temperature-dependence of the PL emission and find the width of the broad-band emission for 2D and 3D structures becomes narrower when the temperature decreases, presumably due to deactivation of some STE states. The difference in the temperature dependence of the spectra with some displaying blue and others exhibiting red shifts, additionally suggests that different mechanisms are responsible for the different structure-types.

Notably, the 1D compound $(2,6\text{-dmpz})_3Pb_2Br_{10}$ stands out, having a PLQY of 12%, much higher than the rest of the examined compounds (<1%). The superior light emission properties of this 1D compound and the temperature evolution characteristics of the spectra provide new insights

on structure-property relationships of halide perovskites and point to new design strategies (i.e. tuning the connectivity modes and dimensionality) towards white-light optoelectronic applications.

4.3 Experimental Details

4.3.1 Synthesis

Materials. $PbBr_2$ (98%),1-methylpiperazine (99%), 1-ethylpiperazine (98%), 4-(aminomethyl)piperidine (96%), 2,6-dimethylpiperazine (97%) , homopiperazine (98%), hexamethyleneimine (98%) , heptamethyleneimine (98%), hydrobromic acid (ACS reagent, 48%) were purchased from Sigma-Aldrich and used as received.

Synthesis. The following procedure was used for the syntheses of all compounds. An amount of 1.10 g (3 mmol) of $PbBr_2$ was dissolved in 4 ml HBr under heating and stirring at 122 °C (A). 1 ml HBr was added into a separate vial of 3 mmol of 4-(aminomethyl)piperidine (B). The protonated 4-(aminomethyl)piperidine solution was added into A under heating for 2 min and cooled to room temperature. Plate-like crystals precipitate during slow-cooling. Yield 726 mg, (37.8% based on Pb content). The cation input varies for the rest of the compound while $PbBr_2$ stays constant: 1-methylpiperazine (200 mg, 2 mmol), 1-ethylpiperazine (342 mg, 3 mmol), 2,6-dimethylpiperazine (342 mg, 3 mmol), homopiperazine (300 mg, 3 mmol), hexamethyleneimine (297 mg, 3 mmol) and heptamethyleneimine (339 mg, 3 mmol).

4.3.2 Single Crystal X-ray Diffraction

Full sphere data were collected after screening for ten frames using either a STOE IPDS 2 or IPDS 2T diffractometer with graphite-monochromatized Mo Kα radiation (λ = 0.71073 Å) (50 kV/40 mA) under N_2 at 293K ((4amp)$PbBr_4$, (epz)$PbBr_4$, (hep)$PbBr_3$, $(mpz)_2Pb_3Br_{10}$ and (hmp)$PbBr_4$). The collected data was integrated and applied with numerical absorption corrections using the STOE X-AREA programs. The rest of the compounds were collected either using a Bruker DUO or Molly instrument with MoKα IμS microfocus source (λ = 0.71073 Å) with MX Optics at 250K. The collected data was integrated and applied with numerical absorption corrections using the APEX3 software. Crystal structures were solved by direct methods and refined by full-matrix least-squares on F^2 using the OLEX2 program package.[372]

4.4.3 Optical Absorption Spectroscopy

Optical diffuse reflectance measurements were performed using a Shimadzu UV-3600 UV-VIS-NIR spectrometer operating in the 200–1000 nm region using $BaSO_4$ as the reference of 100% reflectance. The band gap of the material was estimated by converting reflectance to absorption according to the Kubelka–Munk equation: $\alpha/S = (1–R)^2(2R)^{-1}$, where R is the reflectance and α and S are the absorption and scattering coefficients, respectively.[373]

4.4.4 Steady-state and Time-resolved Photoluminescence

The samples were excited with 330 nm photons produced from an optical parametric amplifier, which is pumped by a titanium: sapphire amplifier with 800-nm output at 2-kHz repetition rate. Time-integrated photoluminescence (PL) spectra were captured with a CCD camera; time-resolved PL spectra were captured with a streak camera. During the measurements, the samples were mounted in a vacuum cryostat and maintained under $<10^{-7}$ Torr pressure. Quantum yield measurements were performed with a Horiba Jobin-Yvon Nanolog Spectrofluorimeter equipped with an integrating sphere. The samples were measured in powder form following an earlier report.[374]

4.4.5 Electronic Structure Calculations

First-principles calculations are based on density functional theory (DFT) as implemented in the SIESTA package.[375-376] Calculations have been carried out on experimental structures with the GGA functional in the revPBE form.[377] Core electrons are described with Troullier-Martins pseudopotentials.[378] The valence wavefunctions are developed over double-ζ polarized basis set of finite-range numerical pseudoatomic orbitals.[379] In our calculations, spin-orbit coupling is taken into account through the on-site approximation as proposed by Fernández-Seivane et al.[380] In all cases, an energy cutoff of 150 Ry for real-space mesh size has been used.

4.5 Results and Discussion

4.5.1 Crystal Structure

The hybrid lead bromide compounds presented here cover a wide variety of structural types in the perovskite family. Direct combination of the cation source in Figure 29a and $PbBr_2$ mixing in aqueous HBr at 122°C followed by slow-cooling of the solutions to room temperature yields colorless crystals, as seen in Figure 29b. Detailed synthesis procedures are listed in Methods

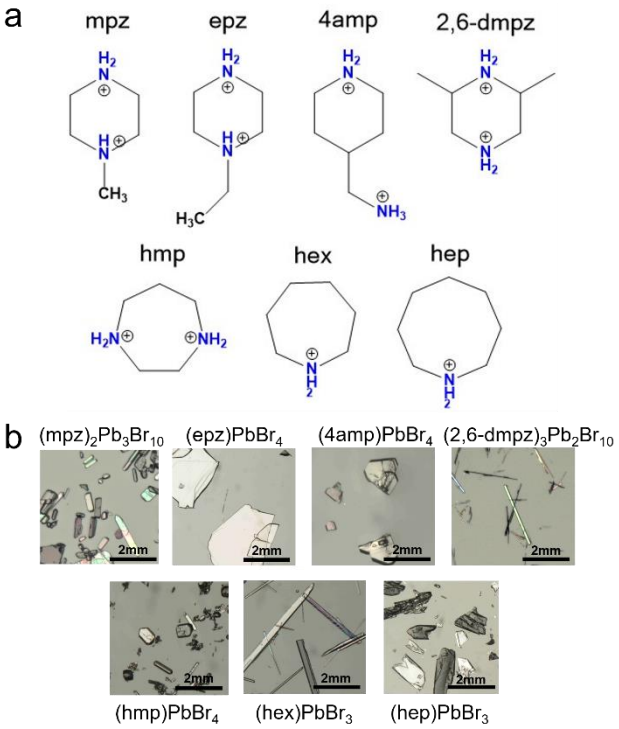

Figure 29. (a) Organic cations used in this work. mpz =1-methylpiperazine, epz =1-ethylpiperazine, 4amp = 4-(aminomethyl)piperidine, 2,6-dmpz = 2,6-dimethylpiperazine , hmp = homopiperazine , hex = hexamethyleneimine, hep = heptamethyleneimine . (b) Optical microscopic images of the hybrid perovskite compounds synthesized using the cations listed above.

section.

The 1D "perovskitoids"[128] (which refers to exclusively 1D face-sharing ABX_3 compounds) $(hep)PbBr_3$ and $(hex)PbBr_3$ belong to the common $CsNiBr_3$ structure-type,[381] with face-sharing

Table 7. Summary of structural characteristics and band gaps of $(2,6\text{-dmpz})_3Pb_2Br_{10}$, $(epz)PbBr_4$, $(4amp)PbBr_4$, (hmp)PbBr4, $(mpz)_2Pb_3Br_{10}$, $(hep)PbBr_3$ and $(hex)PbBr_3$.

Cations	Formula	Dimensionality	space group	connectivity modes	E_g (eV)
2,6-dmpz	$(C_6H_{16}N_2)_3Pb_2Br_{10}$	1D	*P*-1	corner- and edge-sharing	3.16
epz	$(C_6H_{16}N_2)PbBr_4$	(110)-oriented 2D	*Pc*	corner-sharing	3.12
4amp	$(C_6H_{16}N_2)PbBr_4$	(100)-oriented 2D	$Pca2_1$	corner-sharing	2.92
mpz	$(C_5H_{14}N_2)_2Pb_3Br_{10}$	three-layered 2D	*C*2/*c*	corner- and edge-sharing	2.97
hmp	$(C_5H_{14}N_2)PbBr_4$	3D	*C*2/*m*	corner- and edge-sharing	3.04
hep	$(C_7H_{16}N)PbBr_3$	1D	*Cc*	face-sharing	3.50
hex	$(C_6H_{14}N)PbBr_3$	1D	$P2_1$	face-sharing	3.41

polymeric $[PbBr_3]^-$ c hains (Figure 30). [86, 382-389] Usually, a bulky cationic template, which is capable of separating the inorganic sections far apart, will lead to the formation of such low dimensional structure type.[128, 390] $(hep)PbBr_3$ and $(hex)PbBr_3$ crystallize in non-centrosymmetric monoclinic space groups *Cc* and $P2_1$, respectively. In Figure 30a, b, the infinite $[PbBr_3]^-$ chains in the structure extend along the c-axis for $(hep)PbBr_3$ (a-axis for $(hex)PbBr_3$), and the individual chains are crystallographically nonequivalent, which lower the symmetry. The monovalent organic cation rings are aligned parallel to the b-axis for $(hep)PbBr_3$ (c-axis for $(hex)PbBr_3$), surrounding the inorganic chains. Due to the larger size of hep than hex, the lattice parameter along the longest axis of the unit cell increases from 37.860(2) Å for hex to 39.660(8) Å to hex. As shown in Figure 30e and f, the difference between the shortest and longest Pb-Br bond length is larger for $(hep)PbBr_3$ than that for $(hex)PbBr_3$ (2.91 Å and 3.18 Å vs. 2.98 Å and 3.10 Å). The Br-Pb-Br

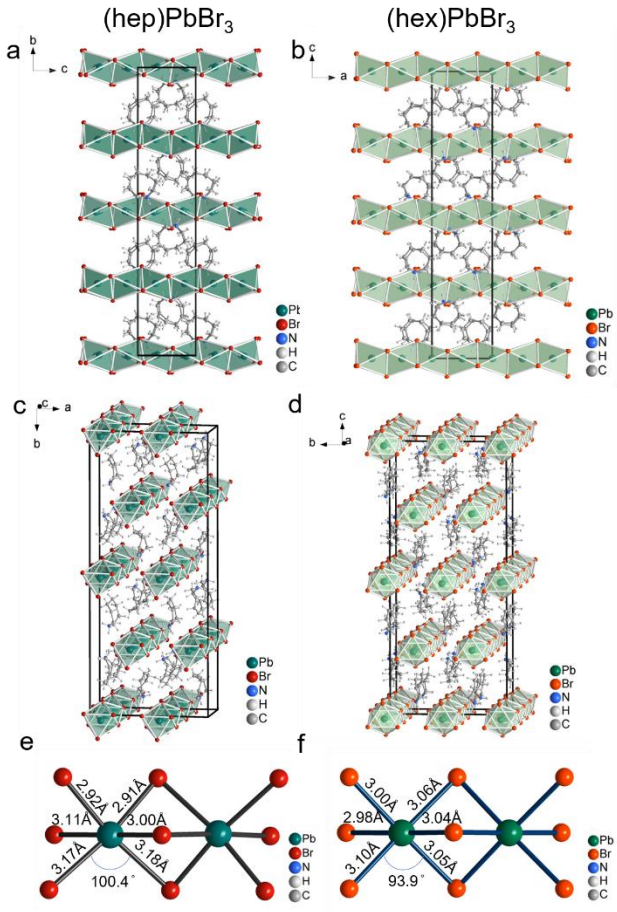

Figure 30. Crystal structures of (a), (c), (e) (hep)$PbBr_3$ and (b), (d), (f) (hex)$PbBr_3$. (a) and (b) show the side-view of the face-sharing 1D chains. In (e) and (f), it is clear that (hep)$PbBr_3$ has a more distorted structure than (hex)$PbBr_3$ (Br-Pb-Br angle 100.4˚ vs. 93.9˚, Pb-Br bond length 2.91 Å (shortest) and 3.18 Å (longest) vs. 2.98 Å (shortest) and 3.10 Å (longest).

angles depicted in Figure 30e and f show a larger distortion for (hep)$PbBr_3$ (100.4˚) than that for (hex)$PbBr_3$ (93.9˚), with respect to a regular octahedron (90˚).

An exotic type of 1D structure combining edge- and corner-sharing double chains and single corner-sharing chains resulted from the use of the 2,6-dmpz cation (Figure 29a). Because of highly asymmetric unit, $(2,6\text{-dmpz})_3Pb_2Br_{10}$ crystalizes in the triclinic space group *P*-1. The edge- and corner-sharing double anionic chain backbone has previously seen in $(C_{10}H_{12}N_2)_2[Pb_2Br_8]$.[391] The hydrogen bonding pulls out a Br- anion from the perovskite lattice, in a similar fashion to the

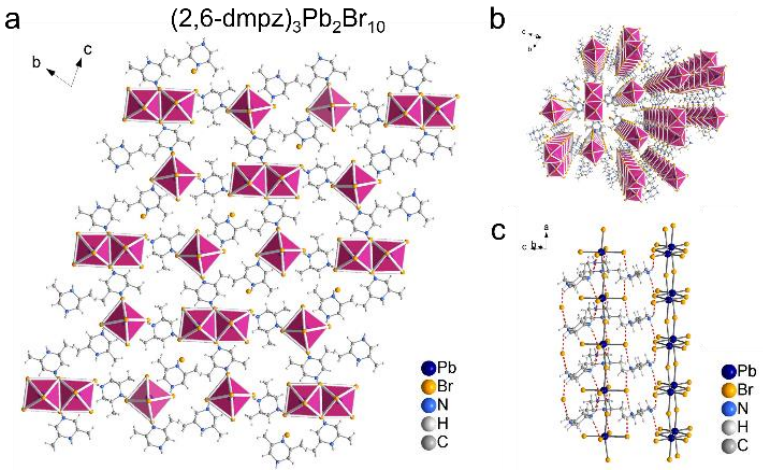

Figure 31. Crystal structure of $(2,6\text{-dmpz})_3Pb_2Br_{10}$, which consists of two types of 1D chains as seen in (a) and (b). (c) Hydrogen bonding network associated with both chains.

$(en)_2PbBr_6$ compound,[84] breaking the double-chain into a single corner-sharing chain and isolated Br^- anions, which is shown in Figure 31a, making this structure unique. In Figure 31c, the discrete hydrogen bonding networks help to keep the continuity of the 1D single chains and double chains. The closest donor-acceptor distances (N-H···Br distance) occur with the isolated Br^- and the cations, which are 3.28 Å and 3.29 Å.

$(4amp)PbBr_4$ and $(epz)PbBr_4$ represent (100)-oriented and (110)-oriented 2D perovskites, respectively, which are composed only of corner-sharing octahedra. The (110)-oriented type is much rarer as the corrugated layers are only able to form under specific hydrogen bonding interactions.[358, 360] The (100)-oriented 2D perovskite $(4amp)PbBr_4$ crystalizes in the non-centrosymmetric orthorhombic space group $Pca2_1$. The 4amp cations align in an unusual pattern, with the $-CH_2NH_3^+$ arms ordered in pairs, and with each pair arranged in an up-down configuration normal to the *ac*-plane (Figure 32a). The inorganic layers of $(4amp)PbBr_4$ exhibit large in-plane distortion, where the Pb-Br-Pb angle is 146˚, one of the smallest Pb-Br-Pb angles reported. The

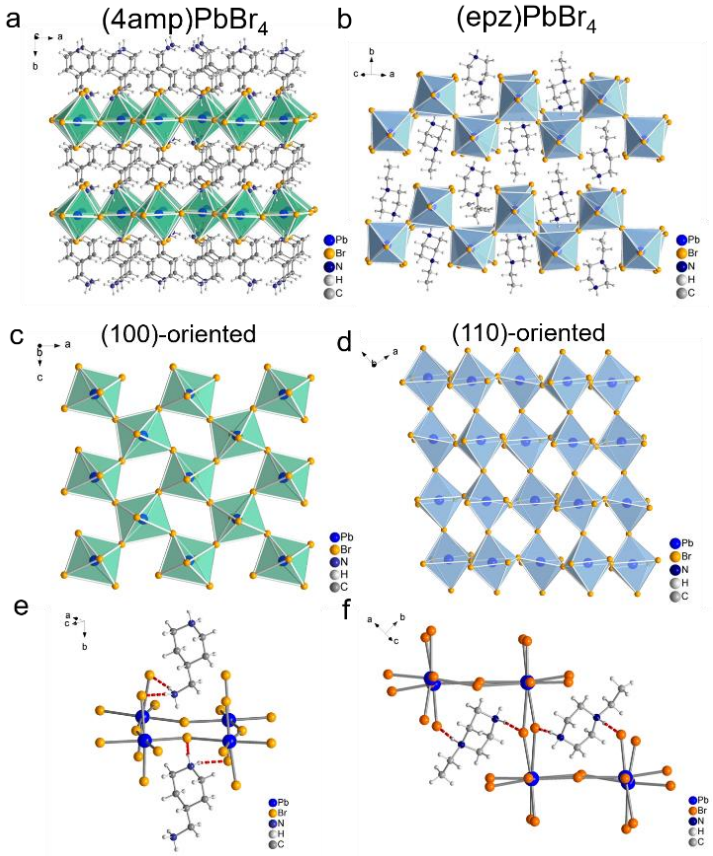

Figure 32. Crystal structures of (a), (c) and (e) (4amp)$PbBr_4$ and (b), (d) and (f) (epz)$PbBr_4$. (c), (d) Viewing perpendicular to the layers. (e), (f) Hydrogen bonds between the organic cations and inorganic layers.

highly distorted l ayers are induced by strong hydrogen bonding, where the closest donor-acceptor distances are 3.33 Å and 3.35 Å.

(epz)$PbBr_4$ crystalizes in the non-centrosymmetric monoclinic space group *Pc*. The ability to stabilize a (110)-oriented 2D perovskite is closely related to the position of the protonation site of the organic spacer.[113, 358-359] Here, the protonation of the cation happens at 1 and 4 positions on the aliphatic ring as seen in Figure 32f, which fits exactly in the perovskite pockets to form the hydrogen bonds (closest D-A distances: 3.23 Å and 3.24 Å). The use of piperazinium derivatives

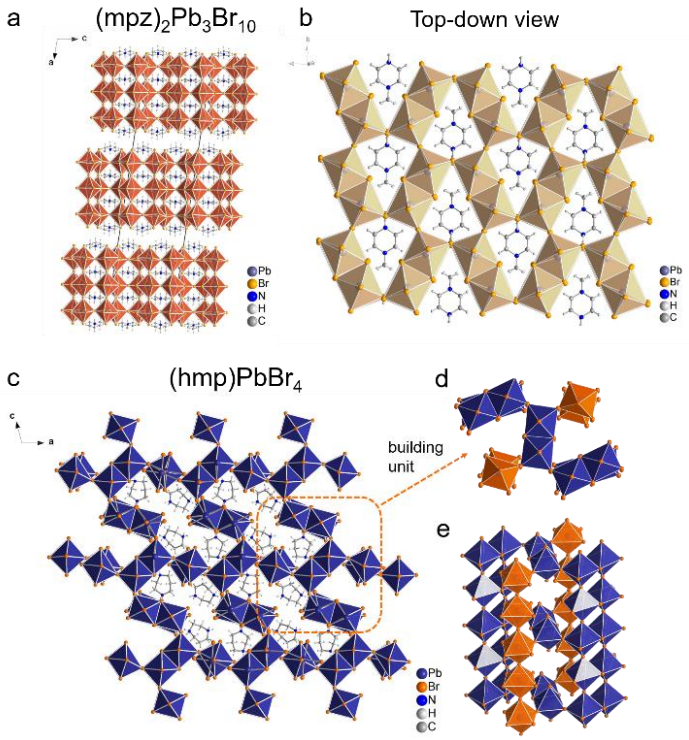

Figure 33. Crystal structures of (a) $(mpz)_2Pb_3Br_{10}$. (b) Top-down view of $(mpz)_2Pb_3Br_{10}$. Structure of $(hmp)PbBr_4$ (c, d and e). (d) and (e), basic building block of $(hmp)PbBr_4$.

as organic cation yield the (110)-type as demonstrated in a (110)-oriented 2D structure $(pipzH_2)[PbCl_4]$ which forms from the use of piperazinium as templates. [172]

Thicker layered 2D and 3D structures are also accessible from the use of asymmetric diammonium cations, with $(mpz)_2Pb_3Br_{10}$ (2D) and $(hmp)PbBr_4$ (3D) forming unique perovskite-related structure types. The crystal structures of $(mpz)_2Pb_3Br_{10}$ and $(hmp)PbBr_4$ are both centrosymmetric, crystalizing in the monoclinic space groups *C*2/*c* and *C*2/*m*, respectively. The unique three-layered structure of $(mpz)_2Pb_3Br_{10}$ is constructed from the basic building unit of edge-sharing $[Pb_2Br_{10}]^{6-}$, linked in a corner-sharing fashion to form ($[Pb_2Br_{10}]_4$) cages that encapsulate in-plane oriented mpz^{2+} cations (Figure 33a). The layer expansion is interrupted at the third layer, terminated by organic cations lying parallel to the layers. Similar organization of the inorganic

layers and organic cations has been seen in $C_6H_9N_3PbBr_4$,[392] which is a single-layered perovskite constructed from ($[Pb_2Br_{10}]_4$) cages.

The 3D structure $(hmp)PbBr_4$ consists of similar building units as the 1D $(2,6\text{-}dmpz)_3Pb_2Br_{10}$, which are however connected in a different fashion. This structure represents a new structural type in the hybrid perovskite family. Rather than isolated 1D chains, the edge-sharing double chains (highlighted in blue, Figure 33d) and corner-sharing threads (highlighted in orange, Figure 33d) are linked to form the 3D framework. Both the chains and the threads run down along the *b*-axis, and they are connected along the *ac*-plane through corner-sharing. The connectivity resembles the triangles seen in $(mpz)_2Pb_3Br_{10}$, but because of the linkage of asymmetric $[PbBr_5]^{3-}$ (corner-sharing) and $[Pb_2Br_{10}]^{6-}$ (edge-sharing) building blocks, as well as the larger ring size of hmp^{2+} over mpz^{2+} the triangles remain "open" (Figure 33e). Within the 3D framework, the extended cavities host the hmp^{2+} cations, with each thus formed channel filled with four organic cations. Although for the vast majority of cases, A_2PbX_4 compounds (A= organic cation) are 2D structures, the use of the relatively small size di-cation of hemp here seems to promote a new example of a $[PbX_4]^{2-}$ stoichiometry, that adopts a 3D rather that a 2D structure. This increase in dimensionality can rationalized by the so-called "counterion effect" which favors higher anion dimensionalities as the size of the counterion shrinks.[390]

4.5.2 Raman Spectroscopy and Structural Distortion

To get a better picture of the local structural dynamics of the hybrid lead bromide perovskites, we performed low-frequency Raman measurements. The Raman spectra were obtained with 473 nm laser excitation in ambient condition. Unlike the 3D ABX_3-type perovskite $CH_3NH_3PbBr_3$ and $CsPbBr_3$ that exhibit broad un-resolved peaks at room temperature,[393] most of the compounds reported here have well-resolved spectra (Figure 34a). Depending on the dimensionality and connectivity mode of the crystal structure, the spectra show very different characteristics, consistent with the different connectivity modes of the $[PbBr_6]^{4-}$ octahedra. The peaks at lower wavenumbers (15-100 cm^{-1}) correspond to the bending of the Br-Pb-Br bonds, while the peaks at higher wavenumbers (100-180 cm^{-1}) originate from the stretching of the Pb-Br bonds, thus providing indirect information for the local environment of the compounds.[394-395]

For the face-sharing 1D compounds $(hep)PbBr_3$ and $(hex)PbBr_3$, the strong bonding pushes the symmetric mode to relatively high energy (142 cm^{-1}), and the rigidity of the face-sharing

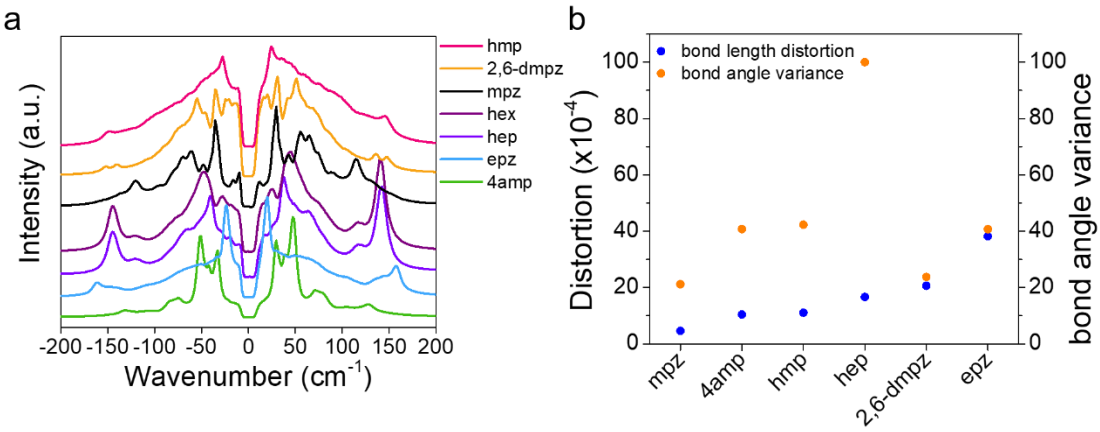

Figure 34. (a) Low frequency Raman spectra of hybrid lead bromide crystals. The spectral region between ±15 cm^{-1} has been deleted because of the use of notch filter. (b) bond length distortion of bond angle variance of the compounds calculated based on the crystal structures.

bonding increases the peak intensity. Edge- and corner-sharing compounds, by contrast, where the bonding becomes less rigid exhibit weak stretching modes. The other 1D compound, (2,6-dmpz)$_3$Pb$_2$Br$_{10}$, with corner- and edge-sharing connectivity shows many weak peaks with two pronounced symmetric modes at 135 cm^{-1} and 148 cm^{-1} likely corresponding to corner- and edge-sharing connectivity, respectively. The weak intensity and the diffuse underlying spectrum suggests the presence of anharmonicity in the structure, analogous to that observed for the MAPbBr$_3$ and CsPbBr$_3$ perovskites.[393]

The 2D compounds (4amp)PbBr$_4$, (epz)PbBr$_4$ and (mpz)$_2$Pb$_3$Br$_{10}$ all have strong Raman stretches at relatively low wavenumbers (~130 cm^{-1}), due to their strongly interconnected structures that promote concerted bending (octahedral tilting) than individual octahedral stretching. The 3D compound, (hmp)PbBr$_4$, has a less-resolved spectrum compared with other compounds, indicating a more dynamically disordered structure consistent with its higher dimensionality and its corner-sharing connectivity.[393]

Based on the refined crystal structures, we calculated the distortion levels of the individual [PbBr$_6$]$^{4-}$ octahedron for the individual compounds (Figure 34b). The bond length distortion[334-335] (eq.1, where d is the mean Pb-Br bond distance and d_n are the six individual Pb-Br bond distances) and bond angle variance[396] (eq.2, θi is the individual Pb-Br-Pb angle) reflect the deviation of the octahedron from the one with no distortion.

$$\Delta d = (\tfrac{1}{6})\sum \left[\frac{d_n - d}{d}\right]^2 \quad (1)$$

$$\sigma^2 = \sum_{i=1}^{12} (\theta i - 90)^2 / 11 \quad (2)$$

Previously, we have associated the distortion level of the 2D lead bromide perovskite with the width of the PL emission, where the larger the distortion, the broader the width of the PL emission. [25, 47] Although this correlation may apply to the 2D systems, it cannot be generalized to the 1D and 3D systems that have different connectivity modes. Here, we do not yet glean a correlation between the emission band width and the distortion level. However, most compounds display a large $PbBr_6$ distortion in the crystal structure. From the calculation, only $(mpz)_2Pb_3Br_{10}$ has a relatively small distortion level for both the angular and bond length distortion. The highest bond length distortion in observed in (110)-oriented 2D perovskite $(epz)PbBr_4$. For the angular distortion, $(hep)PbBr_3$ has the highest due to the face-sharing connectivity of the octahedron that requires bent angles (i.e. Br-Pb-Br angle). In general, the high distortion level of the local octahedral environments implies a more malleable structure which is more susceptible to generating STE states upon photo-excitation, thus producing a broad-band emission spectrum.

4.5.3 Electronic Structure Calculations

To further understand the electronic properties of these materials, we use density functional theory (DFT) for the calculation of the band structures. Because of the presence of heavy elements, spin-orbit coupling was taken into account. We chose two 1D structures and two 2D structures as representative examples to distinguish the effect of dimensionality and connectivity on the band gap. Notice that dimensionality is defined in the present manuscript by the nature of the bonding network. $(2,6\text{-dmpz})_3Pb_2Br_{10}$ is referred in the text as a 1D material for this reason. The band

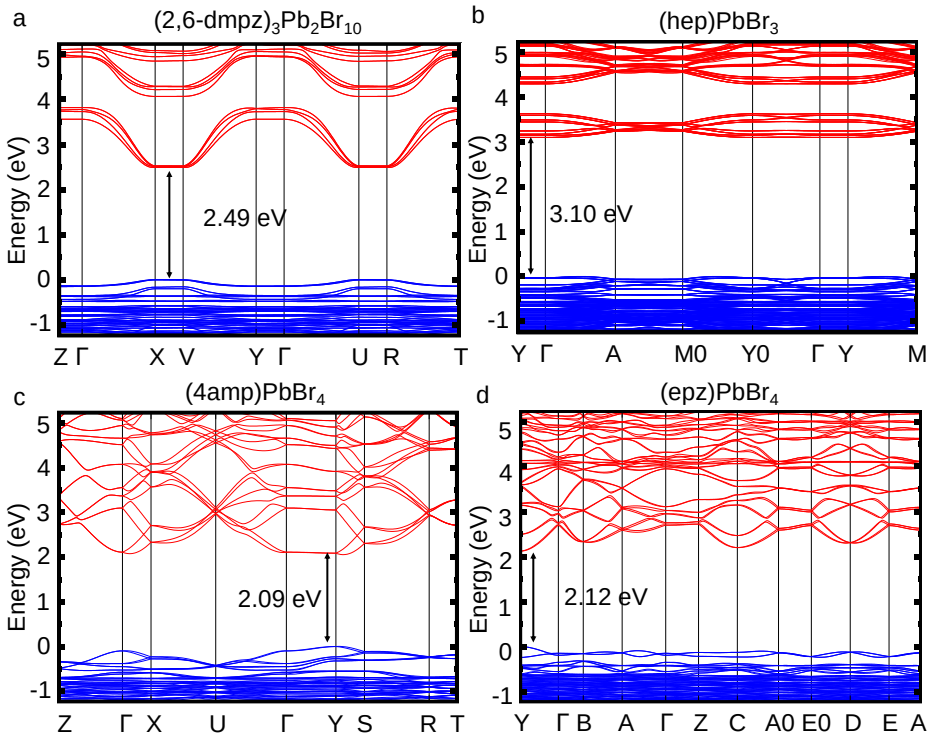

Figure 35. Calculated electronic band structures of (a) $(2,6\text{-dmpz})_3Pb_2Br_{10}$ (2.49 eV), (b) $(hep)PbBr_3$ (3.10 eV), (c) $(4amp)PbBr_4$ (2.09 eV) and (d) $(epz)PbBr_4$ (2.12 eV).

dispersion diagr am in Figure 35a reveals flat electronic dispersions close to the band gap along both X-V and U-R directions. $(2,6\text{-dmpz})_3Pb_2Br_{10}$ can thus also be considered as an array of quantum wires along the ox direction. The 2D materials $(4amp)PbBr_4$ and $(epz)PbBr_4$ can thus be considered as quantum well superlattices with the same criterion (Figures 35c and d). Comparison among the 1D structures $(2,6\text{-dmpz})_3Pb_2Br_{10}$ and $(hep)PbBr_3$ reveals that the former (the 1D material with edge- and corner-sharing) has much more dispersive bands and smaller band gap (2.49 eV) than the latter (1D face-sharing), which has flat bands and much larger band gap (3.10 eV), clearly illustrating that the connectivity of the octahedra is detrimental to the electronic structure. Mixed corner- and edge-sharing affords significantly more dispersion than face-sharing connectivity, especially for the CBM states.

The difference in the band structure for the (100)-oriented and (110)-oriented 2D structures are not very significant in Figure 35c and d, which the (100)-oriented (4amp)$PbBr_4$ has a slightly smaller band gap (2.09 eV) than the (110)-oriented (epz)$PbBr_4$ (2.12 eV), consistent with the experiment. Both compounds have similar dispersion for both the valence and conduction bands. Note that the calculated band gaps are underestimated but still follow the same trend with respect to the experimental result, as shown in Figure C2. All compounds are direct gap semiconductors, with the valence band maximum (VBM) composed of hybridization of Br p and Pb s orbitals and conduction band minimum (CBM) composed of empty Pb p orbitals as seen in the corresponding pDOS in Figure C3.

4.5.4 Optical Properties

Because the new perovskite compounds could potentially be used in future devices it is of fundamental importance to have knowledge of the energy positions of their valence and conduction bands and to understand the trends with which they vary from one member to the next. Experimental determination of such energy values in most perovskites are rare and often frustrate device design in terms of the correct design of interface assembly. Therefore, valance band maxima (VBM), of the different compounds were measured by ambient photoemission spectroscopy (APS) (Figure 36a). The conduction band minima (CBM) were calculated by adding the band gap energy, measured by diffuse reflectance spectroscopy in Figure 36b. We cluster the compounds according to their octahedra connectivity modes. The samples with both corner- and edge-sharing octahedra

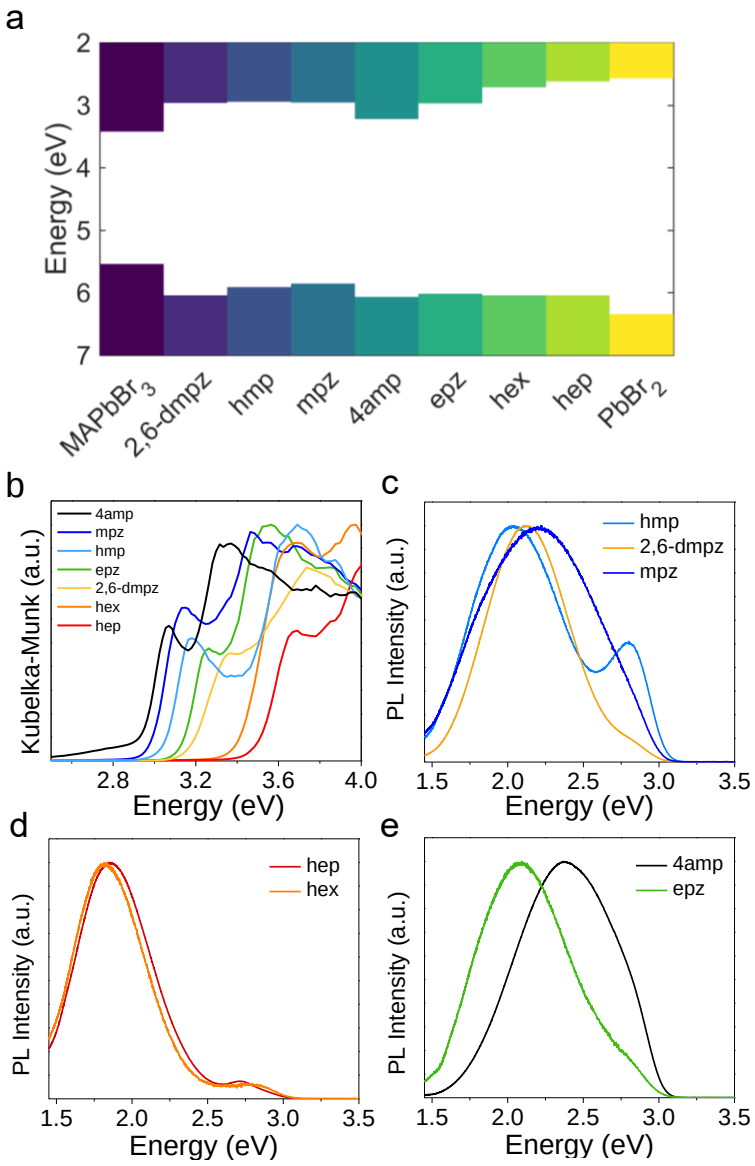

Figure 36. (a) Experimental energy band alignment of hybrid lead bromide compounds. VBM and CBM of the various compounds compared with the 3D $MAPbBr_3$ perovskite and $PbBr_2$. (b) Optical absorption spectra of the compounds reported here. Detailed values are listed in Table 8. Steady-state PL (excited at 330 nm) at room temperature for (c) $(hmp)PbBr_4$, $(2,6\text{-}dmpz)_3Pb_2Br_{10}$ and $(mpz)_2Pb_3Br_{10}$, (d) $(hep)PbBr_3$ and $(hex)PbBr_3$, (e) $(4amp)PbBr_4$ and $(epz)PbBr_4$.

(2,6-dmpz, hmp , mpz), show variation in their VBM, while their CBM is almost constant. In contrary, the compounds with corner-sharing (epz, 4amp), or face-sharing (hep, hex), octahedra has strong variation of the CBM while the VBM remains almost constant.

The optical properties of these materials are dominated by the connectivity mode of the $[PbBr_6]^{4-}$ octahedra, where the band gap follow the general trend of "corner-sharing< edge-sharing< face-sharing", as expected from the corresponding Pb-Br orbital overlap. The same trend has been observed in the lead iodide system.[132] Specifically, for the corner-connected compounds, (4amp)$PbBr_4$ consists of only corner-sharing octahedra and has the smallest band gap (2.93 eV) in the series (see Figure 36b). This bandgap is slightly larger than some other (100)-oriented 2D perovskites, such as (DMAPA)$PbBr_4$ (2.88 eV) and (DMABA)$PbBr_4$ (2.85 eV) because of its sizeable in-plane distortions.[360] The (110)-oriented 2D perovskite (epz)$PbBr_4$ has a larger bang gap of 3.12 eV because of the highly corrugated character of the layer.

The compounds possessing both corner- and edge- sharing octahedra (mpz, hmp and 2,6-dmpz) have larger band gaps 2.97 eV, 3.04 eV and 3.16 eV, respectively than the purely corner-sharing (4amp)$PbBr_4$. As mentioned earlier, the compounds (hep and hex) with face-sharing octahedra have the largest band gap of 3.41 eV and 3.50 eV. For the 1D face-sharing structures, (hep)$PbBr_3$ has a slightly larger band gap than (hex)$PbBr_3$ as the 1D chains are more distorted as described above.

Despite that the optical spectra show sharp absorption edge, the PL spectra of all compounds exhibit broad band emission features at room temperature. Except for (hep)$PbBr_3$ and (hex)$PbBr_3$ which emit in the red, the rest of the compounds emit white-light with different emission width and peak position. In the following discussion, we group the PL emission of these compounds based on the connectivity mode as seen in Table 7. The centers of the PL emission for

$(mpz)_2Pb_3Br_{10}$ (2.20 eV), $(hmp)PbBr_4$ (2.04 eV) and $(2,6\text{- }dmpz)_3Pb_2Br_{10}$ (2.12 eV) are relatively close together (Figure 36b). In addition to the broad emission peak at 2.04 eV, $(hmp)PbBr_4$ has another well-resolved higher energy emission peak at 2.81 eV. For $(hep)PbBr_3$ and $(hex)PbBr_3$ the emissions are very similar, Figure 36c. Both 1D face-sharing compounds have a weak high energy emission peak at ~2.75 eV and the main emission peak at ~1.84 eV. The main emission peak of (hep)PbBr3 at 1.84 eV is far away from the absorption edge at 3.5 eV, demonstrating a large Stokes shift of 1.66 eV. Compounds such as $(tms)_4Pb_3Br_{10}$[397] and $(C_6H_{14}N)PbBr_3$,[398] which are also partially composed of face-sharing components, have similar emission characteristics, in the sense that there is a huge Stokes shift and the emission starting around 3 eV and peaking at 1.77- 1.90 eV. Compared to (100)-oriented $(4amp)PbBr_4$, the (110)-oriented $(epz)PbBr_4$ has a more red-shifted peak emission (2.08 eV), but the emission center for $(4amp)PbBr_4$ occurs at lower

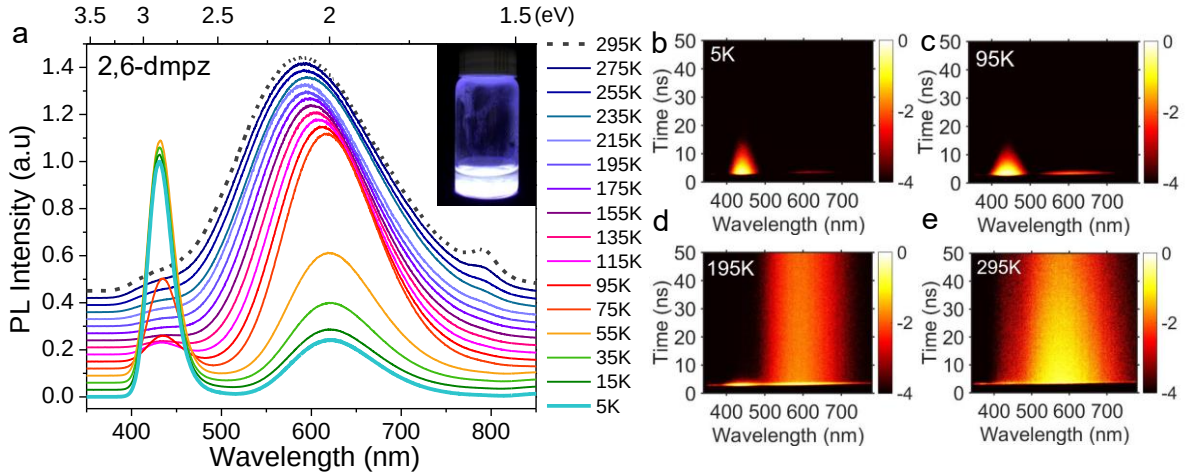

Figure 37. (a) Temperature-dependent (5 – 293 K) steady-state PL spectra of $(2,6\text{-dmpz})_3Pb_2Br_{10}$. Inserted shows the sample emitting white-light under UV flashlight. (b)-(e) 2D TRPL of $(2,6\text{-dmpz})_3Pb_2Br_{10}$ at various temperatures; the colorbar shown on the right of each 2D plot is in log10 scale.

wavelength (2.38 eV), Figure 36e. Except for (hmp)$PbBr_4$ which as a shoulder peak at higher energy, all compounds fit the trend where the larger the band gap, the more red-shifted the center of the emission peak is.

Among all compounds, (2,6-dmpz)$_3Pb_2Br_{10}$ has a PLQY of 12%, which is much higher than the rest (<1%, see Table 8). It is also among the highest PLQY reported for hybrid perovskite white-light emitting materials.[362] The reason for the high PLQY may be attributed to the unique mixed 1D edge-sharing and corner-sharing structure, which shares some similarities with the 1D edge-sharing compound $C_4N_2H_{14}PbBr_4$ that demonstrates a high PLQY of 20%.[362]

To investigate the mechanistic aspects of the broad-band emission, we performed variable-temperature PL. The temperature-dependent PL measurement of (2,6-dmpz)$_3Pb_2Br_{10}$ shows the unusual evolution of the PL emission from 295K to 5K in Figure 37. At 293K, the PL emission is a broad peak from 400 nm to 750 nm (1.65-3.1 eV), centered at 585 nm (2.12 eV). Upon decreasing the temperature, the broad peak starts to become narrower and shifts to longer wavelengths (from 585 nm at 295K to 620 nm at 5K). A new higher energy peak then appears at 115 K, centered at 432 nm (2.87 eV). The two distinct peaks have different intensities and decay lifetimes as seen in Figure 37b-e.

For (2,6-dmpz)$_3Pb_2Br_{10}$, the averaged lifetime of the broad emission peak at 295K is 23.03 ns, which is the longest among all the compounds reported here. The rest of the compounds have much shorter PL lifetimes ranging from 2-4 ns (Table 8, Figure C9), which are comparable to previously reported hybrid lead bromide perovskites.[360] At 195K, the lifetime of the emission of (2,6-

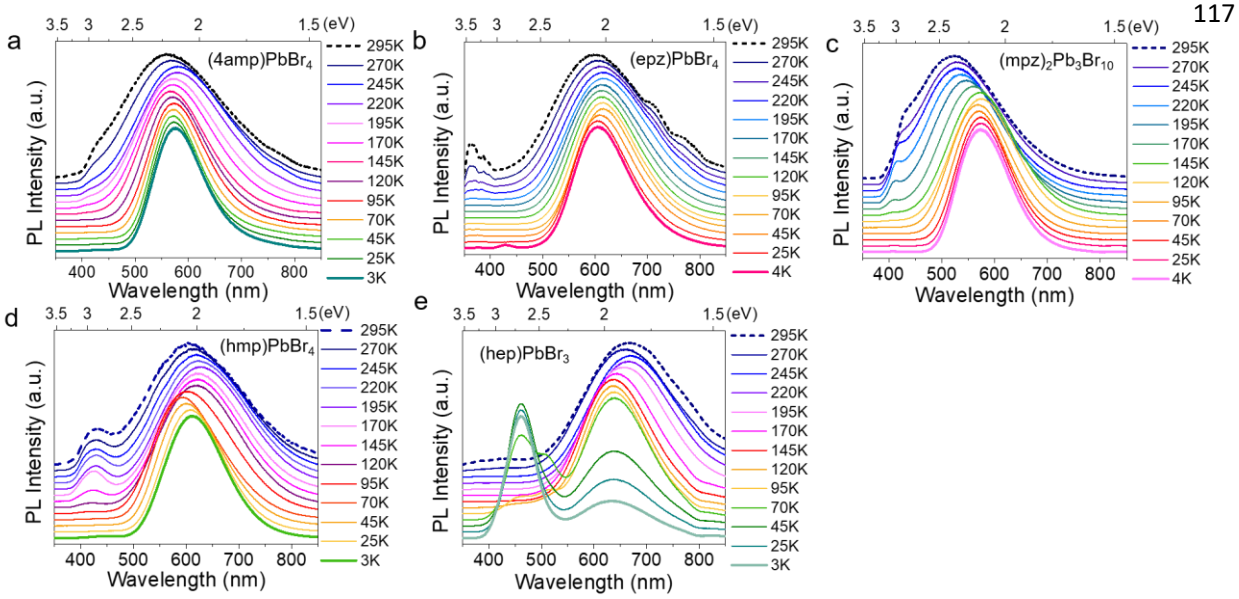

Figure 38. Temperature-dependent (3 – 295 K) steady-state PL spectra (normalized intensity) of (a) (4amp)$PbBr_4$, (b) (epz)$PbBr_4$, (c) $(mpz)_2Pb_3Br_{10}$, (d)(hmp)$PbBr_4$, (e) (hep)$PbBr_3$.

dmpz)$_3Pb_2Br_{10}$ at ~60 0 nm (2.07 eV) is 28.02 ns, whereas the lifetime of the emission at ~450 nm (2.76 eV) is 0.56 ns. The lifetime of the emission at ~600 nm (2.07 eV) becomes increasingly shorter as the temperature decreases, where it reaches the shortest (0.78 ns) at 5K in Figure 37b, whereas the lifetime of the emission at ~450 nm increases to 2.95 ns. Intensity-wise, the peak at ~600 nm reaches its maximum at 235K (Figure C8) and decreases to its minimum value at 5K. The emission at ~450 compound (2,6-dmpz)$_3Pb_2Br_{10}$ nm on the other hand, reaches the maximum intensity value at 15K.

The trend of the temperature dependence for the 2D and 3D compounds can be generally summarized as the bandwidth of the PL broadband emission peak gradually decreasing as the temperature lowers as shown in Figure 38. For example, the full-width at half-maximum (FWHM) of the (100)-oriented 2D compound (4amp)$PbBr_4$ decreases from 420 meV (295K) to 210 meV

Table 8. Commission International de I'Eclairage (CIE) coordinates (x, y), correlated color temperature (CCT), color rendering index (CRI), PL emission center, PL lifetime at room temperature, full-width at half-maximum (FWHM) and photoluminescence quantum yield (PLQY) of the new compounds reported here.

Compound	x	y	CCT	CRI	PL emission center (eV)	τ_{avg} (ns)	FWHM (meV)	PLQY (%)
2,6-dmpz	0.44	0.46	3341	77	2.12	23.03	325	12.24
epz	0.44	0.44	3324	84	2.08	2.7	370	0.97
mpz	0.38	0.42	4242	86	2.20	3.6	485	0.33
hmp	0.41	0.39	3379	90	2.04	2.5	570	0.46
hep	0.52	0.41	1986	89	1.84	4.3	285	0.63
hex	0.54	0.40	1801	88	1.82	*NA*	270	0.35
4amp	0.31	0.39	6275	76	2.38	2.5	420	0.54

(5K). (epz)$PbBr_4$, $(mpz)_2Pb_3Br_{10}$ and (hmp)$PbBr_4$ have shown the same tendency where their emission bandwidth also decreases in Figure 38b, c and d, respectively.

Unlike the higher dimensional compounds, the 1D compound (hep)$PbBr_3$, has similar emission characteristics as the 1D compound $(2,6\text{-dmpz})_3Pb_2Br_{10}$ discussed earlier, where the broad peak at 669 nm (1.85 eV) gradually narrows while another high energy peak at ~460 nm (2.70 eV) surfaces at around 145K. A reported 1D face-sharing compound, [1,5-Bis(1-methylimidazolium)pentane][$PbBr_3$]$_2$, has almost the exact same PL evolution from RT to 10K,[383] suggesting this trend is dimension-dependent.

Upon cooling the width of the PL emission becomes narrower. The different modes of the PL evolution suggest there are several energy transfer processes happening when decreasing the temperature, where the thermally activated processes are less pronounced and locally confined.

Usually at sufficiently low temperature, (the lowest we can measure is 3~5K), the free exciton PL, as compared to self-trapped excitons, should be dominant (higher energy emission, ~450 nm (2.76 eV)). Here we see for 4amp, epz, mpz and hmp the STE emission (~450 nm, 2.75 eV) still dominates the overall emission, suggesting the highly distorted structures prevent the STEs from tunneling back to the free exciton states. Finally, for the 1D structure (hep)$PbBr_3$ in Figure 38e, the free exciton emission at higher energy is dominant over the suppressed broad STE states at low temperature (3- 45K), which is similar to the other 1D compound $(2,6\text{-dmpz})_3Pb_2Br_{10}$.

4.5.5 White-light emission

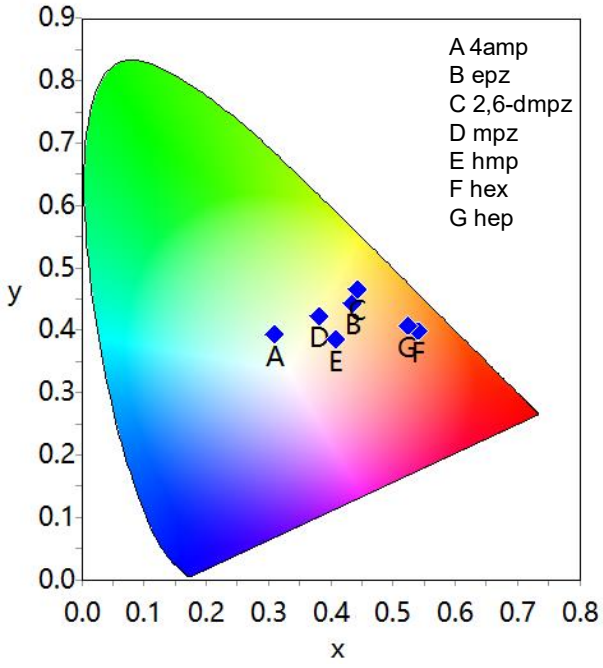

Figure 39. CIE color coordinates of the hybrid lead bromide compounds in 1931 color space chromaticity diagram. The chromaticity coordinates (x, y), CCT and CRI are calculated using the ColorCalculator by OSRAM Sylvania, Inc.

2,6-dmpz)$_3$Pb$_2$Br$_{10}$, (4amp)PbBr$_4$, (epz)PbBr$_4$, (mpz)$_2$Pb$_3$Br$_{10}$ and (hmp)PbBr$_4$ have relatively warm white-light emission as shown in Figure 39 compared to our previously investigated systems α-(DMEN)PbBr$_4$[360] and EA$_4$Pb$_3$Br$_{10-x}$Cl$_x$.[117] The correlated color temperature (CCT) of most compounds are below 4500K (except (4amp)PbBr$_4$, 6275K), producing neutral to warm white-light. The color rendering index (CRI) are quite high (above 85, see Table 8) for most compounds, providing accurate color rendition of the actual objects. (2,6-dmpz)$_3$Pb$_2$Br$_{10}$ has a CIE coordinate of (0.44, 0.46) which has a reddish white-emission comparing to the white point at (0.33, 0.33). Although (2,6-dmpz)$_3$Pb$_2$Br$_{10}$ has the highest PLQY, and better potential of actual application in solid-state lighting,[365] the CRI (77) is lower than most of the compounds reported here. This could be improved by using halide-mixing strategy as shown in earlier reports.[117]

4.6 Conclusions

Seven new hybrid lead bromide compounds, namely (hep)PbBr$_3$, (hex)PbBr$_3$, (2,6-dmpz)$_3$Pb$_2$Br$_{10}$, (4amp)PbBr$_4$, (epz)PbBr$_4$, (mpz)$_2$Pb$_3$Br$_{10}$ and (hmp)PbBr$_4$, perovskites and perovskitoids possess a diverse range of structural types with different octahedral connectivity. The connectivity modes of the [PbBr$_6$]$^{4-}$ octahedra determine the optical band gaps of these materials in a "corner-sharing < edge-sharing < face-sharing" increasing order. Except for the face-sharing (hep)PbBr$_3$ and (hex)PbBr$_3$, the rest of the compounds exhibit white-light emission at room temperature (RT). Temperature-dependent PL studies have revealed that for 1D compounds a

prominent peak at higher energy emerges (free exciton dominates at low temperature) while for 2D and 3D compounds the broad emission peak gradually becomes narrower when decreasing the temperature (STE dominates). The unique 1D compound $(2,6\text{-dmpz})_3Pb_2Br_{10}$ which has a structure that combines corner- and edge-sharing octahedra has the highest PLQY (12%) and longest lifetime (23.03 ns) among them, while the remaining compounds have low PLQY (<1%) and relatively short lifetime (<5 ns). The diversity of the hybrid bromide perovskite as epitomized by the structural types reported here, enriches the expanding hybrid perovskite library. The superior PL properties of the 1D compound demonstrate that dimensional reduction to 1D perovskites can underpin a new direction for exploring suitable candidates for white-light solid-state lighting and other optoelectronic phenomena.

Chapter 5. Hybrid Dion-Jacobson 2D Lead Iodide Perovskites

Reprinted with permission from Mao, L.; Ke, W.; Pedesseau, L.; Wu, Y.; Katan, C.; Even, J.; Wasielewski, M. R.; Stoumpos, C. C.; Kanatzidis, M. G. "Hybrid Dion–Jacobson 2D Lead Iodide Perovskites." *J. Am. Chem. Soc.*, **2018**, *140* (10), 3775–3783.

Author contributions

Ke, W.: fabricated and characterized the solar cell devices.

Pedesseau, L.: Katan, C.; Even, J.: performed the DFT calculations.

Wu, Y.: performed the time-resolved photoluminescence studies.

Stoumpos, C. C and Kanatzidis, M. G.: discussed the results and directed this research.

All authors discussed the results and contributed to revising the manuscript.

5.1 Abstract

The three-dimensional hybrid organic-inorganic perovskites have shown huge potential for use in solar cells and other optoelectronic devices. Although these materials are under intense investigation, derivative materials with lower dimensionality are emerging offering higher tunability of physical properties and new capabilities. Here we present two new series of hybrid two-dimensional (2D) perovskites that adopt the Dion-Jacobson (DJ) structure-type, which are the first complete homologous series reported in halide perovskite chemistry. Lead iodide DJ perovskites adopt a general formula $A'A_{n-1}Pb_nI_{3n+1}$ (A' = 3-(aminomethyl)piperidinium (3AMP) or 4-(aminomethyl)piperidinium (4AMP), A = methylammonium (MA)). These materials have layered structures where the stacking of inorganic layers is unique as they lay exactly on top of another. With a slightly different position of the functional group in the templating cation 3AMP and 4AMP, the as-formed DJ perovskites show different optical properties, with the 3AMP series having smaller band gaps than the 4AMP series. Analysis on the crystal structures and Density functional theory (DFT) calculations suggest that the origin of the systematic band gap shift is the strong but indirect influence of the organic cation on the inorganic framework. Fabrication of photovoltaic devices utilizing these materials as light absorbers reveal that $(3AMP)(MA)_3Pb_4I_{13}$ has the best power conversion efficiency (PCE) of 7.32%, which is much higher than corresponding $(4AMP)(MA)_3Pb_4I_{13}$.

5.2 Introduction

Hybrid organic-inorganic halide perovskites materials with three-dimensional (3D) AMX_3 structures enable solar cells with power conversion efficiency (PCE) over 22%.[9, 13, 24, 290, 399-401] With impressive structural diversity and great potential in optoelectronic applications, two-dimensional (2D) hybrid organic-inorganic halide perovskites are evolving into an important class of high-performance semiconductors.[81, 90, 99-100, 106, 113, 124, 239, 242, 246, 248, 350, 360, 402-403] 2D halide perovskites, $(A')_2(A)_{n-1}B_nX_{3n+1}$ or $(A')(A)_{n-1}B_nX_{3n+1}$, (A' = 1+ or 2+, A = 1+ cation, B = Pb^{2+}, Sn^{2+}, Ge^{2+}, Cu^{2+}, Cd^{2+} etc., X = Cl^-, Br^- and I^-), are classified depending on the stacking orientation of the inorganic layers ((100), (110) or (111) with respect to the ideal cubic perovskite), but also on the number of the inorganic layers (n = 1, 2, 3 etc, in the chemical formula).[81, 128] The single-layered 2D perovskites (n = 1) which have a general formula of A_2BX_4 or ABX_4 (have been extensively explored and there is a large number of structural types reported to date, differing in the nature of the organic spacers and the configuration of the inorganic layers.[81, 94, 186] For the higher number of layers ($n \geq 2$), however, there are only few crystallographically characterized examples: $(PEA)_2(MA)_{n-1}Pb_nI_{3n+1}$ (n = 2, 3)[74, 99] (PEA = phenylethylammonium, MA = methylammonium), $(BA)_2(MA)_{n-1}Pb_nI_{3n+1}$ (n = 2-5) (BA = butylammonium),[139, 145] $(GA)(MA)_nPb_nI_{3n+1}$ (GA = guanidinium, n = 2-3),[159] $(BA)_2(MA)_{n-1}Sn_nI_{3n+1}$ (n = 2-3),[75, 128] $(CH_3C_6H_4CH_2NH_3)_2(MA)Pb_2I_7$,[77] $(HO_2C(CH_2)_3NH_3)_2(MA)Pb_2I_7$,[78] $(C_4H_3SCH_2NH_3)_2(MA)Pb_2I_7$,[404] $(EA)_4Pb_3X_{10}$[117] (X = Cl, Br) (EA = ethylammonium), $(BA)_2(MA)_2Pb_3Br_{10}$[405] and $Cs_2[C(NH_2)_3]Pb_2Br_7$.[406] The layered structures, historically, can be divided into several categories,

based on the nomenclature of oxide perovskites:[407] a) Ruddlesden-Popper (RP) phases,[139, 408] b) Dion-Jacobson (DJ)[409-410] (Figure 1a), the oxide perovskite specific c) Aurivilius (AV) phases[411] and the halide perovskite specific d) alternating cation in the interlayer space (ACI) type.[159] The differences between these categories are shown in the relative stacking of the layers. The halide perovskites are dominated by the RP archetypes which are characterized by two offset layers per unit cell (Figure 1a). having pairs of interdigitated interlayer spacers (1+). The DJ perovskites feature divalent (2+) interlayer spacers, requiring only one cation per formula unit,[84, 174, 412-413] and tend to adopt the $RbAlF_4$ structure-type.[414] Because of this, DJ perovskites have a rich configurational stereochemistry with the layers being able to stack in a perfect (0,0 displacement, as reported here) or imperfect (0, ½ or ½, ½ displacements) arrangement according to the steric demands of the interlayer cations, as derived from oxide chemistry.[415] The oxide DJ perovskites have been studied extensively due to their interesting ion-exchange[416-417] and intercalation[418] properties. In halide perovskites, beyond the single-layer perovskites (n = 1) very little is known regarding the higher n-members in the perovskite hierarchy.

Here we report the first examples of hybrid DJ hybrid 2D lead iodide perovskites which consist of thick perovskite slabs (n>1) with layer number (n) ranging from 1 to 4. We describe two new DJ perovskite series based on bivalent (+2) organic cations deriving from a piperidinium (C_5NH_{12}) organic backbone (Figure 1b). The new DJ perovskites are built from 3AMP (3AMP = 3-(aminomethyl)piperidinium) and 4AMP (4AMP = 4-(aminomethyl)piperidinium) cations between the layers (“spacers”) and methylammonium (MA) cations inside the 2D layers

("perovskitizers") to form (A') $(MA)_{n-1}Pb_nI_{3n+1}$ (A' = 3AMP or 4AMP, n = 1-4) homologous series.[139] With the exception of the n = 1 members, the 3AMP and 4AMP series with a representative crystal structure sequence shown in Figure 1b. We find that the difference in the position of the-$CH_2NH_3^+$ group on the piperidine chair (3- and 4- position with respect to the piperidine nitrogen) influence the crystal structure through different hydrogen bonding modes, which is further reflected on the distortion of the inorganic layers. This difference has a major impact on the optical and electronic properties, which see a narrowing of the bandgap and an enhanced charge transport performance for the least distorted structure (3AMP). Density functional theory calculations (DFT) calculations are in good agreement with the observed trends. We further demonstrate the superior optoelectronic properties of these materials on photovoltaic (PV) devices. Owing to the less distorted crystal structure the 3AMP series shows a superior performance (~7% champion efficiency for n = 4) to the 4AMP series (~5% champion efficiency for n = 4). These two series of examples showcase the power of utilizing different templating organic cations to influence the semiconducting properties of the inorganic part of the perovskites, which broaden the horizons of 2D perovskites for achieving new solar cells and other optoelectronic devices with better characteristics.

5.3 Experimental Details

5.3.1 Synthesis

Materials. PbO (99.9%), 3-(aminomethyl)piperidine (Aldrich^{CPR}), 4-(aminomethyl)piperidine (96%), hydroiodic acid (57 wt. % in H_2O, distilled, stabilized, 99.95%) and hypophosphorous acid solution (50 wt. % in H_2O) were purchased from Sigma-Aldrich and used as received. Methylammonium iodide (>99.5%) was purchased from Luminescence Technology Corp. and used as received.

Synthesis of (3AMP)$(MA)_{n-1}Pb_nI_{3n+1}$. For n = 1, an amount of 669 mg (3 mmol) 99.9% PbO powder was dissolved in 6 mL of hydroiodic acid and 1 mL hypophosphorous acid solution by heating under stirring for 5-10 min at ~130°C until the solution turned to clear bright yellow. 0.5 mL hydroiodic acid was added to 342 mg (3 mmol) 3-(aminomethyl)piperidine (3AMP) in a separate vial under stirring. The protonated 3AMP solution was added into the previous solution under heating and stirring for 5 min. Red plate-like crystals precipitate during slow cooling to room temperature. Yield 963 mg (38.6% based on total Pb content). For n = 2, an amount of 669 mg (3 mmol) 99.9% PbO powder was dissolved in 6 mL of hydroiodic acid and 1 mL hypophosphorous acid solution by heating under stirring for 5-10 min at 130°C until the solution turned to clear bright yellow. 318 mg (2 mmol) of methylammonium iodide (MAI) was added directly to the above solution under heating. 0.5 mL hydroiodic acid was added to 57 mg (0.5 mmol) 3AMP in a separate vial under stirring. The protonated 3AMP solution was added into the previous solution under heating and stirring for 5 min. Dark red plate-like crystals precipitated (Figure 40c) during slow cooling to room temperature. Yield 487 mg (22.4% based on total Pb content). For the synthesis of higher numbers, they follow the same route except the ratio were

change to 37.6 mg (0.33 mmol) 3AMP, 477 mg (3 mmol) MAI, 669 mg (3 mmol) PbO for n = 3, yield 252 mg (12.2% based on total Pb content) and 34.2 mg (0.3 mmol) 3AMP, 636 mg (4 mmol) MAI, 892 mg (4 mmol) PbO for n = 4, yield 301 mg (11.2% based on total Pb content).

Synthesis of (4AMP)$(MA)_{n-1}Pb_nI_{3n+1}$. Similar synthetic procedures were used to synthesize the 4AMP series. However, the amount of 4AMP was reduced as the 4AMP series precipitate faster than the 3AMP. The experimental ratios (4AMP: MAI: PbO) (in mmol) of the 4AMP are 3:0:3 for n = 1, 0.5:2:3 for n = 2, 0.33:3:3 for n = 3 and 0.27:4:4 for n = 4. Yield 1155 mg (46.3%), 684 mg (31.5%), 531 mg (25.6%) and 477 mg (17.7% based on total Pb content), respectively.

Powder X-ray Diffraction. PXRD analysis was performed using a Rigaku Miniflex600 powder X-ray diffractometer (Cu Kα graphite, λ = 1.5406 Å) operating at 40 kV/15 mA with a Kβ foil filter.

5.3.2 Single Crystal X-ray Diffraction

Full sphere data were collected after screening for a few frames using either a STOE IPDS 2 or IPDS 2T diffractometer with graphite-monochromatized Mo Kα radiation (λ = 0.71073 Å) (50 kV/40 mA) under N_2 at 293 K ($(3AMP)PbI_4$, $(4AMP)PbI_4$ and $(3AMP)(MA)_3Pb_4I_{13}$). The collected data was integrated and applied with numerical absorption corrections using the STOE X-AREA programs. The rest of the compounds were collected using a Bruker Molly instrument with MoKα IμS microfocus source (λ = 0.71073 Å) with MX Optics at 250 K. The collected data was integrated and applied with numerical absorption corrections using the APEX3 software.

Crystal structures were solved by charge flipping and refined by full-matrix least squares on F^2 with the Jana2006 package.

5.3.3 Optical Absorption Spectroscopy

Optical diffuse reflectance measurements were performed using a Shimadzu UV-3600 UV-VIS-NIR spectrometer operating in the 200-1000 nm region using $BaSO_4$ as the reference of 100% reflectance. The band gap of the material was estimated by converting reflectance to absorption according to the Kubelka–Munk equation: $\alpha/S = (1–R)^2(2R)^{-1}$, where R is the reflectance and α and S are the absorption and scattering coefficients, respectively.

5.3.4 *Steady State and Time-resolved Photoluminescence*

Steady-state PL spectra were collected using HORIBA LabRAM HR Evolution Confocal RAMAN microscope. 473 nm laser (0.1% power) was used to excite all samples at 50× magnification. Time-resolved photoluminescence (TRPL) spectra were acquired using HORIBA Fluorolog-3 equipped with a 450-W xenon lamp and a TCSPC module (diode laser excitation at λ = 375 nm) and an integrating sphere (Horiba Quanta–φ) for absolute photoluminescence quantum yield determination. The spectra were corrected for the monochromator wavelength dependence and photomultiplier response functions provided by the manufacturer.

5.3.5 Electronic Structure Calculations

First-principles calculations are based on density functional theory (DFT) as implemented in the VASP package.[419-421] All calculations are carried out on the experimentally determined crystal structures. We used the GGA functional in the PBE form, the projector augmented wave (PAW) method[422-423] with the PAW data set supplied in the VASP package with the following valence orbitals: Pb [$5d^{10}6s^{2}6p^{2}$], I [$5s^{2}5p^{5}$], N [$2s^{2}2p^{3}$], H [$1s^{1}$] and C [$2s^{2}2p^{2}$]. In addition, the wavefunctions are expanded using a plane-wave basis set with an energy cut-off of 500 eV. Spin-orbit coupling is systematically taken into account. For band structures, the reciprocal space integration is performed over a 4×4×1 Monkhorst-Pack grid for compounds with n=1 and n=3, and over a 4x4x4 grid for compounds with n=2 and n=4 in their primitive cells.[424-425]

5.3.6 Device Fabrications and Characterization

FTO glass substrates were coated with PEDOT:PSS by spin-coating at 4000 rpm for 30s, and then annealed at 150 °C for 30 min in air. The 2D perovskite precursors with a molar concentration of 0.6 M were prepared by dissolving the 2D perovskite crystal powders in a mixed solvent of DMF and DMSO with a volume ratio of 4:1. After the crystal powders dissolved, adding 0.8 vol% HI into the perovskite precursors. Then the precursors were coated on the substrates with a spin rate of 4000 rpm for 60s in a N2-filled glove box. During the spin-coating, 0.7 mL diethyl ether was dropped on the rotating substrates at 20 s. After spin-coating, the films were annealed at 100 °C for 10 min in the glove box. To complete the devices, C60 (20 nm)/BCP (5 nm)/Ag (100

nm) were sequentially thermally evaporated on top of the perovskites. The active area of the solar cells was 0.09 cm^2.

J-V curves were measured by a Keithley model 2400 instrument under AM1.5G simulated irradiation with a standard solar simulator (Abet Technologies). The light intensity of the solar simulator was calibrated by a National Renewable Energy Laboratory-certified monocrystalline silicon solar cell. EQE curves were measured by an Oriel model QE-PV-SI instrument equipped with a National Institute of Standards and Technology-certified Si diode.

5.4 Results and Discussion

The structural differences between RP and DJ halide perovskites are mainly caused by the inter-layer cations (spacers), where RP phases have two sheets of interdigitating cations (1+) while the DJ phases only have one sheet of inter-layer cations (2+) between the inorganic slabs. The influence of the spacers on inorganic slabs is exerted in many levels, depending on the cation size and shape (steric effect), charge (electrostatic attraction) and the position of the functional groups (H-bonding and dispersion forces). This difference between RP and DJ perovskites is also reflected on the general formula, where RP phase has a general formula of $A'_2A_{n-1}M_nX_{3n+1}$ and DJ phase has a general formula of $(A')(A)_{n-1}M_nX_{3n+1}$ (A' = inter-layer cation). In hybrid DJ phases, the inter-layer organic cations are 2+, having less degrees of freedom, making the layers closer to each other. In RP phases, the organic cations are 1+, which results in more flexible layer stacking.

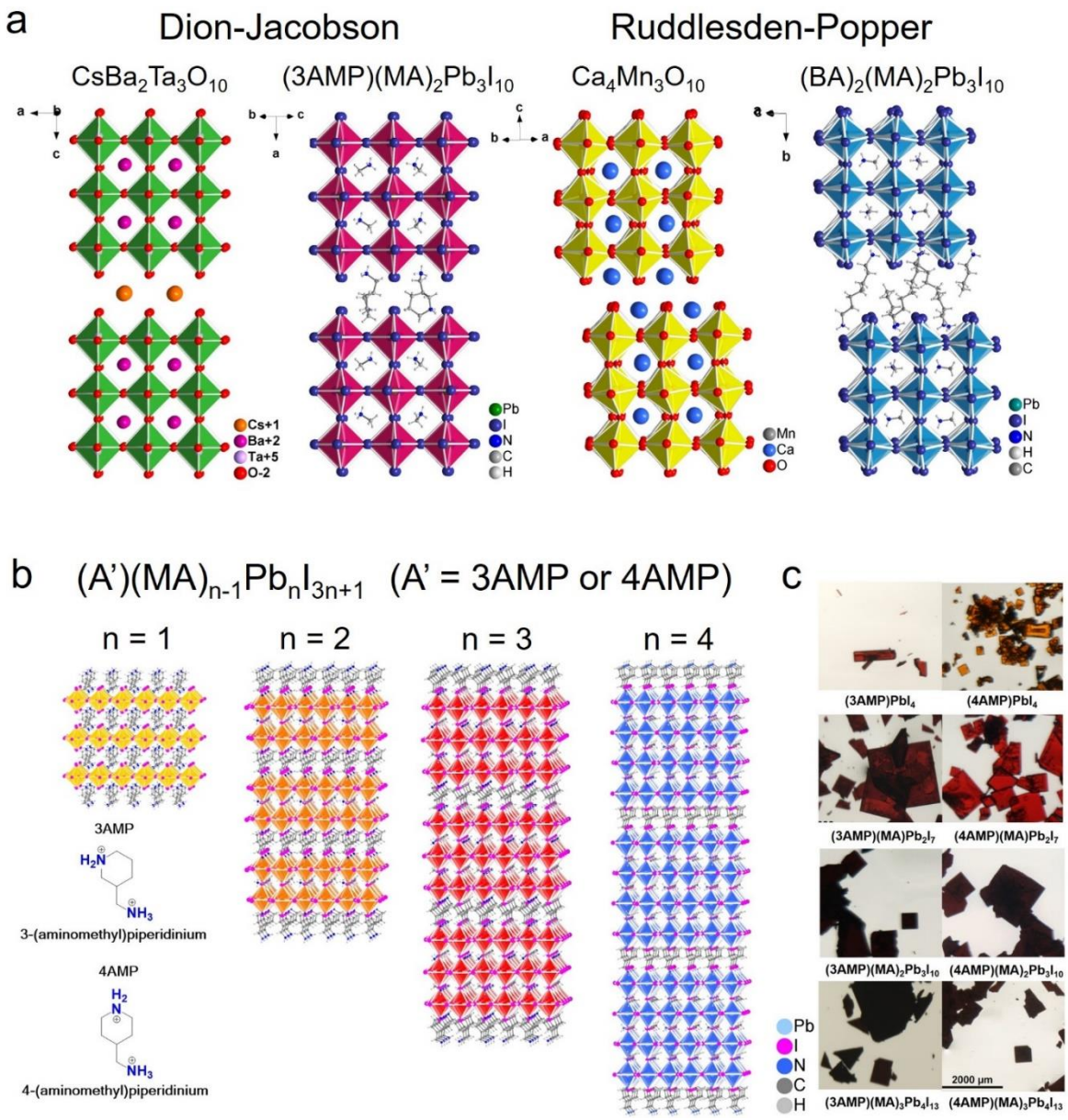

Figure 40. (a) Comparison between Dion-Jacobson phases and Ruddlesden-Popper phases for both oxide and halide perovskite. (b) General crystal structure of the two series of DJ perovskite reported here, from n = 1 to 4. Structures of the cation 3AMP and 4AMP are listed in the lower left corner. (c) Optical images of the 3AMP and 4AMP crystals. Scale bar on the bottom right applies to all.

The Dion-Jacobson series of layered perovskites, $(A')(MA)_{n-1}Pb_nI_{3n+1}$ (A' = 3AMP or 4AMP, n = 1- 4), produce uniform, square plate-like crystals, except 3-AMPPbI_4, which is an elongated plate

Table. 9 Crystal data and structure refinement for (A′)$(MA)_{n-1}Pb_nI_{3n+1}$ (A' = 3AMP).

Compound	(3AMP)PbI_4	(3AMP)$(MA)Pb_2I_7$	(3AMP)$(MA)_2Pb_3I_{10}$	(3AMP)$(MA)_3Pb_4I_{13}$
Empirical formula	$C_6N_2H_{16}PbI_4$	$(C_6N_2H_{16})(CH_3NH_3)Pb_2I_7$	$(C_6N_2H_{16})(CH_3NH_3)_2Pb_3I_{10}$	$(C_6N_2H_{16})(CH_3NH_3)_3Pb_4I_{13}$
Crystal system	Monoclinic			
Space group	$P2_1/c$	*Ia*	*Pa*	*Ia*
Unit cell dimensions	a = 8.6732(6) Å, b = 18.4268(9) Å, c = 20.4522(14) Å, β = 99.306(6) °	a = 8.8581(11) Å, b = 8.8607(4) Å, c = 33.4749(5) Å, β = 90°	a = 8.8616(3) Å, b = 8.8624(3) Å, c = 23.0316(7) Å, β = 90°	a = 8.8627(18) Å, b = 8.8689(18) Å, c = 58.842(12) Å, β = 90°
Volume ($Å^3$)	3225.67(35)	2627.4(3)	1808.79(10)	4625.1(16)
Z	8	4	2	4
Density (g/cm^3)	3.4224	3.6681	3.8024	3.8645
Indepd. refl.	5033 [R_{int} = 0.1102]	4422 [R_{int} = 0.0202]	8035 [R_{int} = 0.0361]	5893 [R_{int} = 0.0405]
Data / restraints / param.	5033 / 32 / 145	4422 / 17 / 115	8035 / 28 / 163	5893 / 19 / 201
Final R indices [I>2σ(I)]	R_{obs} = 0.0869, wR_{obs} = 0.1622	R_{obs} = 0.0323, wR_{obs} = 0.0922	R_{obs} = 0.0395, wR_{obs} = 0.1063	R_{obs} = 0.0901, wR_{obs} = 0.2062
R indices [all data]	R_{all} = 0.1471, wR_{all} = 0.1686	R_{all} = 0.0365, wR_{all} = 0.0941	R_{all} = 0.0612, wR_{all} = 0.1296	R_{all} = 0.1136, wR_{all} = 0.2138
Largest diff. peak and hole	3.97 and -4.88 $e·Å^{-3}$	1.44 and -1.23 $e·Å^{-3}$	2.014 and -1.382 $e·Å^{-3}$	11.07 and -5.34 $e·Å^{-3}$

$R = \Sigma||F_o|-|F_c|| / \Sigma|F_o|$, $wR = \{\Sigma[w(|F_o|^2 - |F_c|^2)^2] / \Sigma[w(|F_o|^4)]\}^{1/2}$ and $w=1/(\sigma^2(I)+0.0004I^2)$

as seen in Figure 40c. For the 3AMP series, the color of the crystal gets progressively darker from n = 1 (red) to n = 4 (black). The 4AMP has a similar trend, but it starts from lighter colors than the 3AMP for the n = 1 (orange) and n = 2 (red) members. The bulk crystals exhibit good stability in ambient environment and can be handled without any protection during characterizations.

Table. 10 Crystal data and structure refinement for (A′)$(MA)_{n-1}Pb_nI_{3n+1}$ (A' = 4AMP).

Compound	(4AMP)PbI_4	(4AMP)$(MA)Pb_2I_7$	(4AMP)$(MA)_2Pb_3I_{10}$	(4AMP)$(MA)_3Pb_4I_{13}$
Empirical formula	$C_6N_2H_{16}PbI_4$	$(C_6N_2H_{16})(CH_3NH_3)Pb_2I_7$	$(C_6N_2H_{16})(CH_3NH_3)_2Pb_3I_{10}$	$(C_6N_2H_{16})(CH_3NH_3)_3Pb_4I_{13}$
Crystal system	Monoclinic			
Space group	*Pc*	*Ia*	*Pc*	*Ia*
Unit cell dimensions	a = 10.4999(13) Å, b = 12.5429(9) Å, c = 12.5289(13) Å, β = 89.984(9)°	a = 8.8412(11) Å, b = 8.8436(4) Å, c = 33.6045(5) Å, β = 90°	a = 23.1333(7) Å, b = 8.8365(3) Å, c = 8.8354(3) Å, β = 90°	a = 8.8587(18) Å, b = 8.8571(18) Å, c = 58.915(12) Å, β = 90°
Volume ($Å^3$)	1650.05(43)	2627.5(4)	1806.11(10)	4622.6(16)
Z	4	4	2	4
Density (g/cm^3)	3.3441	3.6681	3.8081	3.8666
Indepd. refl.	4646 [R_{int} = 0.1198]	4558 [R_{int} = 0.028]	7954 [R_{int} = 0.0291]	8002 [R_{int} = 0.1339]
Data / restraints / param.	4646 / 36 / 141	4558 / 17 / 116	7954 / 18 / 158	8002 / 19 / 202
Final R indices [I>2σ(I)]	R_{obs} = 0.0797, wR_{obs} = 0.1093	R_{obs} = 0.0330, wR_{obs} = 0.0915	R_{obs} = 0.0351, wR_{obs} = 0.0889	R_{obs} = 0.0585, wR_{obs} = 0.0839
R indices [all data]	R_{all} = 0.1618, wR_{all} = 0.1275	R_{all} = 0.0410, wR_{all} = 0.0949	R_{all} = 0.0559, wR_{all} = 0.0970	R_{all} = 0.1700, wR_{all} = 0.1000
Largest diff. peak and hole	4.48 and -4.31 $e·Å^3$	1.69 and -1.20 $e·Å^3$	1.80 and -1.39 $e·Å^3$	4.23 and -2.94 $e·Å^3$

$R = \Sigma||F_o|-|F_c|| / \Sigma|F_o|$, $wR = \{\Sigma[w(|F_o|^2 - |F_c|^2)^2] / \Sigma[w(|F_o|^4)]\}^{1/2}$ and $w=1/(\sigma^2(I)+0.0004I^2)$

Both (A')$(MA)_{n-1}Pb_nI_{3n+1}$ series form isostructural analogues for n>1. Detailed crystallographic data and structural refinements for all eight compounds reported here are listed in Table 9. They consist of n layers (~6.3 Å is the thickness of one octahedron) of corner-sharing

$[PbI_6]^{4-}$ octahedra with $xAMP^{2+}$ (x = 3, 4) separating the perovskite slabs and MA^+ filling in the perovskite voids (Figure 40b). The difference between the two DJ perovskite families is highlighted in Figure 41a and b, where specific crystallographic characteristics are stressed. The n = 1 and n = 2 members of each AMP series are selected as representative examples. For n = 1, the

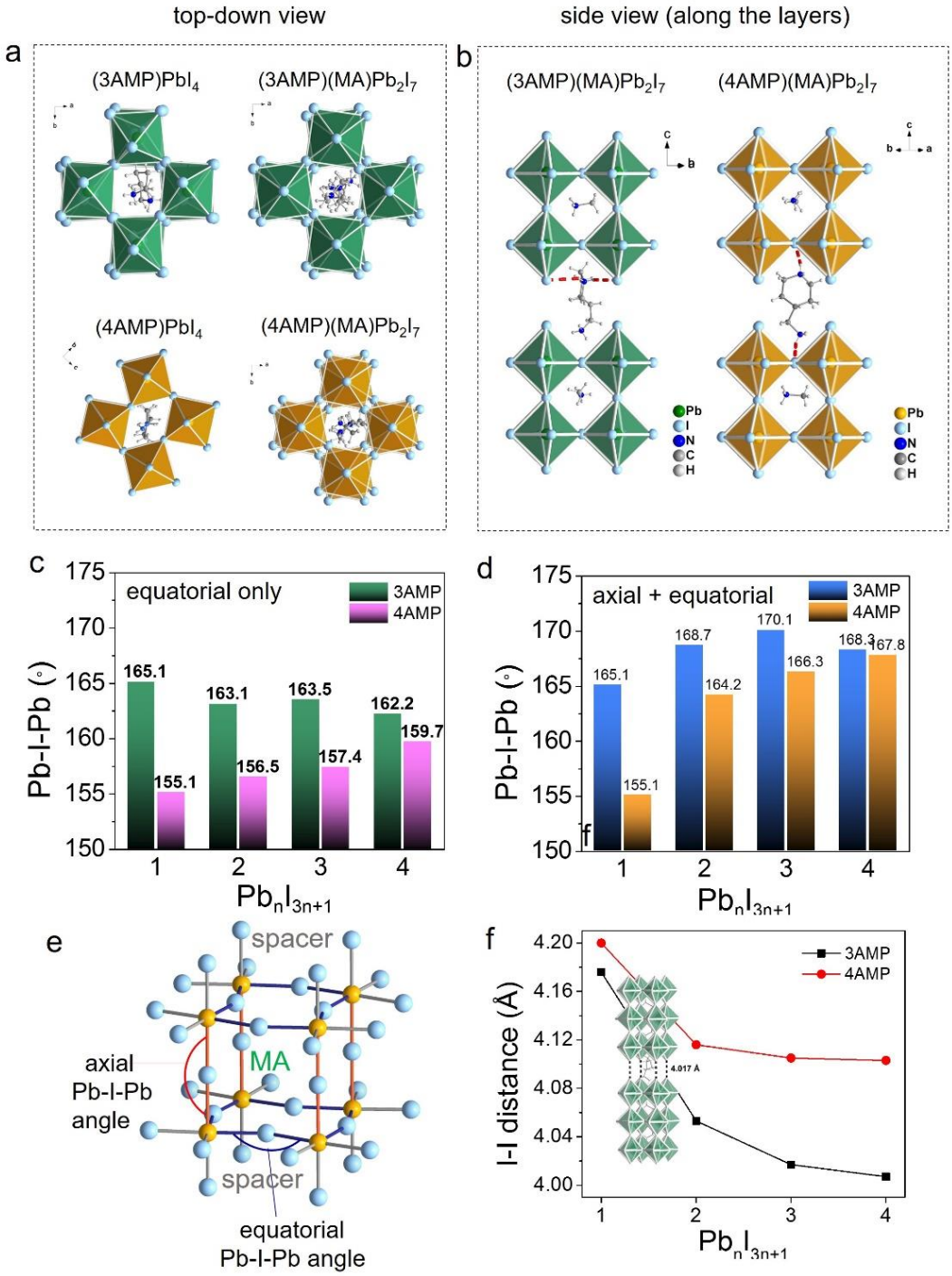

Figure 41. (a) Top-view of (3AMP)PbI_4, (4AM)$PPbI_4$, (3AMP)(MA)Pb_2I_7 and (4AMP)(MA)Pb_2I_7. (b) Side-view of (3AMP)(MA)Pb_2I_7 and (4AMP)(MA)Pb_2I_7, hydrogen bonding is marked in red. (c) Average equatorial Pb-I-Pb angles for 3AMP and 4AMP series from n = 1 to 4. (d) Average axial and equatorial angles for 3AMP and 4AMP. e, Definition of axial and equatorial Pb-I-Pb angles. (f) I···I distance trend in 3AMP and 4AMP, where the 3AMP series has closer distance.

layers stack almost exactly on top of one another from the top-down viewing direction. (3AMP)PbI_4 is somewhat mismatched due to an out-of-plane tilting. (4AMP)PbI_4 matches perfectly as it displays exclusively large in-plane tilting. The 3AMP and 4AMP behave alike when it comes to n = 2, where the difference only lies in the Pb-I-Pb angle. The trend continues for the higher numbers (n = 3 and 4). Viewing along the inorganic layers (Figure 41b), the hydrogen bonding networks for 3AMP and 4AMP are drastically different. In (3AMP)(MA)Pb_2I_7, the 3AMP cation forms weak H-bonds (highlighted in red) with the terminal I^-. Bonding with the terminal I^- has a small effect on the in-plane Pb-I-Pb angles as the terminal I^- does not contribute to the in-plane distortion directly. On the contrary, in (4AMP)(MA)Pb_2I_7, the H-bonds are formed with the bridging I^- anions deeper inside the layers as seen in Figure 41b, which amplify the in-plane distortion.

The differences in hydrogen bonding have an impact on the Pb-I-Pb angles, which are directly related to the optical and electrical these materials (see below). To illustrate this point, we classify the Pb-I-Pb angles into two categories, the axial (along the longest crystallographic axis) and the equatorial (along the inorganic plane) as shown in Figure 41e. In these systems, the axial Pb-I-Pb angles are very close to 180°, as they are much less affected by the interaction (e.g. hydrogen bonding) with the spacing cations. On the other hand, the equatorial Pb-I-Pb angles are much more distorted since they are directly exposed to the spacing cations, especially for the case of n = 1 and n = 2. The evolution of the Pb-I-Pb angles is summarized in Figure 41c and d, where Figure 41c

shows only the averaged equatorial angles and Figure 41d shows the averaged (both axial and equatorial) Pb-I-Pb angles. From Figure 2c, it is clear the gap between the average of the equatorial angles of the 3AMP and 4AMP gradually closes as the layer thickness increases from n = 1 to 4. For 3AMP, the averaged equatorial Pb-I-Pb decreases from 165.1˚ to 162.2˚ while for 4AMP it increases from 155.1˚ to 159.7˚. This indicates that the effect of organic cation on the inorganic slabs is gradually diminished as they get thicker (increasing n number). As the axial Pb-I-Pb angles

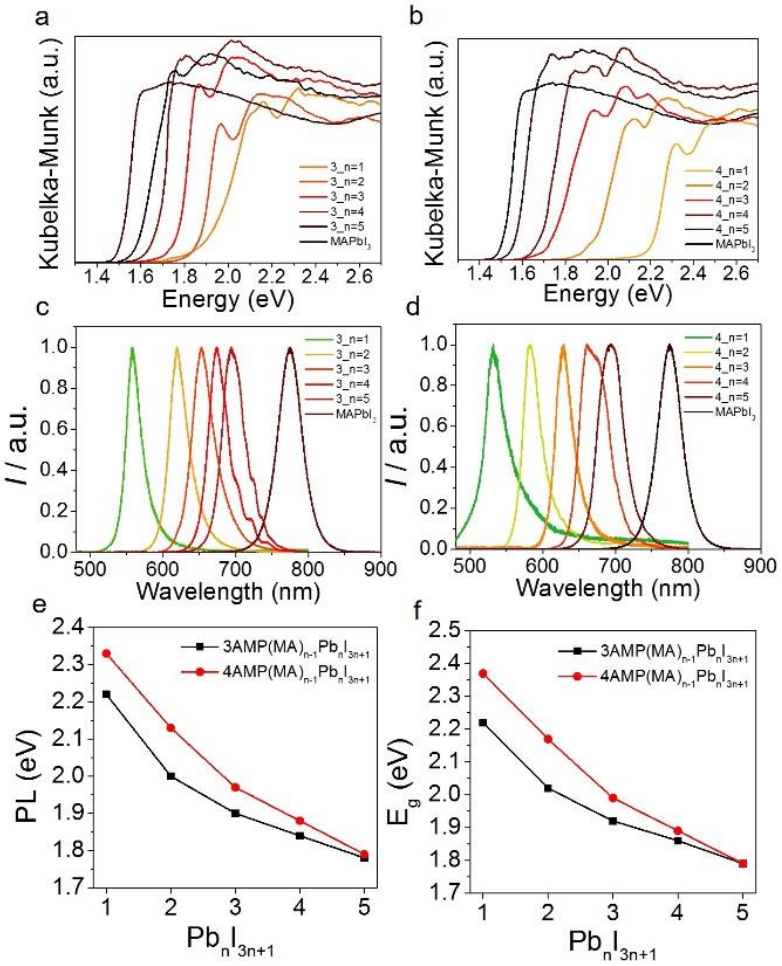

Figure 42. Optical properties of the 3AMP and 4AMP series. (a,b) Optical absorption spectra of 3AMP and 4AMP series. (c,d) Steady-state photoluminescence (PL) spectra of 3AMP and 4AMP series. (e,f) Summary of absorption and PL in energy from n = 1 to 5.

in both series are close to 180˚, when they are averaged with the equatorial angles as shown in Figure 41d, the average is increased for both series up to n = 4.

Another interesting structural feature is that the I···I distance between the inorganic layers is very short. Since the layers lay exactly on top of each other (eclipsed configuration), the I···I distance essentially defines the closest interlayer distance. The 3AMP series has generally smaller I···I distance than 4AMP (Figure 41d), while for both series the I···I distance gradually decreases slightly as the layer gets thicker. This is possibly a result of increased stacking fault formation in the perovskite layers as n increases, expressed indirectly in the determined average crystallographic structure. The close I···I interlayer distance (~ 4.0 Å) is one of the shortest among reported 2D lead iodide perovskites and plays a crucial role in affecting the electronic band structure of these materials which will be discussed below.

The optical band gaps of both 3AMP and 4AMP series follow a general trend that has the energy gap (E_g) decreasing as the layer number (n) increases (Table 11). From n = 1 to n = ∞ ($MAPbI_3$), the band gap decreases from 2.23 eV to 1.52 eV for the 3AMP series, while for the 4AMP the range is much wider (2.38 eV to 1.52 eV) (Figures 42a, b). The spectra of both series show clear excitonic features similarly to other 2D perovskites,[100, 113, 139, 145, 225] which become less

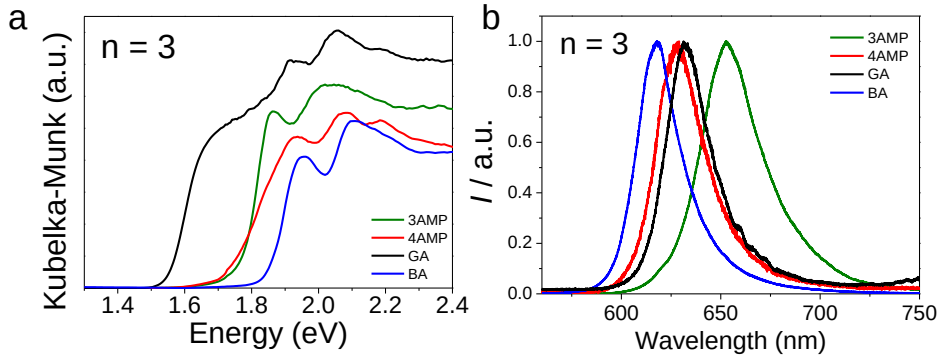

Figure 43. Comparison of the (a) optical absorption spectra and (b) PL spectra between $(3AMP)(MA)_2Pb_3I_{10}$, $(4AMP)(MA)_2Pb_3I_{10}$, $(GA)(MA)_3Pb_3I_{10}$ and $(BA)_2(MA)_2Pb_3I_{10}$.

p rominent as the n number increases and finally disappear for n = ∞. The steady-state photoluminescence (PL) spectra of these materials, shown in Figures 42c, d, exhibit an analogous trend with the band gaps. The 3AMP series demonstrates constantly lower PL emission energy than the 4AMP, until n = 5 when they become equal. Though the evolution of the band gap of both series matches the PL trend, from n = 3 and above, the difference between the two series is negligible (Figures 42e, f). The lifetimes of both AMP series (Figure D6) are comparable to the previously reported 2D layered perovskite PEA (PEA = phenylethylamine) series, for which the

Table 11. Optical properties and color of the $(A')(MA)_{n-1}Pb_nI_{3n+1}$ (A' = 3AMP or 4AMP, n = 1- 4) DJ perovskites.

	Compound	**E_g (eV)**	**PL (eV)**	**Color**	**Compound**	**E_g (eV)**	**PL (eV)**	**Color**
n = 1	$(3AMP)PbI_4$	2.23	2.22	red	$(4AMP)PbI_4$	2.38	2.33	orange
n = 2	$(3AMP)(MA)Pb_2I_7$	2.02	2.00	dark red	$(4AMP)(MA)Pb_2I_7$	2.17	2.13	red
n = 3	$(3AMP)(MA)_2Pb_3I_{10}$	1.92	1.90	black	$(4AMP)(MA)_2Pb_3I_{10}$	1.99	1.97	black
n = 4	$(3AMP)(MA)_3Pb_4I_{13}$	1.87	1.84	black	$(4AMP)(MA)_3Pb_4I_{13}$	1.89	1.88	black

lifetimes lie in the 0.1 – 0.2 ns range.[426] Overall the 3AMP series has longer lifetime than the 4AMP (except n = 1), which indicates slower carrier combination, more ideal for the PV devices.

The optical properties of the DJ iodide perovskites are quite different from those observed in RP perovskites.[139] Relative to the corresponding RP perovskites (Figure 43), the emission energy observed in PL is characteristically red shifted by ~ 0.1 eV in the case of 3AMP (1.90 eV) and 0.03 eV in the case of 4AMP (1.97 eV) with respect to the BA analogue (2.00 eV), taking n = 3 as the reference example.[139] The absorption edges of the compounds containing AMPs (1.70 eV) are also 0.1 eV lower than the BA analogue. The recently reported structural type ACI perovskite $GAMA_3Pb_3I_{10}$ falls in between the RP and DJ perovskites, with a E_g of 1.73 eV and PL emission peak at 1.96 eV. [159]

The optical properties of these materials correlate very well with their structural characteristics. As discussed above, the Pb-I-Pb angles for 3AMP are systematically larger than the 4AMP. The larger Pb-I-Pb bond angles (closer to 180˚), the more the Pb s and I p orbitals overlap.[91, 427-428] The strong anti-bonding interaction pushes up the valence band maximum (VBM), resulting in a reduced band gap. Thus, the systematically narrower band gap observed for 3AMP vs 4AMP can be attributed to the more linear Pb-I-Pb angles (i.e. smaller octahedral tilting (Figure D7)) for the former.

The results of Density Functional Theory (DFT) electronic structure calculations are shown in Figure 44a-g. The calculated band gap for (3AMP)PbI_4 is determined at the Γ point (1.13 eV) (Figure 44a), whereas the band gap of (4AMP)PbI_4 is determined at the BZ edge (1.14 eV) (Figure 44b). The calculated band gaps for the higher numbers between the 3AMP and 4AMP series have larger differences, where E_g is 0.48 eV for n = 2, 3AMP, and 0.70 eV for n = 2, 4AMP (Figure 44c- d). For n = 3, the band gaps at Z point for 3AMP and 4AMP are 0.47 eV and 0.74 eV, respectively (Figure 44e -f). The calculated gap for 3AMP (n = 4) is very small (0.07 eV), much lower than 0.54 eV for n = 4, 4AMP as seen in Figure 44g -h. The DFT computed band gaps do not include many-body interactions needed to properly assess optical response, which is why calculated values are systematic underestimated without GW corrections.[337] The band gaps of 3AMP series DJ are systematically smaller than those computed for 4AMP series as shown in

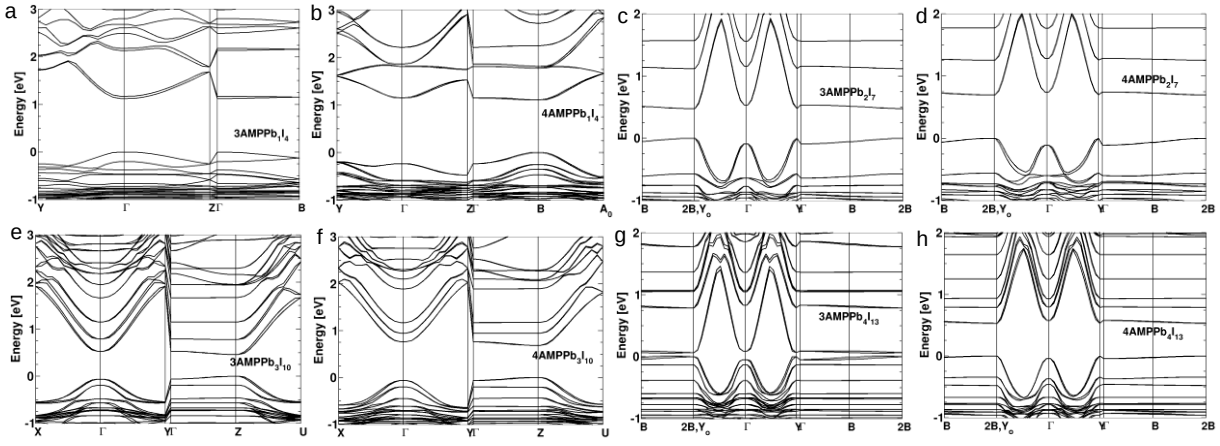

Figure 44. (a-g) DFT calculations of band structures for the 3AMP and 4AMP series with SOC. The calculated gaps are 1.13 eV for (3AMP)PbI_4(*at Γ*), 1.14 eV for (4AMP)PbI_4 (*at B*), 0.48 eV for (3AMP)(MA)Pb_2I_7 *(at Y_o),* 0.70 eV for (4AMP)(MA)Pb_2I_7 *(at Y_o),* 0.47 eV for (3AMP)$(MA)_2Pb_3I_{10}$ *(at Z),* 0.74 eV for (4AMP)$(MA)_2Pb_3I_{10}$ *(at Z),* 0.07eV for (3AMP)$(MA)_3Pb_4I_{13}$ *(at Y_o),* 0.54 eV for (4AMP)$(MA)_3Pb_4I_{13}$ *(at Y_o)*

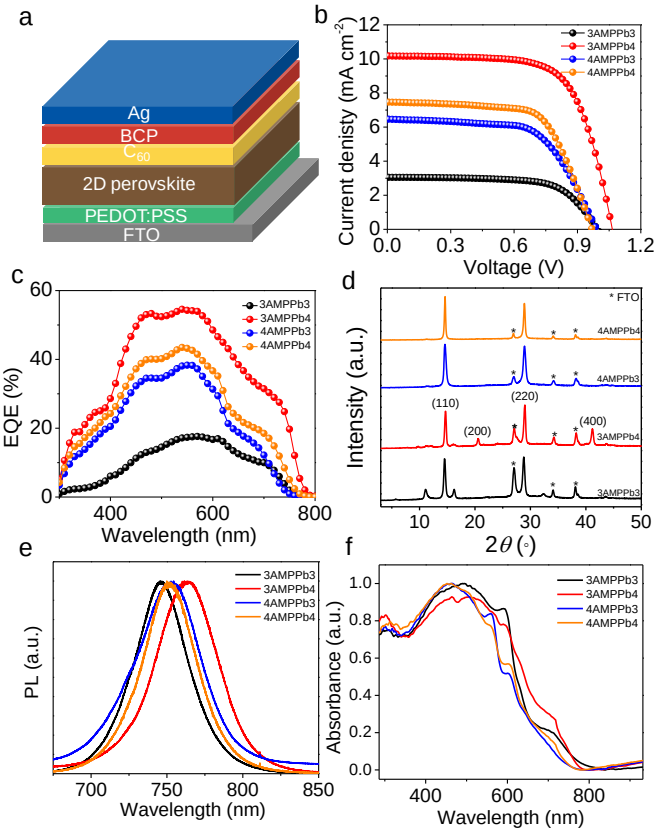

Figure 45. Solar cell architecture for the higher layer numbers (n = 3 and 4) of 3AMP and 4AMP. (a) Scheme of the adopted inverted device structure. (b) J-V curves of the 2D perovskite solar cell devices. (c) External quantum efficiency (EQE) spectra. (d) PXRD of the thin-films. e, steady-state PL spectra, where the emission peaks: 746 nm, 1.66 eV($3AMPPb_3I_{10}$), 764 nm, 1.62 eV ($3AMPPb_4I_{13}$), 752 nm, 1.65 eV ($4AMPPb_3I_{10}$ and $4AMPPb_4I_{13}$). (f) Absorption spectra for the thin-films.

Figure 5h, in agreement with experimental findings. The stacking of perovskite sheets in the DJ structure type, which aligns the perovskite layers, allows for a better interlayer electronic coupling through van der Waals I···I interactions. These I···I contacts participate in anti-bonding interactions that further destabilize the VBM (Figure D9), contributing to the reduction of the band gap as compared to RP phases with respect to the same n-value, as discussed above.

Based on the attractive properties of the new 2D DJ perovskites, in a preliminary study we investigated the higher layer numbers (n = 3 and 4) as light absorbers for solar cells. A planar solar cell structure was adopted for device fabrication (Figure 45a), consisting of a fluorine doped tin oxide (FTO) substrate, a poly(3,4-ethylenedioxythiophene) polystyrene sulfonate (PEDOT:PSS) hole transport layer (HTL), a 2D perovskite light absorber, a C_{60}/BCP electron transport layer (ETL) and a Ag electrode. The devices were fabricated using a modified solvent engineering method. The photocurrent density-voltage (J-V) curves of the solar cells using the 2D DJ perovskites are in Figure 45, (measured using a reverse voltage scan). The thickness of the perovskite films was ~25 0 nm. Among the n = 3 and 4 for 3AMP and 4AMP, (3AMP)$(MA)_3Pb_4I_{13}$ achieved the highest power conversion efficiency (PCE) of 7.32% with a short-circuit current density (J_{sc}) of 10.17 mA·cm^{-2}, an open-circuit voltage (V_{oc}) of 1.06 V, and a fill factor (FF) of 67.60%. This value is significantly higher that the corresponding n = 3 and n = 4 RP perovskites prepared using a regular mesoporous TiO_2 device structure.

The remarkable performance of (3AMP)$(MA)_3Pb_4I_{13}$ can be mainly attributed to the reduced band gap and the improved mobility originating from the increased band dispersion (see above). While the device based on (3AMP)$(MA)_2Pb_3I_{10}$ has the lowest PCE of 2.02% with a J_{sc} of 3.05 mA·cm^{-2}, a V_{oc} of 0.99 V, and a FF of 66.54%, attributed to the largest band gap and the intense presence of a secondary phase, identified as the n = 2 member (2θ = ~11° and ~16°). (4AMP)$(MA)_2Pb_3I_{10}$ and (4AMP)$(MA)_3Pb_4I_{13}$ have PCE below 5%, mainly due to the much lower J_{sc} relative to the 3AMP. The average photovoltaic parameters of the devices using the various

absorbers are summarized in Table D6. The J_{sc} integrated from the external quantum efficiency (EQE) curves (Figure 45) of the devices based for $(3AMP)(MA)_2Pb_3I_{10}$, $(3AMP)(MA)_3Pb_4I_{13}$, $(4AMP)(MA)_2Pb_3I_{10}$ and $(4AMP)(MA)_3Pb_4I_{13}$ are 2.92, 10.16, 5.83, and 7.08 $mA \cdot cm^{-2}$, respectively, which are in good agreement with the trend of the J_{sc} obtained from the J-V curves. In Figure 45d, powder x-ray diffraction (PXRD) of the $(3AMP)(MA)_3Pb_4I_{13}$, $(4AMP)(MA)_2Pb_3I_{10}$ and $(4AMP)(MA)_3Pb_4I_{13}$ films show preferred orientation in the "perpendicular" direction judging from the strongest *hkl* (110) and (220) at ~14° and ~28°, which facilitates the carriers to travel through the layers.[100, 242] Further results of the fabrication of higher quality films and higher efficiency solar cells will be reported in the future.

PL emission properties of the films (Figure 45e) are quite different (red shifted) from the bulk materials, which can be attributed to the so-called "edge effect".[225] The edge effect is observed in single crystals of both $3AMPPbI_4$ and $(3AMP)(MA)_2Pb_3I_{10}$ as seen in Figure D11. The second PL emission at lower energy were observed when excited the sample through "the edge", which is parallel to the layers. The results show larger separation of the higher (2.21 eV from bulk) and lower energy emission (1.64 eV edge) of the n = 1 than for n = 3 (1.91 eV and 1.68 eV) for 3AMP. The lower energy emission (1.68 eV) is very close to the emission of the thin film (1.66 eV). This result is similar to the previously reported $(BA)_2(MA)_2Pb_3I_{10}$ example, where the higher energy emission is 2.00 eV and lower energy emission is 1.70 eV.[225] Attempts for measuring edge states of the other layered number crystals such as n = 2 and 4 were not successful owing to the thin crystal morphology which has caused handing difficulty.

The absorption edges of the films have the same trend as in the EQE spectra, though multiple slopes appear, indicating the formation of some lower layer numbers (Figure 45f). Even though these 2D DJ perovskite devices are not completely optimized, the initial results show great promise as they compare well with the corresponding 2D RP perovskites which lead the 2D perovskite solar cells field.[242, 403, 429]

5.5 Conclusions

We have shown that a new crystal motif based on the DJ class of perovskites forms 2D hybrid lead iodide perovskites. The special spacer cations used 3AMP and 4AMP have strong influence on the overall properties. Detailed crystallographic investigations on all eight compounds (n = 1 to 4, for 3AMP and 4AMP), have provided the structural insights for understanding the structure-property relationships. In particular, by understanding the angular distortion (Pb-I-Pb angle) within the system, we manage to show the subtle difference in the cations causes large differences in the optical properties by affecting the Pb-I-Pb angles, where the 3AMP series has systematically larger angles and smaller band gaps than the 4AMP series. Compared to the most common 2D RP perovskites, namely the BA series, the 3AMP and 4AMP series possess lower band gaps because of a less distorted inorganic framework and closer I···I interlayer distances. Our analysis suggests more superior optoelectronic properties of the 3AMP over the 4AMP series, which as demonstrated in the actual device fabrication, where the preliminary result shows the champion device has PCE over 7%. The strong correlation between the materials and their applications'

performance validates the importance of understanding structure-property relationships and discovering new materials in the halide perovskite systems.

Chapter 6. Seven-layered 2D Hybrid Lead Iodide Perovskite: A Comparison Between Dion-Jacobson and Ruddlesden-Popper Phases

This chapter may appear in the following manuscript:

Mao, L.; Traore, B.; Ke, W.; Katan, C.; Even, J.; Stoumpos, C. C.; and Kanatzidis, M. G. "Seven-layered 2D Hybrid Lead Iodide Perovskite: A Comparison Between Dion-Jacobson and Ruddlesden-Popper Phases". *Manuscript in preparation*

Author contributions

Ke, W.: fabricated and characterized the solar cell devices.

Traore, B.; Katan, C.; Even, J.: performed the DFT calculations.

Stoumpos, C. C and Kanatzidis, M. G.: discussed the results and directed this research.

All authors discussed the results and contributed to revising the manuscript.

6.1 Abstract

Two-dimensional (2D) hybrid perovskites have attracted growing interests due to the high versatility and potential in optoelectronic applications. The 2D family has a general formula of $A'_mA_{n-1}BnX_{3n+1}$, where A' is the organic spacer, A is the small organic cation such as MA or FA, B is a metal and X is halide. Here, we present the highest layer thickness (n = 7) that ever crystallographically characterized of the two main subgroups in 2D family: the Dion-Jacobson (DJ) and Ruddlesden-Popper (RP). The seven-layered DJ phase $(4AMP)(MA)_6Pb_7I_{22}$ (4AMP = 4-aminomethylpyperidinium) shows much less distortion (i.e. Pb-I-Pb angle, bond angle variance and bond length distortion) in the crystal structure, when comparing with the RP phase $(BA)_2(MA)_6Pb_7I_{22}$ (BA = butylammonium). This further influence the optical properties, where the DJ phase has lower energy absorption edge and photoluminescence emission (1.53 eV, 1.71 eV) than the RP phase (1.57 eV, 1.73 eV). DFT calculation reveals an opposite trend with respect to the experimental result, possibly due to complexity of the structure. The discovery and characterization of high-layer thickness 2D hybrid perovskite provide more insights in future material discovery and understanding the structure-property relationship of these semiconductors.

6.2 Introduction

Two-dimensional (2D) halide perovskites are an important class of material that possesses huge potential in optoelectronics.[81, 99-100, 242, 248, 430] Following the success of 3D perovskites that have further improved the record power conversion efficiency (PCE) to 23.3%,[431] the 2D materials have demonstrated higher stability with decent performance of ~14%.[101, 103, 432] From a structural perspective, the 2D perovskites have more parameters to tune, with a general formula of $A'_mA_{n-1}B_nX_{3n+1}$, where A' is the spacing cation, A is a perovskitizer (MA, FA or Cs),[128] B is a metal (Pb, Sn etc.) and X is a halide (Cl, Br, I). The two main classes of multilayered 2D halide perovskites are Dion-Jacobson (DJ)[102, 118] and Ruddlesden-Popper (RP),[139] which are defined by the charge of the interlayer spacing cation.[415] The DJ phase has divalent cation (m = 1), whereas the RP phase incorporates monovalent cation (m = 2). Up till now not many crystallographically characterized high layer thickness ($n \geq 4$) have been reported, except the RP series with butylammonium cations (BA) (n = 1-7),[139, 145] the DJ series with 3-aminomethylpiperidinium (3AMP) and 4-aminomethylpiperidinium (4AMP) (n = 1-4),[102] $(NH_3C_mH_{2m}NH_3)(CH_3NH_3)_{n-1}Pb_nI_{3n+1}$ (m = 4–9; n = 1–4).[155] Due to the quantum confinement effect, the higher the thickness the lower the band gap, which pushes the absorption to a more optimal near IR region for photovoltaics.[434] The limited exploration in high layer thickness prompt us to further elucidate the structural-property relationship in these systems because of their underlying potential for optoelectronics.

Here, we report the highest layered 2D perovskites (n = 7), with detailed crystallographic characterization and structural analysis. The crystal structures are shown in Figure 46. The

difference in the layer conformation is clearly seen in the side view and top-down view of the structures, where the layers of DJ phase overlap exactly on top of each other, showing a (0, 0) displacement. The layers of the RP phase are more flexible showing a (1/2, 1/2) displacement because of the monovalent cation BA that only attaches to one side of the slab (Figure 1c-d). The interlayer requires two sheets of organic cations of BA (singly protonated NH_3^+) whereas the DJ phase only requires one sheets of 4AMP (doubly protonated, NH_3^+ and piperidinium).

6.3 Experimental Details

6.3.1 Synthesis

Materials. PbO (99.9%), 4-(aminomethyl)piperidine (96%), hydroiodic acid (57 wt. % in H_2O, distilled, stabilized, 99.95%) and hypophosphorous acid solution (50 wt. % in H_2O) were purchased from Sigma-Aldrich and used as received. Methylammonium iodide (>99.5%) was purchased from Luminescence Technology Corp. and used as received.

Synthesis of (4AMP)(MA)$_6$Pb$_7$I$_{22}$. An amount of 892 mg (4 mmol) 99.9% PbO powder was dissolved in 4 mL of hydroiodic acid and 0.5 mL hypophosphorous acid solution by heating under stirring for 5-10 min at 130°C until the solution turned to clear bright yellow. 636 mg (4 mmol) of methylammonium iodide (MAI) was added directly to the above solution under heating. 0.5 mL hydroiodic acid was added to 23 mg (0.2 mmol) 4AMP in a separate vial under stirring. The protonated 4AMP solution was added into the previous solution under heating and stirring for 5

min. Black plate-like crystals precipitated during slow cooling to room temperature. Yield 312 mg (12.0% based on total Pb content).

6.3.2 Optical Absorption Spectroscopy

Optical diffuse reflectance measurements were performed using a Shimadzu UV-3600 UV-VIS-NIR spectrometer operating in the 200 – 1000 nm region using $BaSO_4$ as the reference of 100% reflectance. The band gap of the material was estimated by converting reflectance to absorption according to the Kubelka–Munk equation: $\alpha/S = (1–R)^2(2R)^{-1}$, where R is the reflectance and α and S are the absorption and scattering coefficients, respectively.

6.3.3 *Steady State Photoluminescence*

Steady-state PL spectra were collected using HORIBA LabRAM HR Evolution Confocal RAMAN microscope. 473 nm laser (0.1% power) was used to excite all samples at 50× magnification.

6.3.4 DFT Simulations

The calculations were performed within the Density Functional Theory (DFT)[1-2] as implemented in SIESTA package[3] with a basis set of finite-range of numerical atomic orbitals. We used the Generalized Gradient Approximation (GGA) with Perdew-Burke-Ernzerhof (PBE) functional[4] to describe the exchange-correlation term, and norm-conserving Troullier-Martins

pseudopotentials were used for each atomic species to account for the core electrons.[5] $1s^1$, $2s^22p^2$, $2s^22p^3$, $5s^25p^5$ and $5d^{10}6s^26p^2$ were used as valence electrons for H, C, N, I, and Pb respectively. Polarized Double-Zeta (DZP) basis set with an energy shift of 50 meV and a Mesh cutoff 200 Rydberg were used for the calculations. The Brillouin zone was sampled with 6x6x2, and 2x6x6 Monckhorst-Pack grids for $(BA)_2(MA)_6Pb_7I_{22}$ and $(4AMP)(MA)_6Pb_7I_{22}$ respectively. The densities of states (DOS) were generated with a Gaussian smearing of 0.1 eV. The electronic properties were calculated using the experimental lattice parameters and atomic coordinates. Spin-Orbit coupling (SOC) was taken into account in the calculation of the electronic band structures.

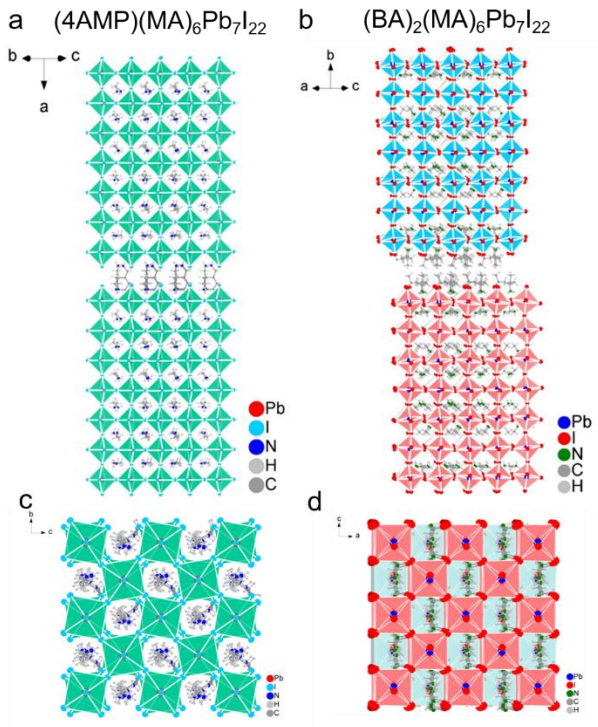

Figure 46. Crystal strucuture of (a) DJ phase $(4AMP)(MA)_6Pb_7I_{22}$ and (b) RP phase $(BA)_2(MA)_6Pb_7I_{22}$. Top-down view of the layers in (c) $(4AMP)(MA)_6Pb_7I_{22}$ and (d) $(BA)_2(MA)_6Pb_7I_{22}$. The layers of DJ perovskite lay on top of each other, whereas the RP phase shows an offset shifting of one octahedral unit.

Table 12. Single crystal X-ray diffraction refinement details for the DJ phase (4AMP)$(MA)_6Pb_7I_{22}$.

Empirical formula	$(C_6N_2H_{16})(CH_3NH_3)_6Pb_7I_{22}$
Formula weight	4550.74
Temperature, wavelength	293(2) K, 0.71073 Å
Space group	*Pc*
Unit cell dimensions	a = 48.605(10) Å, α = 90°
	b = 8.8635(18) Å, β = 90.13(3)°
	c = 8.8638(18) Å, γ = 90°
Volume	3818.6(13) $Å^3$
Density (calculated)	3.958 g/cm^3
θ range, completeness to θ = 26.000°	2.298 to 29.253°, 91.1%
Reflections collected, independent	23035, 14637 [R_{int} = 0.1065]
Data / restraints / parameters	14637 / 32 / 342
Goodness-of-fit	1.032
Final R indices [I > 2σ(I)]	R_{obs} = 0.1197, wR_{obs} = 0.3400

$R = \Sigma||F_o|-|F_c|| / \Sigma|F_o|$, $wR = \{\Sigma[w(|F_o|^2 - |F_c|^2)^2] / \Sigma[w(|F_o|^4)]\}^{1/2}$ and $w=1/[\sigma^2(Fo^2)+(0.2000P)^2]$ where $P=(Fo^2+2Fc^2)/3$

6.4 Results and Discussion

To quantify the subtle differences in the crystal structures, we dissect the structures into individual slabs, where each slab is a representative unit composing the whole structure. In Figure 47a-b, the seven-layered inorganic slabs of the DJ phase and RP phase are placed horizontally, with individually labeled Pb-I-Pb angles. The Pb-I-Pb angle can be viewed as a parameter that quantifies the distortion across the Pb/I inorganic framework. The overall averaged Pb-I-Pb angles are calculated to be 169º for the DJ phase and 165º for the RP phase. The main contribution of the higher averaged angle of the DJ phase comes from the axial Pb-I-Pb angles (perpendicular to the layers, parallel to a-axis) as seen in Figure 47a,[102] which are approaching the ideal 180º. The axial angles (perpendicular to the layers, parallel to b-axis) in the RP phase are all below 170º (Figure

47b). The bond angle variance (BAV) and distortion index (DI) further reflect the distortion within the [PbI_6] unit. We have labeled the individual [PbI_6] octahedron in Figure 2c-d, in which all seven

Table 13. Atomic coordinates ($x10^4$) and equivalent isotropic displacement parameters ($Å^2x10^3$) for $(4AMP)(MA)_6Pb_7I_{22}$ at 293(2) K with estimated standard deviations in parentheses.

Label	x	y	z	Occupancy	U_{eq}^*
Pb(1)	5343(2)	2502(4)	5946(6)	1	39(1)
Pb(2)	4035(1)	2500(4)	5937(4)	1	40(1)
Pb(3)	6650(1)	2498(3)	5939(4)	1	39(1)
Pb(4)	2724(1)	2492(4)	5972(4)	1	45(1)
I(7)	4030(2)	4585(8)	8827(11)	1	79(3)
I(5AA)	5343(3)	403(8)	8844(11)	1	89(3)
I(11)	6650(2)	4586(8)	8841(10)	1	77(2)
I(3AA)	7958(2)	-411(8)	3877(10)	1	80(3)
I(13)	2724(2)	407(8)	8865(11)	1	85(3)
I(4AA)	4694(2)	2507(10)	5968(13)	1	84(2)
I(15)	3383(2)	2501(13)	5985(14)	1	99(3)
I(18)	5999(2)	2519(9)	5963(12)	1	80(3)
I(20)	2080(2)	2531(10)	5986(12)	1	82(3)
I(2)	5342(2)	4617(8)	3053(10)	1	77(2)
I(6AA)	4034(3)	383(8)	3053(11)	1	90(3)
I(5)	6641(3)	371(9)	3048(10)	1	85(3)
I(1AA)	2725(2)	4584(8)	3064(11)	1	86(3)
Pb(5)	7964(1)	2488(3)	5964(3)	1	39(1)
I(0AA)	7303(2)	2496(9)	5973(11)	1	70(2)
Pb(0A)	9278(1)	2501(4)	5957(5)	1	47(1)
I(2AA)	8611(2)	2550(11)	5971(13)	1	86(3)
I(8)	9275(2)	4509(8)	8927(10)	1	80(3)
I(12)	7955(2)	5399(8)	8045(9)	1	80(3)
I(14)	9268(3)	463(8)	2969(10)	1	89(3)
Pb(1A)	1395(2)	2504(3)	5961(5)	1	47(1)
I(4)	762(2)	2492(19)	5997(17)	1	136(5)
I(9)	1402(2)	5479(8)	3913(10)	1	81(3)

I(7AA)	9916(3)	2510(20)	5973(19)	1	148(6)
I(1)	1411(3)	466(8)	2972(10)	1	88(3)
N(5)	3470(40)	7780(160)	6270(170)	1	170(50)
H(5A)	3635	7551	5852	1	198
H(5B)	3467	7379	7195	1	198
H(5C)	3458	8777	6339	1	198
N(2)	7230(40)	1880(170)	10490(160)	1	200(50)
H(2A)	7088	1596	11062	1	242
H(2B)	7335	1082	10303	1	242
H(2C)	7166	2249	9622	1	242
N(6)	2210(60)	2000(300)	11700(300)	1	300(110)
H(6A)	2239	2646	12469	1	357
H(6B)	2369	1786	11271	1	357
H(6C)	2150	1112	12156	1	357
C(5)	3240(40)	7200(200)	5300(200)	1	170(50)
H(5D)	3219	6105	5555	1	248
H(5E)	3289	7265	4277	1	248
H(5F)	3078	7694	5539	1	248
N(4)	4820(30)	7390(130)	6570(130)	1	140(40)
H(4A)	4843	8209	7141	1	165
H(4B)	4977	7097	6186	1	165
H(4C)	4747	6656	7137	1	165
C(6)	2000(60)	2600(300)	10600(300)	1	300(110)
H(6D)	1819	2401	11021	1	446
H(6E)	2020	2034	9688	1	446
H(6F)	2030	3618	10472	1	446
N(3)	6100(50)	1900(200)	10900(200)	1	290(90)
H(3A)	6080	1742	11832	1	352
H(3B)	6272	2283	10700	1	352
H(3C)	6080	1081	10332	1	352
C(3)	5900(60)	3100(300)	10300(300)	1	290(90)
H(3D)	5725	2582	10104	1	440
H(3E)	5963	3590	9467	1	440
H(3F)	5865	3796	11138	1	440

N(1)	8550(50)	6980(190)	5400(200)	1	230(70)
H(1A)	8554	7510	4505	1	274
H(1B)	8406	6370	5363	1	274
H(1C)	8705	6441	5433	1	274
C(4)	4620(30)	7760(170)	5320(150)	1	140(40)
H(4D)	4698	7440	4380	1	206
H(4E)	4589	8828	5298	1	206
H(4F)	4450	7244	5491	1	206
C(2)	7390(50)	3060(190)	11300(200)	1	200(50)
H(2D)	7375	2930	12367	1	302
H(2E)	7327	4046	11019	1	302
H(2F)	7584	2976	11021	1	302
C(1)	8530(60)	8000(200)	6700(200)	1	230(70)
H(1D)	8478	9026	6328	1	343
H(1E)	8710	8119	7159	1	343
H(1F)	8400	7675	7386	1	343
C(8)	670(20)	5490(120)	8100(120)	1	170(20)
H(8A)	675	4473	7704	1	199
H(8B)	662	5426	9187	1	199
N(8)	-121(19)	6590(130)	7280(140)	1	170(20)
H(8C)	-68	7095	6464	1	199
H(8D)	-174	7232	7988	1	199
H(8E)	-261	5984	7035	1	199
C(12)	660(20)	7920(110)	5760(130)	1	170(20)
H(12A)	660	8142	4685	1	199
H(12B)	662	8879	6291	1	199
N(7)	922(18)	7090(130)	6130(100)	1	170(20)
H(7A)	1074	7800	6111	1	199
H(7B)	954	6343	5355	1	199
C(9)	402(17)	6190(140)	7580(100)	1	170(20)
H(9)	400	7042	8284	1	199
C(11)	403(18)	7090(140)	6150(120)	1	170(20)
H(11A)	254	7816	6201	1	199
H(11B)	361	6407	5321	1	199

C(7)	921(18)	6310(130)	7630(110)	1	170(20)
H(7C)	1072	5597	7644	1	199
H(7D)	961	7066	8401	1	199
C(10)	114(19)	5650(120)	7860(150)	1	170(20)
H(10A)	91	5546	8940	1	199
H(10B)	97	4652	7423	1	199

*U_{eq} is defined as one third of the trace of the orthogonalized U_{ij} tensor.

Table 14. Anisotropic displacement parameters ($Å^2x10^3$) for $(4AMP)(MA)_6Pb_7I_{22}$ at 293(2) K with estimated standard deviations in parentheses.

Label	U_{11}	U_{22}	U_{33}	U_{12}	U_{13}	U_{23}
Pb(1)	41(2)	39(1)	38(1)	0(2)	1(1)	-3(1)
Pb(2)	40(2)	41(2)	41(2)	2(2)	0(2)	-3(2)
Pb(3)	49(2)	35(2)	35(2)	-2(2)	3(2)	0(2)
Pb(4)	34(2)	52(2)	48(2)	12(2)	-2(2)	-3(2)
I(7)	92(7)	63(4)	82(5)	-6(4)	6(5)	-39(4)
I(5AA)	121(8)	72(5)	75(5)	11(5)	5(5)	44(4)
I(11)	93(7)	80(5)	58(4)	-9(4)	9(4)	-37(4)
I(3AA)	103(7)	79(5)	57(4)	-1(5)	12(5)	-34(4)
I(13)	109(8)	54(4)	92(6)	-2(4)	-4(5)	31(4)
I(4AA)	30(3)	117(6)	105(6)	-7(4)	-2(4)	-15(5)
I(15)	28(3)	137(8)	131(8)	28(4)	7(4)	9(6)
I(18)	38(3)	96(6)	106(7)	2(4)	5(4)	26(5)
I(20)	52(5)	98(6)	98(6)	-20(4)	5(5)	2(5)
I(2)	98(7)	67(4)	66(5)	-10(4)	-5(5)	33(3)
I(6AA)	126(9)	59(4)	86(6)	6(4)	-5(6)	-36(4)
I(5)	123(9)	75(5)	58(5)	9(5)	-3(5)	-33(4)
I(1AA)	109(8)	61(4)	87(6)	-4(4)	-11(5)	44(4)
Pb(5)	55(2)	31(2)	31(2)	-11(2)	4(2)	1(2)
I(0AA)	49(4)	78(4)	82(5)	-18(3)	1(4)	4(4)
Pb(0A)	40(2)	53(2)	49(2)	-5(2)	-3(2)	-8(2)
I(2AA)	33(3)	107(6)	119(7)	30(4)	-1(4)	1(5)
I(8)	104(8)	73(4)	64(5)	6(4)	-12(5)	-35(3)
I(12)	106(8)	81(5)	52(4)	0(4)	1(4)	-43(3)

I(14)	145(10)	57(4)	65(5)	-3(4)	-13(5)	-22(3)
Pb(1A)	61(2)	37(2)	43(2)	3(2)	7(2)	3(2)
I(4)	36(4)	198(14)	174(14)	2(6)	15(7)	-4(10)
I(9)	97(7)	68(4)	78(5)	4(4)	25(5)	37(4)
I(7AA)	71(7)	189(14)	184(15)	-7(8)	-8(10)	-2(10)
I(1)	141(10)	55(4)	68(5)	7(4)	2(5)	-17(3)

The anisotropic displacement factor exponent takes the form: $-2\pi^2[h^2a^{*2}U_{11} + ... \quad + 2hka^*b^*U_{12}]$.

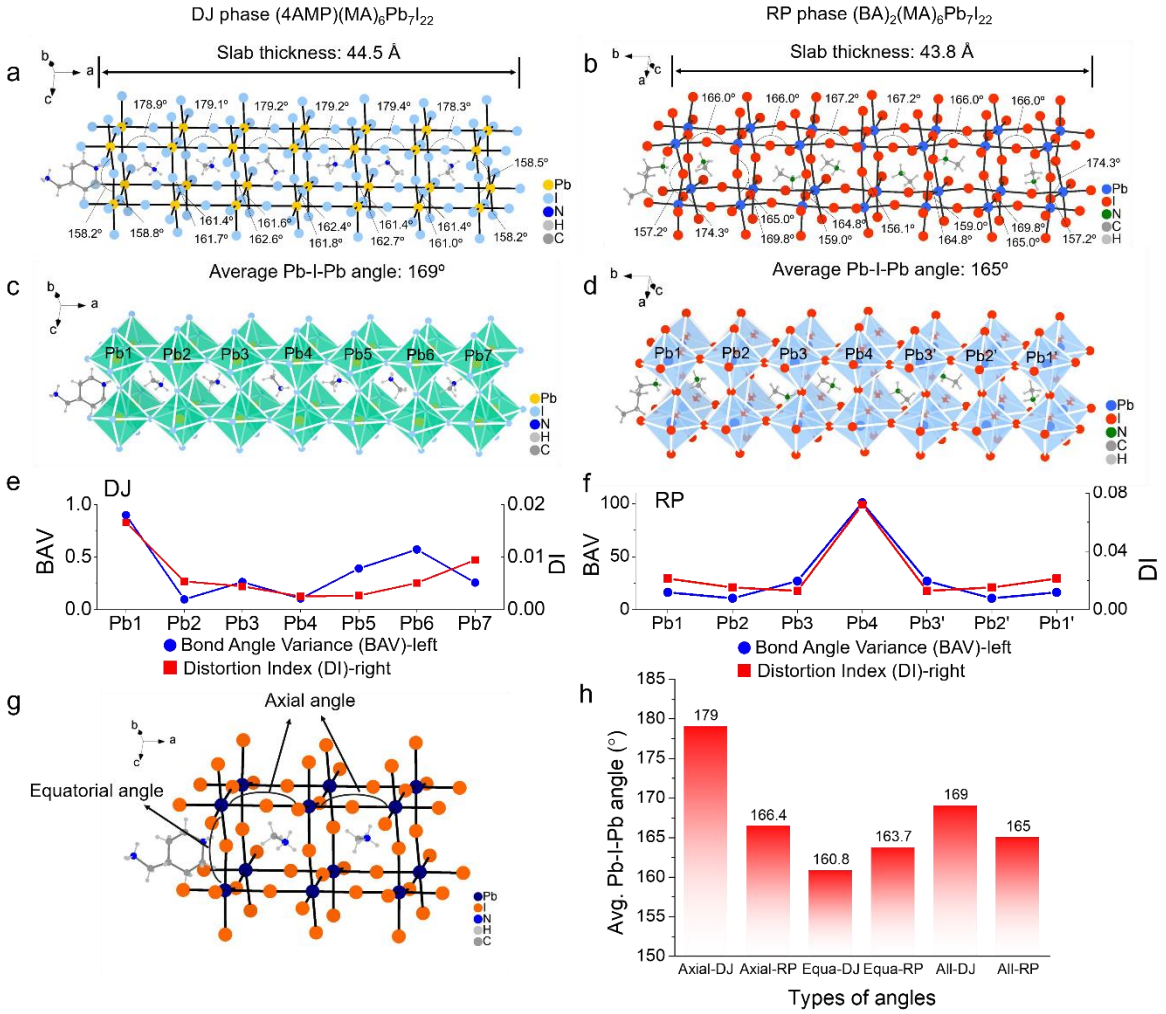

Figure 47. Detailed Pb-I-Pb angles for (a) DJ phase $(4AMP)(MA)_6Pb_7I_{22}$ and (b) RP phase $(BA)_2(MA)_6Pb_7I_{22}$. Crystallographic independent Pb environments in (c) $(4AMP)(MA)_6Pb_7I_{22}$ and (d) $(BA)_2(MA)_6Pb_7I_{22}$. (e,f) Distortion evaluation of individual $[PbI_6]$ octahedron using bond angle variance (BAV) and distortion index (DI) calculated by Vesta software. The DJ phase shows a much lower distortion level than the RP phase both on BAV and DI. (g) Definition of axial (perpendicular to the layers) and equatorial (along the layers) Pb-I-Pb angles. (h) comparison between veraged axial, equatorial and total Pb-I-Pb angles.

Pb environments are different for the DJ phase whereas for the RP phase Pb1 and Pb1', Pb2 and Pb2', Pb3 and Pb3' are the same. The bond angle variance (BAV, quantifying the distortion from I-Pb-I angles inside the [PbI_6]) and distortion index (DI, quantifying the distortion from Pb-I bond length) are calculated using Vesta software.[435] The BAV values of all the [PbI_6] units in the DJ phase are below 1, which on the contrary the BAV values are around 20 and can reach as high as 100 for the RP phase. The difference on the DI is less dramatic but still the DJ phase has smaller value (0.01-0.02) and the RP phase can go as high as 0.08. The other main difference lies in the asymmetric (DJ) and symmetric Pb environment. For the DJ phase, the [PbI_6] unit (Pb1) that's next to the piperidinium ring is the most distorted. For the RP phase, the middle [PbI_6] unit (Pb4) is the most distorted among all units, possibly due to the compression of the adjacent slabs. This also originates from the nature of the organic spacing cations here, where the alkyl chain tails of the BA cations are repellent towards each other, creating a stronger force that going towards the middle. For the DJ system, the 4AMP cations are connecting both ends of two inorganic slabs, serving as springs that have a "cushioning" effect. This is also the reason for the less "stressed" axial Pb-I-Pb angles of the DJ phase and more "stressed" axial Pb-I-Pb angles in the RP phase. To summarize, the seven-layered DJ perovskite (4AMP)$(MA)_6Pb_7I_{22}$ is less distorted than the RP phase $(BA)_2(MA)_6Pb_7I_{22}$, both across the Pb/I network and on individual [PbI_6] units.

The optical properties match the trend that a less distorted structure will lead to a smaller band gap. From UV-vis and steady-state PL spectra (Figure 48a-b), it is evident that the DJ phase has lower absorption edge (1.53 eV) than the RP phase, and is between the 3D perovskite $MAPbI_3$

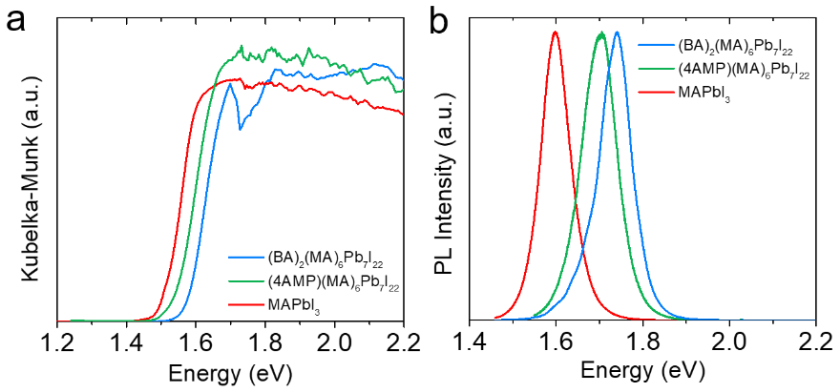

Figure 48. (a) Optical absorption spectra and (b) steady-state photoluminescence spectra of $(4AMP)(MA)_6Pb_7I_{22}$, $(BA)_2(MA)_6Pb_7I_{22}$ and $MAPbI_3$.

(1.50 eV) and the RP phase (1.57 eV). The emission energies of the PL for the DJ and RP phase are further way from the $MAPbI_3$ (1.60 eV), which are 1.70 eV and 1.73 eV, respectively. The PL emission energy keeps decreasing as the layer gets thicker, from 1.83 eV for the n = 5 member of the RP phase and 1.79 eV for the n = 5 member of the DJ phase

We try to further explore the intrinsic differences of the seven-layered DJ phase and RP phase in their electronic structures. Density functional theory (DFT) calculations were conducted based on the experimental crystal structure (Figure 49). Figure 4 compares the electronic band structures of the RP and the DJ. The direct band gaps of 0.20 eV at Γ and 0.26 eV at Y are computed for the RP and DJ phase, respectively. The absence of the inversion center coupled with the presence of a giant spin-orbit coupling in both structures induces little Rashba spin-splitting at mainly the conduction band (CB) for RP and both the valence band (VB) and CB for DJ. We notice flat dispersions (< 1 meV) along YΓ for RP in reciprocal space, which corresponds to its stacking axis in real space, whereas slight dispersions along the stacking axis Γ-Y of DJ are calculated (~31 meV at VBM and ~39 meV at CBM). The latter is due to the interaction between the outer I-I

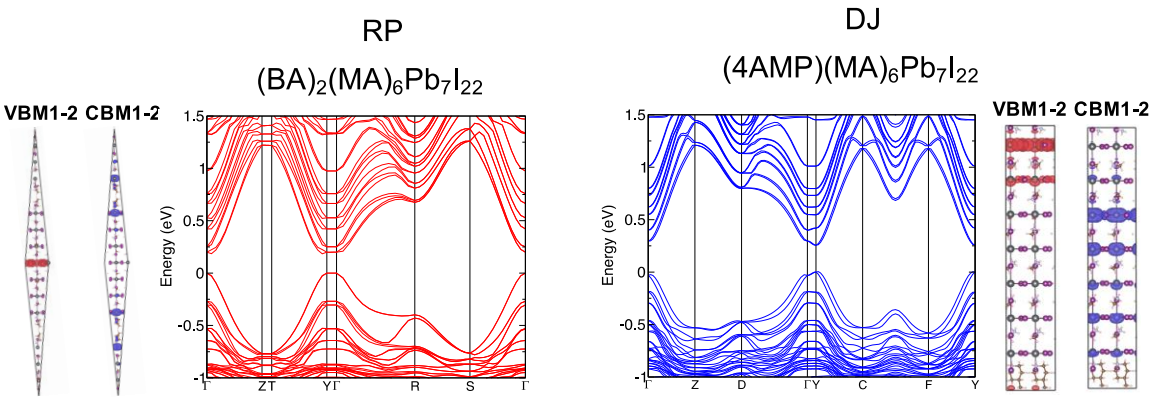

Figure 49. Comparison of the band structures of (left) $(BA)_2(MA)_6Pb_7I_{22}$ and (right) $(4AMP)(MA)_6Pb_7I_{22}$ including spin-orbit coupling effects. For each structure, the localized densities of states (LDOS) of VBM and CBM are also plotted showing different localization of the densities for the two structure types.

atoms that are in direct contact with 4AMP cations as reported earlier.[102] For both systems, we notice seven (7) sub-bands in the CB along the directions of reciprocal space corresponding to the stacking axis, which amounts to the number of Pb-I octahedral planes in each structure. These sub-bands are less distinguishable in the VB and are an indication of diminishing quantum confinement effects as a result of an increased number of octahedra planes, when compared to lower n-values, that ultimately converge to the 3D band structure.[127]

In an apparent contradiction with experiment, our calculations show that BA has a lower band gap as compared to DJ, with a difference amounting to ~60 meV, whereas the experimental data indicates a lower band gap for DJ (~ 30 meV below that of RP). Computed densities of states confirm this trend. As a lready stressed, obtaining very precise structural information on high n-value members *via* X-Ray diffraction is challenging. Using the structure-property analysis based on two characteristic tilt angles (β, δ)[124] allows to link the variation of the octahedral tilts to band gap variation.

The localized densities of states (LDOS) at VBM and CBM for both structure types show different spatial distributions (Figure 49). For RP, VBM is localized at the inner octahedral layer while CBM is located at the outer octahedral planes. For DJ, CBM is mostly localized over the inner layer whereas VBM is asymmetrically localized over one side of the outer layer. The latter asymmetry can be traced back to the two different charged moieties in the 4AMP di-cations ($[NH_2]^+$ versus $[NH_3]^+$) that induces net dipole, which in turn induces the dissymmetry of the electronic density at VBM that localizes on the $[NH_3]^+$ side.

The orbital hybridization can be best seen from wave functions, computed without SOC. For both systems, VBM is made of an anti-bonding hybridization between Pb (6s) and I (5p) while CBM mainly consists of bonding hybridization between Pb (6p) states. We note that the spatial localizations of LDOS computed with SOC (Figure 49) are consistent with their wave functions distributions on the different octahedral planes.

6.5 Conclusions

In conclusion, comparing the structure of DJ phase $(4AMP)(MA)_6Pb_7I_{22}$ and RP phase $(BA)(MA)_6Pb_7I_{22}$, we have found that the DJ phase in all aspects (bond length distortion, bond angle variance and Pb-I-Pb angles) is less distorted than the RP phase, which is indicative of lower band gap energy. Experimentally we have confirmed the trend that the absorption edge and PL emission of the DJ phase is in-between the 3D perovskite $MAPbI_3$ and the RP phase. The

exploration of the structure-property relationship in ultra-high thickness 2D halide perovskite material unlocks the door for the “in-between” species in the halide perovskite family.

Chapter 7. Hybrid 2D Dion-Jacobson Lead Bromide Perovskites: Conformation Control from Interplay Between Large Organic Spacers and Perovskitizer Cations

This chapter may appear in the following manuscript:

Mao, L.; Guo, P.; Kepenekian, M.; He, Y.; Katan, C.; Even, J.; Schaller, R. D.; Stoumpos, C. C.; Kanatzidis, M. G. "Hybrid 2D Dion-Jacobson Lead Bromide Perovskites: Conformation Control from Interplay Between Large Organic Spacers and Perovskitizer Cations". *Manuscript in preparation*

Author contributions

Guo, P.: performed the low-frequency Raman spectroscopy and time-resolved PL.

Kepenekian, M.; Katan, C.; Even, J.: performed the DFT calculations.

He, Y.: performed the electrical measurements.

Stoumpos, C. C and Kanatzidis, M. G.: discussed the results and directed this research.

All authors discussed the results and contributed to revising the manuscript.

7.1 Abstract

Hybrid halide perovskites are groundbreaking materials that have achieved astonishing records in optoelectronics. To gain further insights in the mixed cation system, we use the 3AMP and 4AMP cations (3AMP = 3-(aminomethyl)piperidinium, 4AMP = 4-(aminomethyl)piperidinium) as A' cation that form the Dion-Jacobson (DJ) phase 2D perovskite, to build the solid-solutions composing of both mixed A' and A cations (A = methylammonium (MA) or formamidinium (FA)). Crystal structures and purity of the newly synthesized nine compounds based on the (A')(A)Pb_2Br_7 (A' = 3AMP or 4AMP, A = FA or MA) formula are collected and examined using single crystal X-ray diffraction and powder X-ray diffraction. The conformation mode and distortion of the Pb-Br inorganic framework are severely impacted by the templating A' cation and perovskitizer cation A. The addition of 4AMP into the $(3AMP)_a(4AMP)_{1-a}(FA)_b(MA)_{1-b}Pb_2Br_7$ (a and b = 1, 0.5 or 0) system, decreases the Pb-Br-Pb angle, making the framework more distorted. On the contrary, with more FA incorporated into the system, the Pb-Br-Pb angle increases. This structural evolution together affects he optical band gap, as the the larger the Pb-Br-Pb angle, the band gap becomes smaller. Density Functional Theory (DFT) calculations of the electronic structures reveal the same trend as the experimental result where (3AMP)(FA)Pb_2Br_7 has the smallest band gap while (4AMP)(MA)Pb_2Br_7 has the largest band gap. The different effect from solely the organic cations (both the spacing and perovskitizer cations) in the 2D system highlight the importance of understanding the structural evolution accompanied by compositional tuning.

7.2 Introduction

Hybrid organic-inorganic halide perovskite materials have established themselves as one of the leading semiconducting materials because of their superior performances in optoelectronics.[30-31, 49, 251] The ease of thin-film preparation and favorable properties of the hybrid perovskites such as long carrier diffusion length, long carrier lifetime, high carrier mobility and optimal absorption properties are helping to elevate the performance, currently up to 23.3% power conversion efficiency (PCE).[436] Breakthroughs of perovskite-based materials have also been reported recently in light emitting diodes (LEDs), where the highest external quantum efficiency (EQE) has reached 20%.[437] A recent strategy for fabricating high performance photovoltaic devices is to mix together various of A-site cations (Cs^+, FA^+, MA^+, Rb^+), the integration of which in the device, remarkably, boosts the performance compared with pristine samples.[438-441] This genuine performance upgrade is achieved mainly from an increased charge-carrier mobility,[442] which generally depends on the details of the crystal structure of the perovskite. Other chemical strategies that aid the device performance involving the variation of the composition include halide-mixing and using additives in the thin-films.[13, 443-444] In most cases, even though PCE and physical properties improvement were observed, structural insights were not provided, mainly due to the complications ensuing from the dynamic disordered 3D systems.[43-44, 133]

As an extension to 3D perovskites, 2D hybrid perovskites have attracted increasing interest so much from their highly diverse chemistry,[98-100, 117, 242] as much from the unusual photo-physical properties they possess.[125, 127] Importantly, despite reduction in dimensionality, 2D perovskites

have firmly proved that they exhibit similarly superb optoelectronic characteristics as the 3D perovskites. The dimensional reduction lends additional flexibility to the crystal lattice and as a result, the tolerance factor limitation that occurs in the 3D perovskite is no longer a requirement for a 2D perovskite to form[226, 445]. Typical examples of the defiance of the tolerance factor in 2D perovskite are the 2D perovskites based the tolerance-"forbidden" cations ethylammonium (EA)[117] and isopropylammonium (IPA).[128] An added benefit of the 2D perovskites is that large organic cations with appropriate functional groups can be inserted between the 2D layers by intercalation.[81, 118, 188] Intercalation chemistry has been intensively explored, utilizing supramolecular concepts such as fluoroaryl-aryl interactions and hydrogen bonding,[78, 446] and chemical reactivity such as halogen insertion[165] and Diels-Alder cycloaddition.[447] Aside from the diversity of the organic part, the inorganic lattice can be chemically sliced in a specific layer orientation (100-oriented,[90, 114] 110-oriented[113, 116] and 111-oriented[203, 205] with respect to the ideal cubic perovskite), layer thickness (n = 1-7), metal substitution (Pb, Sn, Ge, Bi, Sb, Cu, Fe etc.), and halide derivatization (Cl, Br and I). Moreover, 2D layered perovskites further divide the into four subcategories, the Ruddlesden−Popper (RP) phases (with 1+ cations)[139] and the Dion−Jacobson (DJ) phases (with 2+ cations),[102] alternating cation and diammonium cation.[155, 159]

Herein, we explore the concept of organic cation mixing aiming to fine-tune the structural features within the new family of (A')(A)Pb_2Br_7 DJ perovskites. Through controlled mixing of both A-site cation (MA, FA), for which we refer to as the "perovskitizer" (meaning that it solely forms the 3D perovskite), and A'-cation (the large organic spacer), we demonstrate that the degree

of distortion of the perovskite in each individual layer can be successfully controlled. We take advantage of the similar size and functionality of the 3AMP and 4AMP cations, to build double solid-solutions composed of both mixed A' and A cations. By combining A' (3AMP/4AMP) and A (MA/ FA), we have synthesized nine different compounds based on the $(A')(A)Pb_2Br_7$ (A' = 3AMP or 4AMP, A = FA or MA) formula, distinctive perovskite distortion modes ranging from out-of-phase tilting to in-phase tilting along with the undistorted structural prototype (Figure 1). The powder X-ray diffraction (PXRD) shows pure phase for each solid solution with only small peak shifts due to the change of the unit cell volume. We identify the inorganic distortion (i.e. the Pb-Br-Pb angles) in the crystal structure using single crystal X-ray diffraction for selected compositions of the $(3AMP)_a(4AMP)_{1-a}(FA)_b(MA)_{1-b}Pb_2Br_7$ (a and b = 1, 0.5 or 0) system. We find a dependence between the Pb-Br-Pb angle on both a and b variables, with the angle becoming smaller (i.e., larger distortion) with increased values of a and b. The optical band gap obeys the general "rule" of the halide perovskites which states that the larger the Pb-Br-Pb angle, the smaller the band gap, which is also seen in the emission energy of the photoluminescence (PL). The compositional mapping employed in this work provides an excellent tool for probing how subtle changes at the organic cation sites drive the structural evolution within the inorganic layer of a given 2D hybrid halide perovskite, thus acting as synthetic knobs to control the semiconducting properties of the materials.

7.3 Experimental Details

7.3.1 Synthesis

Materials. $PbBr_2$ (98%), 3-(aminomethyl)piperidine (Aldrich^{CPR}), 4-(aminomethyl)piperidine (96%), hydrobromic acid (ACS reagent, 48%) were purchased from Sigma-Aldrich and used as received.

Synthesis of (A')(A)Pb_2Br_7 (A' = 3AMP or 4AMP, A = MA or FA). Taking the synthesis of (3AMP)(FA)Pb_2Br_7 as an example, an amount of 1.10 g (3 mmol) of $PbBr_2$ was dissolved in 5 mL of HBr under heating and stirring at 122 °C (vial A). 312 mg (3 mmol) of formamidinium acetate was added into the previous solution after all $PbBr_2$ was dissolved. In a separate vial (vial B), 1 mL HBr was added into 57 mg (0.5 mmol) of 3- (aminomethyl)piperidine. Under heating and stirring at 122 °C, vial B was poured into vial A and the reaction continued for another 5-10 min until the solution became clear. Plate-like yellow crystals precipitated during slow cooling to room temperature. Yield 372 mg (21.8% based on total Pb content). This procedure applies to the rest of the compounds, except the amount of the cations changes to the ratio shown in Table 15.

Table 15. Experimental ratios for the synthesis of (A')(A)Pb_2Br_7 (A' = 3AMP or 4AMP, A = MA or FA).

Compound	3AMP	4AMP	Formamidine acetate	MACl
(4AMP)(MA)Pb_2Br_7	0	57 mg	0	202 mg
(4AMP)$(FA)_{0.5}(MA)_{0.5}Pb_2Br_7$	0	57 mg	156 mg	101 mg
(4AMP)(FA)Pb_2Br_7	0	57 mg	312 mg	0
$(3AMP)_{0.5}$ $(4AMP)_{0.5}$ (MA)Pb_2Br_7	28.5 mg	28.5 mg	0	202 mg
$(3AMP)_{0.5}$ $(4AMP)_{0.5}(FA)_{0.5}(MA)_{0.5}Pb_2Br_7$	28.5 mg	28.5 mg	156 mg	101 mg
$(3AMP)_{0.5}$ $(4AMP)_{0.5}$(FA)Pb_2Br_7	28.5 mg	28.5 mg	312 mg	0
(3AMP)$(FA)_{0.5}(MA)_{0.5}Pb_2Br_7$	57 mg	0	156 mg	101 mg

7.3.2 Powder X-ray Diffraction

PXRD analysis was performed using a Rigaku Miniflex600 powder X-ray diffractometer (Cu Kα graphite, λ = 1.5406 Å) operating at 40 kV/15 mA with a Kβ foil filter.

7.3.3 Single Crystal X-ray Diffraction

Full sphere data were collected after screening for a few frames using either a STOE IPDS 2 or IPDS 2T diffractometer with graphite-monochromatized Mo Kα radiation (λ = 0.71073 Å) (50 kV/40 mA) under N_2 at 293K ((3AMP)(MA)Pb_2Br_7, (3AMP)(FA)Pb_2Br_7, (4AMP)(MA)Pb_2Br_7 and (4AMP)(FA)Pb_2Br_7). The collected data was integrated and applied with numerical absorption corrections using the STOE X-AREA programs. The rest of the compounds were collected using a Bruker Molly instrument with MoKα IμS microfocus source (λ = 0.71073 Å) with MX Optics at 293K. The collected data was integrated and applied with numerical absorption corrections using the APEX3 software. Crystal structures were solved by direct methods (Full-matrix least-squares on F2) and refined by full-matrix least-squares on F^2 using the OLEX2 program package.[372]

7.3.4 Optical Absorption Spectroscopy

Optical diffuse reflectance measurements were performed using a Shimadzu UV-3600 UV-VIS-NIR spectrometer operating in the 200–1000 nm region using $BaSO_4$ as the reference of 100% reflectance. The band gap of the material was estimated by converting reflectance to absorption

according to the Kubelka–Munk equation: $\alpha/S = (1–R)^2(2R)^{-1}$, where R is the reflectance and α and S are the absorption and scattering coefficients, respectively.

7.3.5 Computational Details

First-principles calculations are based on density functional theory (DFT) as implemented in the SIESTA package.[375-376] Experimental structures are used for the inorganic skeleton, well characterized by X-ray diffraction. By contrast, the atomic positions of organic cations have been optimized using the non-local van der Waals density functional of Dion et al. corrected by Cooper (C09). Spin-orbit coupling is taken into account through the on-site approximation as proposed by Fernández-Seivane et al.[380] To prevent conflicts between the on-site treatment and the non-locality of C09, single points calculations are conducted with the revPBE functional on which C09 is based. Core electrons are described with Troullier-Martins pseudopotentials.[378] The valence wavefunctions are developed over double-ζ polarized basis set of finite-range numerical pseudoatomic orbitals. In all cases, an energy cutoff of 150 Ry for real-space mesh size has been used.

7.4 Results and Discussion

Synthesis of the two-layered (A')(A)Pb_2Br_7 (A' = 3AMP or 4AMP, A = FA or MA) series of compounds follows a similar route as we previously reported,[102] changing only the solvent from

hydroiodic acid to hydrobromic acid (see experimental details). To synthesize the solid-solution using mixed cations, the experimental ratios of the A' and A cation was used stoichiometrically, i.e. for $(3AMP)_{0.5}(4AMP)_{0.5}(FA)_{0.5}(MA)_{0.5}Pb_2Br_7$, the experimental ratio of 3AMP:4AMP:FA:MA was 1:1:1:1. The as-synthesized compounds grow as colorless, transparent crystals with a thin, rectangular plate-like morphology (Figure E1). Using powder X-ray diffraction (PXRD), we were able to confirm the compositional purity of the compounds, with all of them exhibiting the characteristic diffraction pattern of the bi-layered perovskite (Figure 51a), in excellent agreement with the calculated ones. The PXRD patterns of the compounds have the trademark characteristics

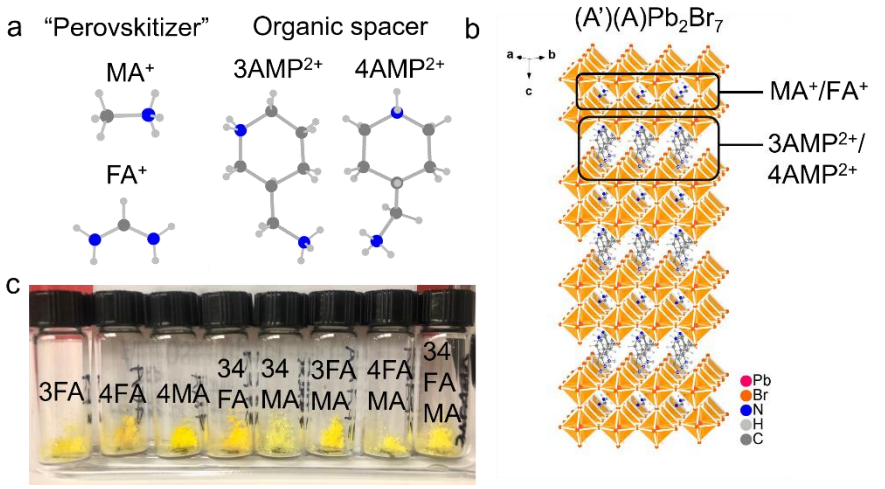

Figure 50. (a) Structures of the "perovskitizer" (MA^+ and FA^+) and organic spacer ($3AMP^{2+}$ and $4AMP^{2+}$) (Blue: nitrogen, dark grey: carbon, light grey: hydrogen). (b) General crystal structure of $(A')(A)Pb_2Br_7$ incorporating both mixed A cation (MA^+/FA^+) and mixed A' cation ($3AMP^{2+}/4AMP^{2+}$). (c) Picture of the resulting 2D compounds. For convenience, $(3AMP)(FA)Pb_2Br_7$ is denoted as 3FA, $(3AMP)_{0.5}(4AMP)_{0.5}(FA)Pb_2Br_7$ is denoted as 34FA, same rule applied to rest of the compounds. 3MA not shown here due to the instability of the compound after filtration.

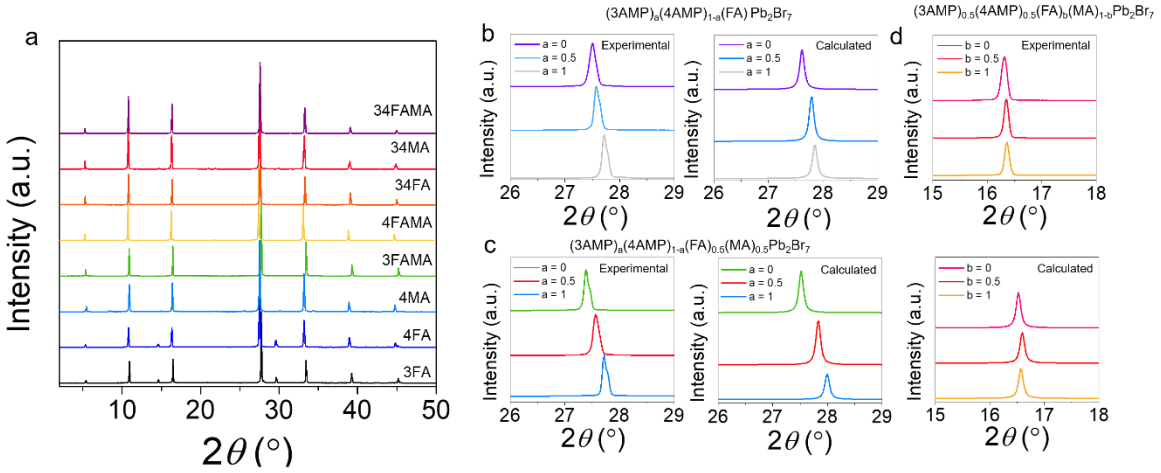

Figure 51. (a) Powder X-ray diffraction (PXRD) patterns of the 2D compounds (3FA = (3AMP)(FA)Pb_2Br_7, 34FA = $(3AMP)_{0.5}(4AMP)_{0.5}(FA)Pb_2Br_7$). (b-d) Zoom-in regions of both the experimental and calculated PXRD patterns showing the gradual lattice parameter change when introducing a new cation.

of a solid-solution with no new peaks emerging showing only a slight peak shift. Typically for crystals of 2D perovskites, due to the strong preferred orientation in the [100] direction of the plates, the (200), (400), (600),…,(h00) reflections are the visible peaks that overshadow the rest of the reflections in the pattern. To evaluate the effect of the addition of A' and A cations, we group the patterns in three triads (Figure 51b-d). The first one, groups the $(3AMP)_a(4AMP)_{1-a}(FA)Pb_2Br_7$ series, where the (10 0 0) peak shifts to higher diffraction angle with increasing amount of 4AMP. This trend is consistent with the long axis expansion (perpendicular to the layers)

Table 16. Crystal Data and Structure Refinement for $(3AMP)_a(4AMP)_{1-a}(FA)_b(MA)_{1-b}Pb_2Br_7$ (a and b = 1, 0.5 or 0).

Compound	$(3AMP)(FA)Pb_2Br_7$	$(3AMP)(MA)Pb_2Br_7$	$(4AMP)(FA)Pb_2Br_7$	$(4AMP)(MA)Pb_2Br_7$
Chemical formula	$(C_6N_2H_{16})[HC(NH_2)_2]Pb_2Br_7$	$(C_6N_2H_{16})(CH_3NH_3)Pb_2Br_7$	$(C_6N_2H_{16})[HC(NH_2)_2]Pb_2Br_7$	$(C_6N_2H_{16})(CH_3NH_3)Pb_2Br_7$
Space group	*Cm*	*Pc*	*Pc*	*Cc*
Unit cell dimensions	a = 8.4615(17) Å, b = 8.4650(17) Å, c = 16.004(3) Å, β = 89.99(3)°	a = 15.952(3) Å, b = 8.4134(17) Å, c = 8.4135(17) Å, β = 90.07(3)°	a = 16.138(3) Å, b = 11.909(2) Å, c = 11.905 (7) Å, β = 90.00(3)°	a = 33.433(7) Å, b = 8.3738(17) Å, c = 8.3760(17) Å, β = 104.45(3)°
Vol ($Å^3$)	1146.3(4) $Å^3$	1129.2(4) $Å^3$	2288.0(8) $Å^3$	2270.8(8) $Å^3$
Z	2	2	4	4
ρ (g/cm^3)	3.288	3.300	3.295	3.282
Indepd. refl.	3034 [R_{int} = 0.0308]	5582 [R_{int} = 0.1475]	11594 [R_{int} = 0.1533]	3739 [R_{int} = 0.1023]
Data / restr. / param.	3034 / 30 / 75	5582 / 30 / 119	11594 / 55 / 236	3739 / 80 / 117
R indices [I>2σ(I)]	R_{obs} = 0.0485, wR_{obs} = 0.1219	R_{obs} = 0.0888, wR_{obs} = 0.2654	R_{obs} = 0.0639, wR_{obs} = 0.1352	R_{obs} = 0.0797, wR_{obs} = 0.1842
R indices [all data]	R_{all} = 0.0587, wR_{all} = 0.1280	R_{all} = 0.1267, wR_{all} = 0.3048	R_{all} = 0.2452, wR_{all} = 0.1972	R_{all} = 0.1812, wR_{all} = 0.2406
Electr. diff. peak/hole ($e \cdot Å^{-3}$)	1.375/-1.601	3.629/-5.168	1.820 /-1.624	1.740/-1.986

determined by single crystal X-ray diffraction, which the long axes for 3FA, 34FA and 4FA having values of 16.004(3), 16.0382(13), 16.138(3), respectively. Similarly, in the $(3AMP)_a(4AMP)_{1-a}(FA)_{0.5}(MA)_{0.5}Pb_2Br_7$ series, the peak shifts to higher angles, correspond to the long axis expansion in the (3FAMA (15.923(2)) < 34FAMA (16.0142(12)) < 4FAMA (16.193(2)) order. Finally, for the $(3AMP)_{0.5}(4AMP)_{0.5}(FA)_b(MA)_{1-b}Pb_2Br_7$ series, the change of the shift becomes

Table 17. Crystal Data and Structure Refinement for $(3AMP)_a(4AMP)_{1-a}(FA)_b(MA)_{1-b}Pb_2Br_7$ (a and b = 1, 0.5 or 0).

Compound	$(3AMP)_{0.5}(4AMP)_{0.5}(FA)_{0.5}(MA)_{0.5}Pb_2Br_7$	$(4AMP)(FA)_{0.5}(MA)_{0.5}Pb_2Br_7$	$(3AMP)_{0.5}(4AMP)_{0.5}(FA)Pb_2Br_7$	$(3AMP)_{0.5}(4AMP)_{0.5}(MA)Pb_2Br_7$
Chemical formula	$(C_6N_2H_{16})[HC(NH_2)_2]_{0.5}(CH_3NH_3)_{0.5}Pb_2Br_7$	$(C_6N_2H_{16})[HC(NH_2)_2]_{0.5}(CH_3NH_3)_{0.5}Pb_2Br_7$	$(C_6N_2H_{16})[HC(NH_2)_2]Pb_2Br_7$	$(C_6N_2H_{16})(CH_3NH_3)Pb_2Br_7$
Space group	*Pc*	*Pc*	*Pc*	*Cc*
Unit cell dimensions	a = 16.0142(12) Å, b = 8.4185(7) Å, c = 8.4164(6) Å, β = 90.024(3)°	a = 16.193(2) Å, b = 8.3678(11) Å, c = 8.3469(10) Å, β = 89.921(6)°	a = 16.0382(13) Å, b = 8.4484(7) Å, c = 8.4494(6) Å, β = 89.9940(15)°	a = 33.2368(17) Å, b = 8.3841(5) Å, c = 8.3801(4) Å, β = 104.599(2)°
Vol ($Å^3$)	1134.66(15)	1131.0(3)	1144.87(16)	2259.8(2)
Z	2	2	2	4
ρ (g/cm^3)	3.372	3.295	3.293	3.2977
Indepd. refl.	5492 [R_{int} = 0.0537]	5029 [R_{int} = 0.0436]	5599 [R_{int} = 0.0510]	5412 [R_{int} = 0.0542]
Data / restr. / param.	5492 / 27 / 119	5029 / 27 / 118	5599 / 29 / 119	5412 / 28 / 118
R indices [I>2σ(I)]	R_{obs} = 0.0438, wR_{obs} = 0.1320	R_{obs} = 0.0581, wR_{obs} = 0.1672	R_{obs} = 0.0505, wR_{obs} = 0.1526	R_{obs} = 0.0466, wR_{obs} = 0.1366
R indices [all data]	R_{all} = 0.0627, wR_{all} = 0.1488	R_{all} = 0.0771, wR_{all} = 0.1832	R_{all} = 0.0765, wR_{all} = 0.1751	R_{all} = 0.0721, wR_{all} = 0.1551
Electr. diff. peak/hole ($e·Å^{-3}$)	1.946/-1.370	3.230/-2.759	1.978/-1.464	2.3068/-1.8194

much less severe, as the change in the unit cell is much smaller, with the long axis expansion following the 34MA < 34FAMA < 34MA order having values of 16.0382(13), 16.0142 (12) and 16.082 (transformed),[448] respectively. The pronounced lattice expansion accentuates the role of the large organic spacer (3AMP vs 4AMP) over the impact of the perovskitizer (FA vs MA), with the large organic spacer causing a much larger change in the unit cell, because it can directly influence the interlayer separation by anchoring deeper or shallower in the inorganic framework

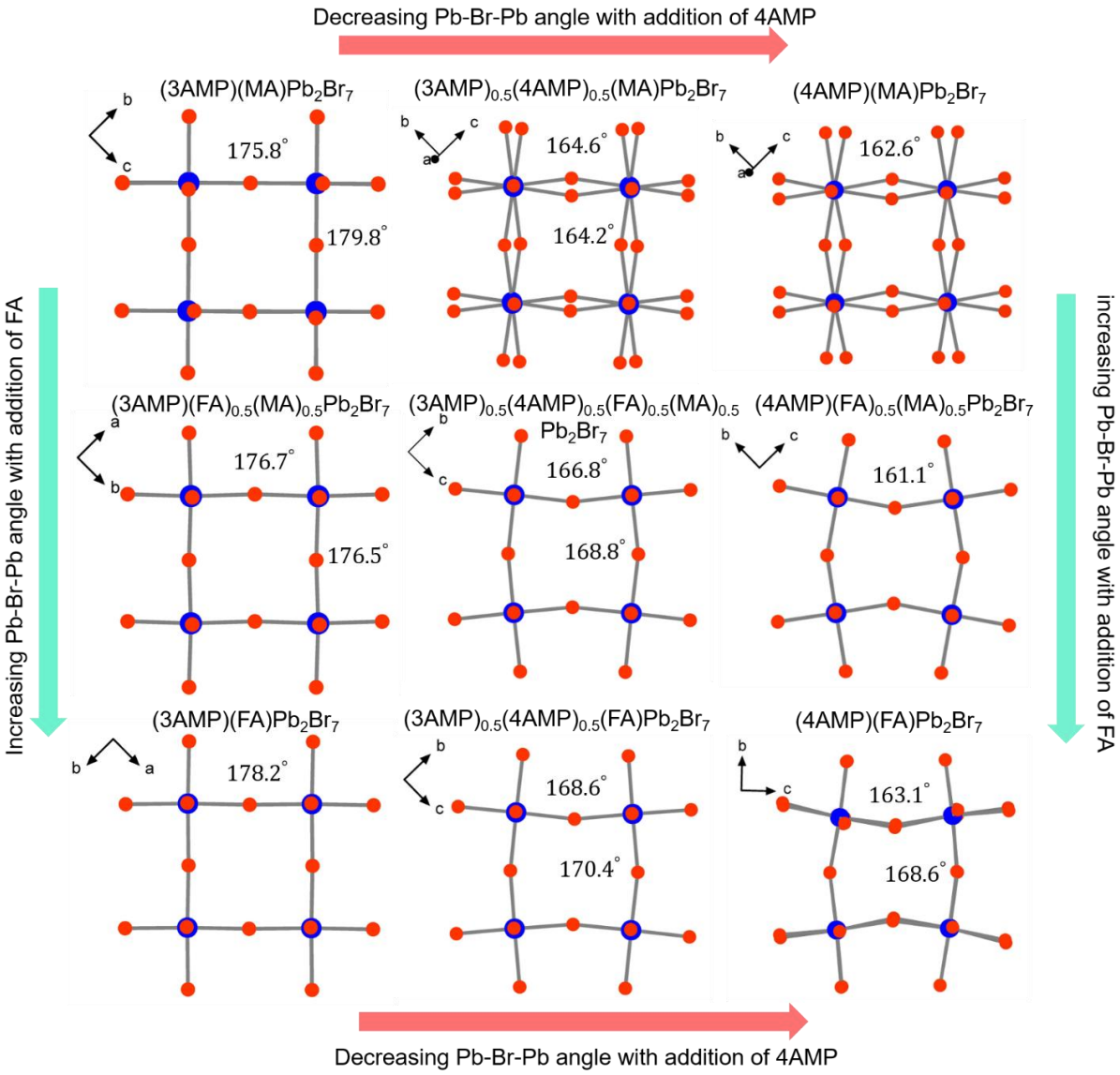

Figure 52. Top-down view of the crystal structure of the nine members of the extended solid solution $(3AMP)_a(4AMP)_{1-a}(FA)_b(MA)_{1-b}Pb_2Br_7$ (a and b = 1, 0.5 or 0). Horizontal Pb-Br-Pb angles in the inorganic framework of each composition are labeled. Atom symbol: orange (Br), blue (Pb), organic cations are omitted here for clarity. The nine structures can be generalized in three types of structural modes: α, β and γ. Mode α:3MA, 3FAMA and 3FA. Mode β: 4MA, 34MA. Mode γ: 34FAMA, 4FAMA, 34FA and 4FA.

dock. On the contrary, the perovskitizer sits within the relatively tight inorganic cage, which can only deform within shorter bounds and therefore the effect is less prominent.

Although mixing A cation is a common strategy, successfully using mixed large A' cation has not been reported before (expect when A cation also act as A' cation in the GA with MA[159]/Cs[158]/FA[160] cases). To take a closer look at the role of the large organic spacer and perovskitizer when incorporated in the crystal structure, we have collected the crystal structure of the nine new compounds (Figure 52). Due to the asymmetry of the organic cations, all structures are solved in non-centrosymmetric monoclinic space groups (*Cm*, *Pc* or *Cc*), as justified previously. The refinement details are provided in Table 14-15. According to their structural distortion, the inorganic Pb-Br frameworks can be divided into three different modes that originate from the parent compounds 3MA, 3FA, 4MA and 4FA. The three compounds (3MA, 3FAMA and 3FA) in the left column belong to the least distorted mode (mode α). 34MA and 4MA (top row middle and

Table 18. Detailed Pb-Br-Pb angles solved from the crystal structures and band gap of the nine compounds with the formula (A')(A)Pb_2Br_7 (A' = 3AMP or 4AMP, A = FA or MA).

Compound	Abbreviation	horizontal Pb-Br-Pb angle 1	horizontal Pb-Br-Pb angle 2	axial Pb-Br-Pb angle	Average Pb-Br-Pb angle	E_g (eV)
(4AMP)(MA)Pb_2Br_7	4MA	162.6	162.6	174.2	166.5	2.82
(4AMP)$(FA)_{0.5}(MA)_{0.5}Pb_2Br_7$	4FAMA	161.1	161.1	179.8	167.3	2.81
(4AMP)(FA)Pb_2Br_7	4FA	163.1	168.6	179.1	170.3	2.78
$(3AMP)_{0.5}$ $(4AMP)_{0.5}$ (MA)Pb_2Br_7	34MA	164.6	164.2	179.8	169.5	2.73
$(3AMP)_{0.5}$ $(4AMP)_{0.5}(FA)_{0.5}(MA)_{0.5}Pb_2Br_7$	34FAMA	166.8	168.8	179.8	171.8	2.73
$(3AMP)_{0.5}$ $(4AMP)_{0.5}$(FA)Pb_2Br_7	34FA	168.6	170.4	177.7	172.2	2.73
(3AMP)(MA)Pb_2Br_7	3MA	175.8	179.8	173.4	176.3	NA
(3AMP)$(FA)_{0.5}(MA)_{0.5}Pb_2Br_7$	3FAMA	176.5	176.7	176.3	176.5	2.66

right) are heavily distorted and together belong to the same mode (mode β) that has the perovskite octahedra connecting out-of-phase along the long axis, so that Br anions do not overlap with each other viewing perpendicular to the layers. The remaining four compounds (34FAMA, 4FAMA, 34FA and 4FA) share another structural mode (mode γ), that has the octahedra tilting in-phase resulting in an eclipsed overlap of the Br anions. Two types of Pb-Br-Pb angles exist in the structure, where the horizontal Pb-Br-Pb angles are the ones along the layers and the axial Pb-Br-Pb angles are the ones perpendicular to the layers (see Table 18). Bases on this analysis, we were

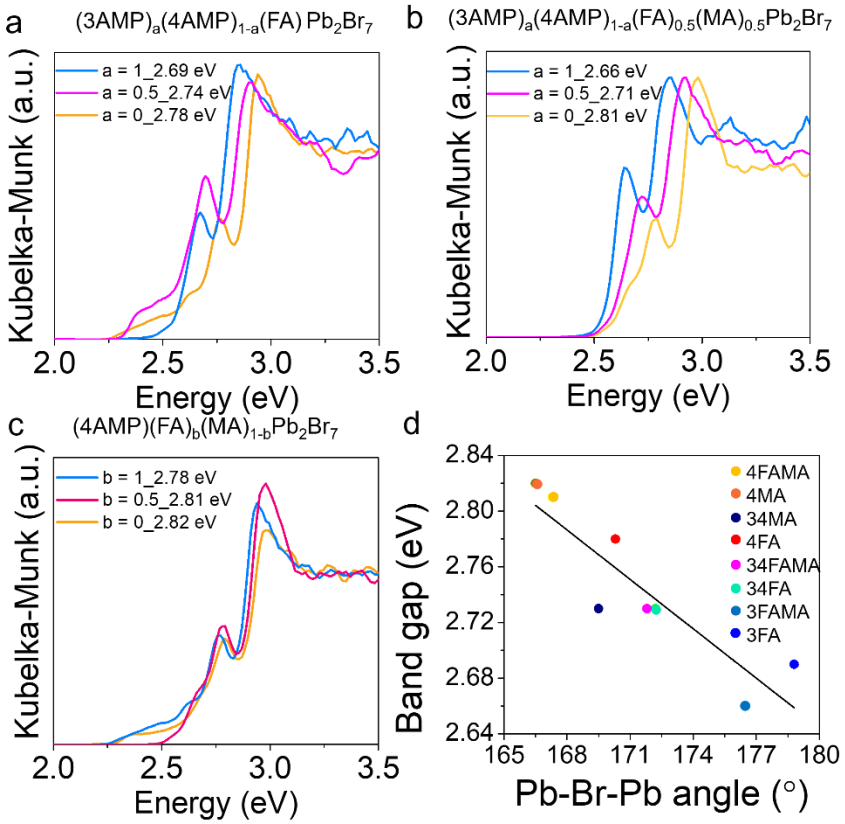

Figure 53. Optical absorption spectra of (a) $(3AMP)_a(4AMP)_{1-a}(FA)Pb_2Br_7$ (a = 0, 0.5, 1); (b) $(3AMP)_a(4AMP)_{1-a}(FA)_{0.5}(MA)_{0.5}Pb_2Br_7$ (a = 0, 0.5, 1); (c) $(4AMP)(FA)_b(MA)_{1-b}Pb_2Br_7$ (b = 0, 0.5,1). (d) Correlation between the Pb-Br-Pb angle and band gap. Black line is for guidance of the eyes.

able to quantify the imposed distortion induced by the organic cations to the inorganic lattice. The two clear-cut trends observed relate to the content of 4AMP, for which the Pb-Br-Pb angle decreases as 4AMP incorporation increases. On the antipode, the addition of FA is also very clear. Irrespectively of whether the system contains 3AMP or 4AMP, the averaged Pb-Br-Pb angle increases with increasing amounts of FA.

The variation of the large organic spacers within the system and the accumulated structural distortion affect the band gap much more than changing the perovskitizer. This is clearly demonstrated in the optical absorption of the $(3AMP)_a(4AMP)_{1-a}(FA)Pb_2Br_7$ and $(3AMP)_a(4AMP)_{1-a}(FA)_{0.5}(MA)_{0.5}Pb_2Br_7$ series. In the optical absorption spectra, we see clear excitonic peaks below the band gap and take the second slope on the higher energy side as the band gap. There are some tails below the excitonic peaks in Figure 53a and 53c, which are not from impurity. When changing the composition of 3AMP vs. 4AMP with a fixed perovskitizer (Figure 53a, b), the band gap changes significantly, by up to 0.15 eV between 3FAMA and 4FAMA. On the other hand, in the $(4AMP)(FA)_b(MA)_{1-b}Pb_2Br_7$ system, varying the perovskitizer content from MA to FA, the band gap changes only marginally (0.04 eV) from 2.82 eV to 2.78 eV as seen in Figure 53c. We further correlate the band gap with the Pb-Br-Pb angle in Figure 53d. The band gap of these materials follows a general trend that, the larger the Pb-Br-Pb angle (less distorted), the smaller the band gap.[91] Increasing Pb-Br-Pb angle results in a higher degree of overlap of Pb s and Br p orbitals, which leads to strengthening of the antibonding interaction that increases the energy level of the valence band maximum (VBM).[449] Similar trend is also seen in

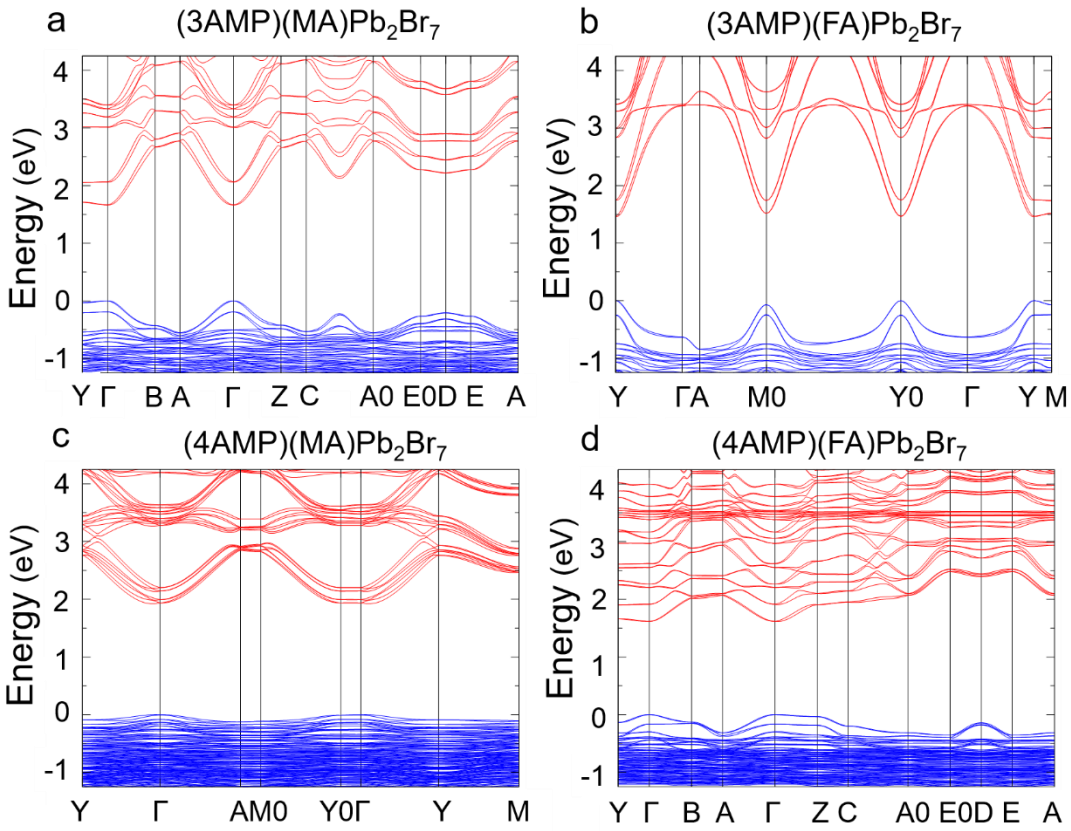

Figure 54. Calculated band structure of (a) (3AMP)(MA)Pb_2Br_7-1.66 eV (at Γ), (b) (3AMP)(FA)Pb_2Br_7-1.46 eV (at Y), (c) (4AMP)(MA)Pb_2Br_7-1.92 eV (at Γ) and (d) (4AMP)(FA)Pb_2Br_7-1.62 eV (at Γ).

the PL evolution of these compounds (Figure E3). The PL emission energy varies from 2.30 to 2.48 eV, comparable to a previously reported two-layered lead bromide compound $(BA)_2(FA)Pb_2B\ r_7$ (2.35 eV).[121] The stronger effect in changing the optical properties of the large organic spacers (3AMP and 4AMP) may be attributed to the higher flexibility of these cations to move outside the 2D inorganic layers whereas the perovskitizers (FA and MA) are trapped inside the cages. The size-effect of the perovskitizer is more prominent than other factors such as hydrogen bonding in this system.

The electronic structures of the original parent compounds (3AMP)(MA)Pb_2Br_7, (3AMP)(FA)Pb_2Br_7, (3AMP)(MA)Pb_2Br_7 and (3AMP)(FA)Pb_2Br_7 were calculated based on

density functional theory (DFT). These compounds are all direct band gap semiconductors with calculated (including spin-orbit coupling) band gap ranging from 1.46 eV to 1.92 eV. The calculated energy gap agrees with the experimental observations that 3AMPs have smaller band gap than the 4AMP, similar to the analogous iodide system. Also in agreement with the experiment, when keeping the same spacing cation, the FA compound has smaller band gap than the MA one, as shown in Figure 54. It is also evident that the FA-based compounds have more dispersed valence bands than the corresponding MA-based compounds.

7.5 Conclusions

We have demonstrated the successful inclusion of hetero-organic-spacers in the 2D halide perovskite system, taking advantage of the similarity of the 3AMP and 4AMP cations. The imperceptible effects of the large organic spacers and perovskitizer are not directly distinguishable but can be indirectly observed by the distortion of the Pb-Br framework. With the aid of single crystal X-ray diffraction, we have determined an underlying structural trend, which indicates that upon addition of 4AMP the Pb-Br-Pb angles tend to decrease whereas addition of FA tends to increase the Pb-Br-Pb angles. The distortion of Pb-Br-Pb angles is directly linked to the optical properties of these materials, as they scale proportionally with the band gap with higher Pb-Br-Pb angles. The indirect tuning of the semiconducting properties by altering the stereochemistry of organic spacers within a simple hybrid perovskite system further improve our understanding of

structure-property relationships and provides an additional design tool towards material exploration and device engineering.

Summary and Future Outlook

Hybrid 2D halide perovskites are a group of versatile semiconductors that possesses great potential in optoelectronics. The properties of the 2D halide perovskites can be tailored for specific applications such as solar cells and LEDs. This thesis focused on synthesizing and characterizing a wide array of hybrid 2D perovskite compounds incorporating different organic cations, which play essential roles in affecting the optical properties of the materials by interacting with the inorganic layers. The first half of the thesis primarily is primarily devoted to the discovery of new white-light emitting hybrid perovskites and the underlying structure-property relationships. Specifically, we correlate the structural distortion with the emission bandwidth, and further apply the rules in new system with different dimensions and connectivity. The second half of the thesis describes a new family of 2D halide perovskite: the Dion-Jacobson phases. The flexible and buildable structure incorporating di-cations enable us to achieve the highest layer thickness (n = 7) reported in 2D halide perovskite history. This group of 2D perovskites has unique structural characteristics and good performance in solar cells. The expansion and future development of the DJ phase perovskite is exciting and promising.

To further enrich the structural aspects and improve the optoelectronic properties for the 2D perovskite family, here are the important aspects to address: (1) Exploration of new structures. The inorganic side of the hybrid structure has limitations and fewer parameters to tune. Functionalization on the organic side will enhance the structural diversity by a lot. (2) Investigation

of the excited state. Many photo-physical processes happened at the excited states, yet we do most of the characterization in the ground state. It is important to understand the properties of the excited states as it is the real functioning condition. (3) Improving the quantum efficiency. For optoelectronic devices, high PLQY of the materials is needed for working devices. The determining factors of what controls the PLQY of the hybrid perovskites are not clear and this is required for improving the current materials and developing new high-performance semiconductors.

References

1. Weber, D., *Z. Naturforsch. B* **1978**, *33*, 1443-1445.

2. Wells, H. L., *Z Anorg. Allg.Chem.* **1893**, *3*, 195-210.

3. Moller, C. K., *Nature* **1958**, *182*, 1436-1436.

4. Moller, C. K., *Mat. Fys. Medd. Dan. Vid. Selsk.* **1959**, *32*, No. 2.

5. Auger, V.; Karantassis, T., *Compt. Rend.* **1925**, *181*, 665-666.

6. Karantassis, T.; Capatos, L., *Compt. Rend.* **1935**, *201*, 74-75.

7. Kojima, A.; Teshima, K.; Shirai, Y.; Miyasaka, T., *J. Am. Chem. Soc.* **2009**, *131*, 6050-6051.

8. Chung, I.; Lee, B.; He, J.; Chang, R. P. H.; Kanatzidis, M. G., *Nature* **2012**, *485*, 486-489.

9. Lee, M. M.; Teuscher, J.; Miyasaka, T.; Murakami, T. N.; Snaith, H. J., *Science* **2012**, *338*, 643-647.

10. Kim, H.-S.; Lee, C.-R.; Im, J.-H.; Lee, K.-B.; Moehl, T.; Marchioro, A.; Moon, S.-J.; Humphry-Baker, R.; Yum, J.-H.; Moser, J. E.; Grätzel, M.; Park, N.-G., *Sci. Rep.* **2012**, *2*, 591.

11. Burschka, J.; Pellet, N.; Moon, S.-J.; Humphry-Baker, R.; Gao, P.; Nazeeruddin, M. K.; Gratzel, M., *Nature* **2013**, *499*, 316-319.

12. Heo, J. H.; Im, S. H.; Noh, J. H.; Mandal, T. N.; Lim, C.-S.; Chang, J. A.; Lee, Y. H.; Kim, H.-j.; Sarkar, A.; NazeeruddinMd, K.; Gratzel, M.; Seok, S. I., *Nat. Photon.* **2013**, *7*, 486-491.

13. Mei, A.; Li, X.; Liu, L.; Ku, Z.; Liu, T.; Rong, Y.; Xu, M.; Hu, M.; Chen, J.; Yang, Y.; Grätzel, M.; Han, H., *Science* **2014**, *345*, 295-298.

14. Gao, P.; Gratzel, M.; Nazeeruddin, M. K., *Energy Environ. Sci.* **2014**, *7*, 2448-2463.

15. Kazim, S.; Nazeeruddin, M. K.; Grätzel, M.; Ahmad, S., *Angew. Chem. Int. Ed.* **2014**, *53*, 2812-2824.

16. Correa-Baena, J.-P.; Saliba, M.; Buonassisi, T.; Grätzel, M.; Abate, A.; Tress, W.; Hagfeldt, A., *Science* **2017**, *358*, 739-744.

17. Liu, M.; Johnston, M. B.; Snaith, H. J., *Nature* **2013**, *501*, 395-398.

18. Stranks, S. D.; Eperon, G. E.; Grancini, G.; Menelaou, C.; Alcocer, M. J. P.; Leijtens, T.; Herz, L. M.; Petrozza, A.; Snaith, H. J., *Science* **2013**, *342*, 341-344.

19. de Quilettes, D. W.; Vorpahl, S. M.; Stranks, S. D.; Nagaoka, H.; Eperon, G. E.; Ziffer, M. E.; Snaith, H. J.; Ginger, D. S., *Science* **2015**, *348*, 683-686.

20. Milot, R. L.; Sutton, R. J.; Eperon, G. E.; Haghighirad, A. A.; Martinez Hardigree, J.; Miranda, L.; Snaith, H. J.; Johnston, M. B.; Herz, L. M., *Nano Lett.* **2016**, *16*, 7001-7007.

21. Park, N.-G., *J. Phys. Chem. Lett.* **2013**, *4*, 2423-2429.

22. Jung, H. S.; Park, N.-G., *Small* **2015**, *11*, 10-25.

23. Stranks, S. D.; Snaith, H. J., *Nat. Nanotechnol.* **2015**, *10*, 391-402.

24. Yang, W. S.; Park, B.-W.; Jung, E. H.; Jeon, N. J.; Kim, Y. C.; Lee, D. U.; Shin, S. S.; Seo, J.; Kim, E. K.; Noh, J. H.; Seok, S. I., *Science* **2017**, *356*, 1376-1379.

25. O'Regan, B.; Grätzel, M., *Nature* **1991**, *353*, 737.

26. Zhang, W.; Eperon, G. E.; Snaith, H. J., *Nat. Energy* **2016**, *1*, 16048.

27. Brenner, T. M.; Egger, D. A.; Kronik, L.; Hodes, G.; Cahen, D., *Nat. Rev. Mater.* **2016**, *1*, 15007.

28. Stranks, S. D.; Snaith, H. J., *Nat. Nanotechnol.* **2015**, *10*, 391-402.

29. Huang, J.; Yuan, Y.; Shao, Y.; Yan, Y., *Nat. Rev. Mater.* **2017**, *2*, 17042.

30. Park, N.-G.; Grätzel, M.; Miyasaka, T.; Zhu, K.; Emery, K., *Nat. Energy* **2016**, *1*, 16152.

31. Kovalenko, M. V.; Protesescu, L.; Bodnarchuk, M. I., *Science* **2017**, *358*, 745-750.

32. García de Arquer, F. P.; Armin, A.; Meredith, P.; Sargent, E. H., *Nat. Rev. Mater.* **2017**, *2*, 16100.

33. Sutherland, B. R.; Sargent, E. H., *Nat. Photon.* **2016**, *10*, 295-302.

34. Kagan, C. R.; Mitzi, D. B.; Dimitrakopoulos, C. D., *Science* **1999**, *286*, 945-947.

35. Choi, J.; Han, J. S.; Hong, K.; Kim, S. Y.; Jang, H. W., *Adv. Mater.* **2018**, *30*, 1704002.

36. Jia, Y.; Kerner, R. A.; Grede, A. J.; Rand, B. P.; Giebink, N. C., *Nat. Photon.* **2017**, *11*, 784-788.

37. Eaton, S. W.; Lai, M.; Gibson, N. A.; Wong, A. B.; Dou, L.; Ma, J.; Wang, L.-W.; Leone, S. R.; Yang, P., *Proc. Natl. Acad. Sci.* **2016**, *113*, 1993-1998.

38. Zhu, H.; Fu, Y.; Meng, F.; Wu, X.; Gong, Z.; Ding, Q.; Gustafsson, M. V.; Trinh, M. T.; Jin, S.; Zhu, X. Y., *Nat. Mater.* **2015**, *14*, 636-642.

39. Kim, Y. C.; Kim, K. H.; Son, D.-Y.; Jeong, D.-N.; Seo, J.-Y.; Choi, Y. S.; Han, I. T.; Lee, S. Y.; Park, N.-G., *Nature* **2017**, *550*, 87-91.

40. He, Y.; Matei, L.; Jung, H. J.; McCall, K. M.; Chen, M.; Stoumpos, C. C.; Liu, Z.; Peters, J. A.; Chung, D. Y.; Wessels, B. W.; Wasielewski, M. R.; Dravid, V. P.; Burger, A.; Kanatzidis, M. G., *Nat. Commun.* **2018**, *9*, 1609.

41. Yakunin, S.; Sytnyk, M.; Kriegner, D.; Shrestha, S.; Richter, M.; Matt, G. J.; Azimi, H.; Brabec, C. J.; Stangl, J.; Kovalenko, M. V.; Heiss, W., *Nat. Photon.* **2015**, *9*, 444-449.

42. Wei, W.; Zhang, Y.; Xu, Q.; Wei, H.; Fang, Y.; Wang, Q.; Deng, Y.; Li, T.; Gruverman, A.; Cao, L.; Huang, J., *Nat. Photon.* **2017**, *11*, 315-321.

43. Poglitsch, A.; Weber, D., *J. Chem. Phys.* **1987**, *87*, 6373-6378.

44. Yaffe, O.; Guo, Y.; Tan, L. Z.; Egger, D. A.; Hull, T.; Stoumpos, C. C.; Zheng, F.; Heinz, T. F.; Kronik, L.; Kanatzidis, M. G.; Owen, J. S.; Rappe, A. M.; Pimenta, M. A.; Brus, L. E., *Phys. Rev. Lett.* **2017**, *118*, 136001.

45. Even, J.; Pedesseau, L.; Katan, C., *J. Phys. Chem. C* **2014**, *118*, 11566-11572.

46. Walsh, A., *J. Phys. Chem. C* **2015**, *119*, 5755-5760.

47. Miyata, K.; Meggiolaro, D.; Trinh, M. T.; Joshi, P. P.; Mosconi, E.; Jones, S. C.; De Angelis, F.; Zhu, X.-Y., *Sci. Adv.* **2017**, *3*, e1701217.

48. Kepenekian, M.; Robles, R.; Katan, C.; Sapori, D.; Pedesseau, L.; Even, J., *ACS Nano* **2015**, *9*, 11557-11567.

49. Stoumpos, C. C.; Kanatzidis, M. G., *Acc. Chem. Res.* **2015**, *48*, 2791-2802.

50. Stoumpos, C. C.; Malliakas, C. D.; Kanatzidis, M. G., *Inorg. Chem.* **2013,** *52*, 9019-9038.

51. Protesescu, L.; Yakunin, S.; Bodnarchuk, M. I.; Krieg, F.; Caputo, R.; Hendon, C. H.; Yang, R. X.; Walsh, A.; Kovalenko, M. V., *Nano Lett.* **2015**, *15*, 3692-3696.

52. Bekenstein, Y.; Koscher, B. A.; Eaton, S. W.; Yang, P.; Alivisatos, A. P., *J. Am. Chem. Soc.* **2015**, *137*, 16008-16011.

53. Akkerman, Q. A.; D'Innocenzo, V.; Accornero, S.; Scarpellini, A.; Petrozza, A.; Prato, M.; Manna, L., *J. Am. Chem. Soc.* **2015,** *137*, 10276-10281.

54. Aleksandrov, K. S., *Crystallogr. Rep.* **1995**, *40*, 279-301.

55. Nakamura, S.; Senoh, M.; Mukai, T., *Appl. Phys. Lett.* **1993**, *62*, 2390-2392.

56. Takashi, M., *Jap. J. Appl. Phys.* **2005**, *44*, 8263-8268.

57. Dingle, R.; Wiegmann, W.; Henry, C. H., *Phys. Rev. Lett.* **1974**, *33*, 827-830.

58. Turner, D. B.; Nelson, K. A., *Nature* **2010**, *466*, 1089-1092.

59. Arlt, G.; Hennings, D.; de With, G., *J. Appl. Phys.* **1985**, *58*, 1619-1625.

60. Mokhlisse, R.; Couzi, M.; Chanh, N.; Haget, Y.; Hauw, C.; Meresse, A., *J. Phys. Chem. Solids* **1985**, *46*, 187-195.

61. Ishihara, T.; Takahashi, J.; Goto, T., *Sol. State Commun.* **1989**, *69*, 933-936.

62. Nakajima, T.; Yamauchi, H.; Goto, T.; Yoshizawa, M.; Suzuki, T.; Fujimura, T., *J. Magn. Magn. Mater.* **1983**, *31*, 1189-1190.

63. I., D. Y.; Tamotsu, I.; Yusei, M., *Bull. Chem. Soc. Jpn.* **1986**, *59*, 563-567.

64. Ishihara, T.; Takahashi, J.; Goto, T., *Phys. Rev. B* **1990**, *42*, 11099-11107.

65. Hong, X.; Ishihara, T.; Nurmikko, A. V., *Phys. Rev. B* **1992**, *45*, 6961-6964.

66. Hirasawa, M.; Ishihara, T.; Goto, T., *J. Phys. Soc. Jpn.* **1994**, *63*, 3870-3879.

67. Ishihara, T., *J. Lumin.* **1994**, *60*, 269-274.

68. Muljarov, E. A.; Tikhodeev, S. G.; Gippius, N. A.; Ishihara, T., *Phys. Rev. B* **1995**, *51*, 14370-14378.

69. Papavassiliou, G. C.; Patsis, A. P.; Lagouvardos, D. J.; Koutselas, I. B., *Synth. Met*. **1993**, *57*, 3889-3894.

70. Papavassiliou, G. C.; Koutselas, I. B., *Synth. Met*. **1995**, *71*, 1713-1714.

71. Koutselas, I. B.; Ducasse, L.; Papavassiliou, G. C., *J. Phys. Condens. Matter* **1996**, *8*, 1217.

72. Papavassiliou, G. C., *Mol. Cryst. Liq. Cryst. Sci. Technol., Sect. A* **1996**, *286*, 231-238.

73. Koutselas, I. B.; Mitzi, D. B.; Papavassiliou, G. C.; Papaioannou, G. J.; Krautscheid, H., *Synth. Met.* **1997**, *86*, 2171-2172.

74. Calabrese, J.; Jones, N. L.; Harlow, R. L.; Herron, N.; Thorn, D. L.; Wang, Y., *J. Am. Chem. Soc.* **1991**, *113*, 2328-2330.

75. Mitzi, D. B.; Feild, C. A.; Harrison, W. T. A.; Guloy, A. M., *Nature* **1994**, *369*, 467-469.

76. Mitzi, D. B.; Wang, S.; Feild, C. A.; Chess, C. A.; Guloy, A. M., *Science* **1995**, *267*, 1473-1476.

77. Papavassiliou, G. C.; Mousdis, G. A.; Raptopoulou, C.; Terzis, A., Z. *Naturforsch. B Chem. Sci*. **2000**, *55*, 536-540.

78. Mercier, N., *CrystEngComm* **2005**, *7*, 429-432.

79. Zhu, X.-H.; Mercier, N.; Riou, A.; Blanchard, P.; Frère, P., *Chem. Commun*. **2002**, 2160-2161.

80. Geselle, M.; Fuess, H., *Z. Kristallogr. - New Cryst. Struct.* **1997**, *212*, 241-242.

81. Saparov, B.; Mitzi, D. B., *Chem. Rev.* **2016**, *116*, 4558-4596.

82. Mercier, N.; Louvain, N.; Bi, W., *CrystEngComm.* **2009**, *11*, 720-734.

83. Cheng, Z.; Lin, J., *CrystEngComm.* **2010**, *12*, 2646-2662.

84. Lemmerer, A.; Billing, D. G., *CrystEngComm.* **2012**, *14*, 1954-1966.

85. Billing, D. G.; Lemmerer, A., *Acta Crystallogr. E* **2003**, *59*, m381-m383.

86. Billing, D. G.; Lemmerer, A., *CrystEngComm.* **2006**, *8*, 686-695.

87. Billing, D. G.; Lemmerer, A., *CrystEngComm.* **2007**, *9*, 236-244.

88. Mitzi, D. B., *Synthesis, Structure, and Properties of Organic-Inorganic Perovskites and Related Materials. In Progress in Inorganic Chemistry, Karlin, K. D., Ed. John Wiley & Sons, Inc.:* **1999**; *Vol. 48*, pp 1-121.

89. Li, Y.; Zheng, G.; Lin, C.; Lin, J., *Cryst. Growth. Des*. **2008**, *8*, 1990-1996.

90. Mao, L.; Tsai, H.; Nie, W.; Ma, L.; Im, J.; Stoumpos, C. C.; Malliakas, C. D.; Hao, F.; Wasielewski, M. R.; Mohite, A. D.; Kanatzidis, M. G., *Chem. Mater.* **2016**, *28*, 7781-7792.

91. Knutson, J. L.; Martin, J. D.; Mitzi, D. B., *Inorg. Chem.* **2005**, *44*, 4699-4705.

92. Takahashi, Y.; Obara, R.; Nakagawa, K.; Nakano, M.; Tokita, J.-y.; Inabe, T., *Chem. Mater.* **2007**, *19*, 6312-6316.

93. Billing, D. G.; Lemmerer, A., *Acta Cryst. B* **2007**, *63*, 735-747.

94. Du, K.-z.; Tu, Q.; Zhang, X.; Han, Q.; Liu, J.; Zauscher, S.; Mitzi, D. B., *Inorg. Chem.* **2017**, *56*, 9291-9302.

95. Mitzi, D. B., *Chem. Mater.* **1996**, *8*, 791-800.

96. Mitzi, D. B., *Inorg. Chem.* **2000**, *39*, 6107-6113.

97. Mitzi, D. B.; Liang, K., *Chem. Mater.* **1997**, *9*, 2990-2995.

98. Quan, L. N.; Yuan, M.; Comin, R.; Voznyy, O.; Beauregard, E. M.; Hoogland, S.; Buin, A.; Kirmani, A. R.; Zhao, K.; Amassian, A.; Kim, D. H.; Sargent, E. H., *J. Am. Chem. Soc.* **2016**. *138*, 2649–2655.

99. Smith, I. C.; Hoke, E. T.; Solis-Ibarra, D.; McGehee, M. D.; Karunadasa, H. I., *Angew. Chem. Int. Ed.* **2014**, *53*, 11232-11235.

100. Cao, D. H.; Stoumpos, C. C.; Farha, O. K.; Hupp, J. T.; Kanatzidis, M. G., *J. Am. Chem. Soc.* **2015**, *137*, 7843-50.

101. Proppe, A. H.; Quintero-Bermudez, R.; Tan, H.; Voznyy, O.; Kelley, S. O.; Sargent, E. H., *J. Am. Chem. Soc.* **2018**, *140*, 2890-2896.

102. Mao, L.; Ke, W.; Pedesseau, L.; Wu, Y.; Katan, C.; Even, J.; Wasielewski, M. R.; Stoumpos, C. C.; Kanatzidis, M. G., *J. Am. Chem. Soc.* **2018**, *140*, 3775-3783.

103. Zhou, N.; Shen, Y.; Li, L.; Tan, S.; Liu, N.; Zheng, G.; Chen, Q.; Zhou, H., *J. Am. Chem. Soc.* **2017**, *140*, 459-465.

104. Wang, N.; Cheng, L.; Ge, R.; Zhang, S.; Miao, Y.; Zou, W.; Yi, C.; Sun, Y.; Cao, Y.; Yang, R.; Wei, Y.; Guo, Q.; Ke, Y.; Yu, M.; Jin, Y.; Liu, Y.; Ding, Q.; Di, D.; Yang, L.; Xing, G.; Tian, H.; Jin, C.; Gao, F.; Friend, R. H.; Wang, J.; Huang, W., *Nat. Photon.* **2016**, *10*, 699-705.

105. Quan, L. N.; Zhao, Y.; García de Arquer, F. P.; Sabatini, R.; Walters, G.; Voznyy, O.; Comin, R.; Li, Y.; Fan, J. Z.; Tan, H.; Pan, J.; Yuan, M.; Bakr, O. M.; Lu, Z.; Kim, D. H.; Sargent, E. H., *Nano Lett.* **2017**, *17*, 3701-3709.

106. Congreve, D. N.; Weidman, M. C.; Seitz, M.; Paritmongkol, W.; Dahod, N. S.; Tisdale, W. A., *ACS Photon.* **2017**, *4*, 476-481.

107. Luo, J.; Li, L.; Sun, Z.; Wang, P.; Hu, W.; Wang, S.; Ji, C.; Hong, M., *Angew. Chem. Int. Ed.* **2017**, *56*, 12150-12154.

108. Sun, C.; Xu, G.; Jiang, X.-M.; Wang, G.-E.; Guo, P.-Y.; Wang, M.-S.; Guo, G.-C., *J. Am. Chem. Soc.* **2018**, *140*, 2805-2811.

109. Shiguo, H.; Peng, W.; Jing, Z.; Xitao, L.; Zhihua, S.; Xiaoying, H.; Lina, L.; Chengmin, J.; Weichuan, Z.; Bing, T.; Weida, H.; Maochun, H.; Junhua, L., *Laser Photonics Rev.* **2018**, *12*, 1800060.

110. Weidman, M. C.; Goodman, A. J.; Tisdale, W. A., *Chem. Mater.* **2017**, *29*, 5019-5030.

111. Dou, L.; Wong, A. B.; Yu, Y.; Lai, M.; Kornienko, N.; Eaton, S. W.; Fu, A.; Bischak, C. G.; Ma, J.; Ding, T., *Science* **2015**, *349*, 1518-1521.

112. Dohner, E. R.; Hoke, E. T.; Karunadasa, H. I., *J. Am. Chem. Soc.* **2014**, *136*, 1718-1721.

113. Dohner, E. R.; Jaffe, A.; Bradshaw, L. R.; Karunadasa, H. I., *J. Am. Chem. Soc.* **2014**, *136*, 13154-13157.

114. Smith, M. D.; Jaffe, A.; Dohner, E. R.; Lindenberg, A. M.; Karunadasa, H. I., *Chem. Sci.* **2017**, *8*, 4497-4504.

115. Smith, M. D.; Karunadasa, H. I., *Acc. Chem. Res.* **2018**, *51*, 619-627.

116. Mao, L.; Wu, Y.; Stoumpos, C. C.; Wasielewski, M. R.; Kanatzidis, M. G., J. *Am. Chem. Soc.* **2017**, *139*, 5210–5215.

117. Mao, L.; Wu, Y.; Stoumpos, C. C.; Traore, B.; Katan, C.; Even, J.; Wasielewski, M. R.; Kanatzidis, M. G., *J. Am. Chem. Soc.* **2017**, *139*, 11956-11963.

118. Mao, L.; Guo, P.; Kepenekian, M.; Hadar, I.; Katan, C.; Even, J.; Schaller, R. D.; Stoumpos, C. C.; Kanatzidis, M. G., *J. Am. Chem. Soc.* **2018**, *140*, 13078–13088

119. Wang, M.-S.; Guo, G.-C., *Chem. Commun.* **2016**, *52*, 13194-13204.

120. Saouma, F. O.; Stoumpos, C. C.; Wong, J.; Kanatzidis, M. G.; Jang, J. I., *Nat. Commun.* **2017**, *8*, 742.

121. Li, L.; Shang, X.; Wang, S.; Dong, N.; Ji, C.; Chen, X.; Zhao, S.; Wang, J.; Sun, Z.; Hong, M.; Luo, J., *J. Am. Chem. Soc.* **2018**, *140*, 6806-6809.

122. Shi, E.; Gao, Y.; Finkenauer, B. P.; Akriti; Coffey, A. H.; Dou, L., *Chem. Soc. Rev.* **2018**.

123. Wang, Z.; Lin, Q.; Chmiel, F. P.; Sakai, N.; Herz, L. M.; Snaith, H. J., *Nat. Energy* **2017**, *2*, 17135.

124. Pedesseau, L.; Sapori, D.; Traore, B.; Robles, R.; Fang, H.-H.; Loi, M. A.; Tsai, H.; Nie, W.; Blancon, J.-C.; Neukirch, A.; Tretiak, S.; Mohite, A. D.; Katan, C.; Even, J.; Kepenekian, M., *ACS Nano* **2016**, *10*, 9776-9786.

125. Guo, P.; Stoumpos, C. C.; Mao, L.; Sadasivam, S.; Ketterson, J. B.; Darancet, P.; Kanatzidis, M. G.; Schaller, R. D., *Nat. Commun.* **2018**, *9*, 2019.

126. Straus, D. B.; Kagan, C. R., *J. Phys. Chem. Lett.* **2018**, *9*, 1434-1447.

127. Blancon, J. C.; Stier, A. V.; Tsai, H.; Nie, W.; Stoumpos, C. C.; Traoré, B.; Pedesseau, L.; Kepenekian, M.; Katsutani, F.; Noe, G. T.; Kono, J.; Tretiak, S.; Crooker, S. A.; Katan, C.; Kanatzidis, M. G.; Crochet, J. J.; Even, J.; Mohite, A. D., *Nat. Commun.* **2018**, *9*, 2254.

128. Stoumpos, C. C.; Mao, L.; Malliakas, C. D.; Kanatzidis, M. G., *Inorg. Chem.* **2017**, *56*, 56-73.

129. Kamminga, M. E.; Fang, H.-H.; Filip, M. R.; Giustino, F.; Baas, J.; Blake, G. R.; Loi, M. A.; Palstra, T. T. M., *Chem. Mater.* **2016**, *28*, 4554-4562.

130. Smith, M. D.; Watson, B. L.; Dauskardt, R. H.; Karunadasa, H. I., *Chem. Mater.* **2017**, *29*, 7083-7087.

131. Stoumpos, C. C.; Mao, L.; Malliakas, C. D.; Kanatzidis, M. G., *Inorg. Chem.* **2017**, *56*, 56-73.

132. Kamminga, M. E.; de Wijs, G. A.; Havenith, R. W. A.; Blake, G. R.; Palstra, T. T. M., *Inorg. Chem.* **2017**, *56*, 8408-8414.

133. Fabini, D. H.; Laurita, G.; Bechtel, J. S.; Stoumpos, C. C.; Evans, H. A.; Kontos, A. G.; Raptis, Y. S.; Falaras, P.; Van der Ven, A.; Kanatzidis, M. G.; Seshadri, R., *J. Am. Chem. Soc.* **2016**, *138*, 11820-11832.

134. Vargas, B.; Ramos, E.; Pérez-Gutiérrez, E.; Alonso, J. C.; Solis-Ibarra, D., *J. Am. Chem. Soc.* **2017**, *139*, 9116-9119.

135. Tulsky, E. G.; Long, J. R., *Chem. Mater.* **2001**, *13*, 1149-1166.

136. McClure, E. T.; Ball, M. R.; Windl, W.; Woodward, P. M., *Chem. Mater.* **2016**, *28*, 1348-1354.

137. Slavney, A. H.; Hu, T.; Lindenberg, A. M.; Karunadasa, H. I., *J. Am. Chem. Soc.* **2016**, *138*, 2138-2141.

138. Connor, B. A.; Leppert, L.; Smith, M. D.; Neaton, J. B.; Karunadasa, H. I., *J. Am. Chem. Soc.* **2018**, *140*, 5235-5240.

139. Stoumpos, C. C.; Cao, D. H.; Clark, D. J.; Young, J.; Rondinelli, J. M.; Jang, J. I.; Hupp, J. T.; Kanatzidis, M. G., *Chem. Mater.* **2016**, *28*, 2852-2867.

140. Nakajima, T.; Yamauchi, H.; Goto, T.; Yoshizawa, M.; Suzuki, T.; Fujimura, T., *J. Magn. Magn. Mater.* **1983**, *31*, 1189-1190.

141. Geselle, M.; Fuess, H., *Z. Kristallogr. - New Cryst. Struct.* **1997**, *212*, 241-242.

142. Peterson, E. R.; Willett, R. D., *J. Chem. Phys.* **1972**, *56*, 1879-1882.

143. Meresse, A.; Daoud, A., *Acta Cryst. C* **1989**, *45*, 194-196.

144. Doudin, B.; Chapuis, G., *Acta Cryst.* B **1990**, *46*, 175-180.

145. Stoumpos, C. C.; Soe, C. M. M.; Tsai, H.; Nie, W.; Blancon, J.-C.; Cao, D. H.; Liu, F.; Traoré, B.; Katan, C.; Even, J.; Mohite, A. D.; Kanatzidis, M. G., *Chem* **2017**, *2*, 427-440.

146. Mitzi, D. B., *Chem. Mater.* **1996**, *8*, 791-800.

147. Lemmerer, A.; Billing, D. G., *Dalton Trans.* **2012**, *41*, 1146-1157.

148. Zhong, W.-W.; Di, Y.-Y.; Kong, Y.-X.; Lu, D.-F.; Dou, J.-M., *J. Chem. Thermodyn.* **2014**, *72*, 100-107.

149. Billing, D. G.; Lemmerer, A., *New J. Chem.* **2008**, 32, 1736-1746.

150. Corradi, A. B.; Ferrari, A. M.; Pellacani, G. C.; Saccani, A.; Sandrolini, F.; Sgarabotto, P., *Inorg. Chem.* **1999**, *38*, 716-721.

151. Tichy, K.; Benes, J.; Kind, R.; Arend, H., *Acta Cryst. B* **1980**, *36*, 1355-1367.

152. Courseille, C.; Chanh, N. B.; Maris, T.; Daoud, A.; Abid, Y.; Laguerre, M., *Phys. Status Solidi A* **1994**, *143*, 203-214.

153. Amami, M.; Zouari, R.; Ben Salah, A.; Burzlaff, H., *Acta Cryst. E* **2002**, *58*, m357-m359.

154. Safdari, M.; Svensson, P. H.; Hoang, M. T.; Oh, I.; Kloo, L.; Gardner, J. M., *J. Mater. Chem. A* **2016**, *4*, 15638-15646.

155. Li, X.; Hoffman, J.; Ke, W.; Chen, M.; Tsai, H.; Nie, W.; Mohite, A. D.; Kepenekian, M.; Katan, C.; Even, J.; Wasielewski, M. R.; Stoumpos, C. C.; Kanatzidis, M. G., *J. Am. Chem. Soc.* **2018**. *140*, 12226–12238

156. Mousdis, G. A.; Papavassiliou, G. C.; Raptopoulou, C. P.; Terzis, A., *J. Mater. Chem.* **2000**, *10*, 515-518.

157. Pradeesh, K.; Yadav, G. S.; Singh, M.; Prakash, G. V., *Mater. Chem. Phys*. **2010**, 124, 44-47.

158. Nazarenko, O.; Kotyrba, M. R.; Wörle, M.; Cuervo-Reyes, E.; Yakunin, S.; Kovalenko, M. V., *Inorg. Chem.* **2017**, 56, 11552-11564.

159. Soe, C. M. M.; Stoumpos, C. C.; Kepenekian, M.; Traoré, B.; Tsai, H.; Nie, W.; Wang, B.; Katan, C.; Seshadri, R.; Mohite, A. D.; Even, J.; Marks, T. J.; Kanatzidis, M. G., *J. Am. Chem. Soc.* **2017**, *139*, 16297-16309.

160. Nazarenko, O.; Kotyrba, M. R.; Yakunin, S.; Aebli, M.; Rainò, G.; Benin, B. M.; Wörle, M.; Kovalenko, M. V., *J. Am. Chem. Soc.* **2018**, *140*, 3850-3853.

161. Daub, M.; Hillebrecht, H., *Z. Kristallog. – Cryst. Mater.*, **2018**, *233*, 555-564.

162. Lemmerer, A.; Billing, D. G., *CrystEngComm* **2010**, *12*, 1290-1301.

163. Louvain, N.; Bi, W.; Mercier, N.; Buzaré, J.-Y.; Legein, C.; Corbel, G., *Dalton Trans.* **2007**, 965-970.

164. Li, Y.; Zheng, G.; Lin, J., *Eur. J. Inorg. Chem.* **2008**, *2008*, 1689-1692.

165. Solis-Ibarra, D.; Karunadasa, H. I., *Angew. Chem. Int. Ed.* **2014**, *53*, 1039-1042.

166. Lermer, C.; Birkhold, S. T.; Moudrakovski, I. L.; Mayer, P.; Schoop, L. M.; Schmidt-Mende, L.; Lotsch, B. V., *Chem. Mater.* **2016**, *28*, 6560-6566.

167. Wang, Z.-X.; Liao, W.-Q.; Ye, H.-Y.; Zhang, Y., Dalton Trans. 2015, 44, 20406-20412.

168. Billing, D. G.; Lemmerer, A., *CrystEngComm* **2009**, *11*, 1549-1562.

169. Li, X. N.; Li, P. F.; Liao, W. Q.; Ge, J. Z.; Wu, D. H.; Ye, H. Y., *Eur. J. Inorg. Chem.* **2017**, *2017*, 938-942.

170. Billing, D. G.; Lemmerer, A., *Acta Crystallogr. C* **2006**, *62*, m269-m271.

171. Lorena, G. S.; Hasegawa, H.; Takahashi, Y.; Harada, J.; Inabe, T., *Chem. Lett.* **2014**, *43*, 1535-1537.

172. Bonamartini Corradi, A.; Ferrari, A. M.; Righi, L.; Sgarabotto, P., *Inorg. Chem.* **2001**, *40*, 218-223.

173. Apostolico, L.; Kociok-Kohn, G.; Molloy, K. C.; Blackman, C. S.; Carmalt, C. J.; Parkin, I. P., *Dalton Trans.* **2009**, *47*, 10486-10494.

174. Rayner, M. K.; Billing, D. G., *Acta Cryst. E* **2010**, *66*, m660-m660.

175. Braun, M.; Frey, W., *Z. Kristallogr. - New Cryst. Struct.* **1999**, *214*, 331-332.

176. Papavassiliou, G. C.; Mousdis, G. A.; Raptopoulou, C. P.; Terzis, A., *Z. Naturforsch.* **1999**, *54*, 1405.

177. Jin, Y.; Yu, C.-H.; Zhang, W., *J. Coord. Chem.* **2014**, *67*, 1156-1173.

178. Liao, W.-Q.; Zhang, Y.; Hu, C.-L.; Mao, J.-G.; Ye, H.-Y.; Li, P.-F.; Huang, S. D.; Xiong, R.-G., *Nat. Commun.* **2015**, *6*, 7338.

179. Papavassiliou, G. C.; Koutselas, I.; Terzis, A.; Whangbo, M.-H., *Solid State Commun.* **1994**, *91*, 695-698.

180. Mitzi, D. B., *J. Solid State Chem.* **1999**, *145*, 694-704.

181. Mitzi, D. B.; Dimitrakopoulos, C. D.; Kosbar, L. L., *Chem. Mater.* **2001**, *13*, 3728-3740.

182. Dammak, H.; Elleuch, S.; Feki, H.; Abid, Y., *Solid State Sci.* **2016**, *61*, 1-8.

183. Li, Y.; Zheng, G.; Lin, C.; Lin, J., *Solid State Sci.* **2007**, *9*, 855-861.

184. Xu, Z.; Mitzi, D. B.; Dimitrakopoulos, C. D.; Maxcy, K. R., *Inorg. Chem.* **2003**, *42*, 2031-2039.

185. Dobrzycki, L.; Woźniak, K., *CrystEngComm* **2008**, *10*, 577-589.

186. Hautzinger, M. P.; Dai, J.; Ji, Y.; Fu, Y.; Chen, J.; Guzei, I. A.; Wright, J. C.; Li, Y.; Jin, S., *Inorg. Chem.* **2017**, *56*, 14991-14998.

187. Lermer, C.; Harm, S. P.; Birkhold, S. T.; Jaser, J. A.; Kutz, C. M.; Mayer, P.; Schmidt-Mende, L.; Lotsch, B. V., *Z. Anorg. Allg. Chem.* **2016**, *642*, 1369-1376.

188. Passarelli, J. V.; Fairfield, D. J.; Sather, N. A.; Hendricks, M. P.; Sai, H.; Stern, C. L.; Stupp, S. I., *J. Am. Chem. Soc.* **2018**, *140*, 7313-7323.

189. Zhu, X.-H.; Mercier, N.; Frère, P.; Blanchard, P.; Roncali, J.; Allain, M.; Pasquier, C.; Riou, A., *Inorg. Chem.* **2003**, *42*, 5330-5339.

190. Mitzi, D. B.; Chondroudis, K.; Kagan, C. R., *Inorg. Chem.* **1999**, *38*, 6246-6256.

191. Daub, M.; Hillebrecht, H., *Angew. Chem. Int. Ed.* **2015,** *54*, 11016-11017.

192. Li, J.; Stoumpos, C. C.; Trimarchi, G. G.; Chung, I.; Mao, L.; Chen, M.; Wasielewski, M. R.; Wang, L.; Kanatzidis, M. G., *Chem. Mater.* **2018**, *30*, 4847-4856.

193. Li, J.; Yu, Q.; He, Y.; Stoumpos, C. C.; Niu, G.; Trimarchi, G. G.; Guo, H.; Dong, G.; Wang, D.; Wang, L.; Kanatzidis, M. G., *J. Am. Chem. Soc.* **2018**, *140*, 11085-11090.

194. Balz, D.; Plieth, K., *Ber. Bunsenges. Phys. Chem.* **1955**, *59*, 545-551.

195. Daub, M.; Haber, C.; Hillebrecht, H., *Eur. J. Inorg. Chem.* **2017**, *2017*, 1120-1126.

196. Guan, J.; Tang, Z.; M. Guloy, A., *Chem. Commun.* **1999**, *18*, 1833-1834.

197. Hu, T.; Smith, M. D.; Dohner, E. R.; Sher, M.-J.; Wu, X.; Trinh, M. T.; Fisher, A.; Corbett, J.; Zhu, X. Y.; Karunadasa, H. I.; Lindenberg, A. M., *J. Phys. Chem. Lett.* **2016**, *7*, 2258-2263.

198. McCall, K. M.; Stoumpos, C. C.; Kostina, S. S.; Kanatzidis, M. G.; Wessels, B. W., *Chem. Mater.* **2017**, *29*, 4129-4145.

199. Leuenberger, B.; Güdel, H. U.; Fischer, P., *J. Solid State Chem.* **1986**, *64*, 90-101.

200. Lazarini, F., *Acta Crystallogr. B* **1977**, *33*, 2961-2964.

201. Yamada, K.; Sera, H.; Sawada, S.; Tada, H.; Okuda, T.; Tanaka, H., *J. Solid State Chem.* **1997**, *134*, 319-325.

202. Peresh, E. Y.; Sidei, V. I.; Zubaka, O. V.; Stercho, I. P., *Inorg. Mater.* **2011**, *47*, 208-212.

203. Lehner, A. J.; Fabini, D. H.; Evans, H. A.; Hébert, C.-A.; Smock, S. R.; Hu, J.; Wang, H.; Zwanziger, J. W.; Chabinyc, M. L.; Seshadri, R., *Chem. Mater.* **2015**, *27*, 7137-7148.

204. Saparov, B.; Hong, F.; Sun, J.-P.; Duan, H.-S.; Meng, W.; Cameron, S.; Hill, I. G.; Yan, Y.; Mitzi, D. B., *Chem. Mater.* **2015**, *27*, 5622-5632.

205. Chang, J.-H.; Doert, T.; Ruck, M., *Z. Anorg. Allg. Chem.* **2016**, *642*, 736-748.

206. Vargas, B.; Torres-Cadena, R.; Rodríguez-Hernández, J.; Gembicky, M.; Xie, H.; Jiménez-Mier, J.; Liu, Y.-S.; Menéndez-Proupin, E.; Dunbar, K. R.; Lopez, N.; Olalde-Velasco, P.; Solis-Ibarra, D., *Chem. Mater.* **2018**, *30*, 5315–5321.

207. Schaak, R. E.; Mallouk, T. E., *Chem. Mater.* **2002**, *14*, 1455-1471.

208. Ruddlesden, S. N.; Popper, P., *Acta Cryst.* **1957**, *10*, 538-539.

209. Ruddlesden, S. N.; Popper, P., *Acta Cryst.* **1958**, *11*, 54-55.

210. Dion, M.; Ganne, M.; Tournoux, M., *Mater. Res. Bull.* **1981**, *16*, 1429-1435.

211. Jacobson, A. J.; Johnson, J. W.; Lewandowski, J. T., *Inorg. Chem.* **1985**, *24*, 3727-3729.

212. Aurivillius, B., *Arkiv for Kemi* **1949**, *1*, 463-480.

213. Aurivillius, B., *Arkiv for Kemi* **1949**, *1*, 499-512.

214. Aurivillius, B., *Arkiv for Kemi* **1950**, *2*, 519-527.

215. Billing, D. G.; Lemmerer, A., *New J. Chem.* **2008**, *32*, 1736-1746.

216. Lemmerer, A.; Billing, D. G., *Dalton. Trans.* **2012**, *41*, 1146-1157.

217. Martínez de Irujo-Labalde, X.; Muñoz-Gil, D.; Urones-Garrote, E.; Ávila-Brande, D.; García-Martín, S., *J. Mater. Chem. A* **2016**, *4*, 10241-10247.

218. Lee, C.-H.; Orloff, N. D.; Birol, T.; Zhu, Y.; Goian, V.; Rocas, E.; Haislmaier, R.; Vlahos, E.; Mundy, J. A.; Kourkoutis, L. F.; Nie, Y.; Biegalski, M. D.; Zhang, J.; Bernhagen, M.; Benedek, N. A.; Kim, Y.; Brock, J. D.; Uecker, R.; Xi, X. X.; Gopalan, V.; Nuzhnyy, D.; Kamba, S.; Muller, D. A.; Takeuchi, I.; Booth, J. C.; Fennie, C. J.; Schlom, D. G., *Nature* **2013**, *502*, 532.

219. Yan, L.; Niu, H. J.; Duong, G. V.; Suchomel, M. R.; Bacsa, J.; Chalker, P. R.; Hadermann, J.; van Tendeloo, G.; Rosseinsky, M. J., *Chem. Sci.* **2011**, *2*, 261-272.

220. Glasser, L., *Inorg. Chem.* **2017**, *56*, 8920-8925.

221. Hao, F.; Stoumpos, C. C.; Liu, Z.; Chang, R. P.; Kanatzidis, M. G., *J. Am. Chem. Soc.* **2014**, *136*, 16411-16419.

222. Wright, A. D.; Verdi, C.; Milot, R. L.; Eperon, G. E.; Pérez-Osorio, M. A.; Snaith, H. J.; Giustino, F.; Johnston, M. B.; Herz, L. M., *Nat. Commun.* **2016**, *7*, 11755.

223. Davies, C. L.; Filip, M. R.; Patel, J. B.; Crothers, T. W.; Verdi, C.; Wright, A. D.; Milot, R. L.; Giustino, F.; Johnston, M. B.; Herz, L. M., *Nat. Commun.* **2018**, *9*, 293.

224. Yaffe, O.; Chernikov, A.; Norman, Z. M.; Zhong, Y.; Velauthapillai, A.; van der Zande, A.; Owen, J. S.; Heinz, T. F., *Phys. Rev. B* **2015**, *92*, 045414.

225. Blancon, J.-C.; Tsai, H.; Nie, W.; Stoumpos, C. C.; Pedesseau, L.; Katan, C.; Kepenekian, M.; Soe, C. M. M.; Appavoo, K.; Sfeir, M. Y.; Tretiak, S.; Ajayan, P. M.; Kanatzidis, M. G.; Even, J.; Crochet, J. J.; Mohite, A. D., *Science* **2017**, *355*, 1288-1292.

226. Kieslich, G.; Sun, S.; Cheetham, A. K., *Chem. Sci.* **2014**, *5*, 4712-4715.

227. Li, Z.; Yang, M.; Park, J.-S.; Wei, S.-H.; Berry, J. J.; Zhu, K., *Chem. Mater.* **2016**, *28*, 284-292.

228. Zhou, N.; Shen, Y.; Li, L.; Tan, S.; Liu, N.; Zheng, G.; Chen, Q.; Zhou, H., *J. Am. Chem. Soc.* **2018**, *140*, 459-465.

229. Zhang, X.; Ren, X.; Liu, B.; Munir, R.; Zhu, X.; Yang, D.; Li, J.; Liu, Y.; Smilgies, D.-M.; Li, R.; Yang, Z.; Niu, T.; Wang, X.; Amassian, A.; Zhao, K.; Liu, S., *Energy Environ. Sci.* **2017**, *10*, 2095-2102.

230. Yamada, K.; Nakada, K.; Takeuchi, Y.; Nawa, K.; Yamane, Y., *Bull. Chem. Soc. Jpn.* **2011**, *84*, 926-932.

231. Eperon, G. E.; Stranks, S. D.; Menelaou, C.; Johnston, M. B.; Herz, L. M.; Snaith, H. J., *Energy Environ. Sci.* **2014**, *7*, 982.

232. Hao, F.; Stoumpos, C. C.; Chang, R. P. H.; Kanatzidis, M. G., *J. Am. Chem. Soc.* **2014**, *136*, 8094-8099.

233. Cheng, P.; Wu, T.; Liu, J.; Deng, W.-Q.; Han, K., *J. Phys. Chem. Lett*. **2018**, *9*, 2518-2522.

234. Im, J.; Stoumpos, C. C.; Jin, H.; Freeman, A. J.; Kanatzidis, M. G., *J. Phys. Chem. Lett*. **2015**, *6*, 3503-3509.

235. Goyal, A.; McKechnie, S.; Pashov, D.; Tumas, W.; Schilfgaarde, M. v.; Stevanović, V., *Chem. Mater*. **2018**, *30*, 3920-3928.

236. Nagane, S.; Ghosh, D.; Hoye, R. L. Z.; Zhao, B.; Ahmad, S.; Walker, A. B.; Islam, M. S.; Ogale, S.; Sadhanala, A., *J. Phys. Chem. C* **2018**, *122*, 5940-5947.

237. Adjokatse, S.; Fang, H.-H.; Loi, M. A., *Materials Today* **2017**, *20*, 413-424.

238. Yang, S.; Lin, Z.; Wang, J.; Chen, Y.; Liu, Z.; Yang, E.; Zhang, J.; Ling, Q., *ACS Appl. Mater. Interfaces* **2018**, *10*, 15980-15987.

239. Lanzetta, L.; Marin-Beloqui, J. M.; Sanchez-Molina, I.; Ding, D.; Haque, S. A., *ACS Energy Lett.* **2017**, *2*, 1662-1668.

240. Lanty, G.; Jemli, K.; Wei, Y.; Leymarie, J.; Even, J.; Lauret, J.-S.; Deleporte, E., *J. Phys. Chem. Lett.* **2014**, *5*, 3958-3963.

241. Lin, Y.; Bai, Y.; Fang, Y.; Wang, Q.; Deng, Y.; Huang, J., *ACS Energy Lett.* **2017**, *2*, 1571-1572.

242. Tsai, H.; Nie, W.; Blancon, J.-C.; Stoumpos, C. C.; Asadpour, R.; Harutyunyan, B.; Neukirch, A. J.; Verduzco, R.; Crochet, J. J.; Tretiak, S.; Pedesseau, L.; Even, J.; Alam, M. A.;

Gupta, G.; Lou, J.; Ajayan, P. M.; Bedzyk, M. J.; Kanatzidis, M. G.; Mohite, A. D., *Nature* **2016**, *536*, 312-316.

243. Nie, W.; Tsai, H.; Asadpour, R.; Blancon, J.-C.; Neukirch, A. J.; Gupta, G.; Crochet, J. J.; Chhowalla, M.; Tretiak, S.; Alam, M. A.; Wang, H.-L.; Mohite, A. D., *Science* **2015**, *347*, 522-525.

244. Soe, C. M. M.; Nie, W.; Stoumpos, C. C.; Tsai, H.; Blancon, J.-C.; Liu, F.; Even, J.; Marks, T. J.; Mohite, A. D.; Kanatzidis, M. G., *Adv. Ener. Mater.* **2018**, *8*, 1700979.

245. Cohen, B.-E.; Wierzbowska, M.; Etgar, L., *Sustain. Energ. Fuels* **2017**, *1*, 1935-1943.

246. Liao, Y.; Liu, H.; Zhou, W.; Yang, D.; Shang, Y.; Shi, Z.; Li, B.; Jiang, X.; Zhang, L.; Quan, L. N.; Quintero-Bermudez, R.; Sutherland, B. R.; Mi, Q.; Sargent, E. H.; Ning, Z., *J. Am. Chem. Soc.* **2017**, *139*, 6693-6699.

247. Liu, X.-K.; Gao, F., *J. Phys. Chem. Lett.* **2018**, *9*, 2251-2258.

248. Yuan, M.; Quan, L. N.; Comin, R.; Walters, G.; Sabatini, R.; Voznyy, O.; Hoogland, S.; Zhao, Y.; Beauregard, E. M.; Kanjanaboos, P.; Lu, Z.; Kim, D. H.; Sargent, E. H., *Nat. Nanotechnol.* **2016**, *11*, 872-877.

249. Xiao, Z.; Kerner, R. A.; Zhao, L.; Tran, N. L.; Lee, K. M.; Koh, T.-W.; Scholes, G. D.; Rand, B. P., *Nat. Photon.* **2017**, *11*, 108-115.

250. Tsai, H.; Nie, W.; Blancon, J.-C.; Stoumpos, C. C.; Soe, C. M. M.; Yoo, J.; Crochet, J.; Tretiak, S.; Even, J.; Sadhanala, A.; Azzellino, G.; Brenes, R.; Ajayan, P. M.; Bulović, V.; Stranks, S. D.; Friend, R. H.; Kanatzidis, M. G.; Mohite, A. D., *Adv. Mater.* **2018**, *30*, 1704217.

251. Lin, Y.-H.; Pattanasattayavong, P.; Anthopoulos, T. D., *Adv. Mater.* **2017**, *29*, 1702838.

252. Mitzi, D. B.; Dimitrakopoulos, C. D.; Rosner, J.; Medeiros, D. R.; Xu, Z.; Noyan, C., *Adv. Mater.* **2002**, *14*, 1772-1776.

253. Matsushima, T.; Hwang, S.; Sandanayaka, A. S. D.; Qin, C.; Terakawa, S.; Fujihara, T.; Yahiro, M.; Adachi, C., *Adv. Mater.* **2016**, *28*, 10275-10281.

254. Wang, J.; Su, R.; Xing, J.; Bao, D.; Diederichs, C.; Liu, S.; Liew, T. C. H.; Chen, Z.; Xiong, Q., *ACS Nano* **2018**. *12*, 8382-8389.

255. Feng, J.; Gong, C.; Gao, H.; Wen, W.; Gong, Y.; Jiang, X.; Zhang, B.; Wu, Y.; Wu, Y.; Fu, H.; Jiang, L.; Zhang, X., *Nat. Electron.* **2018**, *1*, 404-410.

256. Shibuya, K.; Koshimizu, M.; Takeoka, Y.; Asai, K., *Nucl. Instr. Meth. Phys. Res. B* **2002**, *194*, 207-212.

257. Kengo, S.; Masanori, K.; Hidetoshi, M.; Yusa, M.; Yosuke, K.; Keisuke, A., *Jpn. J. Appl. Phys.* **2004**, *43*, L1333.

258. Nie, W., *Adv. Mater.* **1993**, *5*, 520-545.

259. Ishihara, T., *Physica Status Solidi (b)* **1990**, *159*, 371-378.

260. Ishi, J.; Mizuno, M.; Kunugita, H.; Ema, K.; Iwamoto, S.; Hayase, S.; Kondo, T.; Ito, R., *J. Nonlinear Opt. Phys. Mater.* **1998**, *07*, 153-159.

261. Stoumpos, C. C.; Kanatzidis, M. G., *Adv. Mater.* **2016**, *28*, 5778-5793.

262. Kojima, A.; Teshima, K.; Shirai, Y.; Miyasaka, T., *J. Am. Chem. Soc.* **2009**, *131*, 6050-6051.

263. Zhou, H.; Chen, Q.; Li, G.; Luo, S.; Song, T.-b.; Duan, H.-S.; Hong, Z.; You, J.; Liu, Y.; Yang, Y., *Science* **2014**, *345*, 542-546.

264. Jeon, N. J.; Noh, J. H.; Yang, W. S.; Kim, Y. C.; Ryu, S.; Seo, J.; Seok, S. I., *Nature* **2015**, *517*, 476-480.

265. Li, X.; Bi, D.; Yi, C.; Décoppet, J.-D.; Luo, J.; Zakeeruddin, S. M.; Hagfeldt, A.; Grätzel, M., *Science* **2016**, *353*, 58-62.

266. Smith, I. C.; Hoke, E. T.; Solis-Ibarra, D.; McGehee, M. D.; Karunadasa, H. I., *Angew.Chem. Int. Ed.* **2014**, *126*, 11414-11417.

267. Cao, D. H.; Stoumpos, C. C.; Farha, O. K.; Hupp, J. T.; Kanatzidis, M. G., *J. Am. Chem. Soc.* **2015**, *137*, 7843-7850.

268. Yuan, M.; Quan, L. N.; Comin, R.; Walters, G.; Sabatini, R.; Voznyy, O.; Hoogland, S.; Zhao, Y.; Beauregard, E. M.; Kanjanaboos, P., Lu, Z., Kim, D. H., Sargent, E. H. *Nat. Nanotechnol.* **2016**. *11*, 872-877.

269. Dohner, E. R.; Hoke, E. T.; Karunadasa, H. I., *J. Am. Chem. Soc.* **2014**, *136*, 1718-1721.

270. Dohner, E. R.; Jaffe, A.; Bradshaw, L. R.; Karunadasa, H. I., *J. Am. Chem. Soc.* **2014**, *136*, 13154-13157.

271. Wang, M.-S.; Guo, G.-C., *Chem. Commun.*, **2016**, *52*, 13194-13204.

272. Kim, Y.-H.; Cho, H.; Lee, T.-W., *Proc. Natl. Acad. Sci.* **2016**, *113*, 11694-11702.

273. Mitzi, D.; Wang, S.; Feild, C.; Chess, C.; Guloy, A., *Science* **1995**, *267*, 1473-1476.

274. Hu, T.; Smith, M. D.; Dohner, E. R.; Sher, M.-J.; Wu, X.; Trinh, M. T.; Fisher, A.; Corbett, J.; Zhu, X.-Y.; Karunadasa, H. I.; Lindenberg, A. M., *J. Phys. Chem. Lett.* 2016, *7*, 2258−2263.

275. Yangui, A.; Garrot, D.; Lauret, J.-S.; Lusson, A.; Bouchez, G.; Deleporte, E.; Pillet, S.; Bendeif, E.-E.; Castro, M.; Triki, S., *J. Phys. Chem. C.* **2015**, *119*, 23638-23647.

276. Li, Y.; Lin, C.; Zheng, G.; Cheng, Z.; You, H.; Wang, W.; Lin, J., *Chem. Mater.* **2006**, *18*, 3463-3469.

277. Wang, G.-E.; Xu, G.; Wang, M.-S.; Cai, L.-Z.; Li, W.-H.; Guo, G.-C., *Chem. Sci.* **2015**, *6*, 7222-7226.

278. Dolomanov, O. V.; Bourhis, L. J.; Gildea, R. J.; Howard, J. A.; Puschmann, H., J. *Appl. Crystallogr.* **2009**, *42*, 339-341.

279. Kortüm, G.; Braun, W.; Herzog, G., *Angew. Chem. Int. Ed.* **1963**, *2*, 333-341.

280. Guan, J.; Tang, Z.; Guloy, A. M., *Chem. Commun.* **1999**, 1833-1834.

281. Mao, L.; Tsai, H.; Nie, W.; Ma, L.; Im, J.; Stoumpos, C. C.; Malliakas, C. D.; Hao, F.; Wasielewski, M. R.; Mohite, A. D.; Kanatzidis, M. G., *Chem. Mater.* **2016**. *28*, 7781–7792.

282. Steiner, T., *Angew.Chem. Int. Ed.* **2002**, *41*, 48-76.

283. Lufaso, M. W.; Woodward, P. M., *Acta Cryst. B* **2004**, *60*, 10-20.

284. Alonso, J.; Martinez-Lope, M.; Casais, M.; Fernandez-Diaz, M., *Inorg. Chem.* **2000**, *39*, 917-923.

285. Kataoka, T.; Kondo, T.; Ito, R.; Sasaki, S.; Uchida, K.; Miura, N., *Phys. Rev. B* **1993**, *47*, 2010.

286. Galkowski, K.; Mitioglu, A.; Miyata, A.; Plochocka, P.; Portugall, O.; Eperon, G. E.; Wang, J. T.-W.; Stergiopoulos, T.; Stranks, S. D.; Snaith, H. J., *Energy Environ. Sci.* **2016**, *9*, 962-970.

287. Miyata, A.; Mitioglu, A.; Plochocka, P.; Portugall, O.; Wang, J. T.-W.; Stranks, S. D.; Snaith, H. J.; Nicholas, R. J., *Nat. Phys.* **2015**, *11*, 582-587.

288. Gélvez-Rueda, M. C.; Cao, D. H.; Patwardhan, S.; Renaud, N.; Stoumpos, C. C.; Schatz, G. C.; Hupp, J. T.; Farha, O. K.; Savenije, T. J.; Kanatzidis, M. G.; Grozema, F. C., *J. Phys. Chem. C* **2016**, *120*, 16577-16585.

289. D'Andrade, B. W.; Forrest, S. R., *Adv. Mater.* **2004**, *16*, 1585-1595.

290. Kojima, A.; Teshima, K.; Shirai, Y.; Miyasaka, T., *J. Am. Chem. Soc.* **2009**, *131*, 6050-6051.

291. Stoumpos, C. C.; Kanatzidis, M. G., *Acc. Chem. Res.* **2015**, *48*, 2791-2802.

292. Stranks, S. D.; Snaith, H. J., *Nat. Nanotechnol.* **2015**, *10*, 391-402.

293. Stoumpos, C. C.; Kanatzidis, M. G., *Adv. Mater.* **2016**, *28*, 5778-5793.

294. Park, N.-G.; Grätzel, M.; Miyasaka, T.; Zhu, K.; Emery, K., *Nat. Energy* **2016**, *1*, 16152.

295. Correa-Baena, J.-P.; Abate, A.; Saliba, M.; Tress, W.; Jacobsson, T. J.; Grätzel, M.; Hagfeldt, A., *Energy Environ Sci.* **2017**, *10*, 710-727.

296. Xiao, Z.; Meng, W.; Wang, J.; Mitzi, D. B.; Yan, Y., *Mater. Horiz.* **2017**, *4*, 206-216.

297. Im, J.-H.; Lee, C.-R.; Lee, J.-W.; Park, S.-W.; Park, N.-G., *Nanoscale* **2011**, *3*, 4088-4093.

298. Kim, H.-S.; Lee, C.-R.; Im, J.-H.; Lee, K.-B.; Moehl, T.; Marchioro, A.; Moon, S.-J.; Humphry-Baker, R.; Yum, J.-H.; Moser, J. E., *Sci. Rep.* **2012**, *2*, 591.

299. Saparov, B.; Mitzi, D. B., *Chem. Rev.* **2016**, *116*, 4558-4596.

300. Mitzi, D.; Feild, C.; Harrison, W.; Guloy, A., *Nature* **1994**, *369*, 467-469.

301. Smith, I. C.; Hoke, E. T.; Solis-Ibarra, D.; McGehee, M. D.; Karunadasa, H. I., *Angew. Chem. Int. Ed.* **2014**, *126*, 11414-11417.

302. Cao, D. H.; Stoumpos, C. C.; Farha, O. K.; Hupp, J. T.; Kanatzidis, M. G., *J. Am. Chem. Soc.* **2015**, *137*, 7843-7850.

303. Stoumpos, C. C.; Soe, C. M. M.; Tsai, H.; Nie, W.; Blancon, J.-C.; Cao, D. H.; Liu, F.; Traoré, B.; Katan, C.; Even, J.; Mohite, A. D.; Kanatzidis, M. G., *Chem* **2017**, *2*, 427-440.

304. Yuan, M.; Quan, L. N.; Comin, R.; Walters, G.; Sabatini, R.; Voznyy, O.; Hoogland, S.; Zhao, Y.; Beauregard, E. M.; Kanjanaboos, P.; Lu, Z.; Kim, D. H.; Sargent, E. H., *Nat. Nanotechnol.* **2016**, *11*, 872–877.

305. Hassan, Y.; Song, Y.; Pensack, R. D.; Abdelrahman, A. I.; Kobayashi, Y.; Winnik, M. A.; Scholes, G. D., *Adv. Mater.* **2016**, *28*, 566-573.

306. Stoumpos, C. C.; Cao, D. H.; Clark, D. J.; Young, J.; Rondinelli, J. M.; Jang, J. I.; Hupp, J. T.; Kanatzidis, M. G., *Chem. Mater.* **2016**, *28*, 2852-2867.

307. Aharon, S.; Etgar, L., *Nano lett.* **2016**, *16*, 3230-3235.

308. Shang, M.; Li, C.; Lin, J., *Chem. Soc. Rev.* **2014**, *43*, 1372-1386.

309. Wang, M.-S.; Guo, G.-C., *Chem. Commun.* **2016**, *52*, 13194-13204.

310. Zhao, Y. S.; Fu, H.; Hu, F.; Peng, A.; Yang, W.; Yao, J., *Adv. Mater.* **2008**, *20*, 79-83.

311. Bowers, M. J.; McBride, J. R.; Rosenthal, S. J., *J. Am. Chem. Soc.* **2005**, *127*, 15378-15379.

312. Sapra, S.; Mayilo, S.; Klar, T. A.; Rogach, A. L.; Feldmann, J., *Adv. Mater.* **2007**, *19*, 569-572.

313. Yang, G.; Xu, G.; Chen, B.; Zou, S.; Liu, R.; Zhong, H.; Zou, B., *Chem.Mater.* **2013**, *25*, 3260-3266.

314. Carlos, L.; Sá Ferreira, R.; Pereira, R.; Assunção, M.; de Zea Bermudez, V., *J. Phys. Chem. B* **2004**, *108*, 14924-14932.

315. Mao, L.; Wu, Y.; Stoumpos, C. C.; Wasielewski, M. R.; Kanatzidis, M. G., *J. Am. Chem. Soc.* **2017**, *139*, 5210-5215.

316. Smith, M. D.; Jaffe, A.; Dohner, E. R.; Lindenberg, A.; Karunadasa, H. I., *Chem. Sci.* **2017**, *8*, 4497-4504.

317. Hu, T.; Smith, M. D.; Dohner, E. R.; Sher, M.-J.; Wu, X.; Trinh, M. T.; Fisher, A.; Corbett, J.; Zhu, X.-Y.; Karunadasa, H. I., *J. Phys. Chem. Lett.* **2016**, *7*, 2258-2263.

318. McCall, K. M.; Stoumpos, C. C.; Kostina, S. S.; Kanatzidis, M. G.; Wessels, B. W., *Chem. Mater.* **2017**, *29*, 4129–4145.

319. Thirumal, K.; Chong, W. K.; Xie, W.; Ganguly, R.; Muduli, S. K.; Sherburne, M.; Asta, M.; Mhaisalkar, S.; Sum, T. C.; Soo, H. S.; Mathews, N., *Chem. Mater.* **2017**, *29*, 3947–3953.

320. Kortüm, G.; Braun, W.; Herzog, G., *Angew. Chem. Int. Ed.* **1963**, *2*, 333-341.

321. Hohenberg, P.; Kohn, W., *Phys. Rev.* **1964**, *136*, B864-871.

322. Kohn, W.; Sham, L. J., *Phys. Rev.* **1965**, *140*, A1133-1138.

323. Soler, J. M.; Artacho, E.; Gale, J. D.; García, A.; Junquera, J.; Ordejón, P.; Sánchez-Portal, D., *J. Phys. Condens. Matter* **2002**, *14*, 2745-2779.

324. Cooper, V. R., *Phys. Rev. B* **2010**, *81*, 161104.

325. Yuk, S. F.; Pitike, K. C.; Nakhmanson, S. M.; Eisenbach, M.; Li, Y. W.; Cooper, V. R., *Sci. Rep.* **2017**, *7*, 43482.

326. Troullier, N.; Martins, J. L., *Phys. Rev. B* **1991**, *43*, 1993-2006.

327. Zhang, Y.; Yang, W., *Phys. Rev. Lett.* **1998**, *80*, 890.

328. Even, J.; Pedesseau, L.; Kepenekian, M., *Phys. Chem. Chem. Phys.* **2014**, *16*, 25182-25190.

329. Sapori, D.; Kepenekian, M.; Pedesseau, L.; Katan, C.; Even, J., *Nanoscale* **2016**, *8*, 6369-6378.

330. Stoumpos, C. C.; Mao, L.; Malliakas, C. D.; Kanatzidis, M. G., *Inorg. Chem.* **2016**, *56*, 56-73.

331. Geselle, M.; Fuess, H., *Z. Krist. -New Cryst. St.* **1997**, *212*, 241-242.

332. Im, J.-H.; Chung, J.; Kim, S.-J.; Park, N.-G., *Nanoscale Res. Lett.* **2012**, *7*, 353.

333. Fagnou, K.; Lautens, M., *Angew. Chem. Int. Ed.* **2002**, *41*, 26-47.

334. Alonso, J.; Martinez-Lope, M.; Casais, M.; Fernandez-Diaz, M., *Inorg. Chem.* **2000**, *39*, 917-923.

335. Lufaso, M. W.; Woodward, P. M., *Acta Cryst. B* **2004**, *60*, 10-20.

336. Katan, C.; Pedesseau, L.; Kepenekian, M.; Rolland, A.; Even, J., *J. Mater. Chem. A* **2015**, *3*, 9232-9240.

337. Even, J.; Pedesseau, L.; Dupertuis, M.-A.; Jancu, J.-M.; Katan, C., *Phys. Rev. B* **2012**, *86*, 205301.

338. Bokdam, M.; Sander, T.; Stroppa, A.; Picozzi, S.; Sarma, D.; Franchini, C.; Kresse, G., *Sci. Rep.* **2016**, *6*, 28618.

339. Amat, A.; Mosconi, E.; Ronca, E.; Quarti, C.; Umari, P.; Nazeeruddin, M. K.; Grätzel, M.; De Angelis, F., *Nano Lett*. **2014**, *14*, 3608-3616.

340. Filip, M.; Eperon, G.; Snaith, H.; Giustino, F., *Nat. Commun.* **2013**, *5*, 5757.

341. Smith, M. D.; Pedesseau, L.; Kepenekian, M.; Smith, I. C.; Katan, C.; Even, J.; Karunadasa, H. I., *Chem. Sci.* **2017**, *8*, 1960-1968.

342. Kieslich, G.; Sun, S.; Cheetham, A. K., *Chem. Sci.* **2014**, *5*, 4712-4715.

343. Snaith, H. J., *J. Phys. Chem. Lett.* **2013**, *4*, 3623-3630.

344. Wang, N.; Liu, W.; Zhang, Q., *Small Methods* **2018**, *2*, 1700380.

345. Ning, C.-Z.; Dou, L.; Yang, P., *Nat. Rev. Mater*. **2017**, *2*, 17070.

346. Shi, E.; Gao, Y.; Finkenauer, B. P.; Akriti; Coffey, A. H.; Dou, L., *Chem. Soc. Rev*. **2018**, *47*, 6046-6072

347. Wang, N.; Zhao, K.; Ding, T.; Liu, W.; Ahmed, A. S.; Wang, Z.; Tian, M.; Sun, X. W.; Zhang, Q., *Adv. Ener. Mater.* **2017**, *7*, 1700522.

348. Gu, P.-Y.; Wang, N.; Wang, C.; Zhou, Y.; Long, G.; Tian, M.; Chen, W.; Sun, X. W.; Kanatzidis, M. G.; Zhang, Q., *J. Mater. Chem. A* **2017**, *5*, 7339-7344.

349. Wang, N.; Cheng, L.; Ge, R.; Zhang, S.; Miao, Y.; Zou, W.; Yi, C.; Sun, Y.; Cao, Y.; Yang, R.; Wei, Y.; Guo, Q.; Ke, Y.; Yu, M.; Jin, Y.; Liu, Y.; Ding, Q.; Di, D.; Yang, L.; Xing, G.; Tian, H.; Jin, C.; Gao, F.; Friend, R. H.; Wang, J.; Huang, W., *Nat. Photon.* **2016**, *10*, 699–704

350. Tsai, H.; Nie, W.; Blancon, J. C.; Stoumpos, C. C.; Soe, C. M. M.; Yoo, J.; Crochet, J.; Tretiak, S.; Even, J.; Sadhanala, A., *Adv. Mater.* **2018**, *30*, 1704217.

351. Stoumpos, C. C.; Malliakas, C. D.; Kanatzidis, M. G., Inorg. Chem. 2013, 52, 9019-9038.

352. Sun, C.; Wang, M. S.; Li, P. X.; Guo, G. C., *Angew, Chem. Int. Ed.* **2017**, *56*, 554-558.

353. Lee, B.; Stoumpos, C. C.; Zhou, N.; Hao, F.; Malliakas, C.; Yeh, C.-Y.; Marks, T. J.; Kanatzidis, M. G.; Chang, R. P. H., *J. Am. Chem. Soc.* **2014**, *136*, 15379-15385.

354. Saidaminov, M. I.; Almutlaq, J.; Sarmah, S.; Dursun, I.; Zhumekenov, A. A.; Begum, R.; Pan, J.; Cho, N.; Mohammed, O. F.; Bakr, O. M., *ACS Energy Lett.* **2016**, *1*, 840-845.

355. De Bastiani, M.; Dursun, I.; Zhang, Y.; Alshankiti, B. A.; Miao, X.-H.; Yin, J.; Yengel, E.; Alarousu, E.; Turedi, B.; Almutlaq, J. M.; Saidaminov, M. I.; Mitra, S.; Gereige, I.; AlSaggaf, A.; Zhu, Y.; Han, Y.; Roqan, I. S.; Bredas, J.-L.; Mohammed, O. F.; Bakr, O. M., *Chem. Mater.* **2017**, *29*, 7108-7113.

356. Tran, T. T.; Panella, J. R.; Chamorro, J. R.; Morey, J. R.; McQueen, T. M., *Mater. Horiz.* **2017**, *4*, 688-693.

357. Smith, M. D.; Karunadasa, H. I., *Acc. Chem. Res.* **2018**, *51*, 619-627.

358. Li, Y. Y.; Lin, C. K.; Zheng, G. L.; Cheng, Z. Y.; You, H.; Wang, W. D.; Lin, *J.*, *Chem. Mater.* **2006**, *18*, 3463-3469.

359. Dohner, E. R.; Hoke, E. T.; Karunadasa, H. I., J. Am. Chem. Soc. 2014, 136, 1718-1721.

360. Mao, L.; Wu, Y.; Stoumpos, C. C.; Wasielewski, M. R.; Kanatzidis, M. G., *J. Am. Chem. Soc.* **2017**, *139*, 5210–5215.

361. Cortecchia, D.; Neutzner, S.; Srimath Kandada, A. R.; Mosconi, E.; Meggiolaro, D.; De Angelis, F.; Soci, C.; Petrozza, A., *J. Am. Chem. Soc.* **2017**, *139*, 39-42.

362. Yuan, Z.; Zhou, C.; Tian, Y.; Shu, Y.; Messier, J.; Wang, J. C.; Van De Burgt, L. J.; Kountouriotis, K.; Xin, Y.; Holt, E., *Nat. Commun.* **2017**, *8*, 14051.

363. Long, J. R.; McCarty, L. S.; Holm, R., *J. Am. Chem. Soc.* **1996**, *118*, 4603-4616.

364. Axtell III, E. A.; Liao, J. H.; Pikramenou, Z.; Kanatzidis, M. G., *Chem. Eur. J.* **1996**, *2*, 656-666.

365. Wang, M.-S.; Guo, G.-C., *Chem. Commun.* **2016**, *52*, 13194-13204.

366. Wang, M.-S.; Guo, S.-P.; Li, Y.; Cai, L.-Z.; Zou, J.-P.; Xu, G.; Zhou, W.-W.; Zheng, F.-K.; Guo, G.-C., *J. Am. Chem. Soc.* **2009**, *131*, 13572-13573.

367. Wang, M. S.; Guo, G. C.; Chen, W. T.; Xu, G.; Zhou, W. W.; Wu, K. J.; Huang, J. S., *Angew. Chem. Int. Ed.* **2007**, *46*, 3909-3911.

368. Saidaminov, M. I.; Mohammed, O. F.; Bakr, O. M., *ACS Energy Lett.* **2017**, *2*, 889–896.

369. Lin, H.; Zhou, C.; Tian, Y.; Siegrist, T.; Ma, B., *ACS Energy Lett.* **2018**, *3*, 54-62.

370. Zhang, Z.-J.; Guo, G.-C.; Xu, G.; Fu, M.-L.; Zou, J.-P.; Huang, J.-S., *Inorg. Chem.* **2006**, *45*, 10028-10030.

371. Li, M.-Q.; Hu, Y.-Q.; Bi, L.-Y.; Zhang, H.-L.; Wang, Y.; Zheng, Y.-Z., *Chem. Mater.* **2017**, *29*, 5463-5467.

372. Dolomanov, O. V.; Bourhis, L. J.; Gildea, R. J.; Howard, J. A.; Puschmann, H., *J. Appl. Crystallogr.* **2009**, *42*, 339-341.

373. Kortüm, G.; Braun, W.; Herzog, G., *Angew. Chem. Int. Ed.* **1963**, *2*, 333-341.

374. de Mello, J. C.; Wittmann, H. F.; Friend, R. H., *Adv. Mater.* **1997**, *9*, 230-232.

375. José, M. S.; Emilio, A.; Julian, D. G.; Alberto, G.; Javier, J.; Pablo, O.; Daniel, S.-P., *J. Phys. Condens. Matter* **2002**, *14*, 2745.

376. Artacho, E.; Anglada, E.; Diéguez, O.; Gale, J. D.; García, A.; Junquera, J.; Martin, R. M.; Ordejón, P.; Pruneda, J. M.; Sánchez-Portal, D., *J. Phys. Condens. Matter* **2008**, *20*, 064208.

377. Perdew, J. P.; Burke, K.; Ernzerhof, M., *Phys. Rev. Lett.* **1996**, *77*, 3865-3868.

378. Troullier, N.; Martins, J. L., *Phys. Rev. B* **1991**, *43*, 1993-2006.

379. Artacho, E.; Sánchez-Portal, D.; Ordejón, P.; García, A.; Soler, J. M., *Phys. Status Solidi B* **1999**, *215*, 809-817.

380. Fernández-Seivane, L.; Oliveira, M. A.; Sanvito, S.; Ferrer, J., *J. Phys. Condens. Matter* **2006**, *18*, 7999-8013.

381. Raw, A. D.; Ibers, J. A.; Poeppelmeier, K. R., *J. Solid State Chem.* **2012**, *192*, 34-37.

382. Gomez, V.; Fuhr, O.; Ruben, M., *CrystEngComm* **2016**, *18*, 8207-8219.

383. Tong, Y.-B.; Ren, L.-T.; Duan, H.-B.; Liu, J.-L.; Ren, X.-M., *Dalton Trans.* **2015**, *44*, 17850-17858.

384. Hodorowicz, M. A.; Piaskowska, A.; Stadnicka, K. M., *Acta Cryst. C* **2012**, *68*, m173-m176.

385. Niu, J.-P.; Zhai, Q.-G.; Luo, J.-H.; Li, S.-N.; Jiang, Y.-C.; Hu, M.-C., *Inorg. Chem. Commun.* **2011**, *14*, 663-666.

386. Zimmermann, I.; Keene, T. D.; Hauser, J.; Decurtins, S.; Liu, S.-X., *Acta Cryst. E* **2014**, *70*, 178-182.

387. Corradi, A. B.; Bruni, S.; Cariati, F.; Ferrari, A. M.; Saccani, A.; Sandrolini, F.; Sgarabotto, P., *Inorg. Chimica Acta.* **1997**, *254*, 137-143.

388. Chen, T.; Zhou, Y.; Sun, Z.; Zhang, S.; Zhao, S.; Tang, Y.; Ji, C.; Luo, J., *Inorg. Chem.* **2015**, *54*, 7136-7138.

389. Billing, D. G.; Lemmerer, A., *Acta Cryst. E* **2003**, *59*, m381-m383.

390. Kanatzidis, M. G., *Phosphorus Sulfur Silicon Relat. Elem.* **1994**, 93, 159-172.

391. Salim, T.; Sun, S.; Abe, Y.; Krishna, A.; Grimsdale, A. C.; Lam, Y. M., *J. Mater. Chem. A* **2015**, *3*, 8943-8969.

392. Li, Y.; Zheng, G.; Lin, C.; Lin, J., *Cryst. Growth Des.* **2008**, *8*, 1990-1996.

393. Yaffe, O.; Guo, Y.; Tan, L. Z.; Egger, D. A.; Hull, T.; Stoumpos, C. C.; Zheng, F.; Heinz, T. F.; Kronik, L.; Kanatzidis, M. G.; Owen, J. S.; Rappe, A. M.; Pimenta, M. A.; Brus, L. E., *Phys. Rev. Lett.* **2017**, *118*, 136001.

394. Quarti, C.; Grancini, G.; Mosconi, E.; Bruno, P.; Ball, J. M.; Lee, M. M.; Snaith, H. J.; Petrozza, A.; De Angelis, F., *J. Phys. Chem. Lett.* **2014**, *5*, 279-284.

395. Nakamoto, K., *Infrared and Raman Spectra of Inorganic and Coordination Compounds. Wiley.* **1977**.

396. Robinson, K.; Gibbs, G.; Ribbe, P., *Science* **1971**, *172*, 567-570.

397. Smith, M. D.; Watson, B. L.; Dauskardt, R. H.; Karunadasa, H. I., *Chem. Mater.* **2017**, *29*, 7083-7087.

398. Wu, Z.; Li, L.; Ji, C.; Lin, G.; Wang, S.; Shen, Y.; Sun, Z.; Zhao, S.; Luo, J., *Inorg. Chem.* **2017**, *56*, 8776-8781.

399. Jeon, N. J.; Noh, J. H.; Kim, Y. C.; Yang, W. S.; Ryu, S.; Seok, S. I., *Nat. Mater.* **2014**, *13*, 897-903.

400. Green, M. A.; Ho-Baillie, A.; Snaith, H. J., *Nat. Photon.* **2014**, *8*, 506-514.

401. Li, X.; Ibrahim Dar, M.; Yi, C.; Luo, J.; Tschumi, M.; Zakeeruddin, S. M.; Nazeeruddin, M. K.; Han, H.; Grätzel, M., *Nat. Chem.* **2015**, *7*, 703-711.

402. Stoumpos, C. C.; Kanatzidis, M. G., *Acc. Chem. Res.* **2015**, *48*, 2791-802.

403. Quan, L. N.; Yuan, M.; Comin, R.; Voznyy, O.; Beauregard, E. M.; Hoogland, S.; Buin, A.; Kirmani, A. R.; Zhao, K.; Amassian, A.; Kim, D. H.; Sargent, E. H., *J. Am. Chem. Soc.* **2016**, *138*, 2649–2655.

404. Zhu, X.-H.; Mercier, N.; Riou, A.; Blanchard, P.; Frère, P., *Chem. Commun.* **2002**, 2160-2161.

405. Luo, J.; Li, L.; Sun, Z.; Wang, P.; Hu, W.; Wang, S.; Ji, C.; Hong, M., *Angew. Chem. Int. Ed.* **2017**, *129*, 12318–12322.

406. Nazarenko, O.; Kotyrba, M. R.; Wörle, M.; Cuervo-Reyes, E.; Yakunin, S.; Kovalenko, M. V., *Inorg. Chem.* **2017**, *56*, 11552-11564.

407. Schaak, R. E.; Mallouk, T. E., *Chem. Mater.* **2002**, *14*, 1455-1471.

408. Battle, P. D.; Green, M. A.; Lago, J.; Millburn, J. E.; Rosseinsky, M. J.; Vente, J. F., *Chem. Mater.* **1998**, *10*, 658-664.

409. Dion, M.; Ganne, M.; Tournoux, M., *Mater. Res. Bull.* **1981**, *16*, 1429-1435.

410. Hojamberdiev, M.; Bekheet, M. F.; Zahedi, E.; Wagata, H.; Kamei, Y.; Yubuta, K.; Gurlo, A.; Matsushita, N.; Domen, K.; Teshima, K., *Cryst. Growth Des.* **2016**, *16*, 2302-2308.

411. Kendall, K. R.; Navas, C.; Thomas, J. K.; zur Loye, H.-C., *Chem. Mater.* **1996**, *8*, 642-649.

412. Mousdis, G. A.; Papavassiliou, G. C.; Raptopoulou, C.; Terzis, A., *J. Mater. Chem.* **2000**, *10*, 515-518.

413. Tang, Z.; Guan, J.; Guloy, A. M., *J. Mater. Chem.* **2001**, *11*, 479-482.

414. Bulou, A.; Nouet, J., *J. Phys. C Solid State Phys.* **1982**, *15*, 183-196.

415. Tilley, R. J., *Perovskites: Structure-Property Relationships. John Wiley & Sons:* **2016**; 123-155.

416. Jacobson, A. J.; Lewandowski, J. T.; Johnson, J. W., *Mater. Res. Bull.* **1990**, *25*, 679-686.

417. Gopalakrishnan, J.; Bhat, V., *Inorg. Chem.* **1987**, *26*, 4299-4301.

418. Jacobson, A. J.; Johnson, J. W.; Lewandowski, J. T., *Inorg. Chem.* **1985**, 24, 3727-3729.

419. Kresse, G.; Furthmüller, J., *Phys. Rev. B* **1996**, *54*, 11169-11186.

420. Kresse, G.; Furthmüller, J., *Comput. Mater. Sci.* **1996**, *6*, 15-50.

421. Shishkin, M.; Kresse, G., *Phys. Rev. B* **2006**, *74*, 035101.

422. Blöchl, P. E., *Phys. Rev. B* **1994**, *50*, 17953-17979.

423. Kresse, G.; Joubert, D., *Phys. Rev. B* **1999**, *59*, 1758-1775.

424. Monkhorst, H. J.; Pack, J. D., *Phys. Rev. B* **1976**, *13*, 5188-5192.

425. Pack, J. D.; Monkhorst, H. J., *Phys. Rev. B* **1977**, *16*, 1748-1749.

426. Peng, W.; Yin, J.; Ho, K.-T.; Ouellette, O.; De Bastiani, M.; Murali, B.; El Tall, O.; Shen, C.; Miao, X.; Pan, J., *Nano lett.* **2017**, *17*, 4759-4767.

427. Katan, C.; Pedesseau, L.; Kepenekian, M.; Rolland, A.; Even, J., *J. Mater. Chem. A* **2015**, *3*, 9232-9240.

428. Liu, G.; Kong, L.; Guo, P.; Stoumpos, C. C.; Hu, Q.; Liu, Z.; Cai, Z.; Gosztola, D. J.; Mao, H.-k.; Kanatzidis, M. G.; Schaller, R. D., *ACS Energy Lett.* **2017**, 2518-2524.

429. Zhou, N.; Shen, Y.; Li, L.; Tan, S.; Liu, N.; Zheng, G.; Chen, Q.; Zhou, H., *J. Am. Chem. Soc.* **2017**, *140*, 459-465.

430. Chen, Y.; Sun, Y.; Peng, J.; Tang, J.; Zheng, K.; Liang, Z., *Adv. Mater.* **2018**, *30*, 1703487.

431. NREL's "Best Research-Cell Efficiencies" Chart. https://www.nrel.gov/pv/assets/pdfs/pv-efficiencies-07-17-2018.pdf

432. Fu, W.; Wang, J.; Zuo, L.; Gao, K.; Liu, F.; Ginger, D. S.; Jen, A. K. Y., *ACS Energy Lett.* **2018**, *3*, 2086-2093.

433. Zhou, G.; Jiang, X.; Zhao, J.; Molokeev, M.; Lin, Z.; Liu, Q.; Xia, Z., *ACS Appl. Mater. Interfaces* **2018,** *10*, 24648-24655.

434. Sapori, D.; Kepenekian, M.; Pedesseau, L.; Katan, C.; Even, J., *Nanoscale* **2016**, *8*, 6369-6378.

435. Momma, K.; Izumi, F. *J. Appl. Crystallogr.* **2011**, *44*, 1272-1276.

436. Dunlap-Shohl, W. A.; Zhou, Y.; Padture, N. P.; Mitzi, D. B., *Chem. Rev.* **2018**. DOI: 10.1021/acs.chemrev.8b00318

437. Cao, Y.; Wang, N.; Tian, H.; Guo, J.; Wei, Y.; Chen, H.; Miao, Y.; Zou, W.; Pan, K.; He, Y.; Cao, H.; Ke, Y.; Xu, M.; Wang, Y.; Yang, M.; Du, K.; Fu, Z.; Kong, D.; Dai, D.; Jin, Y.; Li, G.; Li, H.; Peng, Q.; Wang, J.; Huang, W., *Nature* **2018**, *562*, 249-253.

438. Saliba, M.; Matsui, T.; Domanski, K.; Seo, J.-Y.; Ummadisingu, A.; Zakeeruddin, S. M.; Correa-Baena, J.-P.; Tress, W. R.; Abate, A.; Hagfeldt, A.; Grätzel, M., *Science* **2016**, *354*, 206-209.

439. McMeekin, D. P.; Sadoughi, G.; Rehman, W.; Eperon, G. E.; Saliba, M.; Hörantner, M. T.; Haghighirad, A.; Sakai, N.; Korte, L.; Rech, B.; Johnston, M. B.; Herz, L. M.; Snaith, H. J., *Science* **2016**, *351*, 151-155.

440. Saliba, M.; Matsui, T.; Seo, J.-Y.; Domanski, K.; Correa-Baena, J.-P.; Nazeeruddin, M. K.; Zakeeruddin, S. M.; Tress, W.; Abate, A.; Hagfeldt, A.; Grätzel, M., *Energy Environ. Sci.* **2016**, *9*, 1989-1997.

441. Jeon, N. J.; Noh, J. H.; Yang, W. S.; Kim, Y. C.; Ryu, S.; Seo, J.; Seok, S. I., *Nature* **2015**, *517*, 476-480.

442. Rehman, W.; McMeekin, D. P.; Patel, J. B.; Milot, R. L.; Johnston, M. B.; Snaith, H. J.; Herz, L. M., *Energy Environ. Sci.* **2017**, *10*, 361-369.

443. Ke, W.; Xiao, C.; Wang, C.; Saparov, B.; Duan, H.-S.; Zhao, D.; Xiao, Z.; Schulz, P.; Harvey, S. P.; Liao, W.; Meng, W.; Yu, Y.; Cimaroli, A. J.; Jiang, C.-S.; Zhu, K.; Al-Jassim, M.; Fang, G.; Mitzi, D. B.; Yan, Y., *Adv. Mater.* **2016**, *28*, 5214-5221.

444. Li, X.; Dar, M. I.; Yi, C.; Luo, J.; Tschumi, M.; Zakeeruddin, S. M.; Nazeeruddin, M. K.; Han, H.; Grätzel, M., *Nat. Chem.* **2015**, *7*, 703-711.

445. Kieslich, G.; Sun, S.; Cheetham, A. K., *Chem. Sci.* **2015**, *6*, 3430-3433.

446. Mitzi, D. B.; Medeiros, D. R.; Malenfant, P. R. L., *Inorg. Chem.* **2002**, 41, 2134-2145.

447. Ortiz-Cervantes, C.; Román-Román, P. I.; Vazquez-Chavez, J.; Hernández-Rodríguez, M.; Solis-Ibarra, D., *Angew. Chem. Int. Ed.* **2018**, *57*, 13882-13886.

448. Note that 34MA is the only compound with a β angle not equal to ~90 degree, thus the cell is transformed to an β = 90 cell using the matrix (0 -0.5 0.5, 0 0.5 0.5, -0.5 0 -0.5) and the long axis becomes 16.082 Å.

449. Liu, G.; Gong, J.; Kong, L.; Schaller, R. D.; Hu, Q.; Liu, Z.; Yan, S.; Yang, W.; Stoumpos, C. C.; Kanatzidis, M. G.; Mao, H.-k.; Xu, T., *Proc. Natl. Acad. Sci.* **2018**, *115*, 8076-8081.

APPENDIX A

Supporting Information for Chapter 2

Table A1. Pb-Br bond lengths in α-(DMEN)$PbBr_4$ and (DMAPA)$PbBr_4$.

α-(DMEN)$PbBr_4$	Distances (Å)	(DMAPA)$PbBr_4$	Distances (Å)
Pb(1)-Br(1)	2.841(2)	Pb(1)-Br(1)	3.0011(12)
Pb(1)-Br(2)	2.812(2)	Pb(1)-Br(2)	2.9691(8)
Pb(1)-Br(3)	2.965(2)	Pb(1)-Br(2)’	3.0408(8)
Pb(1)-Br(3)’	2.976(2)	Pb(1)-Br(3)	2.9792(11)
Pb(1)-Br(4)	3.1750(17)	Pb(1)-Br(4)	3.0516(8)
Pb(1)-Br(6)	3.273(2)	Pb(1)-Br(4)’	3.0338(8)
Pb(2)-Br(4)	3.0163(18)		
Pb(2)-Br(5)	2.907(2)		
Pb(2)-Br(6)	3.024(2)		
Pb(2)-Br(7)	2.990(2)		
Pb(2)-Br(7)’	3.097(2)		
Pb(2)-Br(8)	3.063(2)		

Table A2. Pb-Br bond lengths in (DMABA)$PbBr_4$.

Label	Distances (Å)	Label	Distances (Å)
Pb(1)-Br(1)	3.002(3)	Pb(3)-Br(9)	2.9706(12)
Pb(1)-Br(2)	3.114(5)	Pb(3)-Br(10)	2.980(3)
Pb(1)-Br(2)’	2.954(4)	Pb(3)-Br(11)	2.996(5)
Pb(1)-Br(3)	2.972(3)	Pb(3)-Br(12)	2.977(3)
Pb(1)-Br(4)	3.044(3)	Pb(3)-Br(13)	3.049(3)
Pb(1)-Br(6)’	3.002(3)	Pb(3)-Br(14)’	3.052(5)
Pb(2)-Br(4)	2.983(3)	Pb(4)-Br(11)’	3.095(5)
Pb(2)-Br(5)	2.905(3)	Pb(4)-Br(13)	3.008(3)
Pb(2)-Br(6)	3.053(3)	Pb(4)-Br(14)	2.949(5)
Pb(2)-Br(7)	3.073(5)	Pb(4)-Br(15)	3.126(3)
Pb(2)-Br(7)’	2.953(5)	Pb(4)-Br(16)	3.0495(12)
Pb(2)-Br(8)	3.153(3)	Pb(4)-Br(17)	2.935(3)

Table A3. Pb-Br-Pb angles in α-(DMEN)$PbBr_4$, (DMAPA)$PbBr_4$ and (DMABA)$PbBr_4$

Compound	Label	Angles (°)
α-(DMEN)$PbBr_4$	Pb(1)-Br(3)-Pb(1)’	165.74(10)
	Pb(2)-Br(4)-Pb(1)	176.86(9)
	Pb(2)-Br(7)-Pb(2)’	151.36(8)
(DMAPA)$PbBr_4$	Pb(1)-Br(2)-Pb(1)’	156.79(3)
	Pb(1)-Br(4)-Pb(1)'	170.90(2)
(DMABA)$PbBr_4$	Pb(1)-Br(2)-Pb(1)’	166.78(13)
	Pb(2)-Br(4)-Pb(1)	170.48(17)
	Pb(1)’-Br(6)-Pb(2)	163.46(14)
	Pb(3)-Br(9)-Pb(3)’	173.0(3)
	Pb(3)-Br(11)-Pb(4)’	169.07(15)
	Pb(4)-Br(13)-Pb(3)	162.91(14)
	Pb(4)-Br(14)-Pb(3)”	167.82(16)
	Pb(4)-Br(16)-Pb(4)”	174.9(3)

Table A4. Atomic coordinates ($x10^4$) and equivalent isotropic displacement parameters ($Å^2x10^3$) for α-(DMEN)$PbBr_4$ at 293(2) K with estimated standard deviations in parentheses.

Label	x	y	z	Occupancy	U_{eq}^*
Pb(1)	-2558(1)	394(1)	4221(1)	1	35(1)
Pb(2)	-68(1)	266(1)	2526(1)	1	43(1)
Br(1)	-3656(2)	683(2)	5028(2)	1	85(1)
Br(2)	-1627(2)	243(3)	5144(2)	1	108(2)
Br(3)	-2308(2)	2878(2)	4194(2)	1	90(1)
Br(4)	-1309(1)	349(2)	3325(1)	1	60(1)
Br(5)	828(1)	961(2)	3461(1)	1	67(1)
Br(6)	1140(2)	281(2)	1688(2)	1	105(2)
Br(7)	-271(2)	2729(2)	2267(1)	1	59(1)
Br(8)	-1122(2)	-505(2)	1621(1)	1	64(1)
N(1)	-3351(14)	2250(20)	7722(11)	1	130(6)
H(1A)	-3556	1715	7510	1	155
H(1B)	-3571	2905	7670	1	155
H1C()	-3380	2047	8084	1	155

N(2)	-2483(17)	2320(20)	6543(13)	1	134(10)
H(2)	-2967	2018	6553	1	161
C(1)	-2609(19)	2360(30)	7560(13)	1	130(6)
H(1D)	-2363	2737	7865	1	155
H(1E)	-2412	1598	7530	1	155
C(2)	-2450(20)	2970(30)	7030(13)	1	130(6)
H(2A)	-1975	3284	7059	1	155
H(2B)	-2775	3597	6993	1	155
C(3)	-2070(20)	1340(40)	6528(18)	1	151(14)
H(3A)	-2248	839	6240	1	227
H(3B)	-2097	963	6888	1	227
H3C()	-1591	1535	6448	1	227
C(4)	-2479(16)	3000(30)	6030(14)	1	108(9)
H(4A)	-2662	3740	6111	1	162
H(4B)	-2770	2639	5749	1	162
H4C()	-2004	3061	5891	1	162
N(3)	-477(8)	2788(14)	3813(7)	1	59(4)
H(3D)	-521	3398	3594	1	71
H(3E)	-882	2402	3813	1	71
H(3F)	-132	2349	3681	1	71
N(4)	86(9)	2542(16)	5321(8)	1	69(5)
H(4)	463	3108	5282	1	83
C(5)	-312(12)	3133(17)	4374(8)	1	61(5)
H(5A)	-722	3505	4537	1	73
H(5B)	70	3683	4362	1	73
C(6)	-98(12)	2167(17)	4746(9)	1	65(6)
H(6A)	-484	1625	4767	1	78
H(6B)	305	1784	4580	1	78
C(7)	385(19)	1580(30)	5681(13)	1	141(16)
H(7A)	45	1370	5963	1	212
H(7B)	812	1833	5862	1	212
H7C()	487	941	5445	1	212
C(8)	-470(14)	3070(20)	5649(10)	1	89(8)
H(8A)	-660	3700	5444	1	133

H(8B)	-282	3324	6003	1	133
H8C()	-839	2522	5718	1	133

*U_{eq} is defined as one third of the trace of the orthogonalized U_{ij} tensor.

Table A5. Atomic coordinates ($x10^4$) and equivalent isotropic displacement parameters ($Å^2x10^3$) for (DMAPA)$PbBr_4$ at 293(2) K with estimated standard deviations in parentheses.

Label	x	y	z	Occupancy	U_{eq}*
Pb(1)	5008(1)	7421(1)	2698(1)	1	25(1)
Br(1)	7973(1)	7769(1)	3922(1)	1	45(1)
Br(2)	4442(1)	9904(1)	2516(1)	1	38(1)
Br(3)	2074(1)	6938(1)	1699(1)	1	41(1)
Br(4)	4806(1)	7614(1)	5122(1)	1	36(1)
N(1)	-2870(6)	5078(5)	362(5)	1	44(2)
H(1A)	-3396	4605	-187	1	53
H(1B)	-2599	5640	11	1	53
H1C()	-3327	5367	779	1	53
N(2)	1550(5)	5236(4)	3570(4)	1	30(1)
H(2)	1667	5787	3008	1	36
C(1)	-1701(8)	4454(6)	1155(7)	1	50(2)
H(1D)	-1211	4136	695	1	60
H(1E)	-2003	3826	1513	1	60
C(2)	-782(8)	5194(5)	2110(7)	1	45(2)
H(2A)	-1260	5509	2581	1	54
H(2B)	-466	5821	1761	1	54
C(3)	392(7)	4500(5)	2888(6)	1	40(2)
H(3A)	122	4054	3435	1	48
H(3B)	665	3976	2399	1	48
C(4)	1315(8)	5901(7)	4515(7)	1	54(2)
H(4A)	473	6295	4187	1	82
H(4B)	2025	6445	4841	1	82
H4C()	1293	5395	5130	1	82
C(5)	2812(7)	4589(6)	4061(7)	1	43(2)
H(5A)	2722	4008	4584	1	65
H(5B)	3529	5095	4492	1	65

H5C()	3008	4241	3426	1	65

*U_{eq} is defined as one third of the trace of the orthogonalized U_{ij} tensor.

Table A6. Atomic coordinates ($x10^4$) and equivalent isotropic displacement parameters ($Å^2x10^3$) for (DMABA)$PbBr_4$ at 293(2) K with estimated standard deviations in parentheses.

Label	x	y	z	Occupancy	U_{eq}*
Pb(1)	7432(1)	-3054(1)	5867(1)	1	33(1)
Pb(2)	7532(1)	-554(1)	5794(1)	1	33(1)
Br(1)	8143(1)	-3254(2)	5815(3)	1	48(1)
Br(2)	7462(2)	-3186(2)	3422(3)	1	48(1)
Br(3)	6722(1)	-2943(2)	5796(4)	1	53(1)
Br(4)	7430(1)	-1786(2)	5728(5)	1	56(1)
Br(5)	8221(1)	-732(2)	5730(4)	1	55(1)
Br(6)	7649(1)	701(1)	5947(5)	1	55(1)
Br(7)	7517(2)	-454(2)	3342(4)	1	60(1)
Br(8)	6802(1)	-208(2)	5715(4)	1	52(1)
Pb(3)	5072(1)	3769(1)	4884(2)	1	33(1)
Pb(4)	5027(1)	1270(1)	4924(2)	1	34(1)
Br(9)	5000	5000	5035(6)	1	58(2)
Br(10)	5778(1)	3967(2)	4917(4)	1	58(1)
Br(11)	5062(2)	3649(2)	7368(4)	1	50(1)
Br(12)	4368(1)	3561(2)	4906(4)	1	48(1)
Br(13)	5156(1)	2505(1)	4844(6)	1	58(1)
Br(14)	4974(2)	1384(2)	7364(4)	1	55(1)
Br(15)	4305(1)	1620(2)	4981(4)	1	52(1)
Br(16)	5000	0	5037(7)	1	65(2)
Br(17)	5728(1)	1145(2)	4934(4)	1	54(1)
N(1)	6985(9)	674(10)	7850(30)	1	68(10)
H(1A)	6912	376	7489	1	82
H(1B)	7145	574	8298	1	82
H1C()	7056	924	7358	1	82
N(2)	5788(9)	183(12)	6980(30)	1	73(9)
H(2)	5709	422	6379	1	88
C(1)	6737(11)	910(30)	8480(50)	1	148(14)
H(1D)	6654	1210	8026	1	177

H(1E)	6844	1089	9105	1	177
C(2)	6449(11)	650(20)	8980(40)	1	148(14)
H(2A)	6299	941	9169	1	177
H(2B)	6512	467	9667	1	177
C(3)	6278(12)	230(20)	8270(40)	1	148(14)
H(3A)	6430	30	7806	1	177
H(3B)	6167	-39	8738	1	177
C(4)	6044(12)	540(20)	7570(50)	1	148(14)
H(4A)	6163	744	7006	1	177
H(4B)	5936	811	8035	1	177
C(5)	5888(10)	-332(14)	6420(30)	1	76(4)
H(5A)	6107	-297	6178	1	115
H(5B)	5753	-396	5782	1	115
H5C()	5870	-640	6924	1	115
C(6)	5509(11)	122(17)	7750(40)	1	76(4)
H(6A)	5569	-107	8369	1	115
H(6B)	5335	-51	7353	1	115
H6C()	5444	483	8006	1	115
N(3)	5511(8)	-2582(10)	6970(30)	1	52(8)
H3C()	5457	-2792	6392	1	63
H(3D)	5532	-2228	6757	1	63
H(3E)	5359	-2604	7492	1	63
N(4)	6704(8)	-1652(13)	8750(20)	1	66(8)
H(4)	6777	-1387	9321	1	79
C(7)	5842(11)	-2798(17)	7480(40)	1	76(4)
H(7A)	5980	-2944	6899	1	92
H(7B)	5806	-3087	8032	1	92
C(8)	5998(11)	-2255(15)	8040(30)	1	76(4)
H(8A)	6059	-1982	7485	1	92
H(8B)	5851	-2084	8569	1	92
C(9)	6286(11)	-2495(16)	8620(40)	1	76(4)
H(9A)	6432	-2653	8073	1	92
H(9B)	6220	-2791	9122	1	92
C(10)	6456(10)	-2034(15)	9270(30)	1	76(4)

H(10A)	6289	-1795	9575	1	92
H(10B)	6559	-2212	9905	1	92
C(11)	6978(11)	-1998(15)	8420(30)	1	76(4)
H(11A)	7089	-2128	9068	1	115
H(11B)	7122	-1779	7969	1	115
H11C()	6903	-2311	7993	1	115
C(12)	6582(11)	-1340(15)	7810(30)	1	76(4)
H(12A)	6546	-1589	7193	1	115
H(12B)	6735	-1060	7596	1	115
H12C()	6383	-1164	8008	1	115
N(5)	6979(8)	744(10)	13780(30)	1	52(8)
H(5D)	7064	493	13322	1	63
H(5E)	6940	587	14438	1	63
H(5F)	7115	1027	13869	1	63
N(6)	5798(6)	-131(9)	12000(20)	1	51(7)
H(6)	5713	-361	11392	1	61
C(13)	6671(9)	956(11)	13300(30)	1	58(9)
H(13A)	6717	1252	12768	1	70
H(13B)	6539	1110	13885	1	70
C(14)	6490(13)	487(16)	12710(40)	1	100(17)
H(14A)	6627	329	12134	1	120
H(14B)	6443	195	13242	1	120
C(15)	6196(8)	665(13)	12210(30)	1	55(8)
H(15A)	6237	997	11766	1	65
H(15B)	6046	766	12791	1	65
C(16)	6040(9)	225(12)	11460(30)	1	64(9)
H(16A)	5940	414	10836	1	76
H(16B)	6207	-13	11163	1	76
C(17)	5511(8)	160(20)	12450(30)	1	88(14)
H(17A)	5507	124	13243	1	133
H(17B)	5321	-5	12137	1	133
H17C()	5520	547	12248	1	133
C(18)	5940(12)	-543(16)	12790(30)	1	96(14)
H(18A)	6106	-750	12423	1	144

H(18B)	5776	-794	13044	1	144
H18C()	6029	-349	13420	1	144
N(7)	5526(8)	2488(11)	7900(30)	1	56(9)
H7C()	5405	2690	7441	1	67
H(7D)	5608	2708	8424	1	67
H(7E)	5407	2224	8216	1	67
N(8)	6698(6)	2988(10)	8710(20)	1	49(6)
H(8)	6787	2754	9308	1	59
C(19)	5797(11)	2219(17)	7240(30)	1	76(4)
H(19A)	5914	1978	7749	1	92
H(19B)	5701	1981	6681	1	92
C(20)	6008(8)	2549(14)	6740(30)	1	60(9)
H(20A)	5889	2783	6225	1	72
H(20B)	6145	2311	6289	1	72
C(21)	6239(10)	2952(15)	7450(30)	1	76(11)
H(21A)	6378	3156	6943	1	91
H(21B)	6110	3220	7853	1	91
C(22)	6427(11)	2639(12)	8200(30)	1	69(11)
H(22A)	6519	2321	7818	1	83
H(22B)	6291	2498	8795	1	83
C(23)	6591(8)	3496(15)	9280(30)	1	66(10)
H(23A)	6430	3402	9824	1	99
H(23B)	6501	3750	8745	1	99
H23C()	6769	3670	9647	1	99
C(24)	6993(9)	3110(17)	7920(40)	1	80(12)
H(24A)	6928	3362	7336	1	120
H(24B)	7066	2767	7590	1	120
H24C()	7164	3276	8337	1	120

*U_{eq} is defined as one third of the trace of the orthogonalized U_{ij} tensor.

Table A7. Anisotropic displacement parameters ($Å^2x10^3$) for α-(DMEN)$PbBr_4$ at 293(2) K with estimated standard deviations in parentheses.

Label	U_{11}	U_{22}	U_{33}	U_{12}	U_{13}	U_{23}
Pb(1)	36(1)	30(1)	39(1)	0(1)	2(1)	0(1)
Pb(2)	55(1)	34(1)	41(1)	4(1)	16(1)	1(1)
Br(1)	76(2)	70(2)	109(2)	-9(2)	55(2)	-16(2)
Br(2)	89(2)	163(3)	73(2)	-18(2)	-44(2)	28(2)
Br(3)	106(2)	27(1)	137(2)	-6(1)	40(2)	-2(2)
Br(4)	60(1)	59(2)	63(2)	-7(1)	28(1)	-11(1)
Br(5)	52(1)	73(2)	77(2)	13(1)	-13(1)	-7(2)
Br(6)	117(2)	79(2)	118(2)	-41(2)	80(2)	-46(2)
Br(7)	79(2)	34(1)	65(2)	1(1)	-1(1)	2(1)
Br(8)	68(2)	57(2)	68(2)	-16(1)	6(1)	7(1)
N(1)	145(16)	139(16)	104(13)	-25(14)	10(13)	-19(12)
N(2)	180(30)	86(17)	140(20)	67(18)	-10(20)	-13(16)
C(1)	145(16)	139(16)	104(13)	-25(14)	10(13)	-19(12)
C(2)	145(16)	139(16)	104(13)	-25(14)	10(13)	-19(12)
N(3)	43(8)	56(10)	78(12)	9(7)	-7(7)	-7(9)
N(4)	70(11)	57(11)	80(14)	18(9)	11(9)	4(9)
C(5)	79(13)	52(12)	50(11)	10(10)	-18(10)	-10(9)
C(6)	90(15)	41(11)	63(13)	0(10)	9(11)	-10(9)
C(7)	200(30)	130(30)	90(20)	120(30)	20(20)	40(20)
C(8)	109(19)	100(20)	55(14)	25(16)	18(13)	6(13)

The anisotropic displacement factor exponent takes the form: $-2\pi^2[h^2a^{*2}U_{11} + ... + 2hka^*b^*U_{12}]$.

Table A8. Anisotropic displacement parameters ($Å^2x10^3$) for (DMAPA)$PbBr_4$ at 293(2) K with estimated standard deviations in parentheses.

Label	U_{11}	U_{22}	U_{33}	U_{12}	U_{13}	U_{23}
Pb(1)	31(1)	22(1)	22(1)	0(1)	11(1)	0(1)
Br(1)	36(1)	48(1)	54(1)	2(1)	19(1)	3(1)
Br(2)	52(1)	21(1)	40(1)	-1(1)	15(1)	1(1)
Br(3)	38(1)	50(1)	34(1)	-6(1)	12(1)	9(1)
Br(4)	46(1)	41(1)	25(1)	9(1)	18(1)	3(1)
N(1)	35(4)	54(3)	35(3)	-5(2)	5(3)	2(2)
N(2)	29(3)	33(2)	29(3)	2(2)	13(2)	3(2)
C(1)	54(6)	44(3)	39(4)	3(3)	2(4)	-10(3)
C(2)	35(4)	42(3)	52(4)	0(3)	9(3)	-14(3)
C(3)	36(4)	43(3)	36(3)	2(3)	8(3)	-11(3)
C(4)	42(5)	68(4)	47(4)	8(4)	10(4)	-29(4)
C(5)	29(4)	52(3)	44(4)	8(3)	8(3)	5(3)

The anisotropic displacement factor exponent takes the form: $-2\pi^2[h^2a^{*2}U_{11} + ... + 2hka^*b^*U_{12}]$.

Table A9. Anisotropic displacement parameters ($Å^2x10^3$) for (DMABA)$PbBr_4$ at 293(2) K with estimated standard deviations in parentheses.

Label	U_{11}	U_{22}	U_{33}	U_{12}	U_{13}	U_{23}
Pb(1)	43(1)	29(1)	28(1)	1(1)	1(1)	-2(1)
Pb(2)	40(1)	31(1)	28(1)	1(1)	1(1)	0(1)
Br(1)	48(2)	56(2)	42(2)	-4(2)	1(2)	-4(2)
Br(2)	60(2)	54(2)	30(2)	-12(2)	-3(2)	-3(2)
Br(3)	48(2)	62(2)	51(2)	-3(2)	1(2)	2(2)
Br(4)	78(3)	30(2)	61(2)	-2(2)	-3(2)	4(2)
Br(5)	44(2)	55(2)	66(2)	-6(2)	2(2)	-18(2)
Br(6)	66(2)	28(2)	72(3)	-2(2)	-5(3)	1(2)
Br(7)	90(3)	61(2)	27(2)	-14(2)	0(2)	-2(2)
Br(8)	51(2)	49(2)	57(2)	-2(2)	7(2)	1(2)
Pb(3)	43(1)	29(1)	28(1)	0(1)	-1(1)	-1(1)
Pb(4)	43(1)	31(1)	29(1)	0(1)	-2(1)	0(1)
Br(9)	84(4)	29(2)	59(4)	8(2)	0	0
Br(10)	43(2)	60(2)	71(2)	4(2)	2(2)	-18(2)
Br(11)	74(3)	46(2)	29(2)	7(2)	-2(2)	2(2)

Br(12)	42(2)	55(2)	47(2)	5(2)	4(2)	3(2)
Br(13)	69(2)	31(2)	73(2)	2(2)	2(3)	0(2)
Br(14)	75(3)	62(2)	27(2)	0(2)	-4(2)	3(2)
Br(15)	54(2)	52(2)	49(2)	-2(2)	-4(2)	7(2)
Br(16)	95(4)	37(2)	65(4)	-17(2)	0	0
Br(17)	48(2)	59(2)	55(2)	0(2)	2(2)	-7(2)
N(1)	60(20)	45(17)	100(30)	1(12)	20(20)	-2(14)
N(2)	90(30)	61(18)	70(20)	17(16)	-6(19)	-28(15)
C(1)	54(16)	260(40)	130(30)	-60(19)	24(15)	-90(20)
C(2)	54(16)	260(40)	130(30)	-60(19)	24(15)	-90(20)
C(3)	54(16)	260(40)	130(30)	-60(19)	24(15)	-90(20)
C(4)	54(16)	260(40)	130(30)	-60(19)	24(15)	-90(20)
C(5)	86(10)	71(8)	72(9)	11(6)	-4(7)	-17(7)
C(6)	86(10)	71(8)	72(9)	11(6)	-4(7)	-17(7)
N(3)	60(20)	33(13)	60(20)	-7(11)	7(16)	-10(11)
N(4)	80(20)	90(20)	33(15)	16(17)	8(15)	2(13)
C(7)	86(10)	71(8)	72(9)	11(6)	-4(7)	-17(7)
C(8)	86(10)	71(8)	72(9)	11(6)	-4(7)	-17(7)
C(9)	86(10)	71(8)	72(9)	11(6)	-4(7)	-17(7)
C(10)	86(10)	71(8)	72(9)	11(6)	-4(7)	-17(7)
C(11)	86(10)	71(8)	72(9)	11(6)	-4(7)	-17(7)
C(12)	86(10)	71(8)	72(9)	11(6)	-4(7)	-17(7)
N(5)	48(19)	51(15)	60(20)	8(12)	-21(15)	5(12)
N(6)	65(19)	29(12)	59(17)	-2(11)	-8(14)	-20(11)
C(13)	100(30)	29(13)	49(18)	10(14)	-21(18)	15(12)
C(14)	150(50)	70(20)	80(30)	50(20)	-40(30)	-50(20)
C(15)	50(20)	59(17)	55(19)	18(15)	-11(15)	-29(14)
C(16)	90(30)	41(15)	60(20)	-1(15)	18(18)	15(14)
C(17)	70(30)	160(40)	37(19)	10(30)	-8(19)	-50(20)
N(7)	50(20)	63(19)	60(20)	-10(12)	15(16)	-17(12)
N(8)	41(16)	58(15)	49(15)	9(12)	7(12)	-8(12)
C(19)	86(10)	71(8)	72(9)	11(6)	-4(7)	-17(7)
C(20)	50(20)	80(20)	44(18)	-40(17)	-3(15)	10(15)
C(21)	100(30)	80(20)	50(20)	30(20)	10(20)	-13(17)

C(22)	120(40)	35(15)	47(19)	7(17)	10(20)	6(13)
C(23)	50(20)	90(20)	60(20)	4(17)	-5(16)	-43(18)
C(24)	50(20)	110(30)	90(30)	10(20)	-10(20)	40(20)

The anisotropic displacement factor exponent takes the form: $-2\pi^2[h^2a^{*2}U_{11} + ... + 2hka^*b^*U_{12}]$.

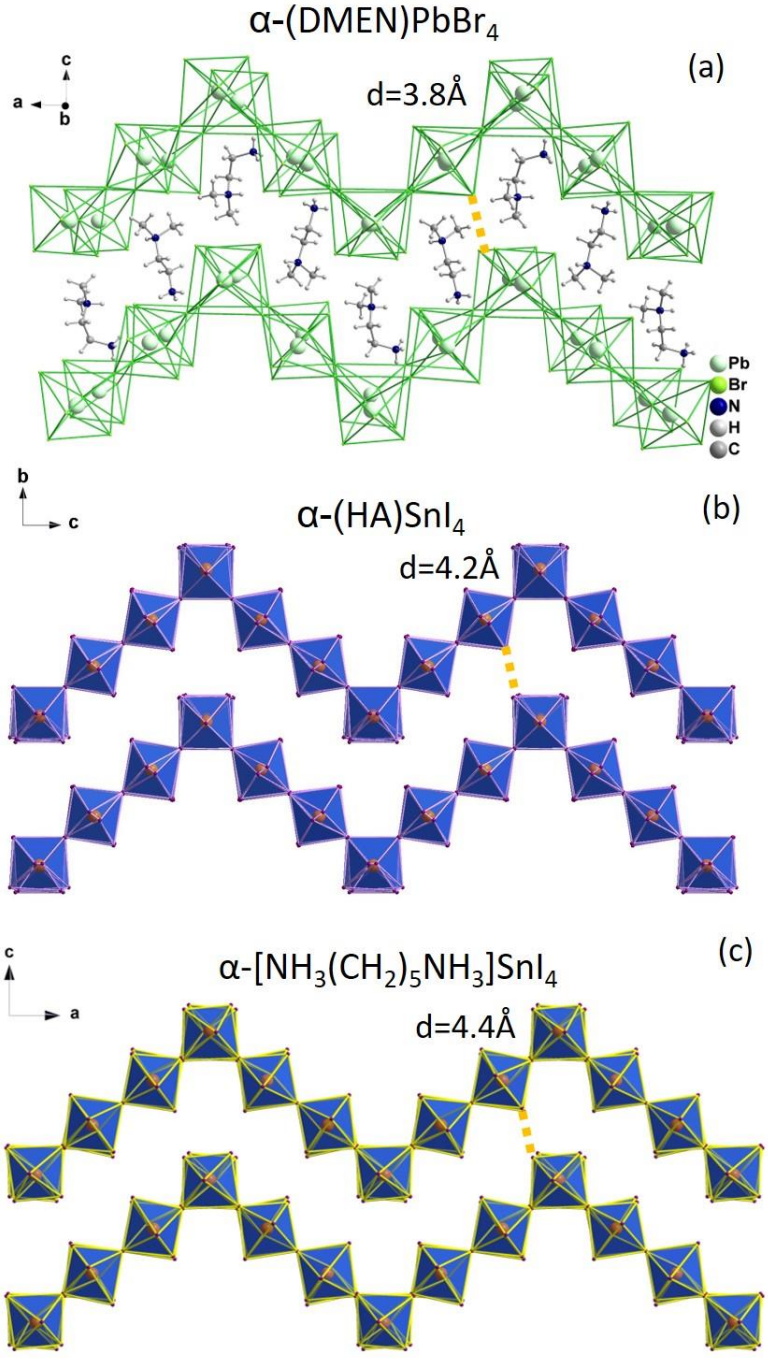

Figure A1. Crystal structures of α-(DMEN)$PbBr_4$, α-(HA)SnI_4[1] and α-[$NH_3(CH_2)_5NH_3$]SnI_4[2], showing the size-dependency of the cation that templates this unique class of structure. The distances labeled in the above figure roughly equal to √2 times bond length (e.g. Sn-I bond length: 3.1-3.2Å; Pb-Br bond length: 2.9Å; √2 × (3.1Å) = 4.3Å; √2 × (2.9Å) = 4Å).

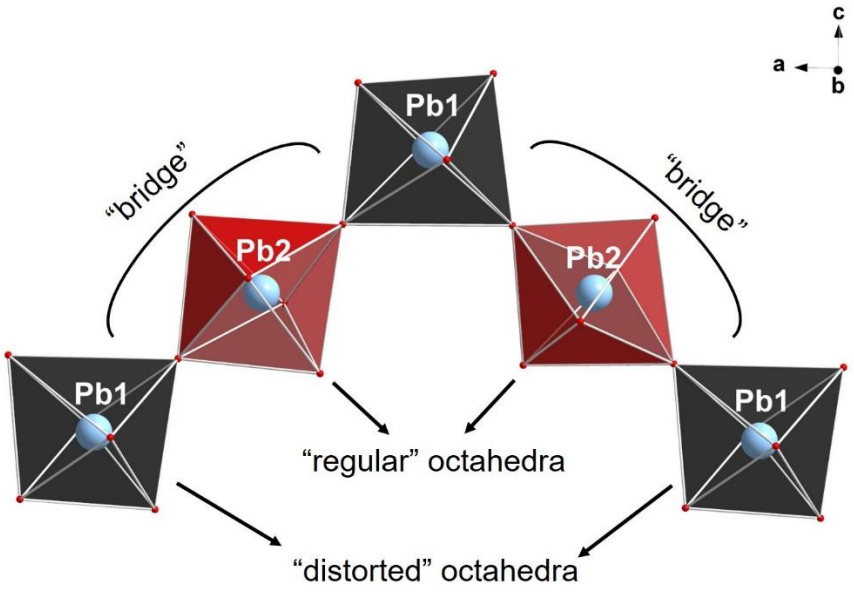

Figure A2. Crystallographically independent Pb composed octahedra in α-(DMEN)$PbBr_4$.

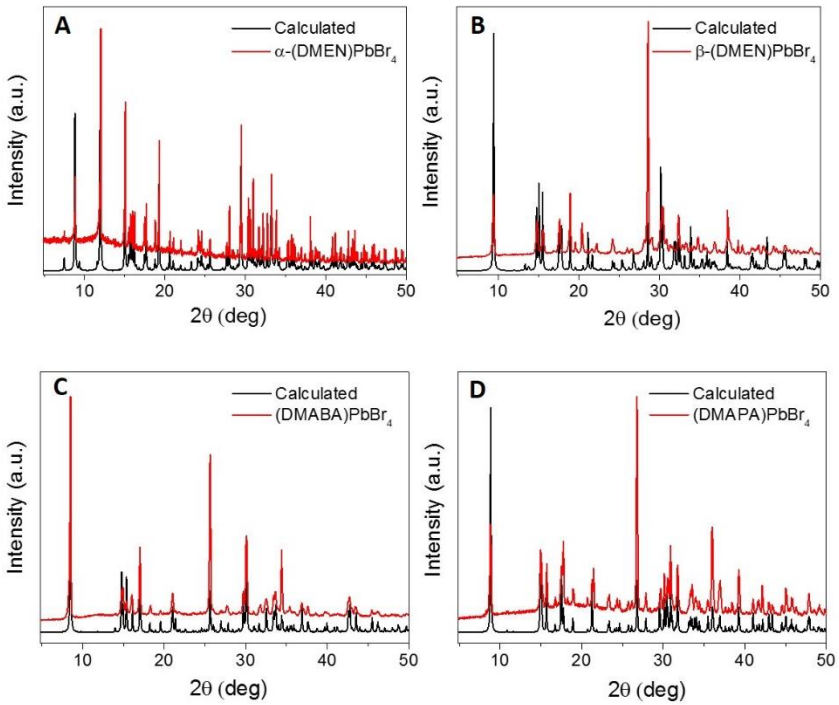

Figure A3. Calculated and experimental PXRD of (A) α-(DMEN)$PbBr_4$, (B) β-((DMEN)$PbBr_4$, (C) (DMABA)$PbBr_4$ and (D) (DMAPA)$PbBr_4$.

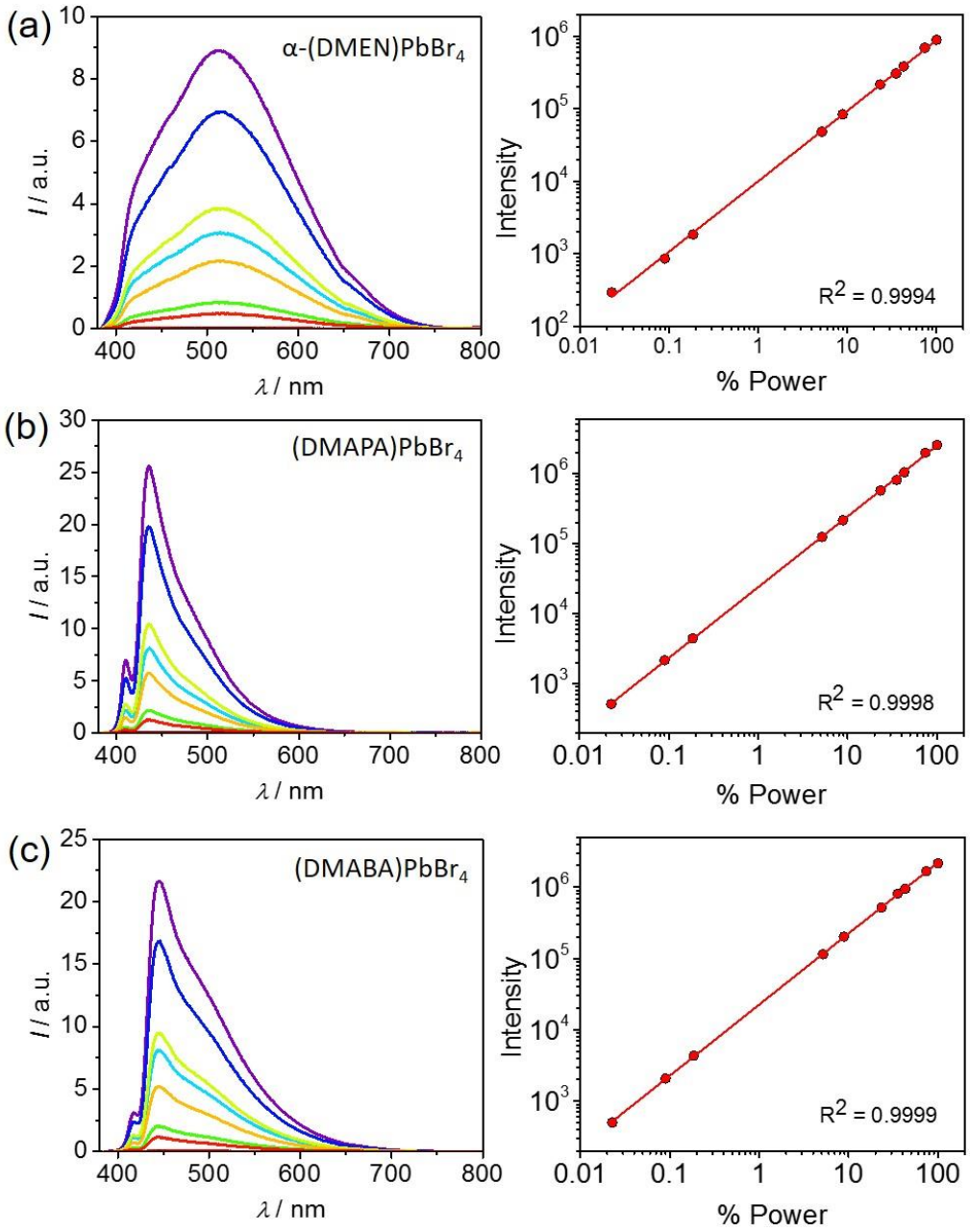

Figure A4. Power-dependent PL of (a) α-(DMEN)$PbBr_4$, (b) (DMABA)$PbBr_4$ and (c) (DMAPA)$PbBr_4$, exhibiting linear dependence on excitation power from 0.068-3mW/cm^2 (λ_{exc} = 370 nm).

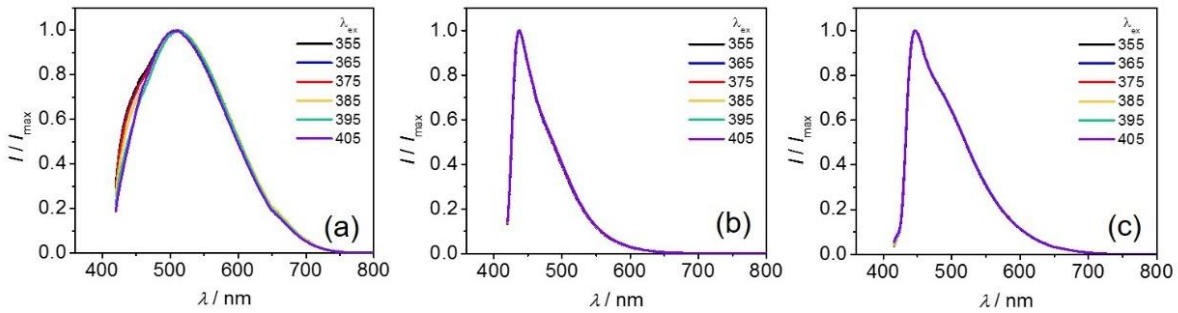

Figure A5. Wavelength-dependent PL (λ_{exc} = 355 to 405 nm) of (a) α-(DMEN)$PbBr_4$, (b) (DMABA)$PbBr_4$ and (c) (DMAPA)$PbBr_4$.

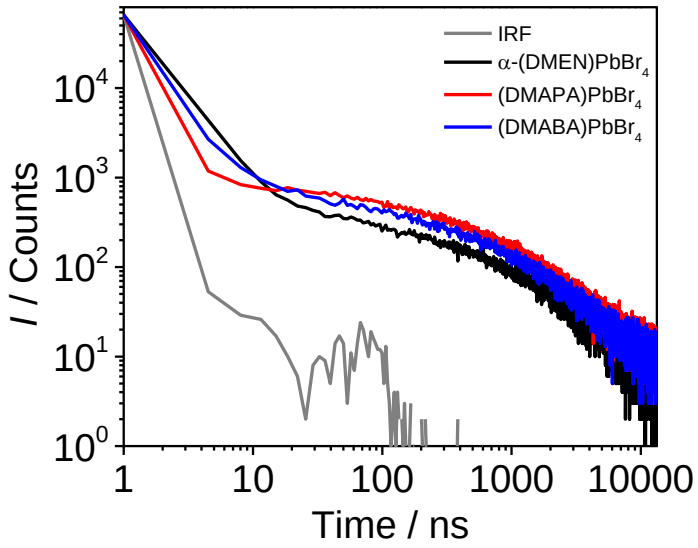

Figure A6. PL decay curves of α-(DMEN)$PbBr_4$, (DMABA)$PbBr_4$ and (DMAPA)$PbBr_4$.

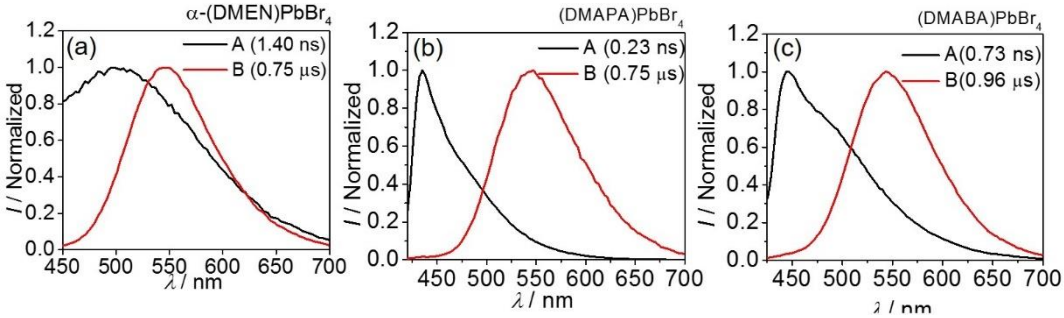

Figure A7. PL Spectra of the shorter wavelength emission A and the longer wavelength emission B for α-(DMEN)PbBr$_4$, (DMABA)PbBr$_4$ and (DMAPA)PbBr$_4$.

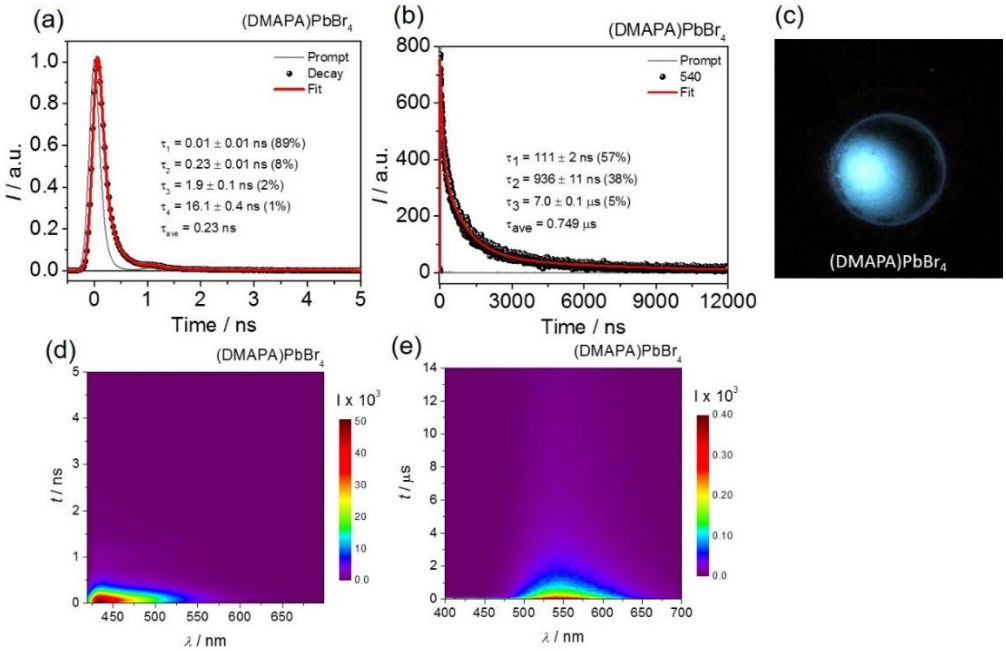

Figure A8. Time-resolved PL of (DMAPA)PbBr$_4$. Fittings of the (a) emission at lower wavelength (~ 430 nm) and (b) emission at higher wavelength (~ 550 nm). (c) Picture of blue light emitting polycrystalline sample of (DMAPA)PbBr$_4$ (λ_{exc} = 365 nm). Two-dimensional TRPL (c) and (d) show the much short-lived emission A within ns scale and long-lived emission B within μs scale.

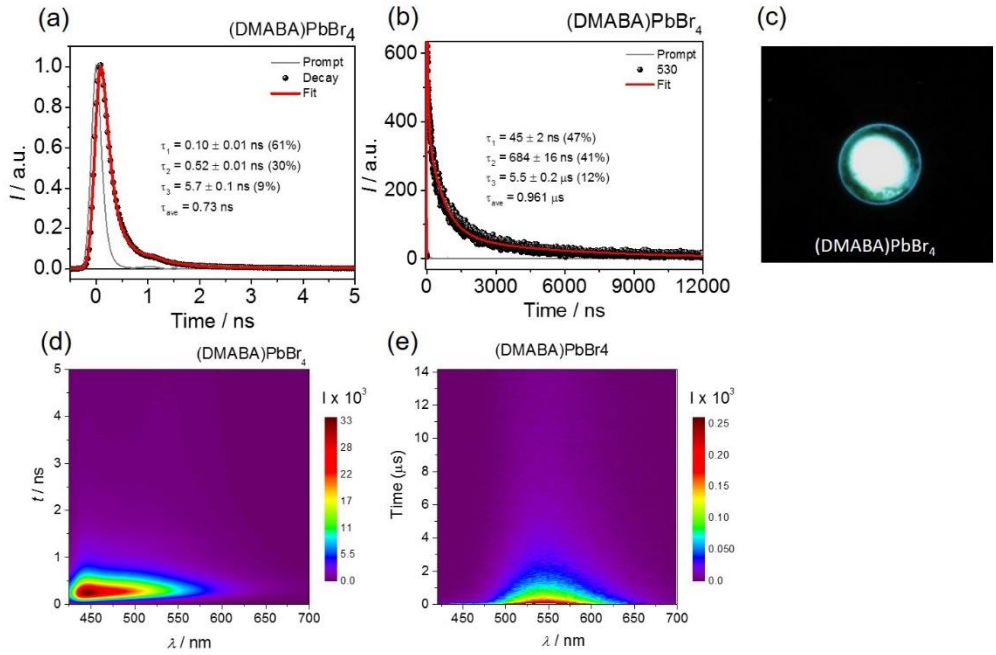

Figure A9. Time-resolved PL of (DMABA)$PbBr_4$. Fittings of the (a) emission at lower wavelength (~ 440 nm) and (b) emission at higher wavelength (~ 550 nm). (c) Picture of pale blue light emitting polycrystalline sample of (DMABA)$PbBr_4$ (λ_{exc} = 365 nm). Two-dimensional TRPL (c) and (d) show the much short-lived emission A within ns scale and long-lived emission B within μs scale.

Film samples were prepared by dissolving 0.5 mmol A in 1 ml dimethylformamide (DMF), then spin-coating the solution onto plain glass substrate at 2500 rpm for 20 s. Films of B were prepared in the same way. (A = α-(DMEN)$PbBr_4$, B = (N-MEDA)$[PbBr_4]^3$ (reference))

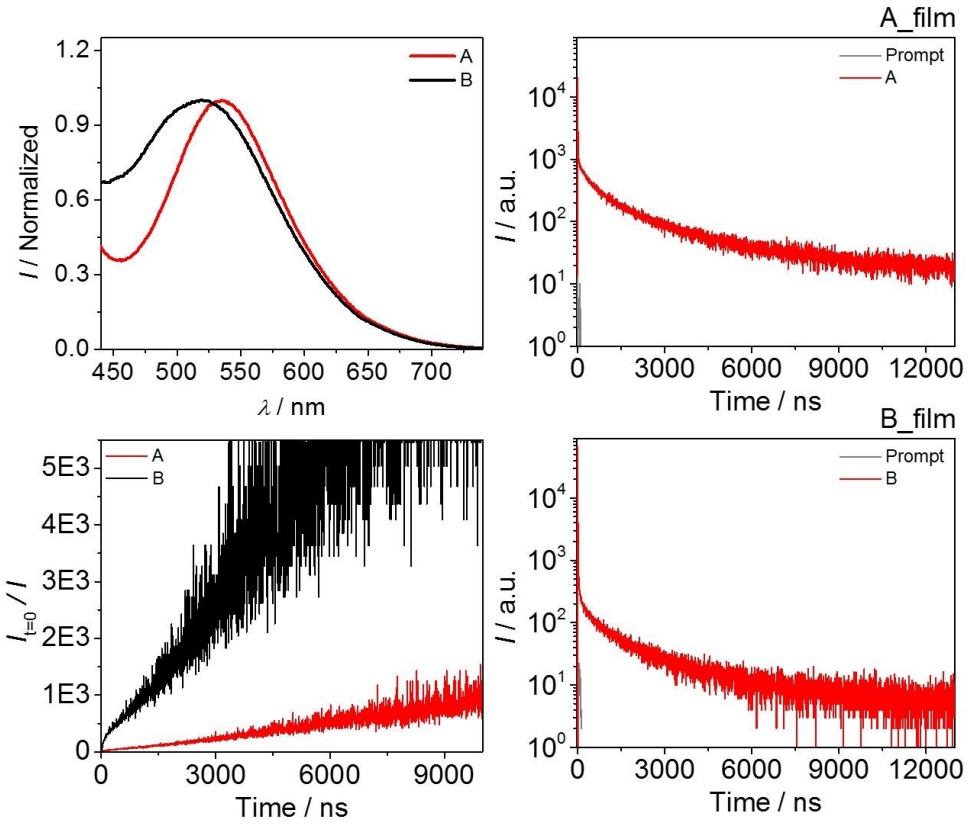

Figure A10. Steady state and time-resolved PL of Film A and B. A shows a longer lifetime than B, possibly due to the more corrugated crystal structure.

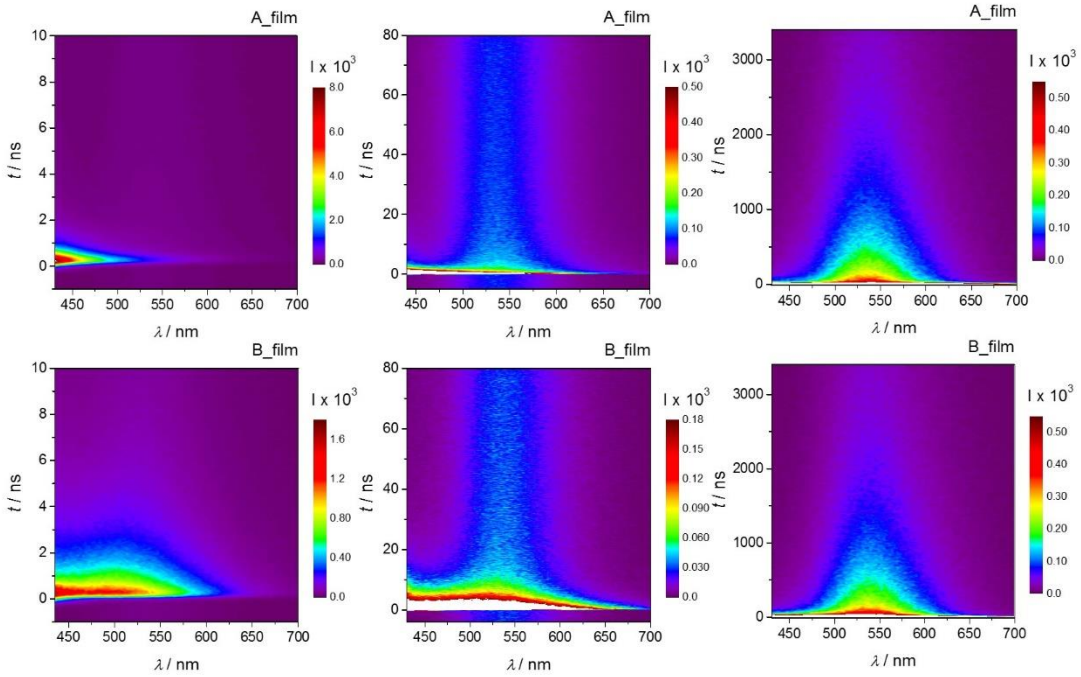

Figure A11. Two-dimensional TRPL of A and B. The emissions from band edge and self-trapped exciton (STE) states have a faster decay than the permanent defect states emission which is long-lasting.

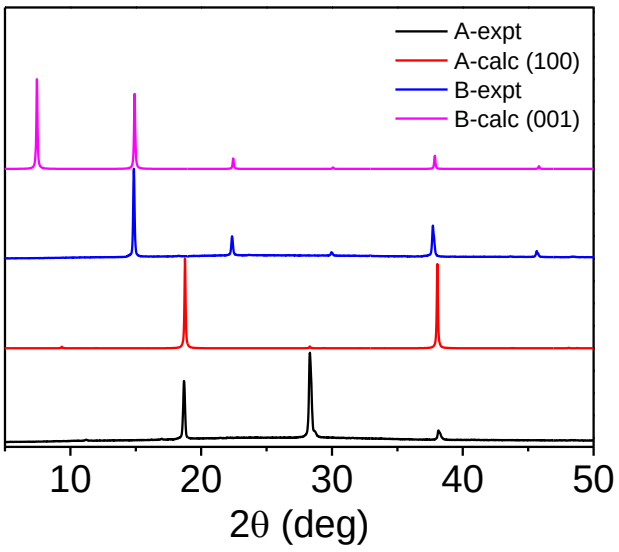

Figure A12. Experimental and calculated PXRD patterns of A and B. Because of strong preferred orientation in the films, we calculated the simulated patterns that have the (100) preferred orientation for A and (001) preferred orientation for B using the Mercury software.[4]

APPENDIX B

Supporting Information for Chapter 3

Table B1. Atomic coordinates ($x10^4$) and equivalent isotropic displacement parameters ($Å^2x10^3$) for $EA_4Pb_3Br_{10}$ at 293 K with estimated standard deviations in parentheses.

Label	x	y	z	Occupancy	U_{eq}*
Pb(1)	385(4)	0	0	1	58(2)
Pb(2)	499(3)	1357(1)	1(3)	1	45(1)
Br(1)	498(12)	642(1)	20(12)	1	85(3)
Br(2)	2435(8)	45(2)	2969(8)	1	65(2)
Br(3)	-1944(8)	1420(2)	-2340(8)	1	114(4)
Br(4)	2826(10)	1345(3)	2485(13)	1	164(6)
Br(5)	480(20)	1940(2)	-583(8)	1	147(5)
N(1)	500(60)	3201(5)	-400(40)	1	80(8)
C(2)	50(50)	2912(6)	260(30)	1	80(8)
C(1)	230(70)	2686(6)	-990(50)	1	80(8)
N(2)	940(40)	4287(7)	740(50)	1	75(8)
C(4)	-620(30)	4436(8)	1020(70)	1	75(8)
C(3)	-320(50)	4744(8)	1480(60)	1	75(8)
H(1n1)	-227.9	3326.65	-168.14	1	95.5
H(2n1)	1403.49	3255.4	-2.58	1	95.5
H(3n1)	588.07	3187.87	-1430.18	1	95.5
H(1c2)	731.94	2867.33	1144.33	1	95.5
H(2c2)	-1030.79	2917.67	618.13	1	95.5
H(1c1)	55.79	2498.63	-535.53	1	95.5
H(2c1)	-529.7	2718.9	-1819.7	1	95.5
H(3c1)	1283.63	2694.32	-1426.71	1	95.5
H(1n2)	769.41	4105.01	553.19	1	89.9
H(2n2)	1407.03	4364.52	-77.77	1	89.9
H(3n2)	1534.16	4305.81	1571.48	1	89.9
H(1c4)	-1241.9	4430.5	63.1	1	89.9
H(2c4)	-1181.77	4339.85	1853.75	1	89.9
H(1c3)	-1293.07	4828.62	1854.33	1	89.9
H(2c3)	461.02	4750.78	2302.24	1	89.9
H(3c3)	49.31	4849.59	571.96	1	89.9

*U_{eq} is defined as one third of the trace of the orthogonalized U_{ij} tensor.

Table B2. Atomic coordinates ($x10^4$) and equivalent isotropic displacement parameters ($Å^2x10^3$) for $EA_4Pb_3Cl_{10}$ at 293 K with estimated standard deviations in parentheses.

Label	x	y	z	Occupancy	U_{eq}*
Pb(1)	236(3)	5000	2615(3)	1	37(1)
Pb(2)	-43(3)	3657(1)	2509(2)	1	38(1)
Cl(1)	2290(30)	3694(4)	-60(30)	1	66(5)
Cl(2)	2380(30)	3518(4)	5030(20)	1	69(5)
Cl(3)	110(40)	4375(3)	2250(17)	1	85(6)
Cl(4)	2250(50)	5000	-393(18)	1	70(11)
Cl(5)	120(50)	3093(3)	1842(11)	1	101(9)
Cl(6)	3100(40)	5000	4340(20)	1	88(13)
N(1)	4940(120)	6821(8)	2190(60)	1	101(10)
C(1)	5200(80)	7142(7)	2540(70)	1	101(10)
C(2)	6610(90)	7171(16)	3750(60)	1	101(10)
N(2)	900(90)	4433(14)	-1570(60)	1	123(15)
C(3)	750(90)	4298(15)	-3260(50)	1	123(15)
C(4)	-620(100)	4075(16)	-3220(70)	1	123(15)
H(1n1)	5893.84	6730.66	2209.47	1	121.6
H(2n1)	4285.17	6746.31	2938.75	1	121.6
H(3n1)	4486.14	6800.73	1218.5	1	121.6
H(1c1)	4203.69	7223.04	3011.97	1	121.6
H(2c1)	5483.74	7241.65	1534.16	1	121.6
H(1c2)	6178.99	7155.93	4861.63	1	121.6
H(2c2)	7406	7018.09	3566.3	1	121.6
H(3c2)	7132.58	7359.16	3613.21	1	121.6
H(1n2)	1920.68	4490.33	-1410.76	1	147.7
H(2n2)	231.55	4582.6	-1498.42	1	147.7
H(3n2)	632.83	4302.87	-826.19	1	147.7
H(1c3)	1782.09	4203.26	-3545.17	1	147.7
H(2c3)	489.4	4448.31	-4053	1	147.7
H(1c4)	-1165.3	4069.58	-4283.38	1	147.7
H(2c4)	-165.52	3884.65	-2981.49	1	147.7
H(3c4)	-1416.58	4127.29	-2386.5	1	147.7

*U_{eq} is defined as one third of the trace of the orthogonalized U_{ij} tensor.

Table B3. Anisotropic displacement parameters ($Å^2x10^3$) for $EA_4Pb_3Br_{10}$ at 293 K with estimated standard deviations in parentheses.

Label	U_{11}	U_{22}	U_{33}	U_{12}	U_{13}	U_{23}
Pb(1)	45(2)	50(1)	78(2)	0	0	-10(2)
Pb(2)	33(2)	58(1)	43(2)	3(2)	2(1)	-5(2)
Br(1)	90(5)	52(2)	113(7)	5(5)	-25(5)	8(5)
Br(2)	72(3)	55(4)	69(4)	42(4)	9(2)	22(3)
Br(3)	23(3)	282(10)	36(4)	34(5)	-20(2)	-49(5)
Br(4)	66(7)	355(14)	70(7)	-75(8)	-43(4)	35(8)
Br(5)	330(15)	58(3)	54(3)	63(9)	-1(8)	1(3)

The anisotropic displacement factor exponent takes the form: $-2\pi^2[h^2a^{*2}U_{11} + ... + 2hka^*b^*U_{12}]$.

Table B4. Anisotropic displacement parameters ($Å^2x10^3$) for $EA_4Pb_3Cl_{10}$ at 293 K with estimated standard deviations in parentheses.

Label	U_{11}	U_{22}	U_{33}	U_{12}	U_{13}	U_{23}
Pb(1)	38(2)	36(1)	36(1)	0	3(2)	0
Pb(2)	38(1)	42(1)	34(1)	1(1)	0(2)	-2(1)
Cl(1)	29(11)	118(11)	52(5)	12(11)	18(7)	4(10)
Cl(2)	36(10)	124(12)	47(4)	-42(13)	-5(6)	-11(13)
Cl(3)	103(14)	59(7)	92(8)	-34(13)	-54(13)	25(7)
Cl(4)	100(30)	60(13)	47(13)	0	38(13)	0
Cl(5)	200(30)	43(6)	62(5)	-51(17)	6(15)	1(4)
Cl(6)	110(30)	110(20)	47(9)	0	23(12)	0

The anisotropic displacement factor exponent takes the form: $-2\pi^2[h^2a^{*2}U_{11} + ... + 2hka^*b^*U_{12}]$.

Table B5. Octahedral distortion angles β and δ for $EA_4Pb_3Cl_{10}$ and $EA_4Pb_3Br_{10}$ as defined in Figure B1.

	$EA_4Pb_3Br_{10}$		**$EA_4Pb_3Cl_{10}$**	
	β (°)	δ (°)	β (°)	δ (°)
Inner-layer	10	1	11	6
Outer-layer1	2	5	2	8
Outer-layer2	3	5	2	8

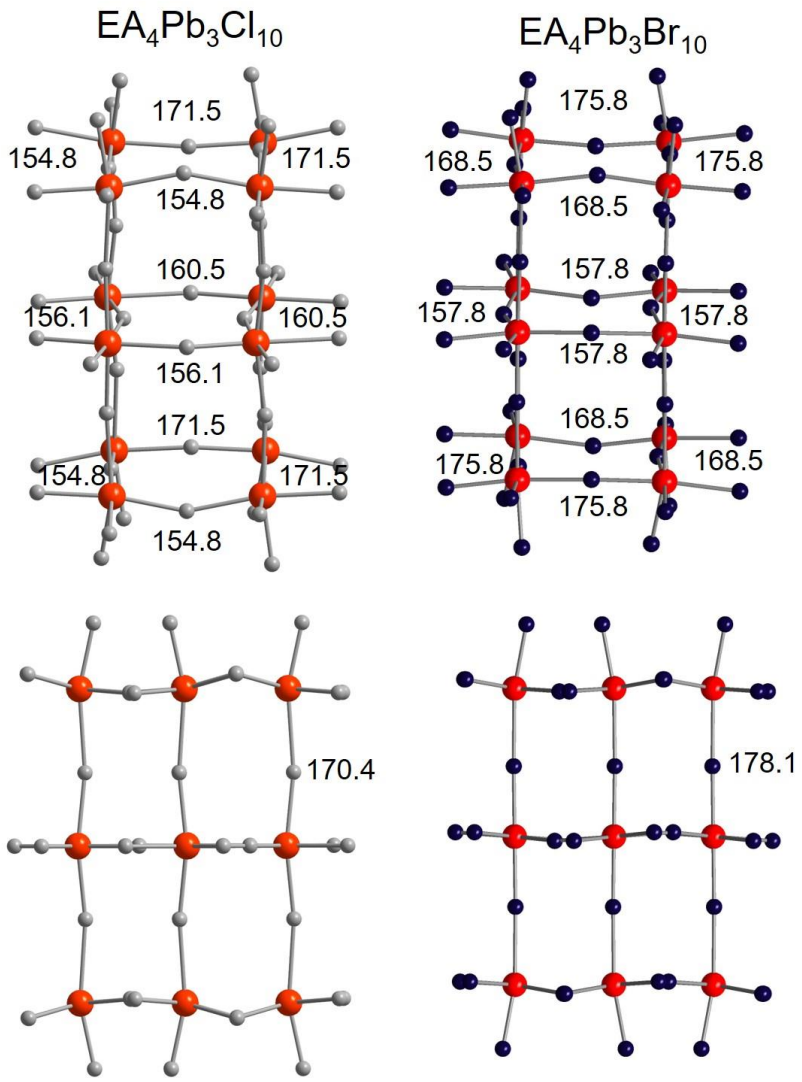

Figure B1. Labeled Pb-X-Pb angle (°) based on crystal structures of $EA_4Pb_3Cl_{10}$ and $EA_4Pb_3Br_{10}$. $EA_4Pb_3Cl_{10}$ have overall smaller Pb-X-Pb angles than $EA_4Pb_3Br_{10}$, suggesting larger distortion.

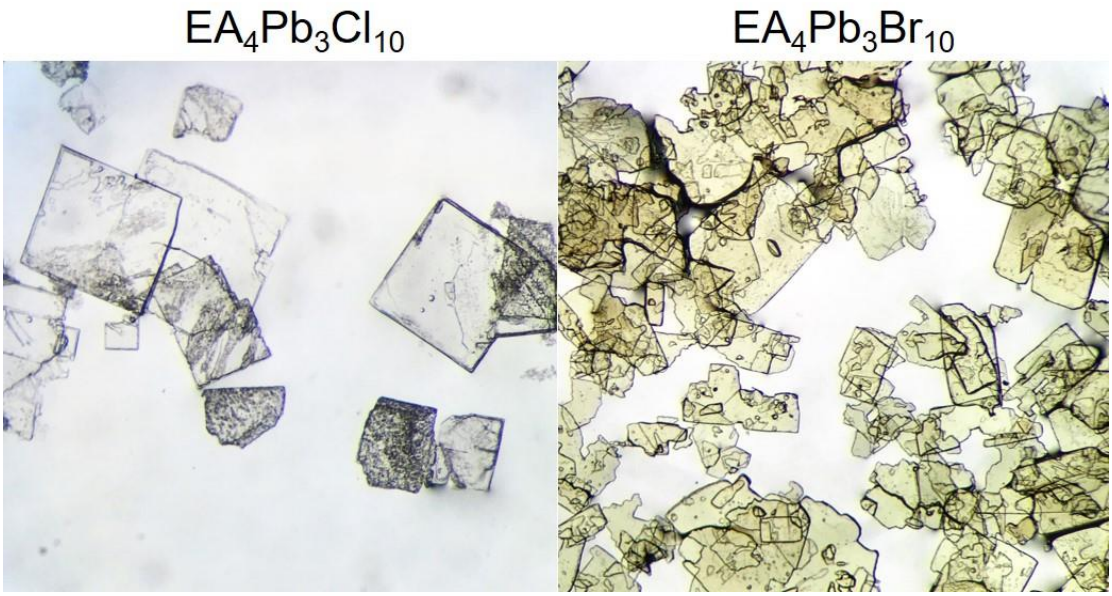

Figure B2. Optical microscope images of $EA_4Pb_3Cl_{10}$ and $EA_4Pb_3Br_{10}$ showing the plate-like morphology.

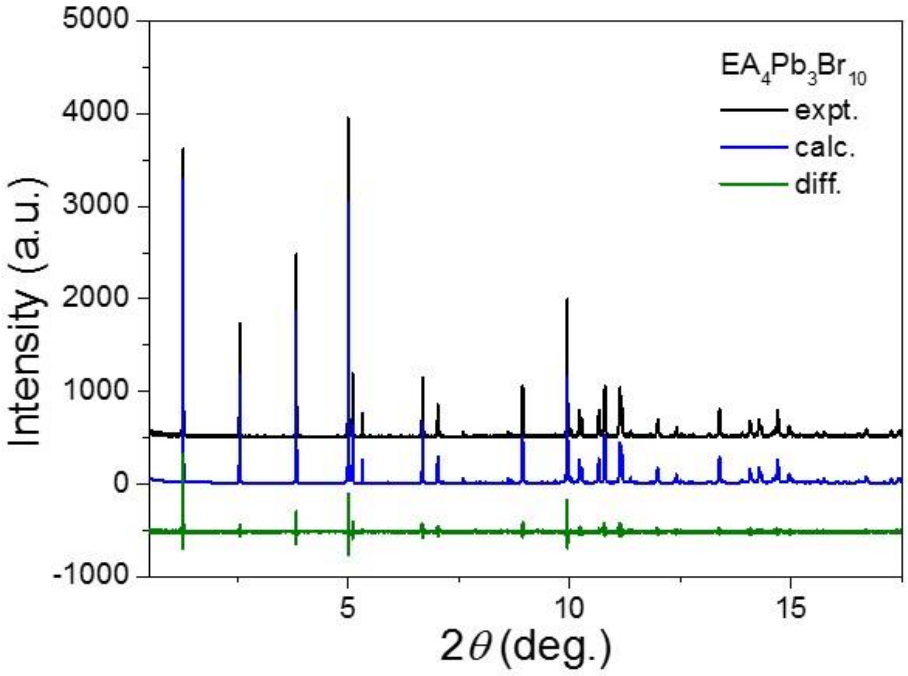

Figure B3. Refined and fitted high-resolution PXRD pattern of $EA_4Pb_3Br_{10}$ based on *C2cb* (identical to *Aba2).*

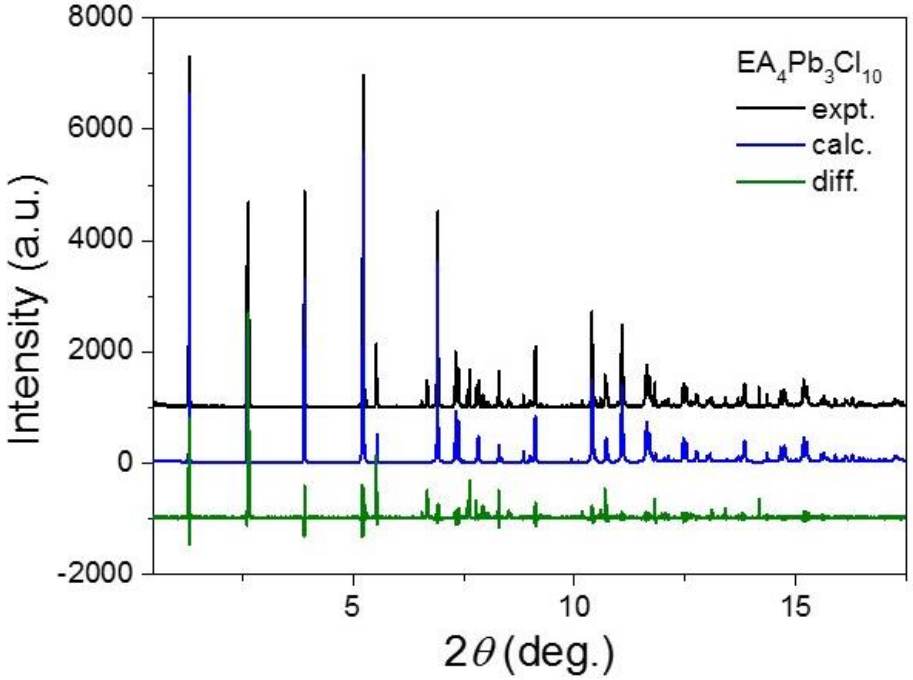

Figure B4. Refined and fitted high-resolution PXRD pattern of $EA_4Pb_3Cl_{10}$ based on $Cmc2_1$ (identical to $A2_1ma$).

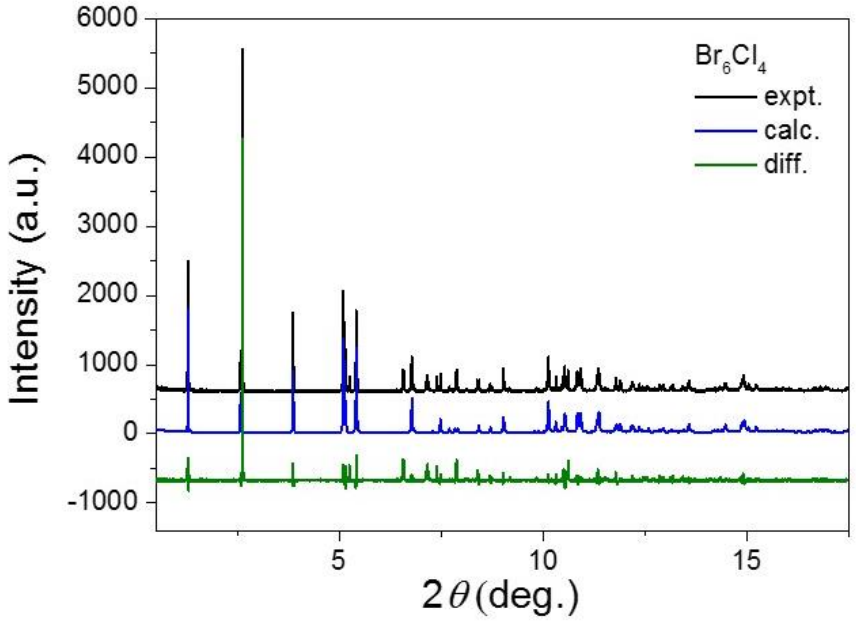

Figure B5. Refined and fitted high-resolution PXRD pattern of $EA_4Pb_3Br_6Cl_4$ based on *C2cb*.

The rest of the intermediates are refined and fitted in the same way.

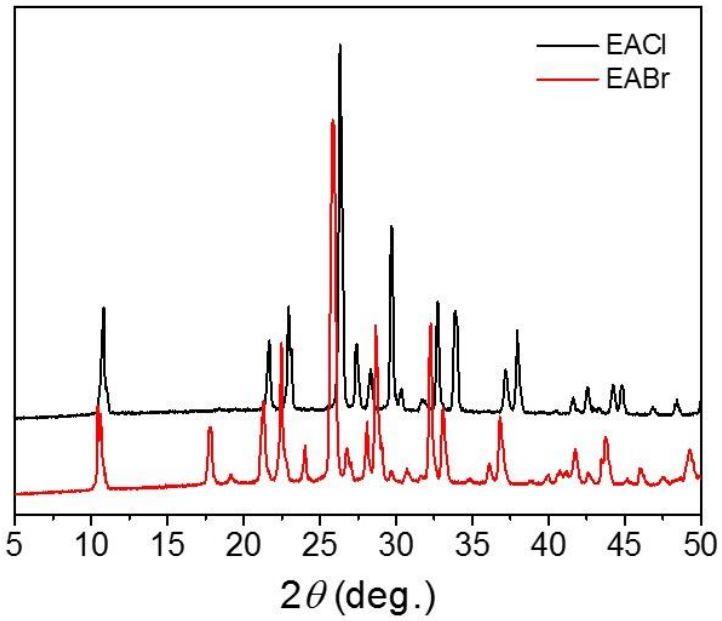

Figure B6. PXRD pattern of precursor EACl and EABr. EACl was synthesized by direct addition of ethylamine hydrochloride (4g, 49mmol) into HCl (20 ml) under stirring and heating at 150°C until solution became clear. Colorless crystals precipitated upon slow cooling to room temperature. EACl powder was obtained after vacuum filtration. EABr was synthesized the same way as decribed aboved.

Table B6. Synthetic ratio for $EA_4Pb_3Br_{10-x}Cl_x$ (x = 2, 4, 6, 8, 9.5) using solid-state grinding method.

Compound	EACl	EABr	$PbCl_2$	$PbBr_2$
x = 9.5	0.571g (7 mmol)	0.126g (1 mmol)	1.669g (6 mmol)	-
x = 8	0.652g (8 mmol)	-	1.112g (4 mmol)	0.734g (2 mmol)
x = 6	0.652g (8 mmol)	-	0.556g (2 mmol)	1.468g (4 mmol)
x = 4	-	1.008g (8 mmol)	1.112g (4 mmol)	0.734g (2 mmol)
x = 2	-	1.008g (8 mmol)	0.556g (2 mmol)	1.468g (4 mmol)

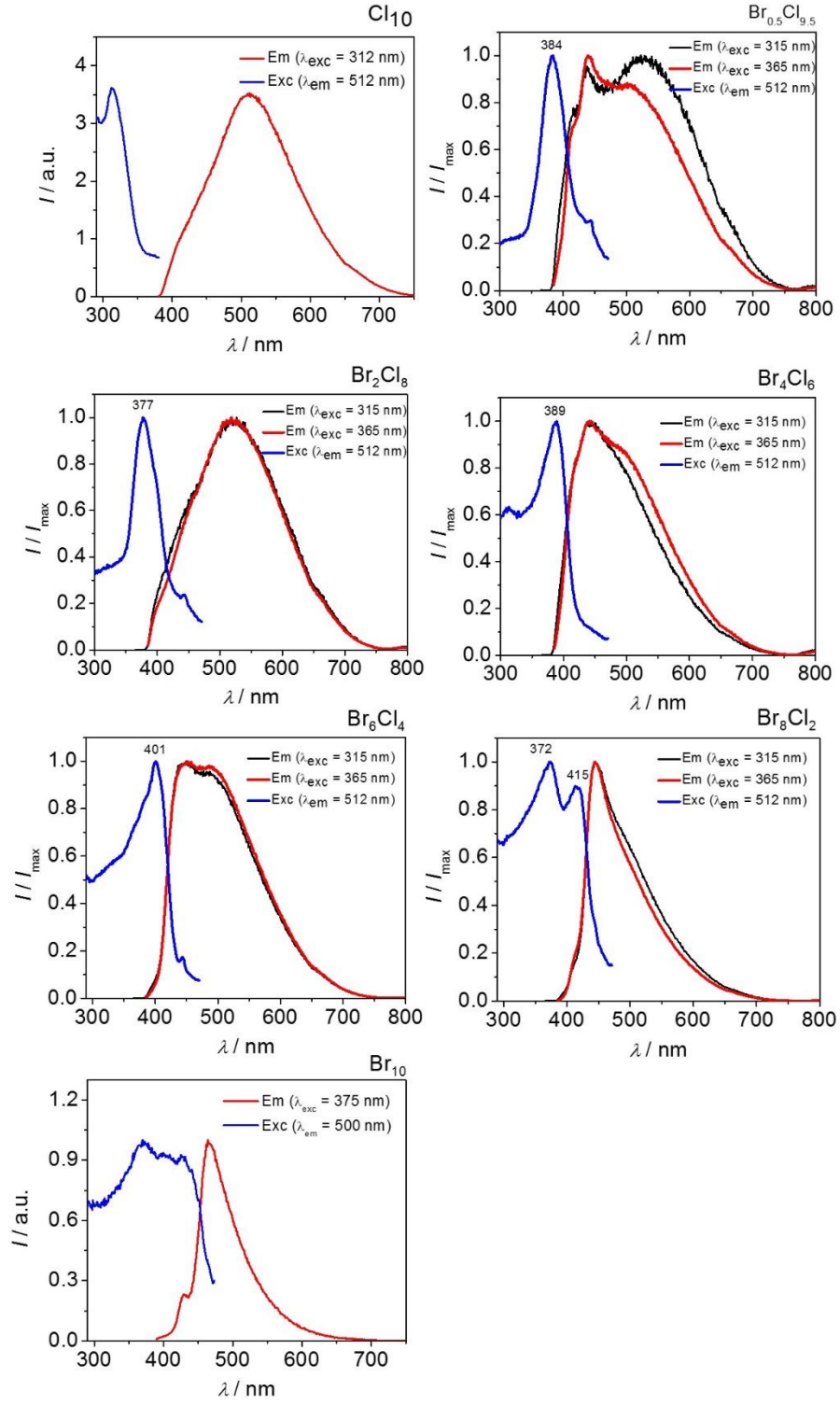

Figure B7. Excitation and emission spectra of $EA_4Pb_3Br_{10-x}Cl_x$ (x = 0, 2, 4, 6, 8, 9.5, 10).

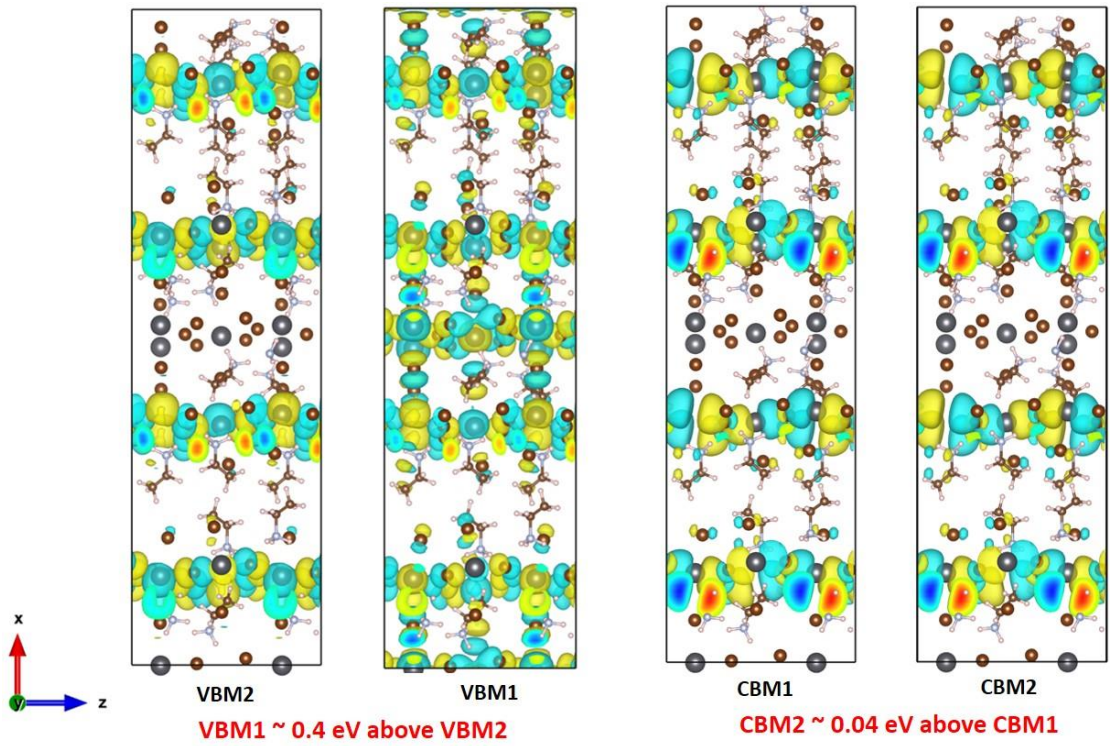

Figure B8. Γ-point wave functions of $EA_4Pb_3Br_{10}$ without spin-obit coupling (SOC). The VBM1 and VBM2 are composed of in-plane anti-bonding hybridization of 4p orbitals of Br and 6s of Pb, whereas the CBM1 and CBM2 are composed of in-plane bonding hybridization dominated by $6p_z$ orbitals of Pb. And for the CBM, wave functions are at the "outer-layers" only.

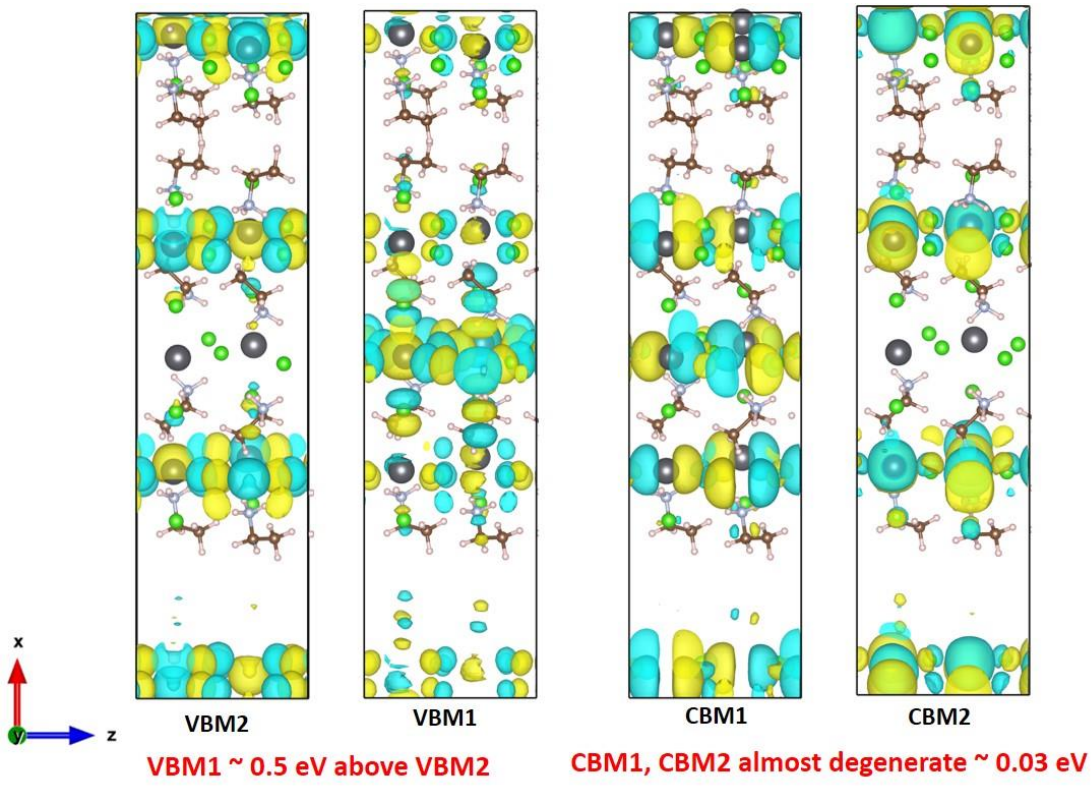

Figure B9. Γ-point wave functions of $EA_4Pb_3Cl_{10}$ without spin-obit coupling (SOC). The VBM1 and VBM2 are composed of in-plane anti-bonding hybridization of 3p orbitals of Cl and 6s of Pb, whereas the CBM1 and CBM2 are composed of in-plane bonding hybridization dominated by 6p orbitals of Pb. For the VBM1, wave functions are mainly on the "inner-layers" unlike $EA_4Pb_3Br_{10}$ and for VBM2 the wave functions are mainly on the "outer-layers" due to symmetry reasons.

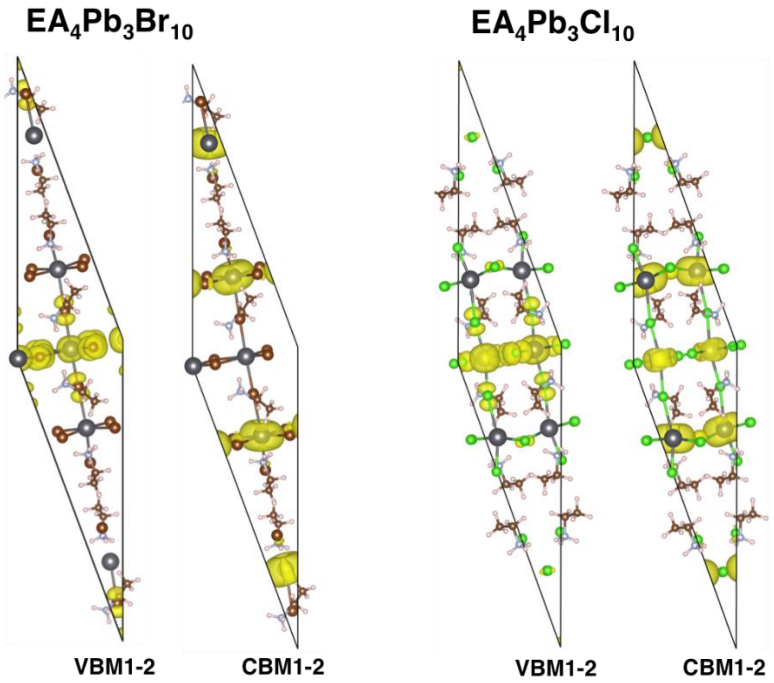

Figure B10. Local density of states integrated over VBM1-2 and CBM1-2 for $EA_4Pb_3Br_{10}$ and $EA_4Pb_3Cl_{10}$, computed with the revPBE functional including SOC.

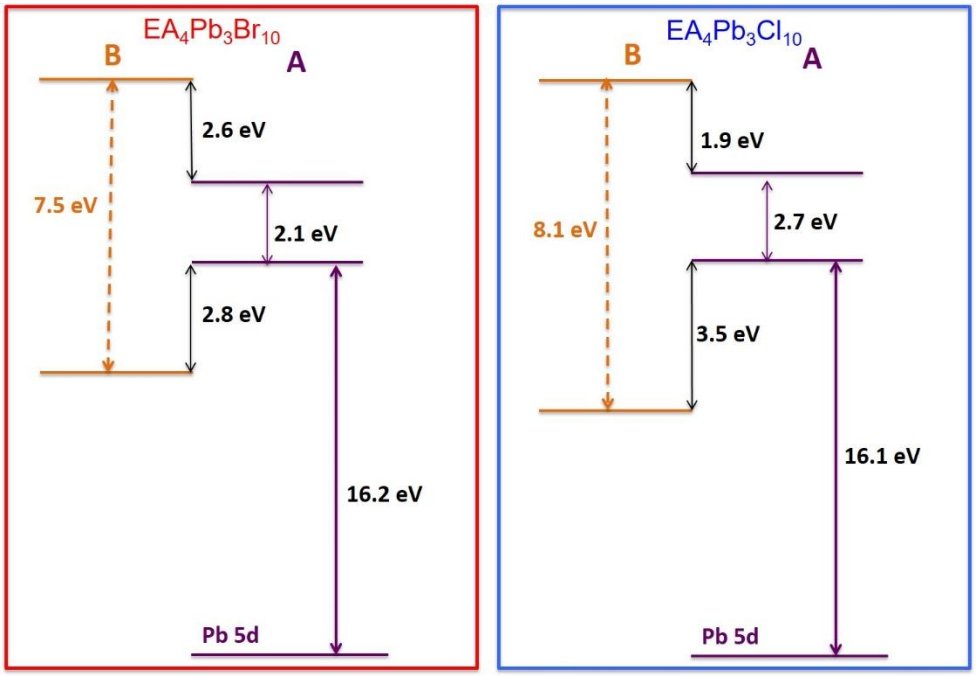

Figure B11. Band alignment between the organic and inorganic parts of $EA_4Pb_3Br_{10}$ and $EA_4Pb_3Cl_{10}$, computed using the VDW-C09 functional based on the method described in reference 1.[1]

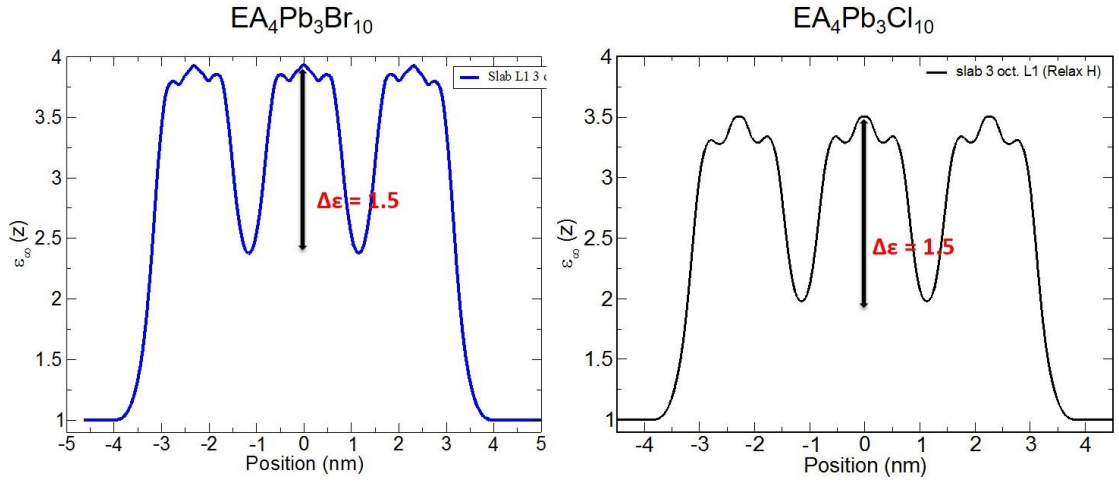

Figure B12. High frequency dielectric profile ε_∞ for $EA_4Pb_3Br_{10}$ (ε_∞ ~3.9) and $EA_4Pb_3Cl_{10}$ (ε_∞ ~3.5). Similar dielectric contrast in both materials; dielectric constants are systematically larger for Br compounds

Table B6. Effective masses, exciton binding energy and exciton Bohr radius of Cs_2PbB_4 and Cs_2PbCl_4 in the 3D and 2D limits. The values are averages of calculated effective masses along [100] and [010] directions.

			$\langle m_h \rangle$	**$\langle m_e \rangle$**	**$\langle a_{b3D} \rangle$ (Å)**	**$\langle E_{b3D} \rangle$ (meV)**	**$\langle a_{b2D} \rangle$ (Å)**	**$\langle E_{b2D} \rangle$ (meV)**
Cs_2PbBr_4	inner layer	β = 10°; δ = 1°	-0.069m_o	0.055m_o	67	28	34	110
	outer layer	β = 2°; δ = 5°	-0.060m_o	0.048m_o	78	24	39	95
	outer layer	β = 3°; δ = 5°	-0.060m_o	0.048m_o	77	24	39	96
Cs_2PbCl_4	inner layer	B = 11°; δ = 6°	-0.087m_o	0.077m_o	45	45	23	181
	outer layer	β = 2°; δ = 8°	-0.074m_o	0.065m_o	54	38	27	154
	outer layer	β = 1°; δ = 8°	-0.073m_o	0.065m_o	54	38	27	153

APPENDIX C

Supporting Information for Chapter 4

Table C1. Crystal Data and Structure Refinement for (hex)$PbBr_3$ and (hep)$PbBr_3$.

Compound	(hex)$PbBr_3$	(hep)$PbBr_3$
Empirical formula	$(C_6NH_{14})PbBr_3$	$(C_7NH_{16})PbBr_3$
Formula weight	547.10	561.13
Temperature	249.99 K	293(2) K
Wavelength	0.71073 Å	
Crystal system	Monoclinic	
Space group	$P2_1$	Cc
Unit cell dimensions	a = 7.9457(4) Å, b = 16.1647(9) Å, c = 37.860(2) Å, β = 89.999(1)°	a = 16.550(3) Å, b = 39.660(8) Å, c = 7.9623(16) Å, β = 90.00(3)°
Volume ($Å^3$)	4862.7(5)	5226.3(18)
Z	16	16
Density (g/cm^3)	2.9890	2.853
Absorption coefficient	23.692 mm^{-1}	22.045 mm^{-1}
F(000)	3904	4032
Crystal size (mm^3)	0.656 x 0.125 x 0.059	0.0143 x 0.0194 x 0.0293
θ range for data collection	1.08 to 27.47°	1.972 to 24.985°
Index ranges	-10<=h<=10, -20<=k<=20, -48<=l<=49	-19<=h<=19, -47<=k<=47, -9<=l<=9
Reflections collected	44028	15674
Independent reflections	21686 [R_{int} = 0.0401]	8230 [R_{int} = 0.0756]
Completeness to θ = 25.242°	99.9%	85.5%
Refinement method	Full-matrix least-squares on F^2	
Data / restraints / parameters	21686 / 42 / 465	8230 / 37 / 248
Goodness-of-fit	1.0104	1.044
Final R indices [I > 2σ(I)]	R_{obs} = 0.0500, wR_{obs} = 0.1378	R_{obs} = 0.0921, wR_{obs} = 0.2670
R indices [all data]	R_{all} = 0.1117, wR_{all} = 0.1639	R_{all} = 0.1588, wR_{all} = 0.3147
Largest diff. peak and hole	2.159 and -2.275 e·$Å^{-3}$	3.313 and -2.537 e·$Å^{-3}$

[1] $R = \Sigma||F_o|-|F_c|| / \Sigma|F_o|$, $wR = \{\Sigma[w(|F_o|^2 - |F_c|^2)^2] / \Sigma[w(|F_o|^4)]\}^{1/2}$ and $w=1/[\sigma^2(Fo^2)+(0.0550P)^2+21.2640P]$ where $P=(Fo^2+2Fc^2)/3$

[2] $R = \Sigma||F_o|-|F_c|| / \Sigma|F_o|$, $wR = \{\Sigma[w(|F_o|^2 - |F_c|^2)^2] / \Sigma[w(|F_o|^4)]\}^{1/2}$ and $w=1/[\sigma^2(Fo^2)+(0.1750P)^2]$ where $P=(Fo^2+2Fc^2)/3$

Table C2. Crystal Data and Structure Refinement for (4amp)$PbBr_4$ and (epz)$PbBr_4$.

Compound	(4amp)$PbBr_4$	(epz)$PbBr_4$
Empirical formula	$(C_6N_2H_{16})PbBr_4$	$(C_6N_2H_{16})PbBr_4$
Formula weight	643.04	643.04
Temperature	293(2) K	
Wavelength	0.71073 Å	
Crystal system	Orthorhombic	Monoclinic
Space group	*Pca*2_1	*Pc*
Unit cell dimensions	a = 17.745(4) Å, b = 10.235(2) Å, c = 7.8299(16) Å,	a = 10.536(2) Å, b = 12.415(2) Å, c = 16.430(3) Å, β = 96.77(3)°
Volume	1422.1(5) $Å^3$	2134.2(8) $Å^3$
Z	4	6
Density (g/cm^3)	2.992	2.983
Absorption coefficient	22.986 mm^{-1}	23.11 mm^{-1}
F(000)	1152	1704
Crystal size (mm^3)	0.0435 x 0.0347 x 0.0141	0.0911 x 0.0549 x 0.0196
θ range for data collection	1.990 to 29.254°	2.733 to 29.206°
Index ranges	-23<=h<=24, -14<=k<=14, -10<=l<=10	-13<=h<=14, -16<=k<=16, -22<=l<=22
Reflections collected	12316	20074
Independent reflections	3840 [R_{int} = 0.0417]	10816 [R_{int} = 0.0876]
Completeness to θ = 26.000°	99.7%	99.9%
Refinement method	Full-matrix least-squares on F^2	
Data / restraints / parameters	3840 / 1 / 122	10816 / 29 / 216
Goodness-of-fit	1.060	0.862
Final R indices [I > 2σ(I)]	R_{obs} = 0.0452, wR_{obs} = 0.1156	R_{obs} = 0.0575, wR_{obs} = 0.1332
R indices [all data]	R_{all} = 0.0559, wR_{all} = 0.1284	R_{all} = 0.1370, wR_{all} = 0.1807
Largest diff. peak and hole	1.636 and -1.850 e·$Å^{-3}$	1.694 and -1.681 e·$Å^{-3}$

[1] $R = \Sigma||F_o|-|F_c|| / \Sigma|F_o|$, $wR = \{\Sigma[w(|F_o|^2 - |F_c|^2)^2] / \Sigma[w(|F_o|^4)]\}^{1/2}$ and $w=1/[\sigma^2(Fo^2)+(0.0790P)^2+2.6940P]$ where $P=(Fo^2+2Fc^2)/3$

[2] $R = \Sigma||F_o|-|F_c|| / \Sigma|F_o|$, $wR = \{\Sigma[w(|F_o|^2 - |F_c|^2)^2] / \Sigma[w(|F_o|^4)]\}^{1/2}$ and $w=1/[\sigma^2(Fo^2)+(0.0870P)^2]$ where $P=(Fo^2+2Fc^2)/3$

Table C3. Crystal Data and Structure Refinement for (hmp)$PbBr_4$ and $(mpz)_2Pb_3Br_{10}$.

Compound	(hmp)$PbBr_4$	$(mpz)_2Pb_3Br_{10}$
Empirical formula	$(C_5N_2H_{14})PbBr_4$	$(C_5N_2H_{14})_2Pb_3Br_{10}$
Formula weight	629.01	1625.03
Temperature	293(2) K	
Wavelength	0.71073 Å	
Crystal system	Monoclinic	
Space group	*C2/m*	*C2/c*
Unit cell dimensions	a = 28.452(6) Å, b = 12.218(2) Å, c = 15.839(3) Å, β = 104.93(3)°	a = 45.062(9) Å, b = 9.5432(19) Å, c = 15.205(3) Å, β = 97.92(3)°
Volume	5320(2) $Å^3$	6476(2) $Å^3$
Z	16	8
Density (g/cm^3)	3.141	3.333
Absorption coefficient	24.663 mm^{-1}	27.906 mm^{-1}
F(000)	4480	5696
Crystal size (mm^3)	0.1314 x 0.0453 x 0.0159	0.1626 x 0.0824 x 0.0236
θ range for data collection	1.824 to 29.320°	1.825 to 29.205°
Index ranges	-38<=h<=38, -16<=k<=16, -21<=l<=21	-59<=h<=61, -13<=k<=13, -18<=l<=20
Reflections collected	24005	24781
Independent reflections	7529 [R_{int} = 0.0744]	8706 [R_{int} = 0.0820]
Completeness to θ = 26.000°	99.9%	99.6%
Refinement method	Full-matrix least-squares on F^2	
Data / restraints / parameters	7529 / 0 / 242	8706 / 0 / 248
Goodness-of-fit	1.053	1.030
Final R indices [I > 2σ(I)]	R_{obs} = 0.0566, wR_{obs} = 0.1289	R_{obs} = 0.0662, wR_{obs} = 0.1497
R indices [all data]	R_{all} = 0.0914, wR_{all} = 0.1467	R_{all} = 0.1231, wR_{all} = 0.1736
Largest diff. peak and hole	2.636 and -1.990 e·$Å^{-3}$	5.254 and -1.680 e·$Å^{-3}$

[1] $R = \Sigma||F_o|-|F_c|| / \Sigma|F_o|$, $wR = \{\Sigma[w(|F_o|^2 - |F_c|^2)^2] / \Sigma[w(|F_o|^4)]\}^{1/2}$ and $w=1/[\sigma^2(Fo^2)+(0.0690P)^2+36.8830P]$ where $P=(Fo^2+2Fc^2)/3$

[2] $R = \Sigma||F_o|-|F_c|| / \Sigma|F_o|$, $wR = \{\Sigma[w(|F_o|^2 - |F_c|^2)^2] / \Sigma[w(|F_o|^4)]\}^{1/2}$ and $w=1/[\sigma^2(Fo^2)+(0.0800P)^2]$ where $P=(Fo^2+2Fc^2)/3$

Table C4. Crystal Data and Structure Refinement for $(2,6\text{-dmpz})_3Pb_2Br_{10}$.

Compound	$(2,6\text{-dmpz})_3Pb_2Br_{10}$
Empirical formula	$(C_5N_2H_{14})_3Pb_2Br_{10}$
Formula weight	1562.10
Temperature	249.96 K
Wavelength	0.71073 Å
Crystal system	Triclinic
Space group	P-1
Unit cell dimensions	a = 6.2455(4) Å, α = 73.597(3)° b = 16.8901(10) Å, β = 84.960(3)° c = 20.1013(11) Å, γ = 88.793(3)°
Volume	2026.2(2) $Å^3$
Z	2
Density (calculated)	2.560 g/cm^3
Absorption coefficient	18.177 mm^{-1}
F(000)	1424
Crystal size	0.185 x 0.067 x 0.033 mm^3
θ range for data collection	1.257 to 28.432°
Index ranges	-8<=h<=8, -22<=k<=22, -26<=l<=26
Reflections collected	31554
Independent reflections	10015 [R_{int} = 0.0381]
Completeness to θ = 26.000°	98.6%
Refinement method	Full-matrix least-squares on F^2
Data / restraints / parameters	10015 / 0 / 331
Goodness-of-fit	0.971
Final R indices [I > 2σ(I)]	R_{obs} = 0.0315, wR_{obs} = 0.0847
R indices [all data]	R_{all} = 0.0441, wR_{all} = 0.0951
Largest diff. peak and hole	1.639 and -1.844 e·$Å^{-3}$

$R = \Sigma||F_o|-|F_c|| / \Sigma|F_o|$, $wR = \{\Sigma[w(|F_o|^2 - |F_c|^2)^2] / \Sigma[w(|F_o|^4)]\}^{1/2}$ and $w=1/[\sigma^2(Fo^2)+(0.0570P)^2+4.4410P]$ where $P=(Fo^2+2Fc^2)/3$

Table C5. Atomic coordinates ($x10^4$) and equivalent isotropic displacement parameters ($Å^2x10^3$) for (hex)$PbBr_3$ at 249.99 K with estimated standard deviations in parentheses.

Label	x	y	z	Occupancy	U_{eq}^*
Pb(01)	-4739(1)	18(1)	-5026(1)	1.000000	24(1)
Pb(02)	259(1)	21(1)	-4975(1)	1.000000	24(1)
Pb(03)	-4735(2)	2476(1)	-2526(1)	1.000000	27(1)
Pb(04)	263(2)	2481(1)	-2474(1)	1.000000	28(1)
Pb(05)	-4964(2)	-1(1)	-2(1)	1.000000	60(1)
Pb(06)	42(2)	1(1)	3(1)	1.000000	63(1)
Pb(07)	260(2)	2477(1)	2527(1)	1.000000	29(1)
Pb(08)	-4740(2)	2476(1)	2472(1)	1.000000	31(1)
Br(09)	-2762(3)	18(1)	-4390(1)	1.000000	36(1)
Br(0A)	-2018(4)	1290(1)	-5256(1)	1.000000	41(1)
Br(0B)	2228(3)	23(1)	-5613(1)	1.000000	37(1)
Br(0C)	-2771(3)	2450(1)	3112(1)	1.000000	40(1)
Br(0D)	2248(3)	2458(1)	1891(1)	1.000000	42(1)
Br(0E)	-7002(4)	1293(1)	-4746(1)	1.000000	42(1)
Br(0F)	-2014(4)	3750(1)	-2754(1)	1.000000	46(1)
Br(0G)	-7017(4)	1205(1)	-2239(1)	1.000000	48(1)
Br(0H)	-7029(4)	-1263(1)	-4747(1)	1.000000	48(1)
Br(0I)	-7019(4)	3765(1)	-2256(1)	1.000000	48(1)
Br(0J)	2453(5)	-14(1)	-616(1)	1.000000	75(2)
Br(0K)	-2014(4)	1202(1)	-2756(1)	1.000000	48(1)
Br(0L)	-2007(4)	-1269(1)	-5247(1)	1.000000	51(1)
Br(0M)	-2539(5)	-6(1)	610(1)	1.000000	72(1)
Br(0N)	-2400(8)	1281(1)	-253(2)	1.000000	124(2)
Br(0O)	-2746(3)	2453(1)	-1886(1)	1.000000	40(1)
Br(0P)	2252(3)	2445(1)	-3112(1)	1.000000	37(1)
Br(0Q)	-7022(4)	1197(1)	2758(1)	1.000000	48(1)
Br(0R)	-7407(8)	1271(1)	258(2)	1.000000	119(2)
Br(0S)	-2026(4)	3754(1)	2250(1)	1.000000	51(1)
Br(0T)	-7386(8)	-1274(1)	256(2)	1.000000	134(2)
Br(0U)	-2397(8)	-1278(1)	-251(2)	1.000000	128(2)
Br(0V)	-7002(4)	3749(1)	2750(1)	1.000000	52(1)

Br(0W)	-2009(4)	1198(1)	2241(1)	1.000000	50(1)
N(5)	-2917(19)	190(7)	-1982(4)	1.000000	51(5)
H(5a)	-3237(19)	730(7)	-1970(4)	1.000000	61(6)
H(5b)	-2947(19)	43(7)	-2214(4)	1.000000	61(6)
C(21)	-6250(30)	-9(11)	1916(8)	1.000000	73(8)
H(21a)	-5570(30)	329(11)	2078(8)	1.000000	87(9)
H(21b)	-6070(30)	-587(11)	1984(8)	1.000000	87(9)
N(4)	-8040(20)	190(7)	1983(5)	1.000000	48(4)
H(4a)	-8250(20)	143(7)	2219(5)	1.000000	57(5)
H(4b)	-8230(20)	725(7)	1921(5)	1.000000	57(5)
N(8)	-7990(18)	197(7)	-3021(4)	1.000000	48(4)
H(8a)	-8116(18)	104(7)	-2785(4)	1.000000	58(5)
H(8b)	-8265(18)	736(7)	-3060(4)	1.000000	58(5)
C(53)	-1130(30)	-2309(11)	-4419(7)	1.000000	76(8)
N(2)	-2880(20)	153(8)	3008(5)	1.000000	60(5)
H(2a)	-3200(20)	694(8)	3008(5)	1.000000	71(6)
H(2b)	-2880(20)	-19(8)	2779(5)	1.000000	71(6)
N(1)	-6100(30)	-2391(9)	4357(7)	1.000000	108(6)
H(1a)	-5500(30)	-1981(9)	4463(7)	1.000000	130(7)
H(1b)	-5740(30)	-2868(9)	4460(7)	1.000000	130(7)
C(39)	-1100(20)	143(10)	-1863(6)	1.000000	61(6)
H(39a)	-660(20)	-376(10)	-1960(6)	1.000000	74(8)
H(39b)	-510(20)	588(10)	-1990(6)	1.000000	74(8)
C(49)	-6220(20)	95(10)	-3106(6)	1.000000	50(6)
H(49a)	-5600(20)	541(10)	-2988(6)	1.000000	60(7)
H(49b)	-5840(20)	-427(10)	-3001(6)	1.000000	60(7)
C(12)	-1120(20)	114(10)	3139(6)	1.000000	51(6)
H(12a)	-580(20)	-287(10)	2981(6)	1.000000	61(7)
H(12b)	-650(20)	653(10)	3074(6)	1.000000	61(7)
C(7)	-7870(20)	-2277(9)	4503(5)	1.000000	42(5)
H(7c)	-7890(20)	-2460(9)	4750(5)	1.000000	50(6)
H(7d)	-8150(20)	-1687(9)	4500(5)	1.000000	50(6)
C(10)	-4180(20)	-323(9)	3198(5)	1.000000	45(5)
H(10a)	-5190(20)	-364(9)	3051(5)	1.000000	54(6)

H(10b)	-3760(20)	-885(9)	3242(5)	1.000000	54(6)
C(41)	-4200(20)	-299(9)	-1798(5)	1.000000	42(5)
H(41a)	-5240(20)	-304(9)	-1937(5)	1.000000	50(6)
H(41b)	-3810(20)	-871(9)	-1773(5)	1.000000	50(6)
C(2)	-5350(30)	-2432(11)	3993(6)	1.000000	86(11)
H(2c)	-4610(30)	-1951(11)	3962(6)	1.000000	104(13)
H(2d)	-4640(30)	-2926(11)	3980(6)	1.000000	104(13)
C(9)	-4620(30)	81(10)	3544(5)	1.000000	54(6)
H(9a)	-4670(30)	679(10)	3505(5)	1.000000	64(7)
H(9b)	-5750(30)	-100(10)	3609(5)	1.000000	64(7)
C(46)	-8570(30)	-115(12)	-3825(8)	1.000000	133(14)
H(46a)	-8470(30)	-719(12)	-3825(8)	1.000000	159(17)
H(46b)	-9070(30)	52(12)	-4051(8)	1.000000	159(17)
N(7)	-2970(30)	-2297(9)	-4523(7)	1.000000	108(6)
H(7a)	-3290(30)	-1757(9)	-4531(7)	1.000000	130(7)
H(7b)	-3040(30)	-2495(9)	-4748(7)	1.000000	130(7)
C(8)	-3490(40)	-73(12)	3849(8)	1.000000	126(15)
H(8c)	-3500(40)	417(12)	4002(8)	1.000000	151(18)
H(8d)	-3950(40)	-536(12)	3987(8)	1.000000	151(18)
C(6)	-9180(30)	-2736(10)	4305(6)	1.000000	75(8)
H(6a)	-8870(30)	-3321(10)	4295(6)	1.000000	90(10)
H(6b)	-10250(30)	-2697(10)	4434(6)	1.000000	90(10)
C(45)	-9690(30)	146(10)	-3530(5)	1.000000	54(6)
H(45a)	-9570(30)	742(10)	-3490(5)	1.000000	65(8)
H(45b)	-10860(30)	31(10)	-3591(5)	1.000000	65(8)
C(20)	-5470(50)	105(12)	1532(9)	1.000000	126(14)
H(20a)	-4860(50)	632(12)	1527(9)	1.000000	151(16)
H(20b)	-4640(50)	-336(12)	1494(9)	1.000000	151(16)
C(44)	-9220(30)	-315(9)	-3206(5)	1.000000	48(5)
H(44a)	-8730(30)	-852(9)	-3267(5)	1.000000	57(7)
H(44b)	-10210(30)	-409(9)	-3057(5)	1.000000	57(7)
C(16)	-9220(30)	-345(9)	1790(6)	1.000000	45(5)
H(16a)	-8690(30)	-884(9)	1749(6)	1.000000	54(6)
H(16b)	-10230(30)	-434(9)	1934(6)	1.000000	54(6)

C(13)	-370(40)	-61(12)	3488(6)	1.000000	115(13)
H(13a)	420(40)	-526(12)	3468(6)	1.000000	138(16)
H(13b)	260(40)	424(12)	3570(6)	1.000000	138(16)
C(26)	-310(40)	-2450(11)	1055(7)	1.000000	78(9)
H(26a)	-250(40)	-1854(11)	1102(7)	1.000000	94(11)
H(26b)	800(40)	-2688(11)	1104(7)	1.000000	94(11)
C(48)	-5730(50)	92(13)	-3483(7)	1.000000	210(20)
H(48a)	-4790(50)	487(13)	-3503(7)	1.000000	250(30)
H(48b)	-5240(50)	-456(13)	-3528(7)	1.000000	250(30)
C(3)	-6560(30)	-2456(10)	3688(7)	1.000000	69(8)
H(3a)	-6820(30)	-1883(10)	3625(7)	1.000000	82(9)
H(3b)	-5960(30)	-2700(10)	3487(7)	1.000000	82(9)
C(55)	-1490(30)	-2592(10)	-3684(7)	1.000000	75(8)
C(5)	-9440(30)	-2425(10)	3941(5)	1.000000	58(6)
H(5c)	-10590(30)	-2527(10)	3861(5)	1.000000	70(8)
H(5d)	-9200(30)	-1831(10)	3927(5)	1.000000	70(8)
C(27)	-1570(40)	-2832(12)	1296(12)	1.000000	210(20)
H(27a)	-1810(40)	-3396(12)	1215(12)	1.000000	250(30)
H(27b)	-1090(40)	-2869(12)	1534(12)	1.000000	250(30)
C(38)	-460(40)	180(12)	-1499(6)	1.000000	111(12)
H(38a)	580(40)	-148(12)	-1490(6)	1.000000	133(14)
H(38b)	-140(40)	756(12)	-1451(6)	1.000000	133(14)
C(33)	-6340(30)	-2424(12)	-1327(9)	1.000000	123(5)
H(33a)	-5930(30)	-2751(12)	-1527(9)	1.000000	148(6)
H(33b)	-6340(30)	-1846(12)	-1404(9)	1.000000	148(6)
C(42)	-4530(40)	53(11)	-1449(6)	1.000000	92(10)
H(42a)	-5030(40)	598(11)	-1495(6)	1.000000	110(12)
H(42b)	-5440(40)	-286(11)	-1349(6)	1.000000	110(12)
N(3)	-2370(30)	-2349(9)	499(7)	1.000000	110(9)
H(3c)	-2330(30)	-2523(9)	270(7)	1.000000	132(11)
H(3d)	-2460(30)	-1788(9)	496(7)	1.000000	132(11)
C(4)	-8200(30)	-2911(11)	3729(9)	1.000000	123(12)
H(4c)	-8670(30)	-3022(11)	3494(9)	1.000000	148(15)
H(4d)	-8000(30)	-3444(11)	3844(9)	1.000000	148(15)

C(56)	-3340(30)	-2388(12)	-3684(9)	1.000000	108(6)
H(56a)	-3810(30)	-2763(12)	-3506(9)	1.000000	130(7)
H(56b)	-3390(30)	-1837(12)	-3577(9)	1.000000	130(7)
C(32)	-8160(40)	-2662(12)	-1277(9)	1.000000	123(5)
H(32a)	-8770(40)	-2433(12)	-1480(9)	1.000000	148(6)
H(32b)	-8210(40)	-3265(12)	-1302(9)	1.000000	148(6)
C(22)	-4430(30)	-2457(10)	1035(6)	1.000000	66(8)
H(22a)	-5020(30)	-1927(10)	1013(6)	1.000000	80(9)
H(22b)	-5260(30)	-2861(10)	1118(6)	1.000000	80(9)
C(18)	-8350(40)	-286(12)	1232(10)	1.000000	120(13)
H(18a)	-8190(40)	-875(12)	1283(10)	1.000000	144(15)
H(18b)	-8770(40)	-250(12)	989(10)	1.000000	144(15)
C(23)	-3940(30)	-2709(11)	674(7)	1.000000	90(10)
H(23a)	-4900(30)	-2587(11)	519(7)	1.000000	108(13)
H(23b)	-3810(30)	-3312(11)	676(7)	1.000000	108(13)
C(17)	-9700(40)	3(11)	1461(8)	1.000000	93(10)
H(17a)	-10790(40)	-204(11)	1384(8)	1.000000	112(12)
H(17b)	-9730(40)	609(11)	1473(8)	1.000000	112(12)
C(19)	-6650(50)	97(13)	1233(12)	1.000000	175(17)
H(19a)	-6820(50)	678(13)	1168(12)	1.000000	210(20)
H(19b)	-6040(50)	-157(13)	1036(12)	1.000000	210(20)
C(36)	-3290(40)	188(13)	-1147(10)	1.000000	180(20)
H(36a)	-3250(40)	782(13)	-1096(10)	1.000000	210(30)
H(36b)	-3740(40)	-87(13)	-937(10)	1.000000	210(30)
C(37)	-1550(40)	-101(12)	-1201(9)	1.000000	139(14)
H(37a)	-1610(40)	-706(12)	-1217(9)	1.000000	167(17)
H(37b)	-940(40)	26(12)	-983(9)	1.000000	167(17)
C(28)	-3180(30)	-2363(11)	1314(7)	1.000000	83(9)
H(28a)	-3730(30)	-2509(11)	1538(7)	1.000000	100(10)
H(28b)	-2900(30)	-1774(11)	1328(7)	1.000000	100(10)
C(14)	-1710(40)	-267(12)	3746(10)	1.000000	146(15)
H(14a)	-1120(40)	-175(12)	3971(10)	1.000000	175(19)
H(14b)	-1760(40)	-871(12)	3723(10)	1.000000	175(19)
C(47)	-6870(40)	267(12)	-3790(10)	1.000000	124(13)

H(47a)	-6240(40)	120(12)	-4004(10)	1.000000	149(16)
H(47b)	-7030(40)	867(12)	-3797(10)	1.000000	149(16)
C(25)	-740(50)	-2583(13)	677(9)	1.000000	220(30)
H(25a)	150(50)	-2308(13)	541(9)	1.000000	270(30)
H(25b)	-600(50)	-3178(13)	635(9)	1.000000	270(30)
C(51)	-4250(20)	-2746(9)	-4311(5)	1.000000	37(5)
H(51a)	-5290(20)	-2783(9)	-4449(5)	1.000000	44(6)
H(51b)	-3850(20)	-3311(9)	-4270(5)	1.000000	44(6)
C(50)	-4660(30)	-2360(11)	-3961(6)	1.000000	82(9)
H(50a)	-5660(30)	-2631(11)	-3868(6)	1.000000	98(10)
H(50b)	-4940(30)	-1778(11)	-4002(6)	1.000000	98(10)
N(6)	-6740(30)	-2412(9)	-485(8)	1.000000	123(5)
H(6c)	-6630(30)	-2185(9)	-266(8)	1.000000	148(6)
H(6d)	-6500(30)	-2959(9)	-460(8)	1.000000	148(6)
C(34)	-5050(50)	-2494(12)	-1042(8)	1.000000	123(5)
H(34a)	-4910(50)	-3082(12)	-988(8)	1.000000	148(6)
H(34b)	-3980(50)	-2295(12)	-1138(8)	1.000000	148(6)
C(30)	-8550(40)	-2373(12)	-568(9)	1.000000	123(5)
H(30a)	-9100(40)	-2807(12)	-429(9)	1.000000	148(6)
H(30b)	-8970(40)	-1844(12)	-477(9)	1.000000	148(6)
C(35)	-5350(40)	-2054(12)	-702(8)	1.000000	123(5)
H(35a)	-5610(40)	-1473(12)	-753(8)	1.000000	148(6)
H(35b)	-4310(40)	-2066(12)	-563(8)	1.000000	148(6)
C(31)	-9220(50)	-2456(12)	-952(8)	1.000000	123(5)
H(31a)	-9770(50)	-1930(12)	-1006(8)	1.000000	148(6)
H(31b)	-10110(50)	-2875(12)	-944(8)	1.000000	148(6)
C(54)	-570(50)	-2371(12)	-4039(7)	1.000000	138(15)
H(55a)	-950(30)	-2291(10)	-3490(7)	1.000000	90(10)
H(55b)	-1360(30)	-3185(10)	-3638(7)	1.000000	90(10)
H(54a)	370(50)	-2761(12)	-4047(7)	1.000000	165(18)
H(54b)	-60(50)	-1830(12)	-3991(7)	1.000000	165(18)
H(53a)	-620(30)	-2773(11)	-4545(7)	1.000000	92(9)
H(53b)	-630(30)	-1803(11)	-4515(7)	1.000000	92(9)

*U_{eq} is defined as one third of the trace of the orthogonalized U_{ij} tensor.

Table C6. Atomic coordinates ($x10^4$) and equivalent isotropic displacement parameters ($Å^2x10^3$) for (hep)$PbBr_3$ at 293(2) K with estimated standard deviations in parentheses.

Label	x	y	z	Occupancy	U_{eq}^*
Pb(1)	6464(2)	4976(1)	8376(3)	1	52(1)
Pb(2)	6465(2)	10022(1)	7798(3)	1	40(1)
Br(5)	6451(7)	9413(2)	5874(10)	1	58(2)
Br(8)	5217(8)	5258(4)	6054(17)	1	117(6)
Br(9)	6446(8)	5585(3)	10396(14)	1	72(3)
Br(11)	7716(7)	5241(2)	6113(14)	1	68(3)
Br(13)	7715(6)	9762(2)	10092(13)	1	65(3)
Br(14)	5214(9)	10254(4)	5127(18)	1	115(6)
Pb(3)	3933(3)	7496(1)	8079(6)	1	79(2)
Br(7)	3940(10)	6912(2)	5688(19)	1	79(3)
Br(10)	3931(9)	8084(2)	10665(18)	1	77(3)
Br(17)	2709(11)	7746(5)	5270(30)	1	170(11)
Br(18)	5207(9)	7746(3)	5890(30)	1	128(7)
Pb(0A)	3975(2)	7497(2)	3078(4)	1	79(2)
Br(2)	5216(8)	7250(3)	10290(30)	1	133(7)
N(1)	1240(50)	7002(18)	5040(70)	1	78(8)
H(1A)	693	6917	4960	1	93
H(1B)	1214	7239	4733	1	93
N(4)	6230(50)	6978(19)	6300(80)	1	88(10)
H(4C)	6308	7203	6752	1	106
H(4D)	5669	6918	6480	1	106
C(8)	3690(60)	9490(20)	4880(90)	1	80(8)
H(8A)	3735	9710	4400	1	96
H(8B)	3118	9428	4888	1	96
N(21)	3740(40)	5497(14)	11430(70)	1	57(14)
H(21A)	3181	5523	11799	1	69
H(21B)	3893	5266	11672	1	69
N(2)	3970(50)	9501(19)	6650(90)	1	80(8)
H(2C)	3905	9728	7071	1	96
H(2D)	4544	9447	6683	1	96
C(3)	3750(80)	5540(30)	9560(80)	1	108(13)

H(3A)	4106	5362	9172	1	129
H(3B)	3210	5469	9212	1	129
C(7)	1440(70)	7000(20)	6880(90)	1	78(8)
H(7A)	1784	7193	7066	1	93
H(7B)	934	7049	7454	1	93
C(27)	6550(80)	6372(17)	7590(90)	1	88(10)
H(27A)	7018	6297	8205	1	106
H(27B)	6124	6390	8431	1	106
C(10)	4000(70)	8866(16)	3610(100)	1	80(8)
H(10A)	3429	8826	3365	1	96
H(10B)	4302	8786	2649	1	96
C(4)	1380(70)	6100(18)	6620(90)	1	78(8)
H(4A)	973	5952	7097	1	93
H(4B)	1854	5963	6388	1	93
C(25)	6270(60)	6150(20)	4860(80)	1	88(10)
H(25A)	6255	5926	4330	1	106
H(25B)	5719	6230	4752	1	106
C(20)	4250(70)	5720(20)	12510(150)	1	108(13)
H(20A)	4753	5757	11916	1	129
H(20B)	4376	5596	13518	1	129
C(24)	6710(70)	6352(18)	3580(120)	1	88(10)
H(24A)	6501	6271	2510	1	106
H(24B)	7260	6274	3643	1	106
C(19)	3970(80)	6070(20)	13070(120)	1	108(13)
H(19A)	4410	6184	13605	1	129
H(19B)	3538	6039	13896	1	129
C(5)	1600(60)	6356(15)	7910(100)	1	78(8)
H(5A)	1159	6347	8699	1	93
H(5B)	2058	6254	8485	1	93
C(11)	4220(60)	8650(20)	5080(70)	1	80(8)
H(11A)	4709	8538	4752	1	96
H(11B)	3802	8483	5152	1	96
C(2)	1490(60)	6470(16)	3780(110)	1	78(8)
H(2A)	2014	6362	3636	1	93

H(2B)	1206	6429	2741	1	93
C(6)	1810(60)	6718(15)	7860(110)	1	78(8)
H(6A)	2381	6724	7551	1	93
H(6B)	1791	6791	9020	1	93
C(14)	3520(50)	9262(19)	7740(110)	1	80(8)
H(14A)	3321	9379	8728	1	96
H(14B)	3067	9168	7140	1	96
C(13)	4080(60)	8990(20)	8260(90)	1	80(8)
H(13A)	3819	8851	9096	1	96
H(13B)	4555	9090	8779	1	96
C(15)	3930(80)	5830(20)	8410(130)	1	108(13)
H(15A)	4375	5751	7712	1	129
H(15B)	3469	5847	7675	1	129
C(22)	6380(70)	6990(20)	4430(90)	1	88(10)
H(22A)	5855	7032	3922	1	106
H(22B)	6691	7196	4241	1	106
C(9)	4120(60)	9242(17)	3740(110)	1	80(8)
H(9A)	4690	9271	3978	1	96
H(9B)	4038	9328	2611	1	96
C(12)	4360(60)	8770(20)	6850(80)	1	80(8)
H(12A)	4367	8549	7421	1	96
H(12B)	4927	8829	6792	1	96
C(28)	6750(60)	6740(17)	7270(130)	1	88(10)
H(28A)	6822	6841	8366	1	106
H(28B)	7270	6741	6727	1	106
C(18)	3660(80)	6270(30)	11600(110)	1	108(13)
H(18A)	3163	6355	12110	1	129
H(18B)	4027	6460	11691	1	129
C(1)	1700(60)	6835(15)	3670(100)	1	78(8)
H(1C)	1537	6925	2591	1	93
H(1D)	2272	6869	3817	1	93
C(0AA)	1070(50)	6240(20)	5000(90)	1	78(8)
H(0AA)	570	6352	5287	1	93
H(0AB)	916	6043	4344	1	93

C(26)	6300(70)	6055(16)	6680(90)	1	88(10)
H(26A)	5780	5977	7070	1	106
H(26B)	6698	5879	6869	1	106
C(17)	3430(70)	6310(30)	9800(100)	1	108(13)
H(17A)	3320	6546	9540	1	129
H(17B)	2949	6180	9542	1	129
C(23)	6770(70)	6726(16)	3370(120)	1	88(10)
H(23A)	6599	6771	2224	1	106
H(23B)	7347	6775	3397	1	106
C(16)	4150(70)	6180(20)	8850(160)	1	108(13)
H(16A)	4236	6318	7845	1	129
H(16B)	4629	6193	9540	1	129
Br(0A)	2704(10)	7259(5)	10900(30)	1	179(12)

*U_{eq} is defined as one third of the trace of the orthogonalized U_{ij} tensor.

Table C7. Atomic coordinates ($x10^4$) and equivalent isotropic displacement parameters ($Å^2x10^3$) for (4amp)$PbBr_4$ at 293(2) K with estimated standard deviations in parentheses.

Label	x	y	z	Occupancy	U_{eq}*
Pb(1)	1227(1)	5073(1)	1617(2)	1	36(1)
Br(2)	1521(2)	2069(2)	1411(3)	1	47(1)
Br(3)	1130(2)	7857(2)	1856(4)	1	50(1)
Br(4)	2330(2)	5196(2)	4639(3)	1	47(1)
Br(5A)	-371(2)	4973(2)	3356(3)	0.968(11)	51(1)
N(1)	1179(9)	7626(15)	6210(30)	1	50(4)
H(1A)	1146	6730	6604	1	59
H(1B)	1291	7608	4995	1	59
N(2)	1667(10)	12629(15)	7210(20)	1	49(4)
H(2A)	2124	12444	6812	1	59
H(2B)	1650	12452	8326	1	59
H2C()	1569	13472	7048	1	59
C(3)	1839(9)	9732(17)	6590(40)	1	53(5)
H(3A)	2231	10164	7242	1	64
H(3B)	1974	9787	5389	1	64
C(4)	1096(10)	10427(19)	6880(30)	1	44(4)
H(4)	984	10406	8102	1	52

C(5)	444(10)	8277(19)	6470(40)	1	64(6)
H(5A)	303	8214	7668	1	77
H(5B)	61	7840	5802	1	77
C(6)	1097(11)	11827(19)	6310(30)	1	50(5)
H(6A)	1197	11861	5089	1	60
H(6B)	601	12198	6501	1	60
C(7)	1795(12)	8300(20)	7120(40)	1	62(6)
H(7A)	2269	7868	6863	1	74
H(7B)	1710	8239	8339	1	74
C(8)	487(11)	9700(19)	5960(40)	1	61(6)
H(8A)	575	9755	4739	1	73
H(8B)	6	10114	6197	1	73

*U_{eq} is defined as one third of the trace of the orthogonalized U_{ij} tensor.

Table C8. Atomic coordinates ($x10^4$) and equivalent isotropic displacement parameters ($Å^2x10^3$) for (epz)$PbBr_4$ at 293(2) K with estimated standard deviations in parentheses.

Label	x	y	z	Occupancy	U_{eq}*
Pb(1)	3205(5)	6704(1)	3637(3)	1	42(1)
Pb(2)	6679(2)	6840(3)	6951(1)	1	43(1)
Pb(3)	-253(2)	6845(3)	308(1)	1	40(1)
Br(4)	8541(9)	8329(8)	6406(5)	1	57(2)
Br(5)	1388(10)	6774(9)	1993(6)	1	58(2)
Br(6)	4912(10)	6733(7)	5288(6)	1	54(2)
Br(7)	4763(9)	8294(9)	3036(5)	1	72(3)
Br(8)	8205(14)	6985(3)	8626(8)	1	64(1)
Br(9)	946(8)	8741(8)	-234(5)	1	56(2)
Br(10)	1872(7)	5362(7)	-356(5)	1	60(2)
Br(11)	-2086(7)	8359(8)	823(5)	1	50(2)
Br(12)	4594(8)	5361(7)	7619(4)	1	56(2)
Br(13)	-1741(16)	4999(14)	1104(11)	1	83(2)
Br(1)	5444(8)	8694(8)	7511(5)	1	58(2)
Br(2)	1745(9)	8300(6)	4235(5)	1	55(2)
N(1)	4920(40)	1830(30)	5080(20)	1	44(3)
H(1)	5833	1723	5247	1	52
N(5)	1490(40)	8100(30)	7170(20)	1	48(4)

H(5)	580	8163	6975	1	58
C(18)	1520(40)	7260(30)	7830(20)	1	48(4)
H(18A)	906	7437	8199	1	58
H(18B)	2367	7238	8136	1	58
N(2)	4930(30)	4130(20)	5499(16)	1	44(3)
H(2A)	5418	4743	5735	1	52
H(2B)	4063	4369	5341	1	52
C(6)	4750(30)	2760(30)	4500(20)	1	44(3)
H(6A)	3847	2944	4414	1	52
H(6B)	4983	2523	3971	1	52
C(16)	1680(40)	6830(30)	6050(20)	1	48(4)
H(16A)	2187	6658	5611	1	58
H(16B)	793	6877	5810	1	58
C(4)	4930(40)	3280(30)	6130(20)	1	44(3)
H(4A)	4465	3530	6572	1	52
H(4B)	5801	3123	6365	1	52
C(17)	1210(40)	6200(30)	7420(20)	1	48(4)
H(17A)	289	6163	7289	1	58
H(17B)	1448	5640	7826	1	58
N(6)	1810(30)	5930(30)	6665(17)	1	48(4)
H6C()	1402	5286	6417	1	58
H(6D)	2705	5769	6815	1	58
C(3)	4320(40)	2260(30)	5780(20)	1	44(3)
H(3A)	4360	1720	6203	1	52
H(3B)	3424	2407	5599	1	52
C(15)	2090(50)	7910(30)	6400(20)	1	48(4)
H(15A)	3013	7935	6512	1	58
H(15B)	1823	8472	6001	1	58
C(2)	4330(30)	790(20)	4760(20)	1	44(3)
H2C()	4650	601	4247	1	52
H(2D)	3412	858	4661	1	52
C(5)	5500(30)	3770(30)	4750(20)	1	44(3)
H(5A)	6401	3616	4868	1	52
H(5B)	5378	4313	4318	1	52

C(14)	1810(40)	9160(30)	7570(20)	1	48(4)
H(14A)	2713	9155	7787	1	58
H(14B)	1331	9230	8037	1	58
N(3)	8520(50)	7880(30)	3580(30)	1	92(5)
H(3)	9304	8204	3854	1	111
C(13)	1570(40)	10160(30)	7050(20)	1	48(4)
H(13A)	2154	10179	6643	1	73
H(13B)	1695	10791	7390	1	73
H13C()	709	10151	6785	1	73
C(1)	4700(40)	-80(30)	5400(20)	1	44(3)
H(1A)	4582	-773	5144	1	65
H(1B)	4163	-16	5828	1	65
H1C()	5576	12	5617	1	65
C(12)	8470(60)	8640(30)	2900(30)	1	92(5)
H(12A)	7643	8559	2578	1	111
H(12B)	9113	8428	2560	1	111
C(9)	7780(50)	8240(30)	4250(30)	1	92(5)
H(9A)	7981	7772	4719	1	111
H(9B)	6872	8153	4063	1	111
C(10)	8020(60)	9370(30)	4510(30)	1	92(5)
H(10A)	8818	9400	4866	1	111
H(10B)	7346	9597	4826	1	111
C(11)	8650(50)	9800(40)	3100(30)	1	92(5)
H(11A)	9563	9948	3177	1	111
H(11B)	8284	10216	2629	1	111
N(4)	8090(50)	10180(30)	3830(20)	1	92(5)
H4C()	7231	10435	3657	1	111
H(4D)	8584	10792	4057	1	111
C(7)	8130(50)	5970(40)	3370(30)	1	92(5)
H(7A)	7347	5882	3602	1	138
H(7B)	8565	5289	3365	1	138
H7C()	7950	6227	2814	1	138
C(8)	8960(40)	6760(30)	3860(30)	1	92(5)
H(8A)	9844	6653	3770	1	111

H(8B)	8885	6663	4436	1	111

*U_{eq} is defined as one third of the trace of the orthogonalized U_{ij} tensor.

Table C9. Atomic coordinates ($x10^4$) and equivalent isotropic displacement parameters ($Å^2x10^3$) for (hmp)$PbBr_4$ at 293(2) K with estimated standard deviations in parentheses.

Label	x	y	z	Occupancy	U_{eq}*
Pb(1)	4298(1)	5000	3981(1)	1	43(1)
Pb(2)	2349(1)	5000	4898(1)	1	41(1)
Pb(3)	4203(1)	5000	300(1)	1	45(1)
Pb(4)	4265(1)	0	473(1)	1	41(1)
Br(5)	5365(1)	5000	4053(1)	1	46(1)
Br(6)	2724(1)	5000	6870(2)	1	53(1)
Br(7)	4295(1)	0	2278(1)	1	46(1)
Br(8)	2500	2500	5000	1	54(1)
Br(9)	5416(1)	0	1265(1)	1	48(1)
Br(10)	4268(1)	2499(2)	334(1)	1	63(1)
Br(11)	3953(1)	5000	2020(2)	1	77(1)
Br(12)	4639(1)	5000	-1268(2)	1	53(1)
Br(13)	1382(1)	5000	5199(2)	1	56(1)
Br(14)	4370(1)	2592(2)	3932(1)	1	59(1)
Br(15)	3266(1)	5000	4128(2)	1	81(1)
Br(16)	3222(1)	0	205(2)	1	76(1)
Br(17)	1861(1)	5000	3023(2)	1	65(1)
Br(18)	3204(1)	5000	-521(2)	1	99(1)
N(1)	5522(4)	2496(8)	1919(7)	1	53(3)
H(1A)	5477	1878	1522	1	63
H(1B)	5407	3141	1571	1	63
N(2)	5703(4)	2228(10)	4047(6)	1	59(3)
H(2A)	5510	2851	4136	1	70
H(2B)	5754	1767	4561	1	70
N(3)	3481(4)	2200(12)	1933(8)	1	66(3)
H(3A)	3675	2796	2249	1	80
H(3B)	3700	1714	1734	1	80
C(4)	5201(5)	2323(11)	2524(7)	1	50(3)
H(4A)	5129	3028	2743	1	61

H(4B)	4896	2005	2197	1	61
C(5)	3268(5)	1586(12)	2557(9)	1	54(3)
H(5A)	3023	1086	2229	1	65
H(5B)	3522	1151	2936	1	65
C(6)	6049(6)	2629(12)	2309(9)	1	64(4)
H(6A)	6191	3000	1891	1	77
H(6B)	6197	1910	2415	1	77
C(7)	5421(5)	1598(10)	3280(8)	1	55(3)
H(7A)	5165	1193	3444	1	66
H(7B)	5634	1073	3106	1	66
C(8)	6170(5)	3259(12)	3145(10)	1	65(4)
H(8A)	5934	3845	3094	1	78
H(8B)	6486	3597	3211	1	78
C(9)	6183(5)	2630(13)	3972(10)	1	67(4)
H(9A)	6398	2008	4005	1	81
H(9B)	6320	3098	4469	1	81
N(14)	2555(5)	2623(11)	2742(10)	1	80(4)
H(14A)	2502	3281	3047	1	96
H(14B)	2347	2059	2882	1	96
C(11)	3046(5)	2291(12)	3099(8)	1	59(3)
H(11A)	3063	1909	3643	1	70
H(11B)	3244	2945	3242	1	70
C(12)	3135(6)	2662(12)	1160(10)	1	68(4)
H(12A)	2991	2071	769	1	82
H(12B)	3308	3135	851	1	82
C(15)	2389(7)	2840(20)	1824(14)	1	102(7)
H(15A)	2283	2149	1531	1	122
H(15B)	2106	3308	1729	1	122
C(14)	2724(8)	3330(20)	1410(17)	1	123(9)
H14C()	2881	3919	1786	1	148
H(14D)	2533	3662	877	1	148

*U_{eq} is defined as one third of the trace of the orthogonalized U_{ij} tensor.

Table C10. Atomic coordinates ($x10^4$) and equivalent isotropic displacement parameters ($Å^2x10^3$) for $(mpz)_2Pb_3Br_{10}$ at 293(2) K with estimated standard deviations in parentheses.

Label	x	y	z	Occupancy	U_{eq}^*
Pb(1)	5003(1)	2960(1)	4366(1)	1	39(1)
Pb(2)	3640(1)	2882(1)	3770(1)	1	39(1)
Pb(3)	6370(1)	2851(1)	4917(1)	1	40(1)
Br(6)	4320(1)	2917(2)	3989(2)	1	57(1)
Br(7)	5000	1814(3)	2500	1	53(1)
Br(8)	5664(1)	2896(2)	4547(2)	1	57(1)
Br(9)	5000(1)	6101(2)	3760(2)	1	51(1)
Br(10)	3657(1)	1560(2)	1939(2)	1	56(1)
Br(11)	5000	0	5000	1	66(1)
Br(1)	6432(1)	5941(2)	4425(2)	1	50(1)
Br(2)	7011(1)	2360(2)	5045(2)	1	54(1)
Br(3)	3560(1)	5980(2)	3214(2)	1	50(1)
Br(4)	2975(1)	2428(2)	3392(2)	1	53(1)
Br(5)	3720(1)	22(2)	4463(2)	1	71(1)
N(1)	5630(3)	-2895(16)	2761(9)	1	48(3)
H(1)	5410	-2927	2670	1	57
N(2)	2968(3)	3240(14)	6649(8)	1	38(3)
H(2)	3184	3428	6761	1	45
C(3)	5716(5)	-2100(20)	3589(11)	1	59(5)
H(3A)	5932	-2042	3707	1	71
H(3B)	5647	-2602	4077	1	71
C(4)	5716(5)	-2110(20)	2004(12)	1	59(5)
H(4A)	5651	-2624	1460	1	71
H(4B)	5932	-2025	2070	1	71
N(5)	2999(4)	229(14)	6640(11)	1	55(4)
H(5A)	2789	-28	6537	1	66
H(5B)	3117	-624	6688	1	66
N(6)	5668(3)	152(18)	2759(13)	1	69(5)
H(6A)	5564	1045	2711	1	83
H(6B)	5881	331	2830	1	83
C(8)	2879(5)	2401(17)	7386(11)	1	48(4)

H(8A)	2666	2193	7272	1	58
H(8B)	2918	2924	7937	1	58
C(9)	2899(4)	2430(20)	5825(11)	1	51(4)
H(9A)	2945	2986	5328	1	61
H(9B)	2687	2212	5726	1	61
C(10)	3061(5)	1030(20)	7463(13)	1	61(5)
H(10A)	3273	1239	7583	1	73
H(10B)	3007	472	7952	1	73
C(11)	5729(5)	-4340(20)	2802(15)	1	70(6)
H(11A)	5943	-4373	2823	1	105
H(11B)	5637	-4834	2285	1	105
H11C()	5674	-4777	3325	1	105
C(12)	5578(5)	-690(20)	1943(15)	1	70(6)
H(12A)	5638	-201	1437	1	84
H(12B)	5362	-782	1845	1	84
C(13)	3076(4)	1097(18)	5873(14)	1	56(5)
H(13A)	3289	1307	5956	1	67
H(13B)	3029	577	5323	1	67
C(14)	5589(5)	-650(30)	3553(16)	1	82(8)
H(14A)	5666	-151	4092	1	98
H(14B)	5373	-701	3521	1	98
C(15)	2799(5)	4600(20)	6595(13)	1	58(5)
H(15A)	2588	4415	6464	1	87
H(15B)	2861	5171	6134	1	87
H15C()	2839	5081	7153	1	87

*U_{eq} is defined as one third of the trace of the orthogonalized U_{ij} tensor.

Table C11. Atomic coordinates ($x10^4$) and equivalent isotropic displacement parameters ($Å^2x10^3$) for (2,6-dmpz)$_2$Pb$_2$Br$_{10}$ at 296.15 K with estimated standard deviations in parentheses.

Label	x	y	z	Occupancy	U_{eq}*
Pb(01)	3054(2)	3095(1)	8371(1)	1	26(1)
Pb(02)	-4706(2)	1350(1)	4290(1)	1	26(1)
Br(03)	-5170(3)	478(1)	5882(1)	1	30(1)
Br(04)	-4277(3)	2327(1)	2819(1)	1	33(1)
Br(05)	7987(3)	3074(1)	8203(1)	1	32(1)

Br(06)	2981(3)	1334(1)	9433(1)	1	34(1)
Br(07)	-4838(4)	2833(1)	4651(1)	1	39(1)
Br(08)	2707(3)	3828(2)	9490(1)	1	40(1)
Br(09)	32(3)	1150(1)	4230(1)	1	33(1)
Br(0A)	3264(3)	4731(1)	7359(1)	1	41(1)
Br(0B)	11246(3)	1635(1)	11794(1)	1	34(1)
Br(0C)	3453(4)	2254(2)	7191(1)	1	47(1)
N(00D)	6360(20)	1813(7)	11260(6)	1	24(3)
H(00A)	5206	1860	11598	1	28
H(00B)	7700	1830	11464	1	28
N(00E)	-1510(20)	1984(7)	6952(6)	1	29(4)
H(00L)	-2639	2246	7173	1	35
H00N()	-154	2141	7073	1	35
N(00F)	9370(30)	6996(7)	7155(7)	1	33(4)
H(0AA)	10502	7399	7085	1	40
H	8014	7285	7120	1	40
N(00G)	7830(30)	1643(8)	9920(7)	1	35(4)
H00C()	8969	1600	9574	1	42
H(00D)	6474	1630	9727	1	42
N(00H)	8150(20)	5304(8)	7437(7)	1	29(3)
H(1AA)	7051	4886	7512	1	34
H(A)	9524	5033	7472	1	34
N(00I)	-270(20)	925(8)	6092(7)	1	29(3)
H(00P)	-1644	777	5972	1	34
H(00Q)	842	660	5869	1	34
C(00J)	-1580(30)	2291(9)	6189(8)	1	26(4)
H(00R)	-3000	2165	6076	1	32
C(00K)	9390(30)	6409(9)	7864(9)	1	36(5)
H(2AA)	10815	6178	7919	1	43
H(B)	9093	6707	8206	1	43
C(00L)	8080(30)	5883(8)	6706(7)	1	32(5)
H(3AA)	6648	6123	6666	1	38
C(00M)	6300(30)	2533(9)	10635(8)	1	35(5)
H(00M)	4905	2544	10448	1	42

C00N()	-190(30)	631(10)	6859(8)	1	36(5)
H(00S)	1237	717	6974	1	43
H(00T)	-497	47	7017	1	43
C(00O)	6180(30)	990(9)	11115(8)	1	23(4)
H(00O)	4781	953	10943	1	27
C(00P)	7810(30)	5732(8)	7993(8)	1	23(4)
H(4AA)	6370	5969	7976	1	27
C(00Q)	-1650(30)	822(10)	8014(8)	1	35(5)
H(00U)	-289	992	8114	1	52
H(00V)	-1789	237	8194	1	52
H(00W)	-2778	1081	8227	1	52
C(00R)	7940(40)	915(10)	10565(9)	1	38(5)
H(00E)	7760	407	10446	1	45
H(00F)	9328	906	10743	1	45
C(00S)	8050(40)	2449(11)	10094(9)	1	42(5)
H(00G)	9436	2474	10266	1	50
H(00H)	7970	2900	9678	1	50
C(00T)	9670(30)	6564(9)	6593(9)	1	34(5)
H(5AA)	9508	6957	6148	1	40
HC()	11103	6344	6583	1	40
C(00U)	40(30)	1873(10)	5826(7)	1	32(5)
H(00X)	1464	2017	5905	1	38
H(00Y)	-99	2055	5331	1	38
C(00V)	-1270(40)	3222(12)	5948(9)	1	52(6)
H(00Z)	-2350	3474	6188	1	78
H(D)	-1399	3417	5459	1	78
H(E)	119	3360	6047	1	78
C(00W)	-1780(30)	1070(9)	7229(7)	1	26(4)
H(00)	-3217	929	7144	1	31
C(00X)	8470(40)	5407(11)	6174(9)	1	39(5)
H(6AA)	9905	5204	6179	1	58
H(F)	8255	5761	5722	1	58
H(G)	7478	4954	6285	1	58
C(00Y)	7940(40)	5130(12)	8691(9)	1	52(6)

H(7AA)	6908	4700	8755	1	77
H(H)	7654	5404	9044	1	77
H(I)	9353	4900	8719	1	77
C(00Z)	6600(40)	3318(11)	10827(10)	1	56(7)
H(00I)	5768	3293	11255	1	85
H(00J)	6142	3774	10469	1	85
H(00K)	8087	3385	10881	1	85
C(010)	6350(40)	304(10)	11771(10)	1	46(6)
H(01A)	7667	364	11964	1	70
H(01B)	6344	-213	11667	1	70
H01C()	5165	327	12099	1	70

*U_{eq} is defined as one third of the trace of the orthogonalized U_{ij} tensor.

Table C12. Anisotropic displacement parameters ($Å^2x10^3$) for (hex)$PbBr_3$ at 249.99 K with estimated standard deviations in parentheses.

Label	U_{11}	U_{22}	U_{33}	U_{12}	U_{13}	U_{23}
Pb(01)	13(1)	25(1)	33(1)	-8(1)	0(1)	1(1)
Pb(02)	14(1)	25(1)	34(1)	-4(1)	-1(1)	0(1)
Pb(03)	18(1)	29(1)	35(1)	-3(1)	-1(1)	-2(1)
Pb(04)	18(1)	25(1)	40(1)	-3(1)	-4(1)	0(1)
Pb(05)	69(1)	52(1)	60(1)	16(1)	-24(1)	-6(1)
Pb(06)	72(1)	53(1)	62(1)	13(1)	27(1)	9(1)
Pb(07)	19(1)	32(1)	37(1)	2(1)	0(1)	3(1)
Pb(08)	19(1)	31(1)	44(1)	2(1)	2(1)	0(1)
Br(09)	31(1)	53(2)	23(2)	-3(2)	-1(1)	-1(2)
Br(0A)	36(2)	37(2)	49(2)	5(2)	15(2)	20(2)
Br(0B)	34(2)	49(2)	28(2)	-8(2)	-1(1)	-4(2)
Br(0C)	28(2)	51(2)	40(2)	4(2)	-1(2)	-5(2)
Br(0D)	35(2)	49(2)	41(2)	-6(2)	2(2)	3(2)
Br(0E)	48(2)	34(2)	44(2)	3(2)	-12(2)	-16(2)
Br(0F)	32(2)	46(2)	61(2)	7(2)	13(2)	26(2)
Br(0G)	44(2)	42(2)	59(2)	-12(2)	-16(2)	22(2)
Br(0H)	43(2)	37(2)	66(2)	-13(2)	-12(2)	26(2)
Br(0I)	47(2)	41(2)	56(2)	7(2)	-13(2)	-25(2)
Br(0J)	96(3)	84(2)	44(2)	-24(2)	2(2)	4(2)

Br(0K)	55(2)	37(2)	53(2)	-13(2)	12(2)	-21(2)
Br(0L)	57(2)	36(2)	61(2)	-14(2)	10(2)	-24(2)
Br(0M)	92(2)	88(3)	38(2)	-11(2)	-1(2)	0(2)
Br(0N)	242(6)	66(3)	66(3)	34(3)	-3(3)	23(2)
Br(0O)	35(2)	56(2)	29(2)	-5(2)	-1(2)	-4(2)
Br(0P)	28(2)	62(2)	23(2)	-9(2)	-2(1)	1(2)
Br(0Q)	42(2)	42(2)	58(2)	-6(2)	-13(2)	20(2)
Br(0R)	226(6)	67(3)	62(3)	33(3)	-1(3)	-18(2)
Br(0S)	41(2)	46(2)	67(2)	14(2)	15(2)	28(2)
Br(0T)	270(7)	62(3)	72(3)	30(3)	-10(4)	16(2)
Br(0U)	245(7)	63(3)	75(3)	21(3)	23(4)	-18(2)
Br(0V)	43(2)	47(2)	66(2)	15(2)	-11(2)	-24(2)
Br(0W)	49(2)	43(2)	57(2)	-4(2)	9(2)	-15(2)

The anisotropic displacement factor exponent takes the form: $-2\pi^2[h^2a^{*2}U_{11} + ... + 2hka^*b^*U_{12}]$.

Table C13. Anisotropic displacement parameters ($Å^2x10^3$) for (hep)$PbBr_3$ at 293(2) K with estimated standard deviations in parentheses.

Label	U_{11}	U_{22}	U_{33}	U_{12}	U_{13}	U_{23}
Pb(1)	58(2)	68(2)	30(2)	-9(2)	6(2)	5(2)
Pb(2)	42(2)	49(2)	29(2)	11(2)	-5(2)	-1(2)
Br(5)	75(7)	57(5)	41(4)	-23(4)	6(4)	-1(3)
Br(8)	76(9)	173(13)	102(9)	46(8)	-18(7)	-98(9)
Br(9)	85(8)	51(5)	79(7)	28(5)	-15(6)	-9(4)
Br(11)	55(6)	63(5)	87(7)	-15(4)	38(5)	6(4)
Br(13)	54(6)	61(4)	81(6)	18(4)	-27(5)	10(4)
Br(14)	81(9)	162(12)	103(9)	38(8)	10(7)	91(9)
Pb(3)	63(3)	59(2)	115(3)	-5(2)	6(3)	18(2)
Br(7)	86(7)	70(5)	80(5)	-29(6)	29(5)	-19(6)
Br(10)	85(7)	69(5)	77(5)	36(6)	-15(5)	-11(6)
Br(17)	82(11)	182(16)	250(20)	48(11)	47(13)	150(17)
Br(18)	67(9)	56(5)	260(20)	-21(5)	70(11)	-21(8)
Pb(0A)	59(3)	106(4)	71(2)	1(2)	-4(2)	50(3)
Br(2)	63(8)	56(5)	280(20)	16(5)	-64(11)	-5(9)
Br(0A)	89(11)	185(16)	260(20)	-52(11)	-64(14)	167(18)

The anisotropic displacement factor exponent takes the form: $-2\pi^2[h^2a^{*2}U_{11} + ... + 2hka^*b^*U_{12}]$.

Table C14. Anisotropic displacement parameters ($Å^2x10^3$) for (4amp)$PbBr_4$ at 293(2) K with estimated standard deviations in parentheses.

Label	U_{11}	U_{22}	U_{33}	U_{12}	U_{13}	U_{23}
Pb(1)	33(1)	39(1)	37(1)	2(1)	-1(1)	-2(1)
Br(2)	41(1)	46(1)	54(2)	1(1)	-2(1)	0(1)
Br(3)	48(1)	43(1)	59(2)	7(1)	-2(1)	-1(1)
Br(4)	45(1)	52(1)	45(1)	6(1)	-11(1)	-2(1)
Br(5A)	48(2)	56(2)	49(2)	0(1)	16(1)	1(1)
N(1)	45(8)	36(7)	67(13)	0(6)	6(8)	-1(7)
N(2)	47(9)	44(7)	55(10)	-3(7)	6(7)	-4(7)
C(3)	29(7)	47(8)	83(15)	-6(6)	7(12)	2(11)
C(4)	35(8)	55(9)	41(10)	4(7)	10(7)	-5(8)
C(5)	33(8)	58(10)	100(20)	-3(7)	8(13)	-20(14)
C(6)	54(10)	47(9)	50(12)	1(8)	-5(10)	-8(8)
C(7)	47(11)	51(10)	87(18)	-2(9)	-16(11)	-1(11)
C(8)	37(10)	50(10)	96(19)	1(8)	-9(10)	-17(11)

The anisotropic displacement factor exponent takes the form: $-2\pi^2[h^2a^{*2}U_{11} + ... + 2hka^*b^*U_{12}]$.

Table C15. Anisotropic displacement parameters ($Å^2x10^3$) for (epz)$PbBr_4$ at 293(2) K with estimated standard deviations in parentheses.

Label	U_{11}	U_{22}	U_{33}	U_{12}	U_{13}	U_{23}
Pb(1)	43(1)	42(1)	41(1)	1(2)	4(1)	1(2)
Pb(2)	39(2)	51(2)	39(2)	3(2)	2(2)	-1(2)
Pb(3)	39(2)	41(2)	41(2)	0(2)	3(2)	5(2)
Br(4)	58(4)	57(5)	58(4)	-3(4)	7(4)	13(4)
Br(5)	59(4)	59(4)	51(3)	2(3)	-13(3)	-6(4)
Br(6)	56(3)	41(3)	62(4)	0(3)	-7(3)	-3(4)
Br(7)	64(4)	93(6)	62(4)	-37(4)	17(4)	0(4)
Br(8)	68(2)	73(2)	46(2)	11(7)	-15(2)	-3(6)
Br(9)	54(4)	58(5)	60(4)	-10(4)	17(4)	2(4)
Br(10)	39(3)	54(5)	84(5)	0(3)	3(3)	9(4)
Br(11)	34(3)	59(5)	54(4)	7(3)	-2(3)	3(4)
Br(12)	74(5)	54(5)	40(3)	-16(4)	16(3)	-4(3)
Br(13)	74(2)	67(2)	103(3)	-20(2)	-10(2)	36(2)

Br(1)	54(4)	55(5)	64(5)	15(4)	9(4)	-2(4)
Br(2)	66(4)	48(4)	47(3)	5(3)	-11(3)	-10(3)

The anisotropic displacement factor exponent takes the form: $-2\pi^2[h^2a^{*2}U_{11} + ... + 2hka^*b^*U_{12}]$.

Table C16. Anisotropic displacement parameters ($Å^2x10^3$) for (hmp)$PbBr_4$ at 293(2) K with estimated standard deviations in parentheses.

Label	U_{11}	U_{22}	U_{33}	U_{12}	U_{13}	U_{23}
Pb(1)	37(1)	50(1)	42(1)	0	9(1)	0
Pb(2)	43(1)	36(1)	47(1)	0	14(1)	0
Pb(3)	54(1)	38(1)	43(1)	0	16(1)	0
Pb(4)	46(1)	36(1)	44(1)	0	15(1)	0
Br(5)	44(1)	46(1)	48(1)	0	15(1)	0
Br(6)	54(1)	53(1)	54(1)	0	15(1)	0
Br(7)	44(1)	52(1)	44(1)	0	15(1)	0
Br(8)	54(1)	53(1)	58(1)	-2(1)	16(1)	2(1)
Br(9)	61(1)	40(1)	45(1)	0	19(1)	0
Br(10)	82(1)	40(1)	70(1)	3(1)	26(1)	2(1)
Br(11)	90(2)	98(2)	44(1)	0	18(1)	0
Br(12)	73(2)	38(1)	50(1)	0	18(1)	0
Br(13)	52(1)	59(2)	62(1)	0	21(1)	0
Br(14)	66(1)	53(1)	59(1)	-4(1)	17(1)	-6(1)
Br(15)	50(2)	94(2)	108(2)	0	34(2)	0
Br(16)	47(1)	85(2)	84(2)	0	-1(1)	0
Br(17)	63(2)	78(2)	50(1)	0	7(1)	0
Br(18)	71(2)	128(3)	82(2)	0	-7(2)	0
N(1)	68(7)	36(5)	56(6)	6(5)	20(5)	1(4)
N(2)	64(7)	66(7)	43(5)	1(6)	10(5)	-4(5)
N(3)	50(6)	77(8)	80(8)	12(6)	33(6)	2(6)
C(4)	48(7)	52(8)	45(6)	1(6)	1(5)	-5(5)
C(5)	46(6)	53(8)	66(7)	6(6)	19(6)	3(6)
C(6)	77(10)	57(9)	72(8)	27(8)	43(8)	24(7)
C(7)	67(8)	39(6)	60(7)	-11(6)	17(6)	1(5)
C(8)	38(6)	57(9)	100(11)	-3(6)	16(7)	1(8)
C(9)	44(7)	70(10)	73(9)	9(7)	-14(6)	-11(7)
N(14)	82(9)	63(9)	110(11)	12(7)	54(9)	-4(7)

C(11)	72(9)	57(8)	55(7)	22(7)	31(6)	5(6)
C(12)	92(12)	54(9)	65(8)	7(8)	32(8)	11(7)
C(15)	66(11)	127(18)	114(15)	50(12)	25(10)	3(13)
C(14)	75(12)	121(19)	160(20)	26(13)	11(14)	85(17)

The anisotropic displacement factor exponent takes the form: $-2\pi^2[h^2a^{*2}U_{11} + ... + 2hka^*b^*U_{12}]$.

Table C17. Anisotropic displacement parameters ($Å^2x10^3$) for C5 H12 Br4 N2 Pb at 293(2) K with estimated standard deviations in parentheses.

Label	U_{11}	U_{22}	U_{33}	U_{12}	U_{13}	U_{23}
Pb(1)	39(1)	41(1)	37(1)	0(1)	5(1)	0(1)
Pb(2)	37(1)	40(1)	39(1)	1(1)	4(1)	2(1)
Pb(3)	40(1)	40(1)	39(1)	-2(1)	5(1)	1(1)
Br(6)	42(1)	68(2)	61(2)	-5(1)	3(1)	7(1)
Br(7)	53(2)	72(2)	34(1)	0	6(1)	0
Br(8)	42(1)	69(2)	61(2)	3(1)	8(1)	6(1)
Br(9)	58(1)	56(1)	40(1)	1(1)	8(1)	-4(1)
Br(10)	45(1)	84(2)	39(1)	-2(1)	6(1)	0(1)
Br(11)	87(2)	48(2)	65(2)	-2(2)	13(2)	11(2)
Br(1)	60(1)	48(1)	45(1)	-7(1)	11(1)	1(1)
Br(2)	43(1)	54(1)	65(2)	-7(1)	6(1)	-16(1)
Br(3)	57(1)	51(1)	41(1)	9(1)	4(1)	2(1)
Br(4)	42(1)	55(1)	60(1)	3(1)	5(1)	-5(1)
Br(5)	70(2)	50(2)	93(2)	0(1)	13(2)	28(2)
N(1)	53(9)	48(8)	43(7)	-1(7)	5(7)	3(6)
N(2)	44(7)	38(7)	35(6)	-4(6)	19(6)	3(5)
C(3)	67(12)	69(13)	39(8)	8(10)	-4(8)	-19(9)
C(4)	65(12)	70(13)	42(9)	-5(11)	6(8)	7(9)
N(5)	60(9)	27(6)	77(11)	-5(7)	5(8)	7(7)
N(6)	37(8)	46(9)	122(16)	-9(7)	2(9)	16(10)
C(8)	75(12)	38(8)	37(8)	-6(8)	22(8)	-7(7)
C(9)	57(11)	57(11)	37(8)	-2(9)	3(7)	15(8)
C(10)	76(14)	48(10)	56(10)	-15(10)	2(10)	10(9)
C(11)	80(15)	50(12)	79(14)	-13(11)	11(12)	0(10)
C(12)	63(13)	72(14)	74(14)	-5(11)	1(11)	37(12)
C(13)	56(11)	36(8)	78(13)	-10(8)	19(10)	-16(9)

C(14)	62(14)	98(19)	85(16)	14(13)	9(12)	-45(15)
C(15)	63(12)	51(10)	63(12)	13(9)	18(10)	3(9)

The anisotropic displacement factor exponent takes the form: $-2\pi^2[h^2a^{*2}U_{11} + ... + 2hka^*b^*U_{12}]$.

Table C18. Anisotropic displacement parameters ($Å^2x10^3$) for $(2,6\text{-dmpz})_2Pb_2Br_{10}$ at 296.15 K with estimated standard deviations in parentheses.

Label	U_{11}	U_{22}	U_{33}	U_{12}	U_{13}	U_{23}
Pb(01)	20(1)	27(1)	32(1)	-2(1)	-4(1)	-7(1)
Pb(02)	23(1)	26(1)	29(1)	0(1)	-4(1)	-6(1)
Br(03)	19(2)	33(1)	39(1)	-2(1)	-4(1)	-13(1)
Br(04)	23(2)	47(1)	29(1)	-1(1)	-5(1)	-9(1)
Br(05)	25(2)	38(1)	37(1)	-1(1)	-6(1)	-15(1)
Br(06)	30(2)	30(1)	43(1)	-4(1)	-3(1)	-8(1)
Br(07)	49(2)	31(1)	40(1)	5(1)	-9(1)	-13(1)
Br(08)	38(2)	45(1)	38(1)	3(1)	-10(1)	-15(1)
Br(09)	27(2)	32(1)	41(1)	0(1)	-5(1)	-9(1)
Br(0A)	20(2)	34(1)	60(2)	-1(1)	-7(1)	6(1)
Br(0B)	19(2)	38(1)	51(1)	0(1)	-7(1)	-19(1)
Br(0C)	20(2)	76(2)	60(2)	1(1)	-7(1)	-44(2)
N(00D)	22(11)	23(7)	26(7)	-1(5)	-6(6)	-7(5)
N(00E)	39(12)	24(7)	27(7)	-9(6)	-7(7)	-8(6)
N(00F)	27(12)	15(7)	53(9)	-8(6)	5(7)	-5(6)
N(00G)	49(14)	30(8)	27(7)	-9(7)	-5(7)	-9(6)
N(00H)	0(11)	31(8)	52(9)	5(5)	1(7)	-7(6)
N(00I)	12(11)	41(8)	38(8)	3(6)	-4(7)	-19(6)
C(00J)	27(14)	25(8)	29(9)	-5(7)	-6(8)	-8(7)
C(00K)	50(16)	12(8)	50(11)	-3(7)	-14(10)	-14(7)
C(00L)	70(16)	7(7)	18(8)	-11(7)	-18(8)	3(6)
C(00M)	53(17)	17(8)	33(9)	-4(7)	-20(9)	2(7)
C00N()	38(16)	34(9)	33(10)	-10(8)	-12(9)	-3(8)
C(00O)	11(13)	28(8)	30(8)	-3(6)	-5(7)	-10(7)
C(00P)	7(13)	25(8)	40(9)	10(6)	-4(8)	-16(7)
C(00Q)	33(15)	43(10)	28(9)	3(8)	-15(9)	-5(8)
C(00R)	46(18)	29(9)	43(10)	9(8)	2(9)	-20(8)
C(00S)	54(19)	47(11)	27(9)	5(9)	-13(9)	-14(8)

C(00T)	29(15)	14(8)	51(11)	0(7)	0(9)	1(7)
C(00U)	33(15)	60(11)	7(7)	-7(9)	-3(7)	-14(7)
C(00V)	50(20)	61(13)	34(10)	-20(11)	-10(10)	1(9)
C(00W)	22(14)	35(9)	25(8)	1(7)	0(7)	-13(7)
C(00X)	21(17)	57(12)	43(11)	4(9)	7(9)	-23(9)
C(00Y)	80(20)	52(12)	27(10)	1(11)	-7(10)	-10(9)
C(00Z)	70(20)	48(12)	47(12)	12(11)	-20(12)	-8(10)
C(010)	46(18)	30(10)	50(12)	-7(8)	-15(11)	15(8)

The anisotropic displacement factor exponent takes the form: $-2\pi^2[h^2a^{*2}U_{11} + ... \quad + 2hka^*b^*U_{12}]$.

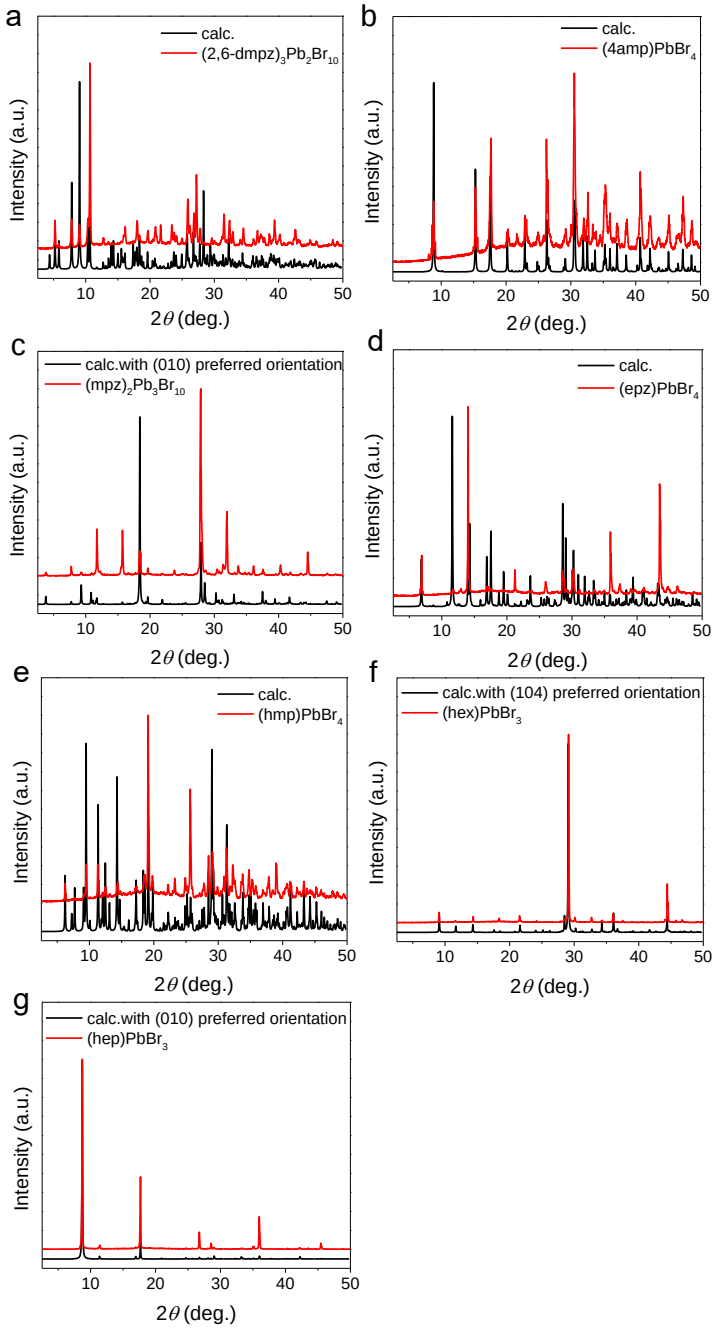

Figure C1. Experimental and calculated Powder X-ray diffraction (PXRD) patterns of (a) (2,6-dmpz)$_3$Pb$_2$Br$_{10}$, (b) (4amp)PbBr$_4$, (c) (mpz)$_2$Pb$_3$Br$_{10}$, (d) (epz)PbBr$_4$, (e) (hmp)PbBr$_4$, (f) (hep)PbBr$_3$ and (g) (hex)PbBr$_3$. PXRD analysis was performed using a Rigaku Miniflex600 powder X-ray diffractometer (Cu Kα graphite, λ = 1.5406 Å) operating at 40 kV/15 mA with a Kβ foil filter. Calculated patterns were simulated using the Mercury software.[1]

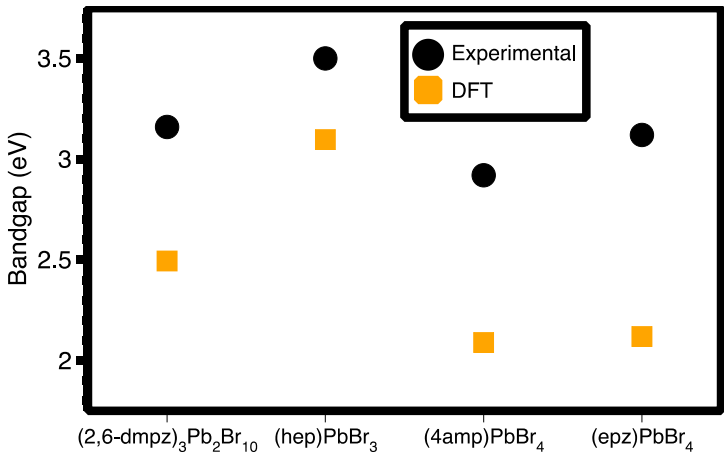

Figure C2. Comparison of the calculated and experimental band gaps of $(2,6\text{-dmpz})_3Pb_2Br_{10}$, $(hep)PbBr_3$, $(4amp)PbBr_4$ and $(epz)PbBr_4$.

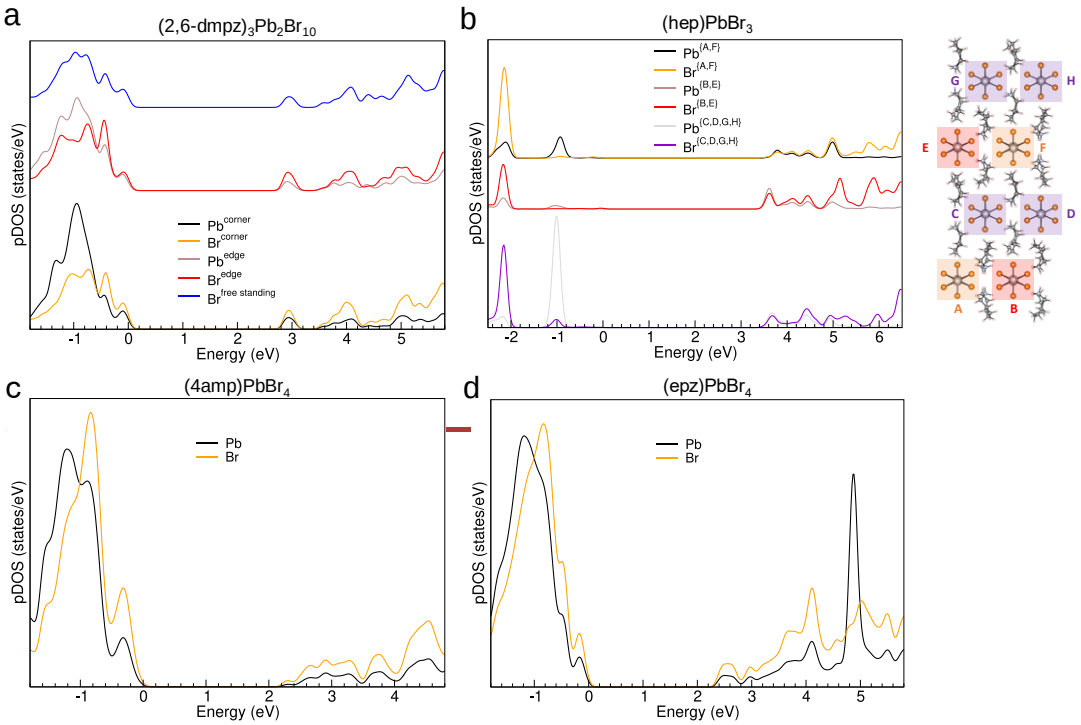

Figure C3. Projected density of states (PDOS) of (a) $(2,6\text{-dmpz})_3Pb_2Br_{10}$, (b) $(hep)PbBr_3$, (c) $(4amp)PbBr_4$ and (d) $(epz)PbBr_4$.

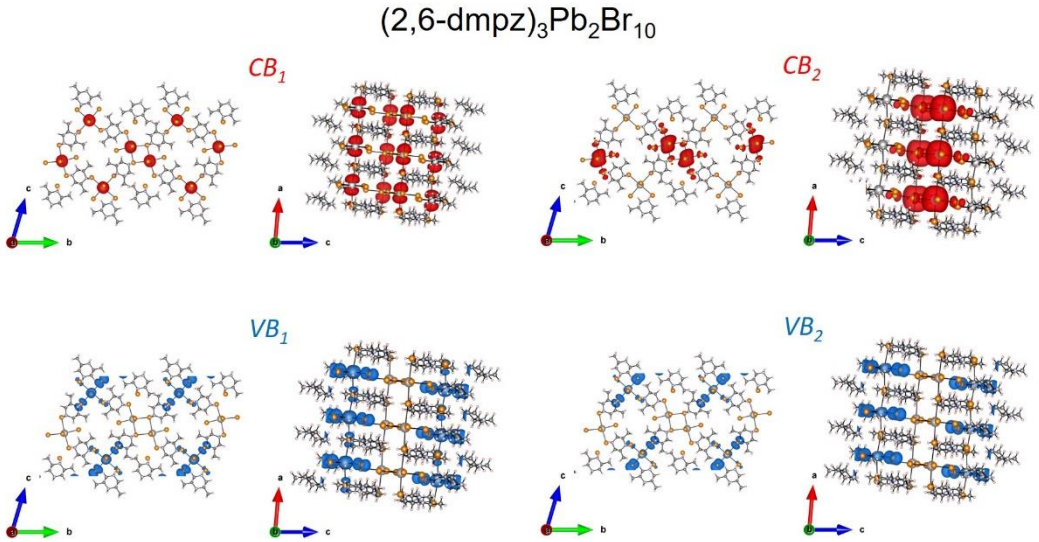

Figure C4. Localized density of states of the conduction band and valence band of (2,6-dmpz)$_3$Pb$_2$Br$_{10}$. CB$_1$ and VB$_1$ are the conduction band minimum and valence band maximum, respectively.

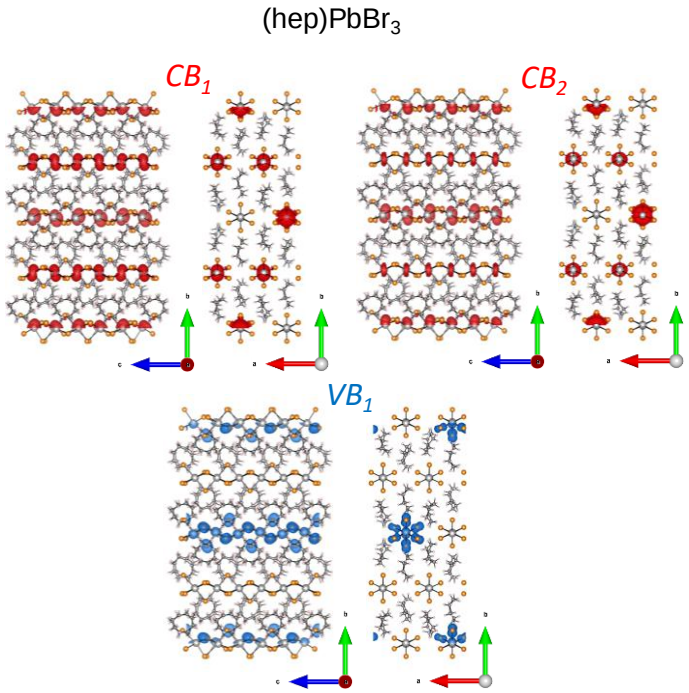

Figure C5. Localized density of states of the conduction band and valence band of (hep)PbBr$_3$. CB$_1$ and VB$_1$ are the conduction band minimum and valence band maximum, respectively.

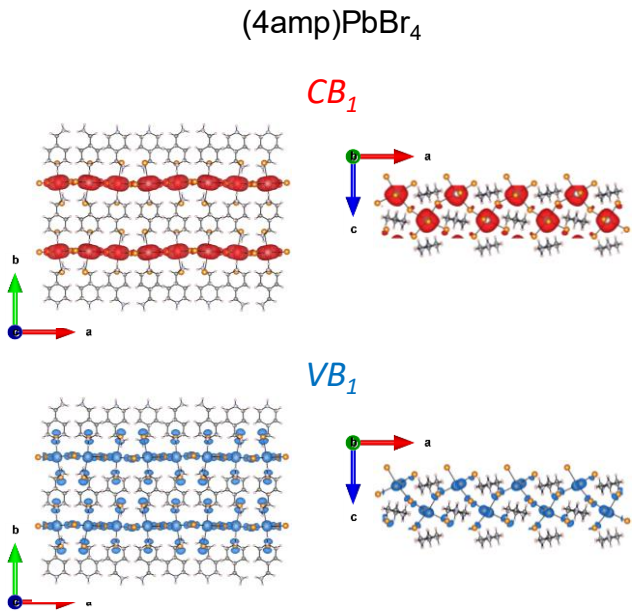

Figure C6. Localized density of states of the conduction band and valence band of (4amp)$PbBr_4$.

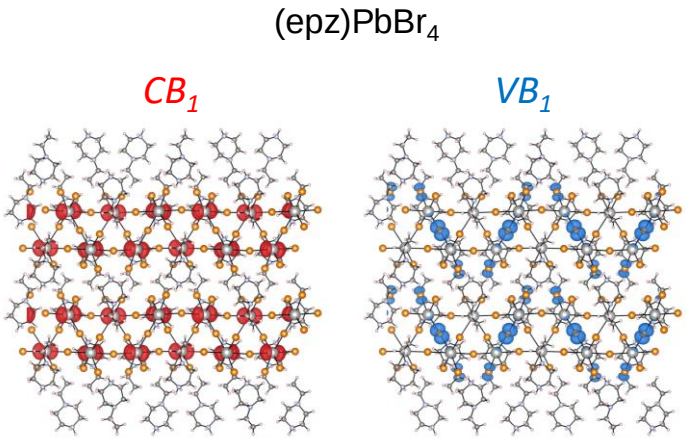

Figure C7. Localized density of states of the conduction band and valence band of (epz)$PbBr_4$.

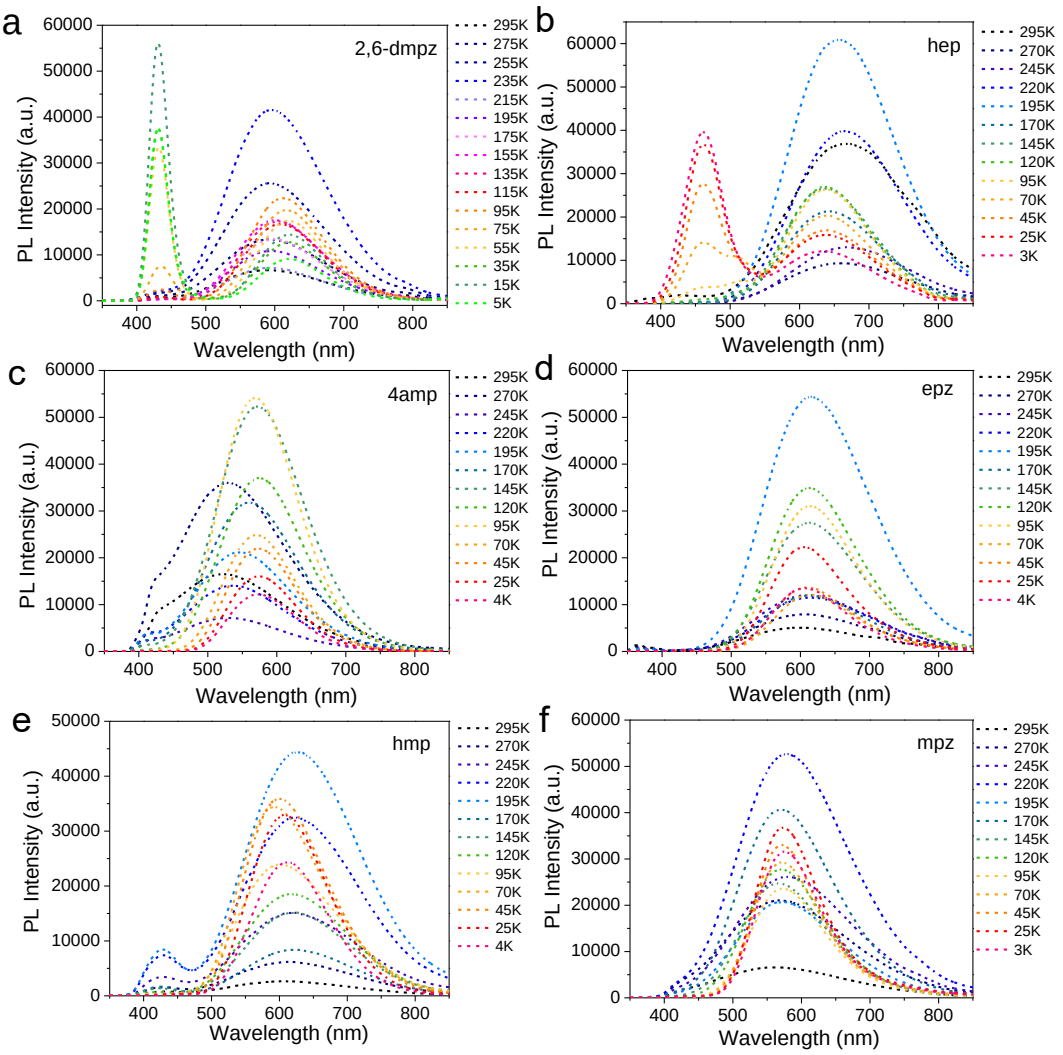

Figure C8. Unnormalized steady-state PL spectra of (a) $(2,6\text{-dmpz})_3Pb_2Br_{10}$, (b) $(hep)PbBr_3$, (c) $(4amp)PbBr_4$, (d) $(epz)PbBr_4$, (e) $(hmp)PbBr_4$ and (f) $(mpz)_2Pb_3Br_{10}$.

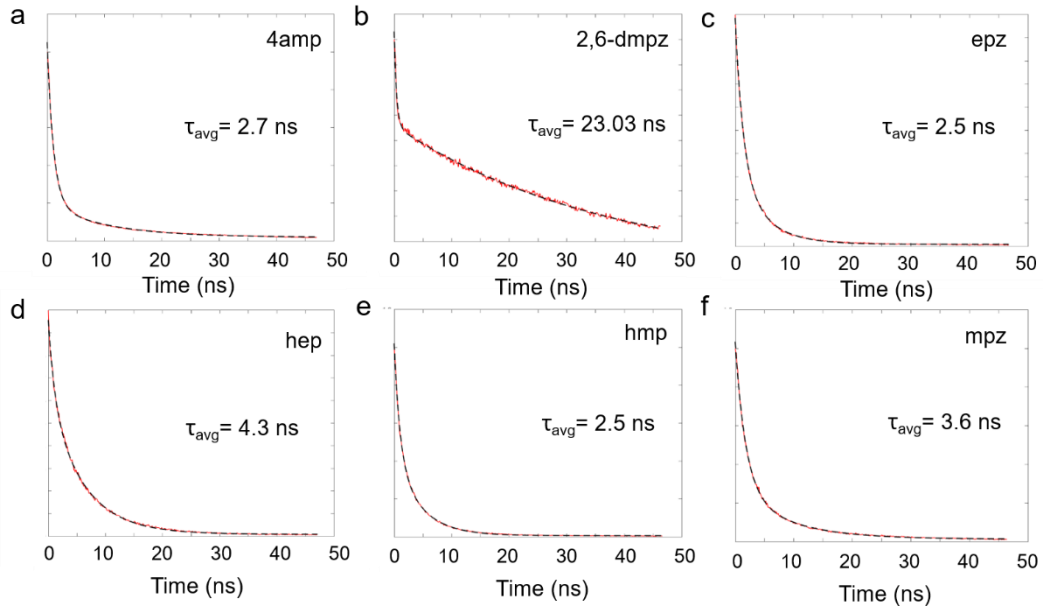

Figure C9. Time-resolved PL decay of (a) (4amp)$PbBr_4$, (b) (2,6-dmpz)$_3Pb_2Br_{10}$, (c) (epz)$PbBr_4$, (d) (hep)$PbBr_3$, (e) (hmp)$PbBr_4$, (f) (mpz)$_2Pb_3Br_{10}$.

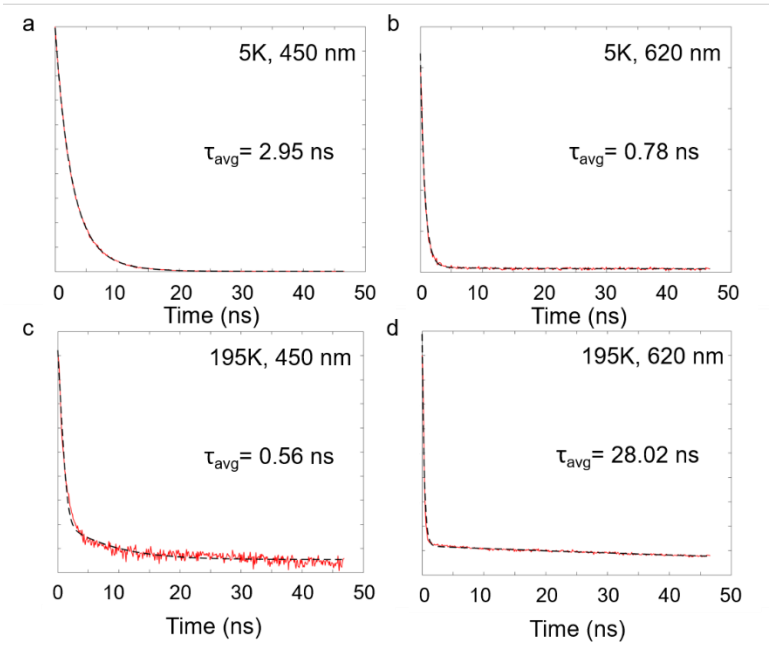

Figure C10. Time-resolved PL decay of (2,6-dmpz)$_3Pb_2Br_{10}$ at different temperatures and emission wavelength.

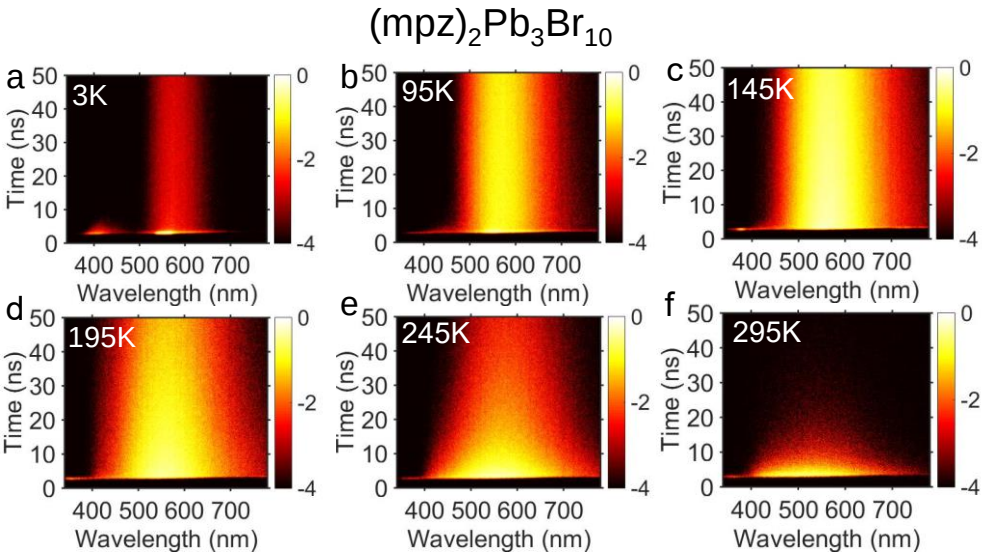

Figure C11. 2D time-resolved PL spectra of $(mpz)_2Pb_3Br_{10}$ at different temperatures.

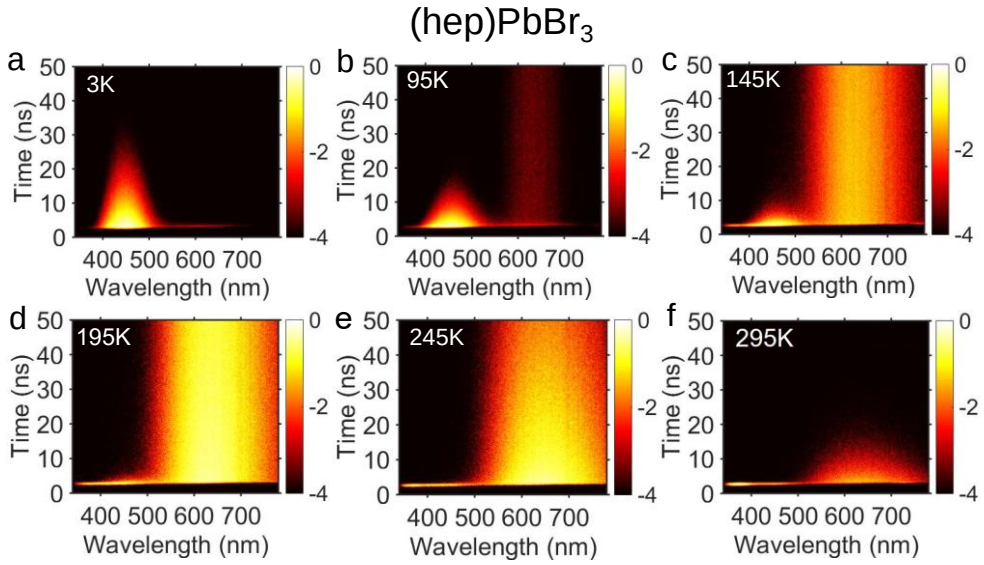

Figure C12. 2D time-resolved PL spectra of $(hep)PbBr_3$ at different temperatures.

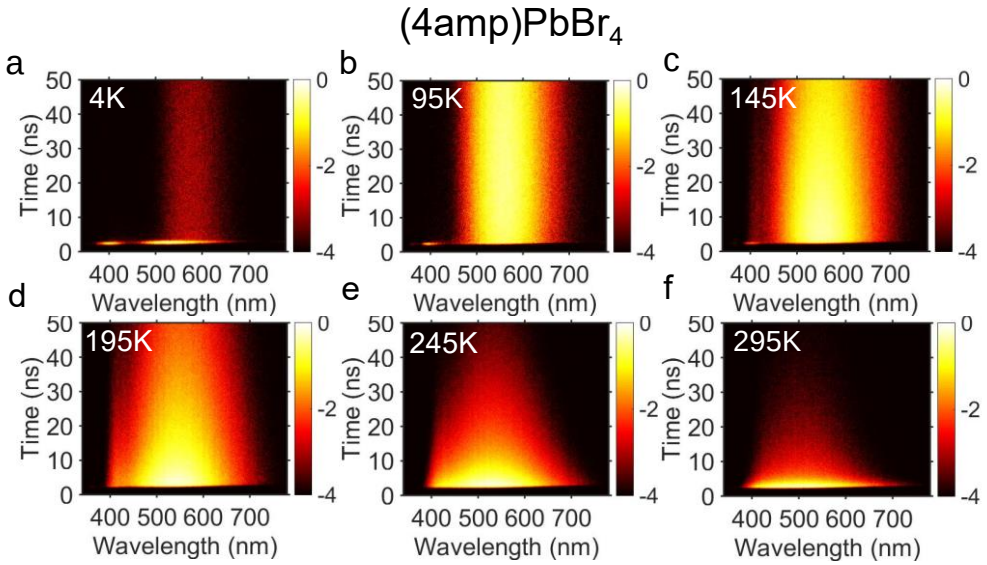

Figure C13. 2D time-resolved PL spectra of (4amp)$PbBr_4$ at different temperatures.

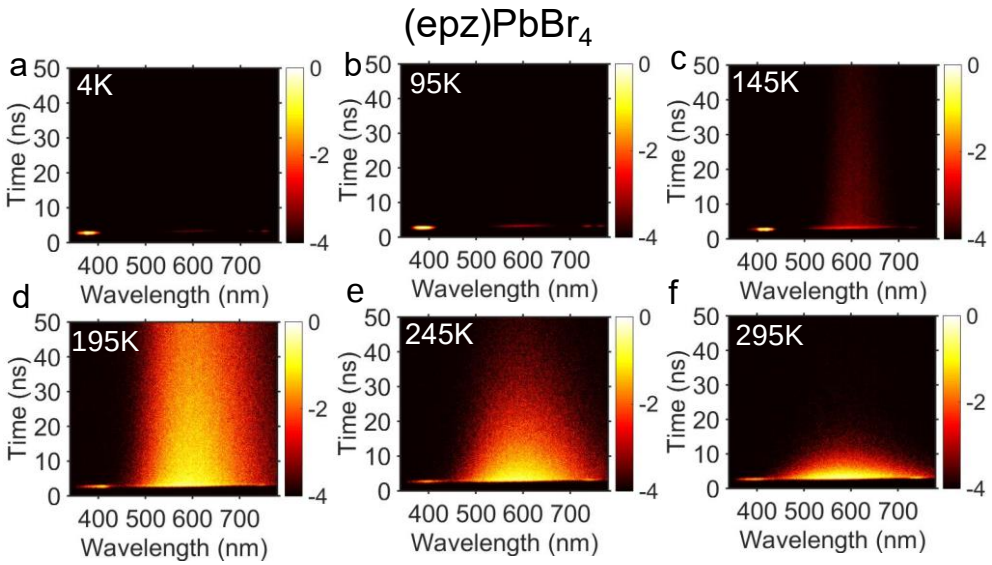

Figure C14. 2D time-resolved PL spectra of (epz)$PbBr_4$ at different temperatures.

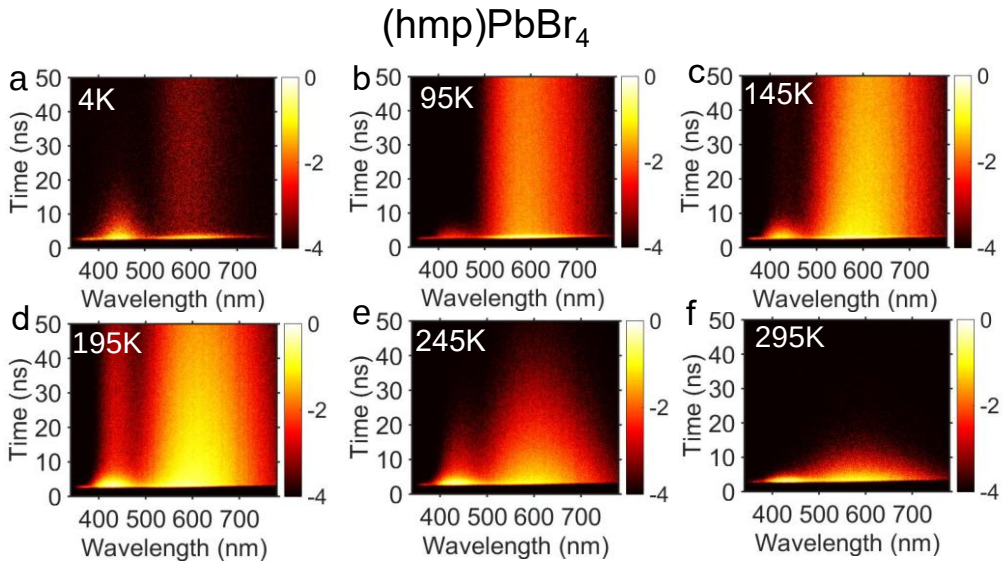

Figure C15. 2D time-resolved PL spectra of (hmp)$PbBr_4$ at different temperatures.

References

1. Macrae, C. F.; Bruno, I. J.; Chisholm, J. A.; Edgington, P. R.; McCabe, P.; Pidcock, E.; Rodriguez-Monge, L.; Taylor, R.; van de Streek, J.; Wood, P. A., *J. Appl. Crystallogr.* **2008,** *41*, 466-470.

APPENDIX D

Supporting Information for Chapter 5

Table D1. Pb-I bond lengths and Pb-I-Pb angles in $3AMPPbI_4$.

Label	Distances (Å)	Label	Angles (°)
Pb(1)-I(1)	3.223(3)	Pb(1)-I(3)-Pb(2)#8	168.83(17)
Pb(1)-I(2)	3.143(3)	Pb(1)-I(4)-Pb(3)#8	163.39(15)
Pb(1)-I(3)	3.164(5)	Pb(1)-I(5)-Pb(2)	164.43(17)
Pb(1)-I(4)	3.225(6)	Pb(1)-I(7)-Pb(3)	163.94(14)
Pb(1)-I(5)	3.208(5)		
Pb(1)-I(7)	3.241(5)		
Pb(2)-I(3)#1	3.196(4)		
Pb(2)-I(5)	3.199(5)		
Pb(2)-I(6)	3.186(3)		
Pb(3)-I(4)#1	3.151(5)		
Pb(3)-I(7)	3.149(4)		
Pb(3)-I(8)	3.164(3)		

Table D2. Pb-I bond lengths and Pb-I-Pb angles in $4AMPPbI_4$.

Label	Distances (Å)	Label	Angles (°)
Pb(1)-I(1)	3.329(7)	Pb(1)-I(1)-Pb(2)#11	154.59(18)
Pb(1)-I(2)	3.108(9)	Pb(1)-I(4)-Pb(1)#5	154.37(18)
Pb(1)-I(3)	3.213(9)	Pb(1)-I(5)-Pb(2)	154.3(2)
Pb(1)-I(4)	3.170(5)	Pb(2)-I(8)-Pb(2)#9	154.2(3)
Pb(1)-I(4)#1	3.258(4)		
Pb(1)-I(5)	3.166(6)		
Pb(2)-I(1)#2	3.107(7)		
Pb(2)-I(5)	3.268(6)		
Pb(2)-I(6)	3.138(11)		
Pb(2)-I(7)	3.246(10)		
Pb(2)-I(8)	3.160(6)		
Pb(2)-I(8)#3	3.270(6)		

Table D3. Pb-I bond lengths and Pb-I-Pb angles in 3AMP(MA)Pb_2I_7.

Label	Distances (Å)	Label	Angles (°)
Pb(1)-I(1)	3.219(3)	Pb(1)-I(1)-Pb(2)	180.0(5)
Pb(1)-I(2)	3.1383(19)	Pb(2)-I(4)-Pb(2)#9	163.40(6)
Pb(1)-I(5)	3.1650(19)	Pb(1)-I(5)-Pb(1)#10	163.16(6)
Pb(1)-I(5)#1	3.1669(18)	Pb(2)#2-I(6)-Pb(2)#9	163.13(6)
Pb(1)-I(7)#2	3.1682(18)	Pb(1)#4-I(7)-Pb(1)#10	162.85(6)
Pb(1)-I(7)#1	3.1681(18)		
Pb(2)-I(1)	3.198(3)		
Pb(2)-I(3)	3.1276(18)		
Pb(2)-I(4)	3.1642(18)		
Pb(2)-I(4)#3	3.1652(18)		
Pb(2)-I(6)#4	3.1667(17)		
Pb(2)-I(6)#3	3.1678(18)		

Table D4. Pb-I bond lengths and Pb-I-Pb angles in 4AMP(MA)Pb_2I_7.

Label	Distances (Å)	Label	Angles (°)
Pb(1)-I(1)	3.233(5)	Pb(1)-I(1)-Pb(2)	179.80(19)
Pb(1)-I(2)	3.090(4)	Pb(2)-I(4)-Pb(2)#9	156.38(10)
Pb(1)-I(5)	3.192(3)	Pb(1)-I(5)-Pb(1)#10	156.81(10)
Pb(1)-I(5)#1	3.193(3)	Pb(2)#2-I(6)-Pb(2)#9	156.08(10)
Pb(1)-I(7)#2	3.185(3)	Pb(1)#4-I(7)-Pb(1)#10	156.48(10)
Pb(1)-I(7)#1	3.200(3)		
Pb(2)-I(1)	3.266(5)		
Pb(2)-I(3)	3.097(3)		
Pb(2)-I(4)	3.188(3)		
Pb(2)-I(4)#3	3.202(3)		
Pb(2)-I(6)#4	3.198(3)		
Pb(2)-I(6)#3	3.191(3)		

Table D5. Pb-I bond lengths and Pb-I-Pb angles in 3AMP$(MA)_2Pb_3I_{10}$.

Label	Distances (Å)	Label	Angles (°)
Pb(1)-I(2)	3.203(4)	Pb(1)-I(2)-Pb(1)#3	156.53(14)
Pb(1)-I(2)#1	3.196(4)	Pb(1)-I(3)-Pb(1)#5	156.57(13)
Pb(1)-I(3)	3.198(4)	Pb(1)-I(4)-Pb(2)	179.84(18)
Pb(1)-I(3)#2	3.203(4)	Pb(1)-I(5)-Pb(3)	179.88(16)
Pb(1)-I(4)	3.185(5)	Pb(2)-I(6)-Pb(2)#5	166.15(15)
Pb(1)-I(5)	3.130(4)	Pb(3)#10-I(7)-Pb(3)#2	167.96(15)
Pb(2)-I(4)	3.178(4)	Pb(2)-I(8)-Pb(2)#1	166.26(15)
Pb(2)-I(6)	3.153(4)	Pb(3)-I(9)-Pb(3)#2	167.80(15)
Pb(2)-I(6)#2	3.158(4)		
Pb(2)-I(8)	3.153(4)		
Pb(2)-I(8)#3	3.160(4)		
Pb(2)-I(10)	3.120(4)		
Pb(3)-I(1)	3.093(3)		
Pb(3)-I(5)	3.304(4)		
Pb(3)-I(7)#4	3.153(4)		
Pb(3)-I(7)#5	3.149(4)		
Pb(3)-I(9)	3.153(4)		
Pb(3)-I(9)#5	3.148(4)		

Table D6. Pb-I bond lengths and Pb-I-Pb angles in $4AMP(MA)_2Pb_3I_{10}$.

Label	Distances (Å)	Label	Angles (°)
Pb(1)-I(2)	3.184(3)	Pb(1)-I(2)-Pb(1)#5	157.73(10)
Pb(1)-I(2)#1	3.184(3)	Pb(1)#11-I(3)-Pb(1)#7	157.80(10)
Pb(1)-I(3)#2	3.183(3)	Pb(1)-I(4)-Pb(2)	179.60(14)
Pb(1)-I(3)#3	3.184(3)	Pb(1)#11-I(5)-Pb(3)	179.58(15)
Pb(1)-I(4)	3.174(4)	Pb(2)#6-I(6)-Pb(2)#1	157.01(10)
Pb(1)-I(5)#2	3.171(4)	Pb(3)#4-I(7)-Pb(3)#7	157.37(10)
Pb(2)-I(4)	3.258(4)	Pb(2)-I(8)-Pb(2)#1	156.95(10)
Pb(2)-I(6)#4	3.185(3)	Pb(3)-I(9)-Pb(3)#7	157.38(10)
Pb(2)-I(6)#5	3.189(3)		
Pb(2)-I(8)	3.186(3)		
Pb(2)-I(8)#5	3.193(3)		
Pb(2)-I(10)	3.087(3)		
Pb(3)-I(1)	3.061(4)		
Pb(3)-I(5)	3.278(4)		
Pb(3)-I(7)#6	3.186(3)		
Pb(3)-I(7)#3	3.187(3)		
Pb(3)-I(9)	3.188(3)		
Pb(3)-I(9)#3	3.182(3)		

Table D7. Pb-I bond lengths and Pb-I-Pb angles in 3AMP$(MA)_3Pb_4I_{13}$.

Label	Distances (Å)	Label	Angles (°)
Pb(4)-I(1)	3.197(6)	Pb(1)-I(2)-Pb(1)#4	158.61(18)
Pb(4)-I(3)	3.196(5)	Pb(4)-I(3)-Pb(3)	176.42(18)
Pb(4)-I(6)	3.175(7)	Pb(1)-I(4)-Pb(2)	176.6(2)
Pb(4)-I(6)#1	3.138(8)	Pb(4)-I(6)-Pb(4)#4	165.7(3)
Pb(4)-I(7)	3.176(8)	Pb(4)-I(7)-Pb(4)#3	166.2(3)
Pb(4)-I(7)#2	3.143(7)	Pb(3)-I(9)-Pb(3)#3	158.13(18)
Pb(1)-I(2)	3.202(5)	Pb(1)-I(10)-Pb(3)	176.4(2)
Pb(1)-I(2)#1	3.170(6)	Pb(3)-I(11)-Pb(3)#4	157.98(19)
Pb(1)-I(4)	3.112(5)	Pb(1)-I(12)-Pb(1)#3	158.46(19)
Pb(1)-I(10)	3.251(6)	Pb(2)-I(14)-Pb(2)#2	166.2(3)
Pb(1)-I(12)	3.210(6)	Pb(2)-I(15)-Pb(2)#1	166.2(3)
Pb(1)-I(12)#2	3.179(6)		
Pb(2)-I(4)	3.313(5)		
Pb(2)-I(8)	3.060(5)		
Pb(2)-I(14)	3.141(8)		
Pb(2)-I(14)#3	3.168(7)		
Pb(2)-I(15)	3.146(8)		
Pb(2)-I(15)#4	3.174(8)		
Pb(3)-I(3)	3.173(5)		
Pb(3)-I(9)	3.204(5)		
Pb(3)-I(9)#2	3.174(6)		
Pb(3)-I(10)	3.131(6)		
Pb(3)-I(11)	3.216(6)		
Pb(3)-I(11)#1	3.178(5)		

Table D8. Pb-I bond lengths and Pb-I-Pb angles in 4AMP$(MA)_3Pb_4I_{13}$.

Label	Distances (Å)	Label	Angles (°)
Pb(1)-I(1)	3.137(9)	Pb(1)-I(2)-Pb(4)	178.9(3)
Pb(1)-I(2)	3.254(7)	Pb(2)-I(3)-Pb(3)	178.6(3)
Pb(1)-I(4)	3.170(7)	Pb(1)-I(4)-Pb(1)#4	157.9(2)
Pb(1)-I(4)#1	3.177(7)	Pb(1)-I(5)-Pb(1)#3	158.6(2)
Pb(1)-I(5)	3.211(7)	Pb(4)-I(7)-Pb(4)#3	160.3(2)
Pb(1)-I(5)#2	3.199(7)	Pb(2)-I(8)-Pb(4)	178.3(4)
Pb(2)-I(3)	3.122(8)	Pb(4)-I(9)-Pb(4)#4	160.5(2)
Pb(2)-I(8)	3.214(10)	Pb(2)-I(10)-Pb(2)#3	162.5(3)
Pb(2)-I(10)	3.116(8)	Pb(3)-I(11)-Pb(3)#2	157.7(3)
Pb(2)-I(10)#2	3.172(8)	Pb(3)-I(12)-Pb(3)#1	158.4(2)
Pb(2)-I(13)	3.181(7)	Pb(2)-I(13)-Pb(2)#4	161.7(2)
Pb(2)-I(13)#1	3.212(7)		
Pb(3)-I(3)	3.284(8)		
Pb(3)-I(6)	3.004(8)		
Pb(3)-I(11)	3.168(8)		
Pb(3)-I(11)#3	3.182(8)		
Pb(3)-I(12)	3.213(7)		
Pb(3)-I(12)#4	3.197(7)		
Pb(4)-I(2)	3.175(7)		
Pb(4)-I(7)	3.173(7)		
Pb(4)-I(7)#2	3.229(8)		
Pb(4)-I(8)	3.166(10)		
Pb(4)-I(9)	3.142(7)		
Pb(4)-I(9)#1	3.169(7)		

Table D9. Atomic coordinates ($x10^4$) and equivalent isotropic displacement parameters ($Å^2x10^3$) for $3AMPPbI_4$ at 293 K with estimated standard deviations in parentheses.

Label	x	y	z	Occupancy	U_{eq}^*
Pb(1)	-44(2)	2492(1)	-75(1)	1	32(1)
Pb(2)	5000	5000	0	1	33(1)
Pb(3)	5000	0	0	1	33(1)
I(1)	493(5)	2086(2)	1478(2)	1	51(2)
I(2)	-517(5)	2692(2)	-1620(2)	1	47(2)
I(3)	-2462(4)	3729(3)	115(2)	1	55(2)
I(4)	-2699(6)	1250(3)	-263(2)	1	70(2)
I(5)	2779(6)	3637(3)	123(2)	1	69(2)
I(6)	4553(5)	4770(2)	-1563(2)	1	46(2)
I(7)	2234(4)	1126(3)	-216(2)	1	49(2)
I(8)	4422(5)	-443(2)	-1515(2)	1	57(2)
N(1)	6340(40)	7974(13)	-3018(12)	1	62(4)
N(2)	4570(50)	7642(19)	-1117(16)	1	62(4)
C(1)	4360(50)	7035(16)	-1612(12)	1	62(4)
C(2)	5060(30)	7232(11)	-2212(9)	1	62(4)
C(3)	5260(40)	7961(10)	-2515(12)	1	62(4)
C(4)	6150(40)	7351(15)	-3497(10)	1	62(4)
C(5)	5950(40)	6623(13)	-3195(12)	1	62(4)
C(6)	4870(40)	6610(11)	-2691(11)	1	62(4)
N(3)	8830(40)	4502(14)	-1900(14)	1	65(4)
N(4)	10660(50)	4800(20)	-3859(15)	1	65(4)
C(7)	10880(40)	5271(18)	-3251(12)	1	65(4)
C(8)	10200(30)	5313(13)	-2624(9)	1	65(4)
C(9)	10350(40)	5893(13)	-2104(11)	1	65(4)
C(10)	9210(40)	5836(14)	-1625(13)	1	65(4)
C(11)	8980(40)	5083(16)	-1380(11)	1	65(4)
C(12)	9960(40)	4560(12)	-2378(13)	1	65(4)
H(1c1)	4853.68	6604.9	-1413.44	1	75
H(2c1)	3265	6937	-1742.07	1	75
H(1c2)	6047.57	7361.41	-1953.38	1	75
H(1c3)	5610.41	8305.52	-2170.57	1	75

H(2c3)	4254.39	8145.99	-2710.1	1	75
H(1c4)	7024.51	7337.8	-3730.6	1	75
H(2c4)	5280.13	7443.87	-3841.68	1	75
H(1c5)	6956.89	6437.9	-2999.28	1	75
H(2c5)	5600.85	6278.26	-3538.79	1	75
H(1c6)	3811.03	6589.75	-2913.2	1	75
H(2c6)	4999.54	6160.68	-2450.55	1	75
H(1c7)	11933.6	5454.05	-3171.48	1	78
H(2c7)	11227.93	5744.74	-3359.91	1	78
H(1c8)	9349	5615.63	-2821.38	1	78
H(1c9)	10246.17	6361.18	-2312.81	1	78
H(2c9)	11392.6	5897.46	-1863.57	1	78
H(1c10)	9533.19	6150.93	-1254.78	1	78
H(2c10)	8220.97	6033.6	-1823.68	1	78
H(1c11)	9816.81	4964.06	-1029.9	1	78
H(2c11)	8073.97	5074.79	-1163.15	1	78
H(1c12)	9640.61	4244.57	-2748.84	1	78
H(2c12)	10953.15	4361.46	-2179.98	1	78
H(1n1)	6223.91	8380.86	-3236.12	1	75
H(2n1)	7300.57	7991.76	-2816.87	1	75
H(1n2)	3656.9	7807.94	-1063.86	1	75
H(2n2)	5060.24	7482.35	-740.51	1	75
H(3n2)	5106.92	7989	-1260.55	1	75
H(1n3)	7879.98	4498.97	-2117.42	1	78
H(2n3)	8918.41	4078.36	-1710.4	1	78
H(1n4)	11125.31	5002.19	-4160.62	1	78
H(2n4)	11061.8	4376.59	-3759.84	1	78
H(3n4)	9668.69	4759.36	-4009.36	1	78

*U_{eq} is defined as one third of the trace of the orthogonalized U_{ij} tensor.

Table D10. Atomic coordinates (x10^4) and equivalent isotropic displacement parameters (Å^{2}x10^3) for 4AMPPbI$_4$ at 293 K with estimated standard deviations in parentheses.

Label	x	y	z	Occupancy	U_{eq}*
Pb(1)	-7(3)	4916(3)	31(2)	1	32(1)
Pb(2)	-9(4)	-82(3)	210(2)	1	43(2)

I(1)	32(8)	7488(5)	686(4)	1	68(3)
I(2)	-2955(7)	4760(10)	-127(6)	1	119(4)
I(3)	3036(8)	4679(8)	-99(6)	1	106(4)
I(4)	45(6)	5565(4)	-2414(3)	1	41(2)
I(5)	33(8)	2439(4)	-451(4)	1	59(2)
I(6)	-2995(9)	-17(9)	284(7)	1	107(3)
I(7)	3081(9)	-79(10)	242(6)	1	108(4)
I(8)	77(10)	-568(6)	-2264(4)	1	96(3)
N(1)	2620(30)	2740(70)	2040(40)	1	133(11)
N(2)	7520(40)	2210(50)	2510(30)	1	133(11)
C(1)	3540(30)	2850(60)	2950(30)	1	133(11)
C(2)	4850(30)	2560(40)	2575(18)	1	133(11)
C(3)	5590(30)	2770(50)	3576(18)	1	133(11)
C(4)	6920(30)	2340(60)	3580(30)	1	133(11)
C(5)	6950(30)	2890(40)	1640(30)	1	133(11)
C(6)	5530(30)	2840(60)	1558(19)	1	133(11)
N(3)	7260(30)	1340(40)	-2200(30)	1	97(6)
N(4)	2950(30)	2470(40)	-2290(30)	1	97(6)
C(7)	7060(30)	2510(40)	-2380(40)	1	97(6)
C(8)	5660(30)	2750(20)	-2350(20)	1	97(6)
C(9)	5150(30)	1660(30)	-2090(30)	1	97(6)
C(10)	3770(30)	1640(40)	-1760(30)	1	97(6)
C(11)	3530(30)	2980(30)	-3260(20)	1	97(6)
C(12)	4860(40)	3380(30)	-3110(30)	1	97(6)
H(1c1)	3286.03	2375.99	3514.52	1	159.8
H(2c1)	3531.47	3567.8	3198.95	1	159.8
H(1c2)	4758.19	1863.76	2260.62	1	159.8
H(1c3)	5612.88	3528.27	3705.27	1	159.8
H(2c3)	5129.16	2502.12	4179.31	1	159.8
H(1c4)	7450.16	2783.6	4021.08	1	159.8
H(2c4)	6929.35	1667.21	3952.04	1	159.8
H(1c5)	7320.36	2699.27	967.49	1	159.8
H(2c5)	7208.87	3614.75	1739.29	1	159.8
H(1c6)	5290.71	2337.67	1011.11	1	159.8

H(2c6)	5207.3	3502.78	1292.2	1	159.8
H(1c7)	7403.73	2704.18	-3059.67	1	116.5
H(2c7)	7484.07	2904.31	-1826.5	1	116.5
H(1c8)	5586.79	3357.69	-1893.93	1	116.5
H(1c9)	5657.47	1350.81	-1530.34	1	116.5
H(2c9)	5280.42	1193.13	-2679.05	1	116.5
H(1c10)	3429.75	945.16	-1898.07	1	116.5
H(2c10)	3708.2	1712.58	-1003.84	1	116.5
H(1c11)	3504.26	2493.96	-3848.26	1	116.5
H(2c11)	2991.94	3557.16	-3491.73	1	116.5
H(1c12)	4839.24	4114.59	-2884.32	1	116.5
H(2c12)	5279.6	3420.53	-3792.8	1	116.5
H(1n1)	2131.73	2185.2	2141.06	1	159.8
H(2n1)	2150.01	3308.22	1994.51	1	159.8
H(3n1)	3038.33	2655.15	1443.28	1	159.8
H(1n2)	7485.65	1542.92	2315.91	1	159.8
H(2n2)	8330	2336.29	2549.53	1	159.8
H(1n3)	6959.93	1159.52	-1575.68	1	116.5
H(2n3)	6876.76	976.99	-2692.53	1	116.5
H(3n3)	8075.73	1196.74	-2215.69	1	116.5
H(1n4)	2746.37	2952.88	-1831.06	1	116.5
H(2n4)	2223.96	2182.68	-2463.51	1	116.5

*U_{eq} is defined as one third of the trace of the orthogonalized U_{ij} tensor.

Table D11. Atomic coordinates (x10^4) and equivalent isotropic displacement parameters (Å^{2}x10^3) for 3AMP(MA)Pb_2I_7 at 250 K with estimated standard deviations in parentheses.

Label	x	y	z	Occupancy	U_{eq}*
Pb(1)	-33(1)	1(1)	1292(1)	1	35(1)
Pb(2)	-33(1)	-1(1)	3209(1)	1	30(1)
I(1)	-33(3)	-1(1)	2254(1)	1	65(1)
I(2)	-31(2)	-3(3)	355(1)	1	97(1)
I(3)	-33(2)	3(3)	4143(1)	1	96(1)
I(4)	2830(2)	-2136(2)	3198(1)	1	80(1)
I(5)	2834(2)	2131(2)	1306(1)	1	78(1)
I(6)	2097(2)	-7131(2)	3196(1)	1	80(1)

I(7)	2092(2)	7125(2)	1307(1)	1	78(1)
N(1)	4250(30)	630(30)	2357(11)	1	247(12)
N(2)	6030(30)	610(30)	296(7)	1	312(8)
N(3)	5760(50)	870(40)	-1045(8)	1	312(8)
C(1)	5460(40)	-550(40)	2330(13)	1	247(12)
C(2)	5350(30)	-300(20)	-392(7)	1	312(8)
C(3)	5690(40)	1020(20)	-129(7)	1	312(8)
C(4)	3810(30)	-400(30)	-208(8)	1	312(8)
C(5)	3790(30)	-1090(40)	201(9)	1	312(8)
C(6)	4930(50)	-360(30)	-826(7)	1	312(8)
C(7)	4850(40)	-350(40)	490(8)	1	312(8)
H(1c1)	5791.3	-642.62	2057.98	1	296.8
H(2c1)	6303.73	-255.41	2494.35	1	296.8
H(3c1)	5075.9	-1499.4	2421.36	1	296.8
H(1c4)	3151.02	-968.91	-380.92	1	374.8
H(2c4)	3362.01	584.2	-197.55	1	374.8
H(1c5)	2782.4	-1061.35	306.84	1	374.8
H(2c5)	4022.23	-2147.18	182.32	1	374.8
H(1c6)	5210.82	-1320.91	-934.7	1	374.8
H(2c6)	3865.94	-211.1	-854.89	1	374.8
H(1c7)	5330.72	-1112.01	651.15	1	374.8
H(2c7)	4285.69	242.7	677.48	1	374.8
H(1n1)	4568.48	1462.01	2249.3	1	296.8
H(2n1)	3450.88	314.12	2230.79	1	296.8
H(3n1)	4027.04	786.83	2606.59	1	296.8
H(1n2)	6901.28	154.25	307.07	1	374.8
H(2n2)	6161.52	1429.98	436.03	1	374.8
H(1n3)	5516.38	1739.44	-945.12	1	374.8
H(2n3)	6727.03	728.33	-1021.68	1	374.8
H(3n3)	5511.49	842.5	-1296.91	1	374.8
H(1c2)	6222.7	-940.88	-398.3	1	374.8
H(1c3)	4852.67	1715.6	-134.75	1	374.8
H(2c3)	6515.97	1583.86	-238.71	1	374.8

*U_{eq} is defined as one third of the trace of the orthogonalized U_{ij} tensor.

Table D12. Atomic coordinates ($x10^4$) and equivalent isotropic displacement parameters ($Å^2x10^3$) for 4AMP(MA)Pb_2I_7 at 250 K with estimated standard deviations in parentheses.

Label	x	y	z	Occupancy	U_{eq}^*
Pb(1)	-33(2)	-2(2)	1285(1)	1	33(1)
Pb(2)	-34(2)	2(2)	3219(1)	1	32(1)
I(1)	-40(6)	0(1)	2247(2)	1	55(1)
I(2)	-33(5)	2(4)	365(1)	1	140(3)
I(3)	-37(4)	-1(4)	4140(1)	1	133(2)
I(4)	2982(4)	-1973(2)	3204(2)	1	58(1)
I(5)	2979(4)	1987(2)	1293(2)	1	60(1)
I(6)	1941(4)	-6970(2)	3204(2)	1	58(1)
I(7)	1941(4)	6986(2)	1294(2)	1	59(1)
N(1)	4310(30)	470(40)	2387(9)	1	195(9)
N(2)	5360(20)	380(20)	483(5)	1	172(4)
N(3)	5380(30)	340(30)	-1064(4)	1	172(4)
C(1)	5640(30)	-570(40)	2353(12)	1	195(9)
C(2)	4951(16)	98(16)	-347(4)	1	149(10)
C(3)	6433(19)	720(30)	-205(5)	1	172(4)
C(4)	4320(20)	-1140(20)	-89(5)	1	172(4)
C(5)	4180(20)	-710(30)	342(5)	1	172(4)
C(6)	4500(30)	-480(30)	-749(5)	1	172(4)
C(7)	6749(17)	420(30)	227(5)	1	172(4)
H(1c1)	6203.44	-328.27	2117.51	1	234.4
H(2c1)	6277.85	-446.53	2582.57	1	234.4
H(3c1)	5295.22	-1596.42	2339.22	1	234.4
H(1c2)	4600.72	1125.82	-344.26	1	179
H(1c3)	6467.5	1788.58	-254.29	1	205.8
H(2c3)	7238.38	311.47	-363.49	1	205.8
H(1c4)	4939.19	-2022.26	-113.5	1	205.8
H(2c4)	3349.81	-1439.34	-189.49	1	205.8
H(1c5)	3191.54	-295.83	389.41	1	205.8
H(2c5)	4210.36	-1610.09	502.04	1	205.8
H(1c6)	4716.47	-1545.09	-765.12	1	205.8
H(2c6)	3441.97	-316.26	-789.95	1	205.8

H(1c7)	7292.96	-510.01	253.33	1	205.8
H(2c7)	7432.3	1178.63	326.4	1	205.8
H(1n1)	4181.55	949.42	2162.8	1	234.4
H(2n1)	3498.36	-55.05	2439.48	1	234.4
H(3n1)	4462.39	1119.78	2576.65	1	234.4
H(1n2)	4972.11	1280.7	498.31	1	205.8
H(2n2)	5615.26	158.63	726.02	1	205.8
H(1n3)	5118.85	7.63	-1297.47	1	205.8
H(2n3)	5197.91	1302.55	-1048.12	1	205.8
H(3n3)	6346.03	181.08	-1028.37	1	205.8

*U_{eq} is defined as one third of the trace of the orthogonalized U_{ij} tensor.

Table D13. Atomic coordinates ($x10^4$) and equivalent isotropic displacement parameters ($Å^2x10^3$) for $3AMP(MA)_2Pb_3I_{10}$ at 250 K with estimated standard deviations in parentheses.

Label	x	y	z	Occupancy	U_{eq}*
Pb(1)	4955(2)	5001(3)	4994(1)	1	29(1)
Pb(2)	4956(2)	4999(2)	7757(1)	1	30(1)
Pb(3)	4956(2)	4999(2)	2200(1)	1	29(1)
I(1)	4972(5)	5006(5)	858(2)	1	102(2)
I(2)	1935(4)	6986(3)	4968(2)	1	54(2)
I(3)	7969(4)	3018(3)	4968(2)	1	55(2)
I(4)	4951(6)	5002(4)	6377(2)	1	64(2)
I(5)	4952(5)	5002(4)	3635(2)	1	55(1)
I(6)	7163(4)	2211(5)	7709(2)	1	76(2)
I(7)	2718(4)	-2235(5)	2190(2)	1	80(2)
I(8)	7742(5)	7209(5)	7710(2)	1	77(2)
I(9)	2187(4)	2764(5)	2190(2)	1	79(2)
I(10)	4972(5)	5006(5)	9112(2)	1	101(2)
N(1)	5340(40)	-1010(40)	764(16)	1	255(9)
N(2)	9260(20)	5610(30)	6198(12)	1	112(6)
N(3)	9670(50)	4200(40)	3288(19)	1	242(16)
N(4)	4110(50)	420(60)	-1070(12)	1	255(9)
C(1)	4770(60)	480(50)	984(14)	1	255(9)
C(2)	10020(60)	5850(40)	3240(30)	1	242(16)
C(3)	4050(50)	1440(30)	525(17)	1	255(9)

C(4)	4690(50)	-1470(30)	191(15)	1	255(9)
C(5)	5560(40)	-150(50)	-818(15)	1	255(9)
C(6)	5410(40)	-270(30)	-171(14)	1	255(9)
C(7)	4100(30)	770(50)	-72(13)	1	255(9)
C(8)	10520(30)	4490(30)	6269(13)	1	112(6)
H(1c1)	5580.4	1024.26	1163.18	1	305.7
H(2c1)	4059.68	308.86	1291.69	1	305.7
H(1c2)	9662.2	6224.76	2874.72	1	291
H(2c2)	9523.21	6382.91	3550.55	1	291
H(3c2)	11087.12	5999.4	3268.68	1	291
H(1c3)	5148.51	-1776.88	1048.07	1	305.7
H(2c3)	6423.51	-972.31	734.78	1	305.7
H(1c4)	5083.52	-2442.24	82.92	1	305.7
H(2c4)	3614.45	-1323.43	197.19	1	305.7
H(1c5)	6360.67	540.74	-911.94	1	305.7
H(2c5)	5783.63	-1122.5	-978.39	1	305.7
H(1c6)	6462.69	-248.78	-68.68	1	305.7
H(1c7)	4120.3	1561.74	-356.23	1	305.7
H(2c7)	3177.63	238.9	-146.5	1	305.7
H(1c8)	11012.89	4657.02	6634.06	1	133.9
H(2c8)	10112.01	3486.87	6259.34	1	133.9
H(3c8)	11230.11	4613.32	5958.76	1	133.9
H(1n1)	4486.9	2323.88	520.05	1	305.7
H(2n1)	3121.79	1630.35	619.43	1	305.7
H(1n2)	9637.3	6495.01	6121.43	1	133.9
H(2n2)	8676.59	5329.31	5914.87	1	133.9
H(3n2)	8740.05	5657.25	6518.18	1	133.9
H(1n3)	9693.73	3791.96	2944.14	1	291
H(2n3)	10334.64	3764.59	3509.46	1	291
H(3n3)	8774.03	4079.87	3437.11	1	291
H(1n4)	3384.04	301.45	-818.49	1	305.7
H(2n4)	4196.85	1378.52	-1151.55	1	305.7
H(3n4)	3896.94	-75.05	-1384.68	1	305.7

*U_{eq} is defined as one third of the trace of the orthogonalized U_{ij} tensor.

Table D14. Atomic coordinates ($x10^4$) and equivalent isotropic displacement parameters ($Å^2x10^3$) for $4AMP(MA)_2Pb_3I_{10}$ at 250 K with estimated standard deviations in parentheses.

Label	x	y	z	Occupancy	U_{eq}^*
Pb(1)	-22(1)	0(2)	-45(2)	1	28(1)
Pb(2)	2759(1)	2(2)	-43(2)	1	34(1)
Pb(3)	-2809(1)	1(2)	-10044(2)	1	30(1)
I(1)	-4133(2)	-10(4)	-10026(6)	1	137(2)
I(2)	-26(2)	-2008(2)	-3037(4)	1	54(1)
I(3)	-26(2)	2009(2)	-7055(4)	1	52(1)
I(4)	1350(2)	0(3)	-32(4)	1	58(1)
I(5)	-1392(2)	0(2)	-10031(4)	1	50(1)
I(6)	2737(2)	-6995(2)	1948(4)	1	62(2)
I(7)	-2787(2)	7002(2)	-12045(4)	1	61(2)
I(8)	2735(2)	-1990(2)	2962(4)	1	61(1)
I(9)	-2792(2)	2003(2)	-13045(4)	1	62(1)
I(10)	4093(2)	-7(4)	-30(5)	1	137(2)
N(1)	-3982(8)	4430(20)	-10620(30)	1	207(5)
N(2)	1133(8)	-810(20)	-5860(20)	1	126(5)
N(3)	-1564(11)	650(20)	-5570(30)	1	151(6)
N(4)	-6048(10)	4380(30)	-10910(30)	1	207(5)
C(1)	-4106(9)	5790(20)	-9650(30)	1	207(5)
C(2)	-1227(12)	-780(30)	-5770(30)	1	151(6)
C(3)	-4507(9)	3514(18)	-11010(30)	1	207(5)
C(4)	-4702(9)	6422(16)	-9850(30)	1	207(5)
C(5)	-5819(8)	5470(30)	-9760(30)	1	207(5)
C(6)	-5176(8)	5288(17)	-9630(20)	1	207(5)
C(7)	-5057(9)	4410(20)	-11050(20)	1	207(5)
C(8)	1433(11)	620(20)	-5400(30)	1	126(5)
H(1c1)	-3824.57	6559.56	-9851.22	1	249
H(2c1)	-4046.98	5530.52	-8604.16	1	249
H(1c2)	-1485.66	-1591.74	-6027.27	1	180.6
H(2c2)	-949.28	-651.75	-6567.7	1	180.6
H(3c2)	-1029.64	-1021.54	-4845.17	1	180.6
H(1c3)	-4449.43	3022.88	-11962.72	1	249

H(2c3)	-4547.08	2699.15	-10294.43	1	249
H(1c4)	-4756.44	7255.19	-9170.36	1	249
H(2c4)	-4734.18	6862.5	-10842.43	1	249
H(1c5)	-5995.53	5276.02	-8798.26	1	249
H(2c5)	-5906.67	6486.32	-10074.53	1	249
H(1c6)	-5147.71	5024.14	-8578.17	1	249
H(1c7)	-5375.48	3751.37	-11260.66	1	249
H(2c7)	-5046.57	5095.45	-11896.94	1	249
H(1c8)	1268.78	1464.74	-5936.65	1	151.4
H(2c8)	1385.5	776.84	-4329.96	1	151.4
H(3c8)	1837.29	548.33	-5632.52	1	151.4
H(1n1)	-3729.37	3855.54	-10165.72	1	249
H(2n1)	-3810.6	4717.52	-11445.25	1	249
H(1n2)	1373.18	-1382.83	-6352.26	1	151.4
H(2n2)	1010.05	-1278.65	-5059.69	1	151.4
H(3n3)	-1555.96	922.98	-4623.69	1	180.6
H(1n3)	-1412.36	1363.66	-6123.68	1	180.6
H(2n3)	-1920.89	505.46	-5847.73	1	180.6
H(1n4)	-6419.54	4275.31	-10791.06	1	249
H(2n4)	-5977.13	4714.93	-11816	1	249
H(3n4)	-5881.04	3502.28	-10790.63	1	249
H(3n2)	840.56	-587.45	-6441.99	1	151.4

*U_{eq} is defined as one third of the trace of the orthogonalized U_{ij} tensor.

Table D15. Atomic coordinates (x10^4) and equivalent isotropic displacement parameters (Å^{2}x10^3) for 3AMP(MA)$_3$Pb$_4$I$_{13}$ at 250 K with estimated standard deviations in parentheses.

Label	x	y	z	Occupancy	U_{eq}*
Pb(4)	5062(2)	4(4)	2775(1)	1	26(1)
Pb(1)	5069(2)	6(3)	609(1)	1	26(1)
Pb(2)	5056(2)	-5(4)	-482(1)	1	31(1)
Pb(3)	5070(2)	-5(3)	1693(1)	1	20(1)
I(2)	2089(5)	2046(6)	595(1)	1	48(2)
I(1)	5137(7)	1(12)	3318(1)	1	91(3)
I(3)	5178(6)	1(8)	2232(1)	1	52(2)
I(4)	5171(6)	-2(9)	80(1)	1	58(2)

I(6)	2245(6)	2213(9)	2758(2)	1	75(3)
I(7)	2839(7)	-2803(8)	2756(2)	1	75(3)
I(8)	5139(6)	3(12)	-1002(1)	1	93(3)
I(9)	2079(5)	-2033(6)	1681(1)	1	48(2)
I(10)	5183(6)	1(4)	1161(1)	1	46(1)
I(11)	3037(5)	2996(6)	1678(1)	1	50(2)
I(12)	3030(5)	-2984(6)	597(1)	1	51(2)
I(14)	7243(6)	-2792(9)	-486(2)	1	83(3)
I(15)	7847(7)	2188(9)	-486(2)	1	83(3)
N(1)	440(130)	320(170)	-909(14)	1	460(30)
C(13)	-670(130)	-160(100)	-1765(12)	1	460(30)
C(3)	580(100)	840(100)	-1409(13)	1	460(30)
C(1)	-860(150)	-300(200)	-1040(13)	1	460(30)
C(2)	-700(80)	70(70)	-1287(12)	1	460(30)
C(4)	740(100)	420(80)	-1655(15)	1	460(30)
C(5)	-1740(90)	-1070(110)	-1390(15)	1	460(30)
N(2)	-1470(90)	-1390(80)	-1637(15)	1	460(30)
N(3)	650(50)	400(60)	2199(10)	1	118(14)
N(4)	760(50)	-350(60)	1074(12)	1	134(16)
C(8)	-630(60)	610(80)	1062(13)	1	134(16)
C(7)	-620(60)	-690(70)	2162(11)	1	118(14)
N(11)	9400(70)	-510(90)	-60(13)	1	200(30)
C(12)	10700(90)	500(110)	1(18)	1	200(30)
H(1c13)	-1357.88	660.34	-1790.22	1	547.2
H(2c13)	-446.02	-504.68	-1915.88	1	547.2
H(1c3)	469.56	1909.1	-1395.48	1	547.2
H(2c3)	1504.99	633.48	-1330.7	1	547.2
H(1c1)	-1791.9	83.79	-982.86	1	547.2
H(2c1)	-873.37	-1402.31	-1023.77	1	547.2
H(1c2)	-792.22	1136.64	-1314.84	1	547.2
H(1c4)	1527.57	-315.41	-1670.9	1	547.2
H(2c4)	1109.29	1268.36	-1738.38	1	547.2
H(1c5)	-1693.27	-1987.48	-1305.13	1	547.2
H(2c5)	-2769.5	-745.27	-1369.63	1	547.2

H(1c8)	-1475.53	46.58	1117.57	1	160.4
H(2c8)	-488.01	1493.46	1153.6	1	160.4
H(3c8)	-803.35	898.71	907.25	1	160.4
H(1c7)	-819.96	-776.34	2001.82	1	141.8
H(2c7)	-352.07	-1654.13	2222.07	1	141.8
H(3c7)	-1511.72	-323.24	2237.32	1	141.8
H(1c12)	11371.35	573.18	-126.48	1	239.3
H(2c12)	10324.72	1481.65	38.99	1	239.3
H(3c12)	11227.3	82.41	128.55	1	239.3
H(1n1)	537.75	1269.1	-941.91	1	547.2
H(2n1)	266.41	220.2	-764.06	1	547.2
H(3n1)	1259.12	-161.31	-944.71	1	547.2
H(1n2)	-2321.12	-1594.99	-1703.38	1	547.2
H(2n2)	-962.72	-2227.19	-1650.01	1	547.2
H(1n3)	661.67	1060.57	2089.29	1	141.8
H(2n3)	522.65	863.56	2327.98	1	141.8
H(3n3)	1499.98	-86.25	2200.97	1	141.8
H(1n4)	537.13	-1277.42	1038.64	1	160.4
H(2n4)	1437.23	-10.33	979.97	1	160.4
H(3n4)	1125.72	-329.26	1211.88	1	160.4
H(1n11)	9288.91	-1194.3	44.66	1	239.3
H(2n11)	8578.18	24.13	-69.83	1	239.3
H(3n11)	9577	-943.4	-189.82	1	239.3

*U_{eq} is defined as one third of the trace of the orthogonalized U_{ij} tensor.

Table D16. Atomic coordinates ($x10^4$) and equivalent isotropic displacement parameters ($Å^2x10^3$) for $4AMP(MA)_3Pb_4I_{13}$ at 293 K with estimated standard deviations in parentheses.

Label	x	y	z	Occupancy	U_{eq}*
Pb(1)	5087(4)	28(4)	4030(1)	1	48(2)
Pb(2)	5091(4)	-39(4)	1856(1)	1	41(1)
Pb(3)	5089(4)	-27(3)	768(1)	1	39(1)
Pb(4)	5090(3)	35(4)	2938(1)	1	35(1)
I(1)	5037(13)	45(17)	4562(2)	1	134(4)
I(2)	5073(9)	-1(9)	3477(2)	1	86(3)
I(3)	5068(7)	5(8)	1326(2)	1	70(2)

I(4)	2117(6)	2019(7)	4009(2)	1	72(2)
I(5)	3056(6)	-2973(7)	4017(2)	1	82(3)
I(6)	5021(16)	-62(19)	258(2)	1	168(6)
I(7)	2174(7)	-2044(8)	2928(2)	1	66(2)
I(8)	5036(12)	3(6)	2401(2)	1	73(2)
I(9)	3018(7)	2912(7)	2923(2)	1	77(2)
I(10)	2993(8)	-2863(8)	1851(2)	1	87(3)
I(11)	7097(8)	-2986(8)	773(2)	1	78(3)
I(12)	8076(7)	2031(8)	764(2)	1	84(3)
I(13)	2198(7)	2087(7)	1846(2)	1	77(3)
N(1)	-380(60)	-570(70)	362(7)	1	158(10)
N(2)	80(60)	-360(60)	-513(8)	1	158(10)
N(3)	-220(50)	500(50)	3495(9)	1	100(14)
N(4)	680(50)	-460(60)	2352(9)	1	103(14)
N(5)	-90(60)	-490(50)	1305(10)	1	115(15)
C(1)	550(70)	340(70)	198(7)	1	158(10)
C(2)	210(40)	-160(40)	-40(7)	1	158(10)
C(3)	860(40)	1140(50)	-170(8)	1	158(10)
C(4)	1120(70)	810(70)	-417(8)	1	158(10)
C(5)	-1220(50)	-790(70)	-139(8)	1	158(10)
C(6)	-1390(50)	-510(70)	-389(8)	1	158(10)
C(7)	-700(60)	-700(50)	3331(10)	1	100(14)
C(8)	-580(50)	670(60)	2338(11)	1	103(14)
C(9)	-800(70)	860(60)	1414(12)	1	115(15)
H(1c1)	1600.84	187.9	229.43	1	189.5
H(2c1)	302.15	1385.99	214.25	1	189.5
H(1c2)	587.58	-1178.97	-46.74	1	189.5
H(1c3)	1790.72	1448.44	-100.68	1	189.5
H(2c3)	208.23	1998.36	-155.18	1	189.5
H(1c4)	1030.3	1729.38	-502.25	1	189.5
H(2c4)	2150.79	502.93	-438.67	1	189.5
H(1c5)	-2071.44	-372.05	-60.52	1	189.5
H(2c5)	-1272.59	-1852.08	-110.4	1	189.5
H(1c6)	-1973.51	-1301.48	-455.95	1	189.5

H(2c6)	-1979.49	388.65	-412.8	1	189.5
H(1c7)	-1764.97	-620.59	3304.04	1	120.5
H(2c7)	-163.41	-581.41	3191.01	1	120.5
H(3c7)	-479.3	-1677.81	3394.43	1	120.5
H(1c8)	-1110.84	544.61	2197.68	1	124
H(2c8)	-1257.66	524.88	2462.83	1	124
H(3c8)	-161.72	1672.31	2344.97	1	124
H(1c9)	-1882.89	772.99	1403.8	1	138
H(2c9)	-513.98	901.85	1571.31	1	138
H(3c9)	-478.1	1757.76	1338.46	1	138
H(1n1)	163.52	-1319.04	413.68	1	189.5
H(2n1)	-659.23	-2.19	474.12	1	189.5
H(3n1)	-1168.27	-929	292.8	1	189.5
H(1n2)	-90.54	-158.51	-655.62	1	189.5
H(2n2)	539.18	-1229.83	-515.45	1	189.5
H(1n3)	-986.73	1074.46	3527.45	1	120.5
H(2n3)	119.18	83.96	3618.69	1	120.5
H(3n3)	491.32	1045.51	3433.96	1	120.5
H(1n4)	1199.38	-442.22	2226.84	1	124
H(2n4)	1261.55	-245.04	2465.97	1	124
H(3n4)	298.22	-1360.43	2370.83	1	124
H(1n5)	-695.8	-866.28	1203.92	1	138
H(2n5)	753.15	-221.16	1239.66	1	138
H(3n5)	105.05	-1171.21	1407.75	1	138

*U_{eq} is defined as one third of the trace of the orthogonalized U_{ij} tensor.

Table D17. Anisotropic displacement parameters ($Å^2x10^3$) for $3AMPPbI_4$ at 293 K with estimated standard deviations in parentheses.

Label	U_{11}	U_{22}	U_{33}	U_{12}	U_{13}	U_{23}
Pb(1)	31(2)	28(2)	38(1)	8(1)	10(1)	2(1)
Pb(2)	34(2)	33(2)	34(2)	9(2)	8(1)	-2(2)
Pb(3)	34(2)	30(2)	36(2)	9(2)	9(2)	0(2)
I(1)	72(3)	41(2)	38(2)	-5(2)	6(2)	3(2)
I(2)	59(2)	44(2)	37(2)	3(2)	5(2)	6(2)
I(3)	26(2)	56(2)	84(3)	28(2)	16(2)	10(2)

I(4)	85(3)	63(3)	64(2)	-34(3)	13(2)	0(2)
I(5)	78(3)	56(3)	78(3)	-20(3)	26(2)	-3(2)
I(6)	61(2)	45(2)	34(2)	3(2)	9(2)	-4(2)
I(7)	28(2)	50(3)	71(2)	28(2)	18(2)	10(2)
I(8)	83(3)	49(3)	37(2)	16(2)	9(2)	-7(2)

The anisotropic displacement factor exponent takes the form: $-2\pi^2[h^2a^{*2}U_{11} + ... + 2hka^*b^*U_{12}]$.

Table D18. Anisotropic displacement parameters ($Å^2x10^3$) for $4AMPPbI_4$ at 293 K with estimated standard deviations in parentheses.

Label	U_{11}	U_{22}	U_{33}	U_{12}	U_{13}	U_{23}
Pb(1)	38(2)	36(2)	20(1)	1(2)	1(1)	1(2)
Pb(2)	42(2)	33(2)	56(2)	1(2)	-2(2)	23(2)
I(1)	96(6)	64(4)	43(3)	-2(4)	0(3)	3(2)
I(2)	22(4)	198(12)	138(5)	15(5)	16(3)	-53(6)
I(3)	32(4)	154(9)	131(4)	-16(5)	4(3)	-43(4)
I(4)	56(3)	56(3)	12(2)	-2(3)	-2(2)	1(2)
I(5)	71(5)	6(2)	100(4)	6(3)	2(4)	7(2)
I(6)	45(5)	108(7)	168(6)	-2(5)	-16(4)	58(5)
I(7)	52(5)	126(8)	144(5)	-24(5)	10(4)	43(5)
I(8)	142(7)	92(5)	55(3)	8(6)	-3(3)	-1(3)

The anisotropic displacement factor exponent takes the form: $-2\pi^2[h^2a^{*2}U_{11} + ... + 2hka^*b^*U_{12}]$.

Table D19. Anisotropic displacement parameters ($Å^2x10^3$) for $3AMP(MA)Pb_2I_7$ at 250 K with estimated standard deviations in parentheses.

Label	U_{11}	U_{22}	U_{33}	U_{12}	U_{13}	U_{23}
Pb(1)	35(1)	32(1)	39(1)	0(1)	0(1)	0(1)
Pb(2)	27(1)	29(1)	36(1)	0(1)	0(1)	0(1)
I(1)	83(1)	83(1)	29(1)	-7(2)	0(1)	1(2)
I(2)	130(2)	128(2)	34(1)	6(2)	-2(2)	-4(1)
I(3)	127(2)	129(2)	31(1)	6(2)	0(1)	-5(1)
I(4)	68(2)	69(2)	104(2)	46(1)	-14(1)	-12(1)
I(5)	74(2)	75(2)	86(2)	-47(1)	14(1)	-13(1)
I(6)	68(2)	66(2)	105(2)	-45(1)	10(1)	-10(1)
I(7)	73(2)	73(2)	87(2)	45(1)	-10(1)	-12(1)

The anisotropic displacement factor exponent takes the form: $-2\pi^2[h^2a^{*2}U_{11} + ... + 2hka^*b^*U_{12}]$.

Table D20. Anisotropic displacement parameters ($Å^2x10^3$) for 4AMP(MA)Pb_2I_7 at 250 K with estimated standard deviations in parentheses.

Label	U_{11}	U_{22}	U_{33}	U_{12}	U_{13}	U_{23}
Pb(1)	39(1)	28(1)	33(1)	1(1)	0(1)	0(1)
Pb(2)	26(1)	40(1)	30(1)	1(1)	0(1)	0(1)
I(1)	71(1)	72(1)	24(1)	-8(2)	0(1)	-1(2)
I(2)	233(5)	157(5)	31(2)	25(2)	-3(3)	-4(2)
I(3)	153(4)	225(6)	19(2)	26(2)	0(2)	-4(2)
I(4)	44(2)	49(2)	83(2)	19(1)	-2(2)	-3(2)
I(5)	47(2)	43(2)	89(2)	-21(1)	6(2)	-2(2)
I(6)	42(2)	49(2)	83(2)	-19(1)	2(2)	-7(2)
I(7)	46(2)	43(2)	89(2)	20(1)	-8(2)	-6(2)

The anisotropic displacement factor exponent takes the form: $-2\pi^2[h^2a^{*2}U_{11} + ... + 2hka^*b^*U_{12}]$.

Table D21. Anisotropic displacement parameters ($Å^2x10^3$) for 3AMP$(MA)_2Pb_3I_{10}$ at 250 K with estimated standard deviations in parentheses.

Label	U_{11}	U_{22}	U_{33}	U_{12}	U_{13}	U_{23}
Pb(1)	28(1)	28(1)	31(1)	0(1)	0(1)	0(1)
Pb(2)	27(1)	28(1)	35(2)	0(1)	1(1)	0(1)
Pb(3)	27(1)	26(1)	35(2)	0(1)	-1(1)	0(1)
I(1)	142(5)	136(5)	29(2)	5(3)	-1(2)	0(2)
I(2)	46(2)	43(3)	74(2)	24(2)	-6(2)	-7(2)
I(3)	43(2)	45(3)	76(2)	23(2)	6(2)	6(2)
I(4)	81(2)	85(2)	27(2)	-1(2)	-1(2)	0(2)
I(5)	75(2)	73(2)	17(2)	0(2)	2(1)	-1(1)
I(6)	70(3)	68(3)	90(2)	49(2)	0(2)	-2(2)
I(7)	61(3)	64(3)	116(3)	40(2)	13(2)	16(2)
I(8)	72(3)	66(3)	93(2)	-50(2)	2(2)	0(2)
I(9)	61(3)	66(3)	111(3)	-39(2)	-16(2)	12(2)
I(10)	135(5)	139(5)	29(2)	-6(3)	0(2)	0(2)

The anisotropic displacement factor exponent takes the form: $-2\pi^2[h^2a^{*2}U_{11} + ... + 2hka^*b^*U_{12}]$.

Table D22. Anisotropic displacement parameters ($Å^2x10^3$) for $4AMP(MA)_2Pb_3I_{10}$ at 250 K with estimated standard deviations in parentheses.

Label	U_{11}	U_{22}	U_{33}	U_{12}	U_{13}	U_{23}
Pb(1)	30(1)	27(1)	27(1)	0(1)	0(1)	0(1)
Pb(2)	29(1)	33(1)	40(1)	0(1)	0(1)	1(1)
Pb(3)	34(1)	31(1)	26(1)	0(1)	0(1)	0(1)
I(1)	37(2)	163(4)	212(6)	-4(2)	4(3)	-24(2)
I(2)	71(2)	46(2)	45(2)	1(2)	-4(2)	-24(2)
I(3)	71(2)	41(2)	44(2)	-1(2)	5(2)	-23(1)
I(4)	20(2)	90(2)	64(2)	-5(1)	2(2)	-4(2)
I(5)	27(2)	51(1)	70(2)	5(1)	-1(2)	4(2)
I(6)	90(2)	45(2)	52(2)	-7(2)	4(2)	-21(2)
I(7)	97(2)	46(2)	40(2)	-4(2)	7(2)	-22(2)
I(8)	88(2)	45(2)	50(2)	-5(2)	-2(2)	22(2)
I(9)	97(2)	47(2)	42(2)	-6(2)	-9(2)	21(2)
I(10)	17(2)	220(5)	174(5)	4(2)	-4(2)	23(2)

The anisotropic displacement factor exponent takes the form: $-2\pi^2[h^2a^{*2}U_{11} + ... + 2hka^*b^*U_{12}]$.

Table D23. Anisotropic displacement parameters ($Å^2x10^3$) for $3AMP(MA)_3Pb_4I_{13}$ at 250 K with estimated standard deviations in parentheses.

Label	U_{11}	U_{22}	U_{33}	U_{12}	U_{13}	U_{23}
Pb(4)	23(2)	24(2)	31(2)	0(2)	4(1)	-1(2)
Pb(1)	20(1)	28(2)	30(2)	0(2)	-1(1)	0(2)
Pb(2)	22(1)	38(2)	31(2)	0(2)	-2(1)	0(2)
Pb(3)	17(1)	24(2)	20(1)	0(2)	2(1)	1(2)
I(2)	32(2)	46(5)	65(3)	16(2)	-3(2)	-3(3)
I(1)	103(4)	114(8)	56(3)	3(4)	-17(3)	0(5)
I(3)	60(2)	88(4)	8(2)	-1(2)	1(2)	0(3)
I(4)	61(2)	89(5)	24(2)	-1(3)	-16(2)	-1(3)
I(6)	58(3)	85(6)	82(4)	49(4)	3(3)	-1(4)
I(7)	74(4)	62(5)	89(4)	-55(4)	-1(3)	-1(4)
I(8)	118(4)	136(8)	26(2)	1(4)	1(2)	0(4)
I(9)	27(2)	47(5)	71(3)	-18(2)	1(2)	5(3)
I(10)	49(2)	75(2)	13(2)	0(2)	-9(2)	0(3)
I(11)	44(2)	38(5)	69(3)	34(2)	5(2)	9(3)

I(12)	47(2)	39(4)	68(3)	-33(2)	-2(2)	-4(3)
I(14)	60(4)	89(6)	100(4)	44(4)	-16(3)	-17(4)
I(15)	76(4)	67(6)	105(5)	-51(4)	14(3)	-20(4)

The anisotropic displacement factor exponent takes the form: $-2\pi^2[h^2a^{*2}U_{11} + ... + 2hka^*b^*U_{12}]$.

Table D24. Anisotropic displacement parameters ($Å^2x10^3$) for $4AMP(MA)_3Pb_4I_{13}$ at 293 K with estimated standard deviations in parentheses.

Label	U_{11}	U_{22}	U_{33}	U_{12}	U_{13}	U_{23}
Pb(1)	52(2)	53(2)	39(2)	-8(2)	-3(2)	-2(2)
Pb(2)	47(2)	31(2)	44(2)	0(2)	10(2)	6(2)
Pb(3)	42(2)	30(2)	45(2)	-6(2)	8(2)	2(2)
Pb(4)	29(2)	38(2)	38(2)	0(1)	-8(2)	1(2)
I(1)	180(8)	173(9)	50(4)	0(7)	15(5)	-16(6)
I(2)	125(5)	120(6)	11(2)	26(5)	-2(3)	2(4)
I(3)	84(4)	77(4)	51(3)	15(3)	9(3)	4(4)
I(4)	51(3)	58(3)	106(5)	31(3)	-13(3)	-8(3)
I(5)	48(3)	56(4)	142(7)	-34(3)	-8(3)	7(4)
I(6)	255(11)	241(12)	8(2)	-6(9)	-8(3)	-5(6)
I(7)	59(3)	63(4)	77(4)	-31(3)	-10(3)	11(3)
I(8)	97(2)	96(2)	27(2)	22(4)	1(2)	1(4)
I(9)	69(3)	60(3)	103(5)	33(3)	30(3)	28(3)
I(10)	85(4)	62(4)	113(7)	-44(3)	13(4)	-7(4)
I(11)	85(4)	64(4)	85(5)	19(3)	-2(4)	-6(4)
I(12)	76(4)	63(4)	112(6)	-24(3)	33(4)	-25(4)
I(13)	68(4)	67(4)	97(5)	42(3)	-20(3)	-27(3)

The anisotropic displacement factor exponent takes the form: $-2\pi^2[h^2a^{*2}U_{11} + ... + 2hka^*b^*U_{12}]$.

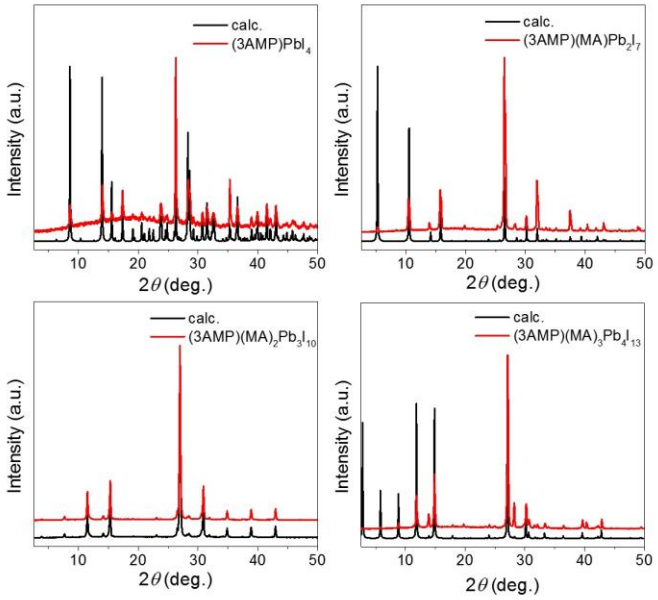

Figure D1. Calculated and experimental PXRD for the 3AMP. The PXRD patterns for n = 2, 3 and 4 are calculated including preferred orientation (001).

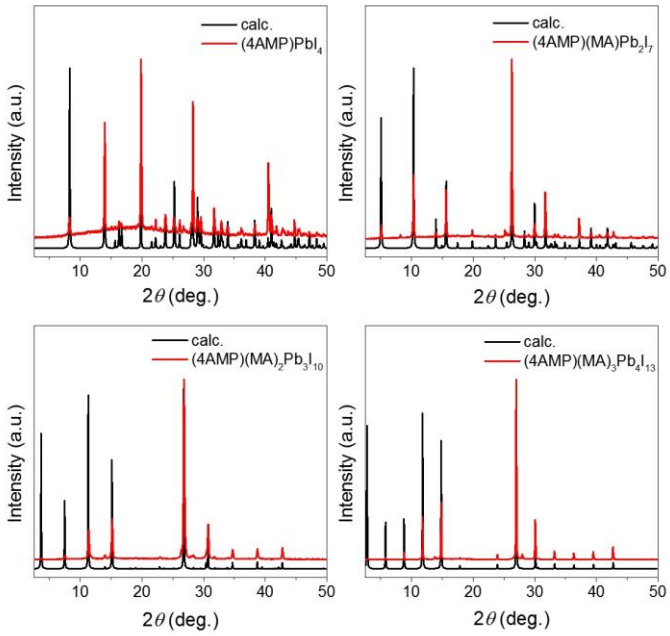

Figure D2. Calculated and experimental PXRD for the 4AMP. The PXRD patterns for n = 3 and 4 are calculated including preferred orientation (001).

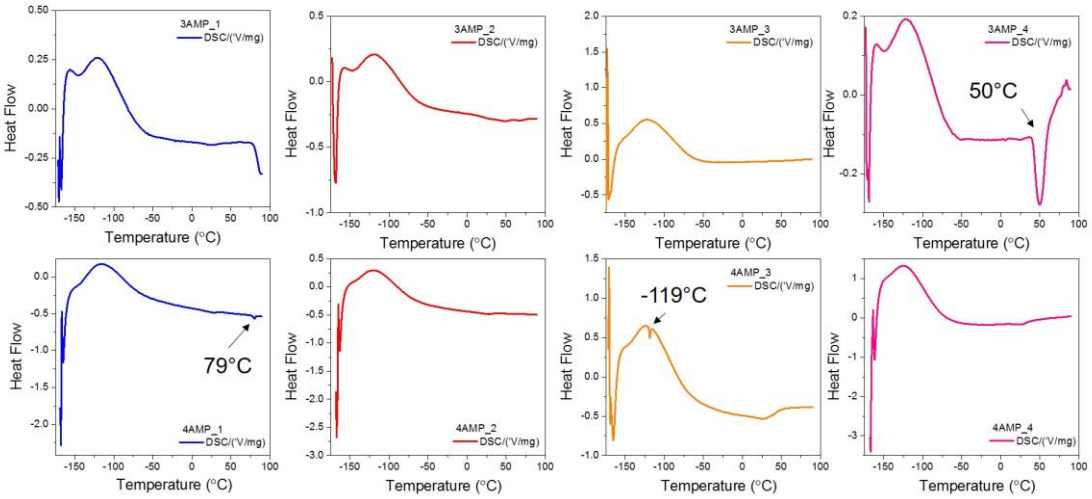

Figure D3. Low temperature DSC. Potential phase transition temperatures are labeled in each figure.

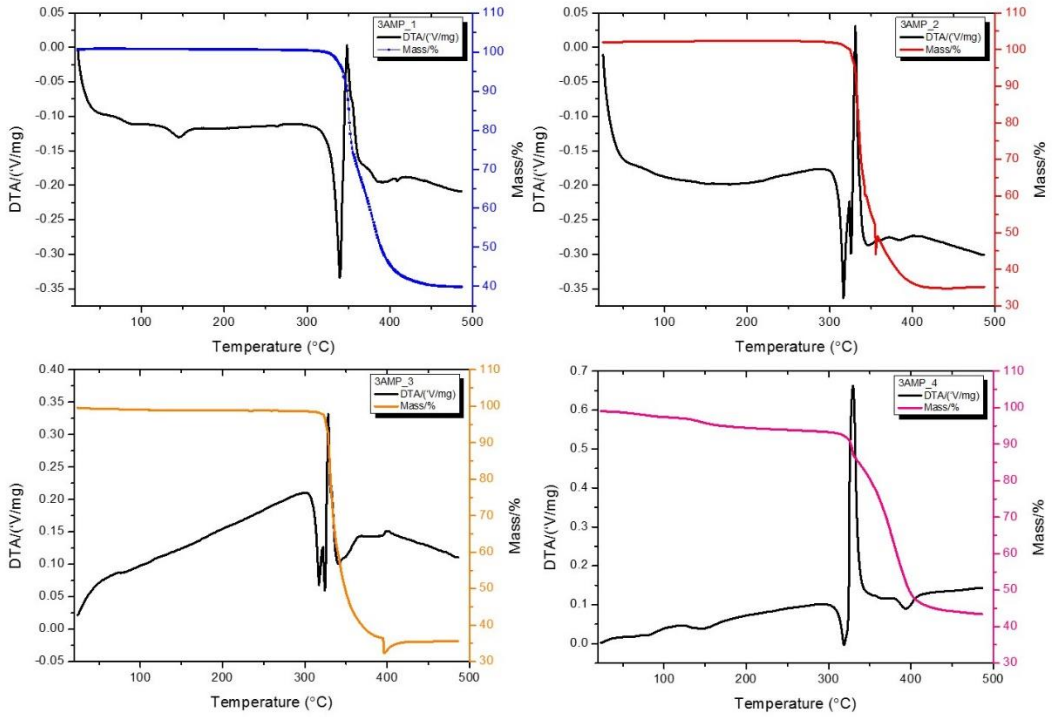

Figure D4. TGA and DTA for the 3AMP series from 25 °C to 480°C. The species which start to disappear at ~150 ºC for 3AMP (n = 4) comes from solvent residue (HI) from incomplete drying.

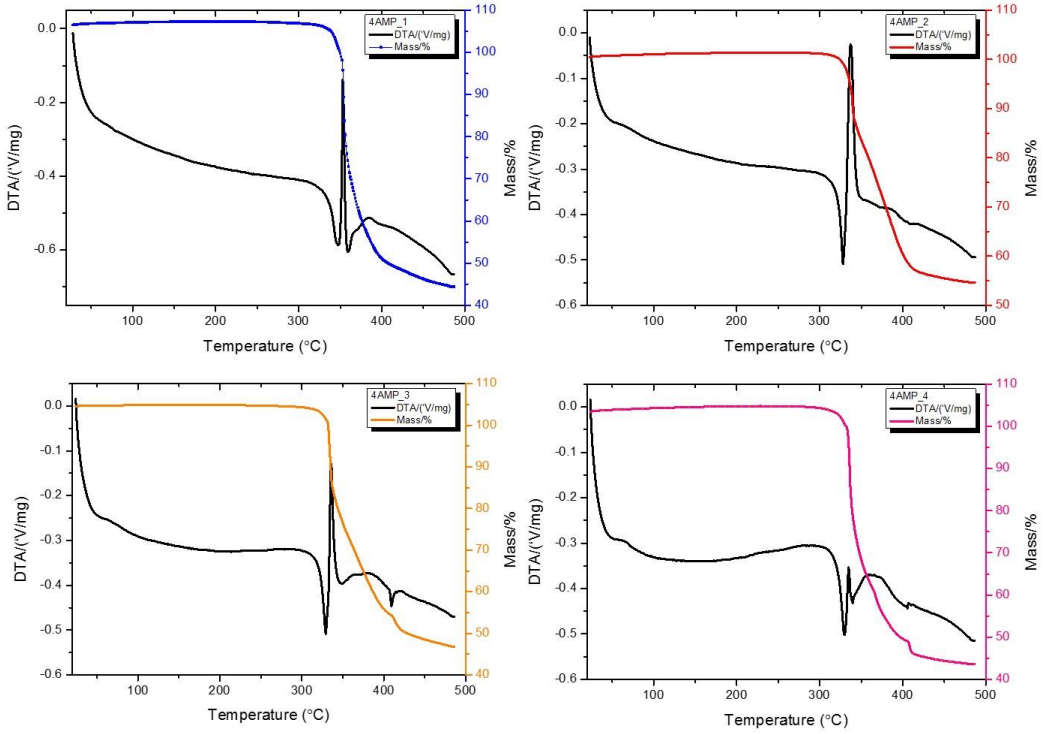

Figure D5. TGA and DTA for the 4AMP series from 25 °C to 480°C.

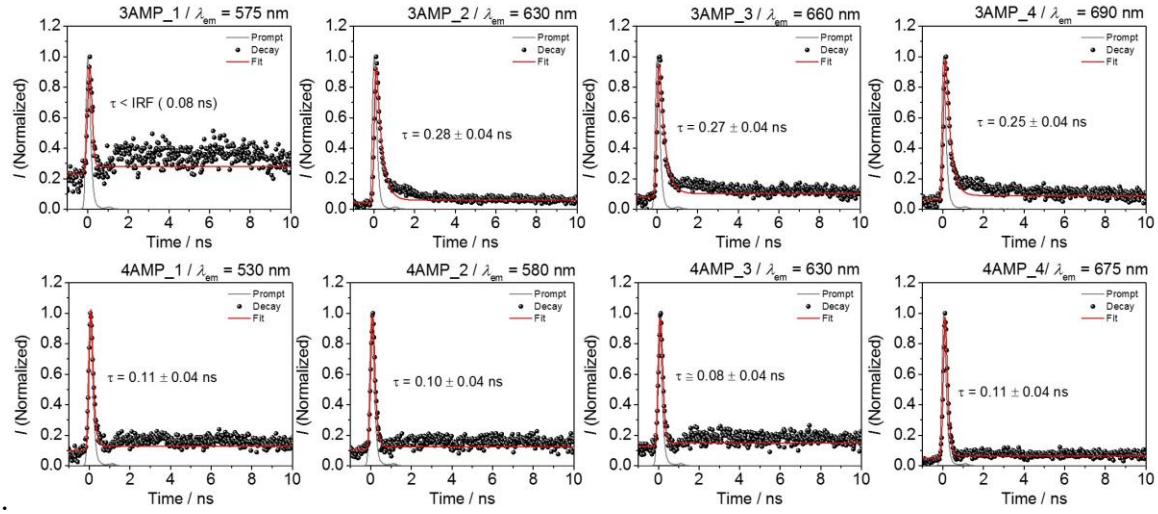

Figure D6. Time-resolved PL decay for the 3AMP and 4AMP series. The 3AMP series show generally longer lifetimes than the 4AMP series.

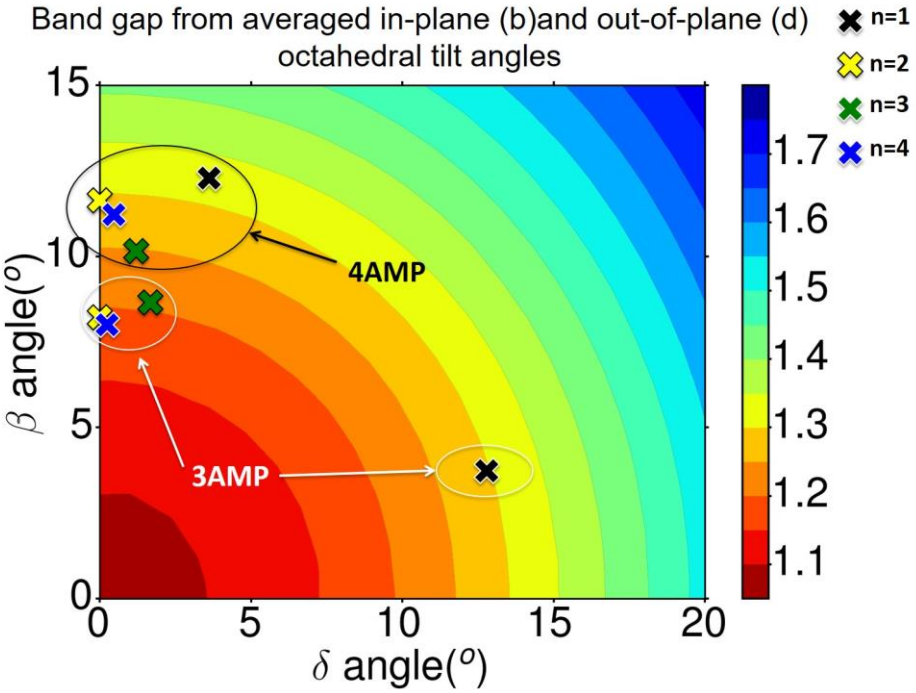

Figure D7. 2D color map of the electronic band gap with respect to octahedral distortions.

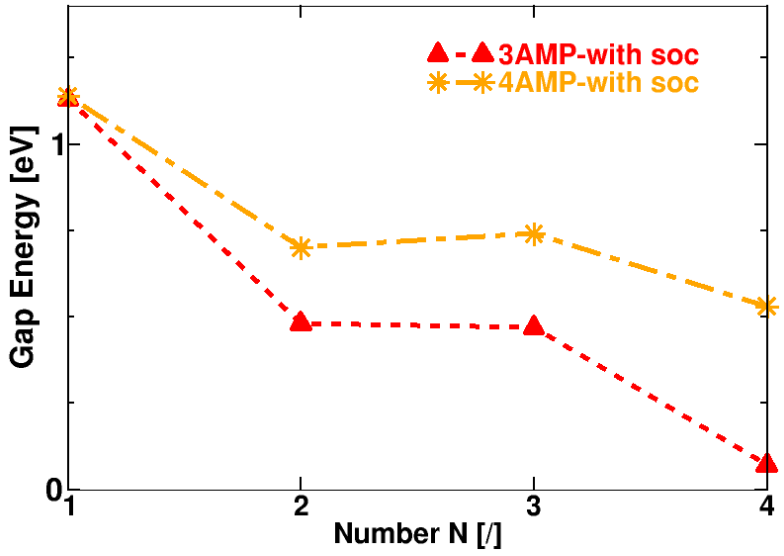

Figure D8. Calculated band gap trend for the 3AMP and 4AMP series.

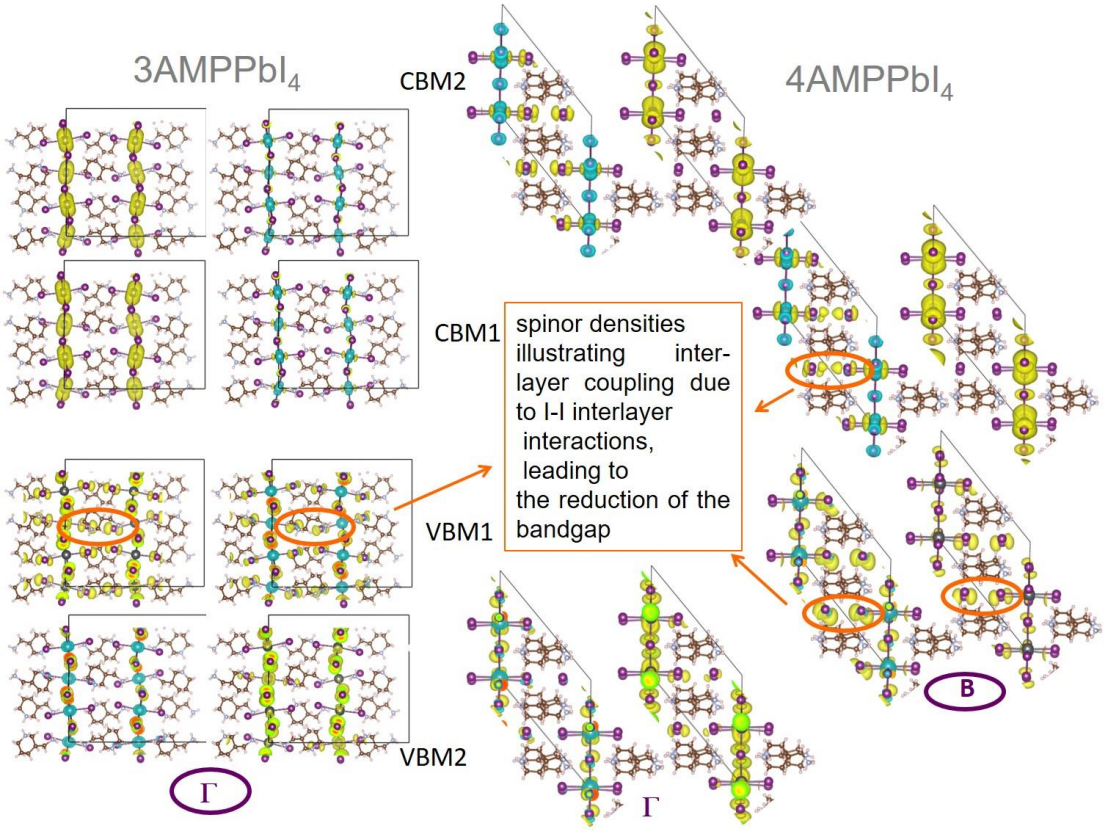

Figure D9. Inter-layer coupling due to I-I interlayer interactions have to be anti-bonding to further destabilize the VBM; this is possible at the BZ center whenever two inorganic sheets build the unit cell (case of 3AMP n=1) or at BZ edge (B-point for 4AMP) if only one layer. For CBM, stabilization (bonding interaction) is less important but does exist. This contributes to reduce the band gap as compared to $(BA)_2PbI_4$ and other analogues.

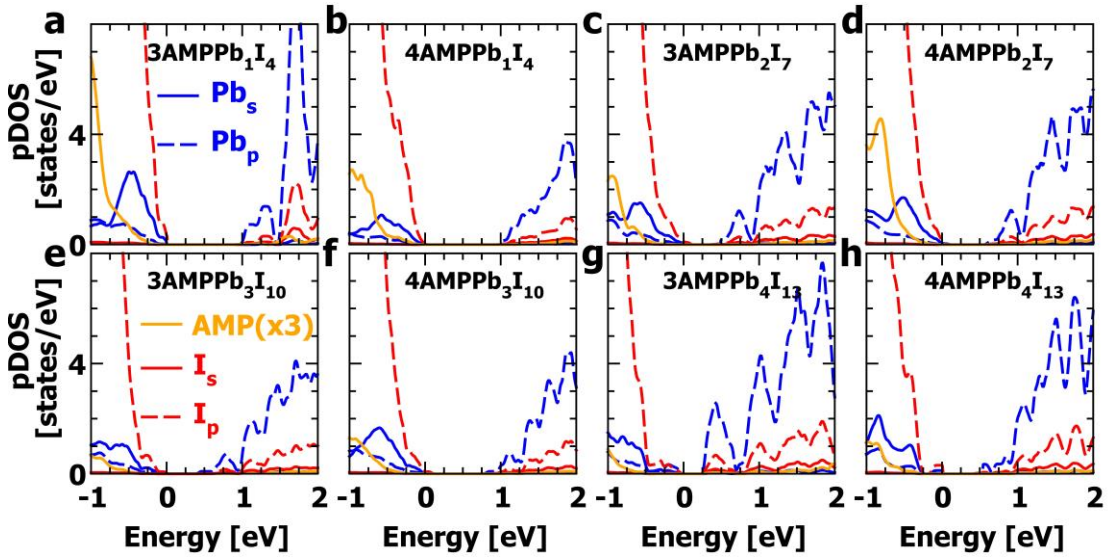

Figure D10. Partial density of states (PDOS) of the 3AMP and 4AMP series.

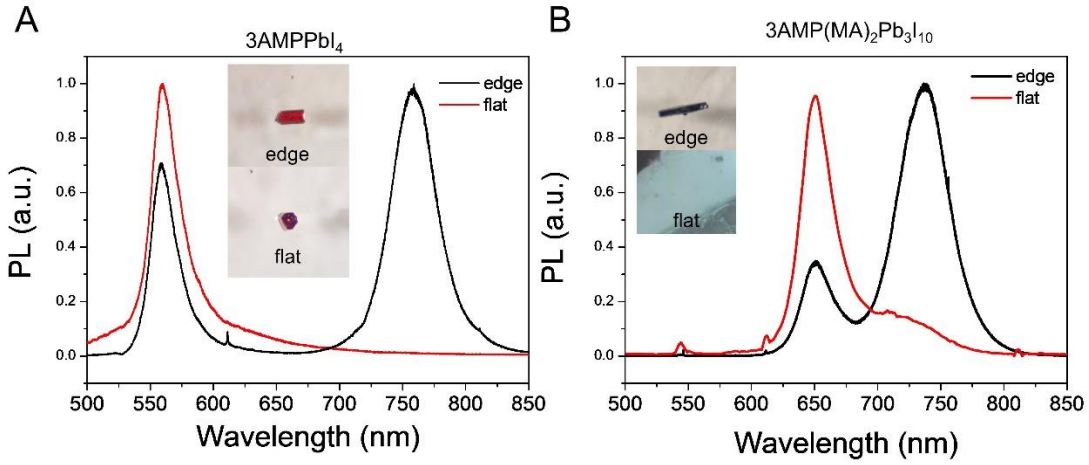

Figure D11. "Edge effect" of (3AMP)PbI_4 (A) and (3AMP)$(MA)_2Pb_3I_{10}$ (B). PL was measured perpendicular to the layers (flat) and parallel to the layers (edge) on single crystals. Inserted show the way crystals were mounted during the measurement.

Table D25. Detailed calculated energy gap at different symmetry points.

	3AMP	**4AMP**
PbI_4	E_{gap} = 1.13 eV (at G) without SOC: E_{gap} = 1.83 eV (at G)	E_{gap} = 1.14 eV (at B) without SOC: E_{gap} = 1.89 eV (at B)
Pb_2I_7	E_{gap} = 0.48 eV (at Y_o) E_{gap} = 0.63 eV(at G)	E_{gap} = 0.70 eV (at Y_o) E_{gap} = 0.85 eV (at G)
Pb_3I_{10}	E_{gap} = 0.47 eV (at Z) E_{gap} = 0.61 eV (at G) without SOC: E_{gap} = 1.17 eV (at Z) E_{gap} = 1.24 eV (at G)	E_{gap} = 0.74 eV (at Z) E_{gap} = 0.91 eV (at G) without SOC: E_{gap} = 1.51 eV (at Z) E_{gap} = 1.60 eV (at G)
Pb_4I_{13}	E_{gap} = 0.07 eV (at Y_o) E_{gap} = 0.14 eV (at G)	E_{gap} = 0.53 eV (at Y_o) E_{gap} = 0.62 eV (at G)

Table D26. Summary of the photovoltaic parameters of solar cells using various perovskite absorbers. Each data is averaged from 6 devices.

	V_{oc} [V]	J_{sc} [mA cm^{-2}]	FF [%]	PCE [%]
3AMPPb$_3$I$_{10}$	0.95 ± 0.09	2.96 ± 0.39	55.18 ± 14.28	1.60 ± 0.62
3AMPPb$_4$I$_{13}$	1.03 ± 0.06	10.16 ± 0.10	64.51 ± 4.01	6.74 ± 0.74
4AMPPb$_3$I$_{10}$	0.96 ± 0.03	6.31 ± 0.10	60.30 ± 1.46	3.67 ± 0.22
4AMPPb$_4$I$_{13}$	0.94 ± 0.03	7.05 ± 0.44	64.05 ± 1.82	4.24 ± 0.50

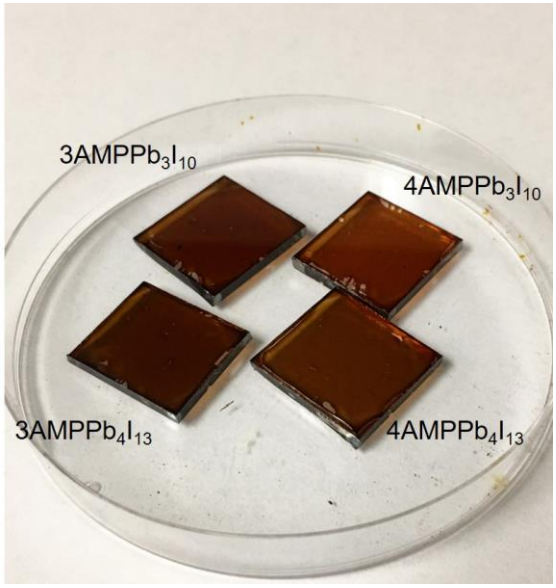

Figure D12. Pictures of thin films of 3AMPPb$_3$I$_{10}$, 4AMPPb$_3$I$_{10}$, 3AMPPb$_4$I$_{13}$ and 4AMPPb$_4$I$_{13}$.

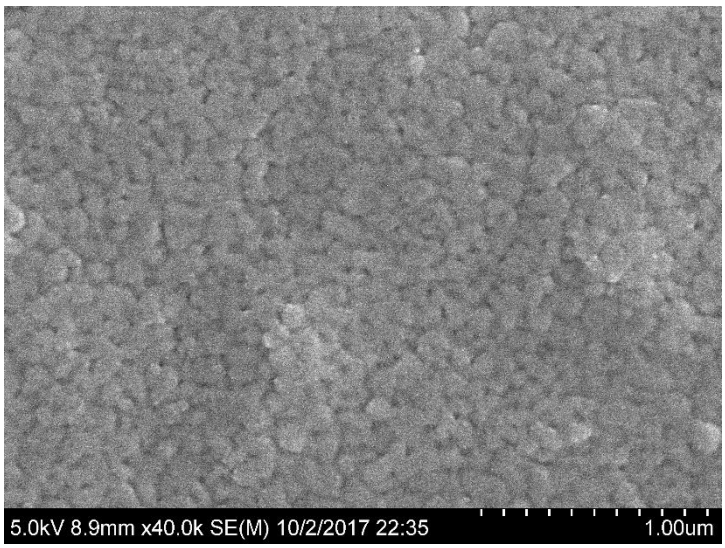

Figure D13. A representative SEM image of $3AMPPb_4I_{13}$ perovskite film deposited on a FTO/PEDOT:PSS substrate.

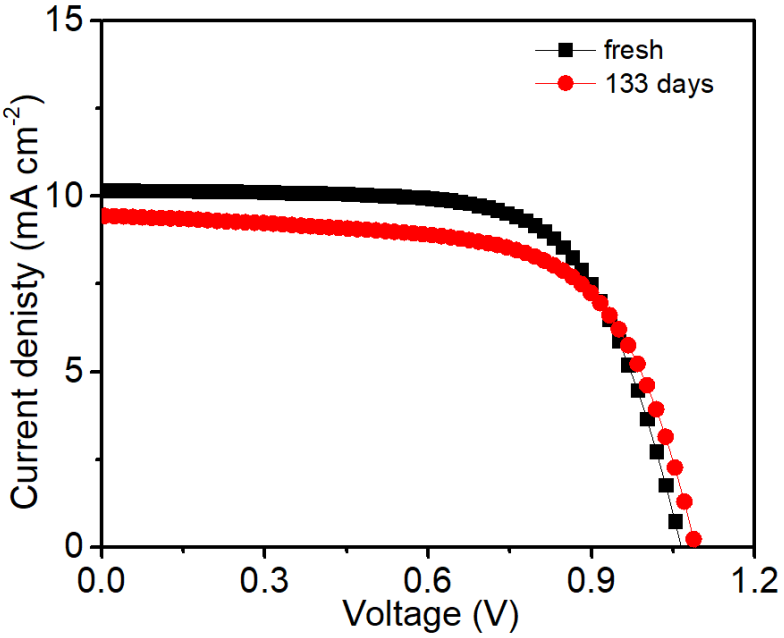

Figure D14. *J-V* curves of a fresh $3AMPPb_4I_{13}$ solar cell without encapsulation and the same cell after storage for 133 days in a N_2-filled glovebox.

APPENDIX E

Supporting Information for Chapter 7

Table E1. Pb-Br bond lengths in (3AMP)(FA)Pb_2Br_7.

Label	Distances (Å)	Label	Distances (Å)
Pb(1)-Br(3)#1	2.978(9)	Pb(2)-Br(4)	3.011(9)
Pb(1)-Br(3)	3.009(9)	Pb(2)-Br(4)#3	3.011(9)
Pb(1)-Br(3)#2	2.978(9)	Pb(2)-Br(4)#2	2.976(9)
Pb(1)-Br(3)#3	3.009(9)	Pb(2)-Br(4)#1	2.976(9)
Pb(1)-Br(6)	3.009(14)	Pb(2)-Br(6)	3.109(14)
Pb(1)-Br(9)	2.887(9)	Pb(2)-Br(8)	2.927(9)

Table E2. Pb-Br bond lengths in (3AMP)(MA)Pb_2Br_7.

Label	Distances (Å)	Label	Distances (Å)
Pb(1)-Br(5)	3.068(11)	Pb(2)-Br(5)	2.941(12)
Pb(1)-Br(6)	3.080(5)	Pb(2)-Br(8)	2.978(11)
Pb(1)-Br(6)#1	2.868(5)	Pb(2)-Br(9)	3.086(5)
Pb(1)-Br(7)#2	2.860(5)	Pb(2)-Br(9)#1	2.863(5)
Pb(1)-Br(7)	3.092(5)	Pb(2)-Br(10)#3	3.085(4)
Pb(1)-Br(2)	2.937(9)	Pb(2)-Br(10)	2.870(5)

Table E3. Pb-Br bond lengths in (4AMP)(FA)Pb_2Br_7.

Label	Distances (Å)	Label	Distances (Å)
Pb(1)-Br(6)	3.095(15)	Pb(3)-Br(7)	2.999(8)
Pb(1)-Br(7)	3.002(9)	Pb(3)-Br(12)#2	3.104(9)
Pb(1)-Br(8)#1	3.003(9)	Pb(3)-Br(13)	3.082(14)
Pb(1)-Br(8)	2.997(9)	Pb(3)-Br(16)#3	3.012(13)
Pb(1)-Br(12)	2.934(10)	Pb(3)-Br(16)	2.986(13)
Pb(1)-Br(14)	2.783(11)	Pb(3)-Br(18)	2.923(14)
Pb(2)-Br(5)	2.879(19)	Pb(4)-Br(9)	2.964(15)
Pb(2)-Br(6)	3.088(15)	Pb(4)-Br(11)	3.008(9)
Pb(2)-Br(10)	2.983(9)	Pb(4)-Br(13)	3.087(14)
Pb(2)-Br(10)#1	3.057(9)	Pb(4)-Br(15)#2	3.066(10)
Pb(2)-Br(11)	3.013(10)	Pb(4)-Br(17)#3	2.958(12)
Pb(2)-Br(15)	2.955(10)	Pb(4)-Br(17)	3.080(11)

Table E4. Pb-Br bond lengths in (4AMP)(MA)Pb_2Br_7.

Label	Distances (Å)	Label	Distances (Å)
Pb(1)-Br(3)	3.08(2)	Pb(2)-Br(3)	3.03(2)
Pb(1)-Br(4)	2.930(10)	Pb(2)-Br(6)	2.929(11)
Pb(1)-Br(4)#1	3.051(9)	Pb(2)-Br(6)#3	3.063(10)
Pb(1)-Br(8)	2.853(14)	Pb(2)-Br(12)#4	2.960(11)
Pb(1)-Br(10)#2	2.943(10)	Pb(2)-Br(12)	3.088(12)
Pb(1)-Br(10)	3.097(11)	Pb(2)-Br(13)	2.927(16)

Table E5. Pb-Br bond lengths in $(3AMP)_{0.5}(4AMP)_{0.5}(FA)_{0.5}(MA)_{0.5}Pb_2Br_7$.

Label	Distances (Å)	Label	Distances (Å)
Pb(1)-Br(4)	2.988(8)	Pb(2)-Br(3)#1	2.998(7)
Pb(1)-Br(4)#1	2.994(7)	Pb(2)-Br(3)	2.983(8)
Pb(1)-Br(5)	2.991(7)	Pb(2)-Br(6)	2.993(7)
Pb(1)-Br(5)#2	3.002(8)	Pb(2)-Br(6)#2	2.999(8)
Pb(1)-Br(7)	3.061(8)	Pb(2)-Br(7)	3.022(8)
Pb(1)-Br(11)	2.840(5)	Pb(2)-Br(10)	2.946(5)

Table E6. Pb-Br bond lengths in $(4AMP)(FA)_{0.5}(MA)_{0.5}Pb_2Br_7$.

Label	Distances (Å)	Label	Distances (Å)
Pb(1)-Br(1)	2.905(10)	Pb(2)-Br(4)	3.022(5)
Pb(1)-Br(3)#1	2.978(6)	Pb(2)-Br(4)#1	2.984(6)
Pb(1)-Br(3)	3.023(5)	Pb(2)-Br(6)	3.021(6)
Pb(1)-Br(5)	3.009(6)	Pb(2)-Br(6)#2	2.975(5)
Pb(1)-Br(5)#2	2.980(5)	Pb(2)-Br(7)	2.863(6)
Pb(1)-Br(9)	3.000(10)	Pb(2)-Br(9)	3.119(10)

Table E7. Pb-Br bond lengths in $(3AMP)_{0.5}(4AMP)_{0.5}(FA)_{0.5}Pb_2Br_7$.

Label	Distances (Å)	Label	Distances (Å)
Pb(1)-Br(3)	3.011(8)	Pb(2)-Br(5)	3.010(7)
Pb(1)-Br(3)#1	2.994(8)	Pb(2)-Br(5)#1	2.994(7)
Pb(1)-Br(6)#2	3.005(8)	Pb(2)-Br(7)	2.990(8)
Pb(1)-Br(6)	2.992(8)	Pb(2)-Br(7)#2	3.004(8)
Pb(1)-Br(8)	3.115(11)	Pb(2)-Br(8)	3.028(11)
Pb(1)-Br(9)	2.842(7)	Pb(2)-Br(1)	2.933(9)

Table E8. Pb-Br bond lengths in $(3AMP)_{0.5}(4AMP)_{0.5}(MA)_{0.5}Pb_2Br_7$.

Label	Distances (Å)	Label	Distances (Å)
Pb(1)-Br(3)#1	2.980(2)	Pb(2)-Br(4)	3.0180(15)
Pb(1)-Br(3)	3.0199(15)	Pb(2)-Br(4)#2	2.983(2)
Pb(1)-Br(6)	3.0694(19)	Pb(2)-Br(6)	2.9954(19)
Pb(1)-Br(8)	3.009(2)	Pb(2)-Br(9)#1	2.9718(18)
Pb(1)-Br(8)#2	2.9739(17)	Pb(2)-Br(9)	3.010(2)
Pb(1)-Br(10)	2.8989(16)	Pb(2)-Br(12)	2.9082(17)

Table E9. Atomic coordinates ($x10^4$) and equivalent isotropic displacement parameters ($Å^2x10^3$) for (3AMP)(FA)Pb_2Br_7 at 293(2) K with estimated standard deviations in parentheses.

Label	x	y	z	Occupancy	U_{eq}^*
Pb(1)	8322(1)	5000	11496(1)	1	48(1)
Pb(2)	8322(1)	5000	7676(1)	1	45(1)
Br(3)	5871(8)	7575(13)	11536(6)	1	87(2)
Br(4)	5876(8)	7583(14)	7692(5)	1	89(2)
Br(6)	8200(20)	5000	9617(9)	1	86(2)
Br(8)	8199(17)	5000	5848(6)	1	139(5)
Br(9)	8188(18)	5000	13299(6)	1	149(6)
N(1)	9260(120)	10000	3220(60)	1	340(30)
H(1A)	9745	9081	2963	0.5	403
H(1B)	9745	10919	2963	0.5	403
N(2)	8120(130)	10000	6400(60)	1	340(30)
H(2A)	7938	10991	6561	0.5	403
H(2B)	8620	9485	6806	0.5	403
H2C()	7200	9524	6296	0.5	403
C(1)	7580(140)	10000	2960(60)	1	340(30)
H1C()	7399	10924	2612	0.5	403
H(1D)	7399	9076	2612	0.5	403
C(2)	6420(100)	10000	3640(70)	1	340(30)
H(2D)	5751	9084	3546	0.5	403
H(2E)	5751	10916	3546	0.5	403
C(3)	6780(110)	10000	4550(60)	1	340(30)
H(3A)	6299	9076	4800	0.5	403
H(3B)	6299	10924	4800	0.5	403
C(4)	8500(110)	10000	4760(50)	1	340(30)
H(4)	8496	8842	4762	0.5	403
C(5)	9730(100)	10000	4100(60)	1	340(30)
H(5A)	10389	10921	4195	0.5	403
H(5B)	10389	9079	4195	0.5	403
C(6)	9090(120)	10000	5650(60)	1	340(30)
H(6A)	9769	9084	5693	0.5	403
H(6B)	9769	10916	5693	0.5	403

C(7)	7090(160)	10000	9630(80)	1	350(40)
H(7)	6510	10000	10125	1	420
N(3)	8720(170)	10000	9670(110)	1	350(40)
H3C()	9267	10000	9222	1	420
H(3D)	9180	10000	10152	1	420
N(4)	6290(120)	10000	8880(80)	1	350(40)
H(4A)	6808	10000	8416	1	420
H(4B)	5273	10000	8871	1	420

*U_{eq} is defined as one third of the trace of the orthogonalized U_{ij} tensor.

Table E10. Atomic coordinates ($x10^4$) and equivalent isotropic displacement parameters ($Å^2x10^3$) for (3AMP)(MA)Pb_2Br_7 at 293(2) K with estimated standard deviations in parentheses.

Label	x	y	z	Occupancy	U_{eq}*
Pb(1)	11006(1)	7498(2)	4392(2)	1	53(1)
Pb(2)	7247(1)	7499(2)	4393(2)	1	54(1)
Br(5)	9087(7)	7451(5)	4621(14)	1	90(2)
Br(6)	11033(6)	4896(11)	1818(10)	1	107(2)
Br(7)	10986(6)	10113(11)	1811(11)	1	118(2)
Br(8)	5390(7)	7746(11)	4660(15)	1	127(4)
Br(9)	7253(6)	4898(11)	1808(10)	1	107(2)
Br(10)	7318(7)	9879(11)	6833(11)	1	119(2)
Br(2)	12838(5)	7739(12)	4648(15)	1	132(4)
N(3)	9180(50)	1770(60)	4390(60)	1	130(15)
H3C()	9216	2101	3383	1	156
H(3D)	8724	1167	4498	1	156
H(3E)	9633	1207	4633	1	156
C(9)	9120(50)	3180(70)	5470(70)	1	130(15)
H(9A)	8735	2951	6322	1	195
H(9B)	8916	4085	4884	1	195
H9C()	9660	3419	5904	1	195
N(2)	5780(60)	1860(120)	5430(120)	1	270(20)
H(2A)	5564	890	5397	1	325
H(2B)	5770	2222	6425	1	325
H2C()	6312	1828	5096	1	325
C(2)	2640(50)	2440(120)	5350(130)	1	270(20)

H(2D)	2603	2908	6396	1	325
H(2E)	2087	2100	5030	1	325
C(4)	4120(50)	1410(80)	5440(110)	1	270(20)
H(4A)	4433	440	5283	1	325
H(4B)	4264	1834	6474	1	325
N(1)	2950(50)	3680(90)	4200(90)	1	270(20)
H(1A)	2618	4635	4333	1	325
H(1B)	2865	3297	3123	1	325
C(3)	3200(60)	1020(80)	5430(120)	1	270(20)
H(3A)	3086	338	4525	1	325
H(3B)	3071	425	6384	1	325
C(5)	4370(40)	2590(80)	4190(90)	1	270(20)
H(5)	4259	2155	3127	1	325
C(7)	5290(40)	2950(100)	4380(140)	1	270(20)
H(7A)	5540	2938	3331	1	325
H(7B)	5339	4020	4790	1	325
C(6)	3860(50)	4070(70)	4440(110)	1	270(20)
H(6A)	4029	4880	3692	1	325
H(6B)	3947	4466	5507	1	325

*U_{eq} is defined as one third of the trace of the orthogonalized U_{ij} tensor.

Table E11. Atomic coordinates ($x10^4$) and equivalent isotropic displacement parameters ($Å^2x10^3$) for (4AMP)(FA)Pb_2Br_7 at 293(2) K with estimated standard deviations in parentheses.

Label	x	y	z	Occupancy	U_{eq}*
Pb(1)	5476(2)	5087(2)	3944(2)	1	35(1)
Pb(2)	1646(2)	5073(3)	3943(2)	1	44(1)
Pb(3)	5467(2)	81(3)	3799(2)	1	48(2)
Pb(4)	1645(2)	52(3)	3798(3)	1	54(2)
Br(5)	-137(11)	5110(20)	3890(20)	1	177(10)
Br(6)	3559(9)	5055(10)	3877(13)	1	71(3)
Br(7)	5459(10)	2591(7)	3593(12)	1	102(5)
Br(8)	5486(9)	4696(10)	6430(7)	1	82(4)
Br(9)	-180(9)	204(17)	3572(17)	1	144(7)
Br(10)	1641(8)	4577(7)	6399(7)	1	61(2)
Br(11)	1659(10)	2569(7)	3582(11)	1	100(5)

Br(12)	5469(7)	7524(7)	4304(9)	1	69(3)
Br(13)	3557(8)	102(10)	3749(10)	1	73(3)
Br(14)	7199(7)	5170(20)	3912(18)	1	161(9)
Br(15)	1640(8)	7528(7)	4303(8)	1	68(3)
Br(16)	5455(11)	296(13)	6297(10)	1	113(5)
Br(17)	1668(10)	421(8)	6358(9)	1	79(3)
Br(18)	7268(8)	223(17)	3577(16)	1	132(6)
C(1)	7480(40)	3430(50)	1980(60)	1	110(9)
H(1A)	7205	3531	2695	1	132
H(1B)	7429	4134	1571	1	132
C(4)	8380(40)	1530(40)	920(60)	1	110(9)
H(4A)	8421	943	1482	1	132
H(4B)	8659	1265	250	1	132
C(2)	8390(30)	3240(50)	2210(50)	1	110(9)
H(2A)	8662	3963	2259	1	132
H(2B)	8444	2873	2930	1	132
N(1)	7020(30)	2550(60)	1340(60)	1	110(9)
H1C()	6640	2938	838	1	132
H(1D)	6685	2140	1873	1	132
C(3)	8830(30)	2550(50)	1350(60)	1	110(9)
H(3)	8681	3028	709	1	132
C(5)	7470(40)	1700(60)	640(60)	1	110(9)
H(5A)	7433	1921	-138	1	132
H(5B)	7194	986	724	1	132
N(3)	6970(50)	2530(100)	7090(80)	1	200(20)
H(3A)	6490	2077	7296	1	243
H(3B)	6835	3302	7287	1	243
N(4)	10230(60)	2450(120)	6470(90)	1	200(20)
H4C()	10172	2537	7208	1	243
H(4D)	10696	2781	6245	1	243
H(4E)	10251	1721	6306	1	243
C(8)	7690(60)	2160(100)	7800(60)	1	200(20)
H(8A)	7603	2428	8565	1	243
H(8B)	7700	1349	7826	1	243

C(10)	8620(50)	2680(120)	6140(60)	1	200(20)
H(10)	8648	1880	5968	1	243
C(13)	9510(50)	2970(100)	5880(90)	1	200(20)
H(13A)	9583	2828	5084	1	243
H(13B)	9560	3778	5979	1	243
C(11)	7870(60)	2970(100)	5440(60)	1	200(20)
H(11A)	7973	2715	4681	1	243
H(11B)	7815	3777	5422	1	243
C(9)	8520(50)	2580(120)	7390(60)	1	200(20)
H(9A)	8615	3313	7724	1	243
H(9B)	8941	2079	7674	1	243
C(12)	7060(60)	2470(120)	5830(70)	1	200(20)
H(12A)	6608	2876	5482	1	243
H(12B)	7030	1695	5596	1	243
N(2)	10370(30)	1960(50)	1190(50)	1	110(9)
H2C()	10334	1677	500	1	132
H(2D)	10285	1415	1691	1	132
H(2E)	10874	2247	1293	1	132
C(7)	9740(30)	2850(50)	1340(70)	1	110(9)
H(7A)	9822	3399	747	1	132
H(7B)	9857	3229	2044	1	132
N(7)	3440(60)	3400(50)	1490(80)	1	121(14)
H7C()	3165	3391	2105	1	145
H(7D)	3606	4021	1204	1	145
N(5)	3730(50)	2440(70)	5510(50)	1	126(15)
H5C()	4093	1910	5495	1	151
H(5D)	3539	2710	4894	1	151
N(6)	3760(50)	2460(70)	7420(50)	1	126(15)
H(6A)	4116	1924	7428	1	151
H(6B)	3577	2734	8039	1	151
N(8)	3390(60)	1490(50)	1370(70)	1	121(14)
H8C()	3115	1442	1981	1	145
H(8D)	3523	886	1006	1	145
C(14)	3620(70)	2450(60)	990(60)	1	121(14)

H(14)	3919	2482	321	1	145
C(6)	3480(70)	2840(70)	6470(50)	1	126(15)
H(6)	3090	3412	6468	1	151

*U_{eq} is defined as one third of the trace of the orthogonalized U_{ij} tensor.

Table E12. Atomic coordinates ($x10^4$) and equivalent isotropic displacement parameters ($Å^2x10^3$) for (4AMP)(MA)Pb_2Br_7 at 293(2) K with estimated standard deviations in parentheses.

Label	x	y	z	Occupancy	U_{eq}*
Pb(1)	1638(2)	2493(4)	3974(7)	1	52(1)
Pb(2)	3523(2)	2505(4)	5863(7)	1	54(1)
Br(3)	2589(6)	2487(10)	4760(30)	1	83(3)
Br(4)	1622(5)	426(13)	1137(18)	1	95(4)
Br(6)	3513(4)	4544(14)	3010(20)	1	94(4)
Br(8)	757(5)	2420(40)	2970(50)	1	222(18)
Br(10)	1629(5)	4585(13)	7015(17)	1	85(3)
Br(12)	3505(5)	450(12)	8905(17)	1	85(3)
Br(13)	4427(5)	2580(30)	6650(50)	1	197(15)
N(2)	4350(20)	7520(100)	6380(130)	1	176(17)
H(2A)	4056	7469	6202	1	211
H(2B)	4417	8116	5487	1	211
N(3)	5840(20)	7880(130)	9170(130)	1	176(17)
H(3A)	5860	8942	9245	1	211
H(3B)	6095	7465	9435	1	211
H3C()	5701	7520	9869	1	211
C(4)	5164(18)	7510(80)	7120(100)	1	176(17)
H(4)	5067	7982	6022	1	211
N(1)	2630(60)	7620(150)	5400(200)	1	210(40)
H(1A)	2897	7374	5486	1	252
H(1B)	2496	6783	5598	1	252
H1C()	2611	8434	6015	1	252
C(1)	2450(50)	8100(200)	3600(300)	1	210(40)
H(1D)	2432	9247	3516	1	315
H(1E)	2178	7653	3217	1	315
H(1F)	2622	7719	2914	1	315
C(7)	5626(18)	7410(130)	7450(120)	1	176(17)

H(7A)	5704	6328	7250	1	211
H(7B)	5717	8106	6681	1	211
C(3)	4990(20)	5860(70)	7010(160)	1	176(17)
H(3D)	5102	5225	6263	1	211
H(3E)	5064	5360	8088	1	211
C(5)	5000(20)	8550(120)	8280(130)	1	176(17)
H(5A)	5065	9655	8095	1	211
H(5B)	5142	8275	9402	1	211
C(6)	4550(20)	8370(130)	8050(130)	1	176(17)
H(6A)	4420	9412	8053	1	211
H(6B)	4491	7749	8948	1	211
C(2)	4520(20)	5860(90)	6410(180)	1	176(17)
H2C()	4408	5193	7130	1	211
H(2D)	4445	5409	5311	1	211

*U_{eq} is defined as one third of the trace of the orthogonalized U_{ij} tensor.

Table E13. Atomic coordinates ($x10^4$) and equivalent isotropic displacement parameters ($Å^2x10^3$) for $(3AMP)_{0.5}(4AMP)_{0.5}(FA)_{0.5}(MA)_{0.5}Pb_2Br_7$ at 292.93 K with estimated standard deviations in parentheses.

Label	x	y	z	Occupancy	U_{eq}*
Pb(1)	14197(1)	2499(2)	9656(1)	1	36(1)
Pb(2)	10399(1)	2499(2)	9655(1)	1	36(1)
Br(3)	10404(4)	4752(8)	6920(12)	1	94(2)
Br(4)	14185(4)	4753(8)	6914(11)	1	93(2)
Br(5)	14184(4)	-290(7)	7454(11)	1	80(2)
Br(6)	10408(4)	-292(7)	7452(10)	1	82(2)
Br(7)	12286(5)	2507(6)	9633(16)	1	76(1)
Br(10)	8559(3)	2502(5)	9653(11)	1	129(3)
Br(11)	15971(3)	2505(7)	9635(13)	1	178(5)
N(1)	8900(30)	2170(60)	5290(70)	1	272(10)
H(1A)	9073	2938	5940	1	327
H(1B)	9339	1613	4955	1	327
H1C()	8549	1535	5803	1	327
N(3)	5720(30)	2310(50)	5050(80)	1	272(10)
H(3A)	5568	2604	6127	1	327

H(3B)	5211	2002	4491	1	327
C(2)	6120(30)	3700(40)	4210(80)	1	272(10)
H(2A)	5865	3768	3174	1	327
H(2B)	5954	4645	4790	1	327
C(3)	7040(30)	3840(40)	3950(70)	1	272(10)
H3C()	7130	4256	2892	1	327
H(3D)	7256	4628	4694	1	327
C(4)	7560(30)	2390(40)	4130(70)	1	272(10)
H(4)	7420	1726	3204	1	327
C(5)	7190(40)	1530(50)	5560(60)	1	272(10)
H(5A)	7163	2233	6464	1	327
H(5B)	7539	621	5835	1	327
C(6)	6320(40)	980(40)	5060(70)	1	272(10)
H(6A)	6352	522	4002	1	327
H(6B)	6131	168	5782	1	327
C(7)	8470(30)	2890(70)	3900(80)	1	272(10)
H(7A)	8691	2484	2907	1	327
H(7B)	8522	4041	3904	1	327
N(2)	12360(40)	1890(40)	5360(70)	1	196(10)
H2C()	12507	1001	4853	1	236
H(2D)	11869	1751	5824	1	236
H(2E)	12745	2109	6097	1	236
C(8)	12310(50)	3220(50)	4210(80)	1	196(10)
H(8A)	12860	3650	4040	1	294
H(8B)	11953	4031	4625	1	294
H8C()	12091	2837	3221	1	294

*U_{eq} is defined as one third of the trace of the orthogonalized U_{ij} tensor.

Table E14. Atomic coordinates ($x10^4$) and equivalent isotropic displacement parameters ($Å^2x10^3$) for $(4AMP)(FA)_{0.5}(MA)_{0.5}Pb_2Br_7$ at 293.01 K with estimated standard deviations in parentheses.

Label	x	y	z	Occupancy	U_{eq}*
Pb(1)	9390(1)	2501(2)	8552(1)	1	41(1)
Pb(2)	5611(1)	2500(1)	8552(1)	1	33(1)
Br(1)	11184(6)	2556(11)	8540(20)	1	206(9)

Br(3)	9360(5)	-455(4)	6471(9)	1	74(2)
Br(4)	5592(5)	-468(4)	6490(8)	1	70(2)
Br(5)	9353(5)	4601(4)	5626(9)	1	82(2)
Br(6)	5592(5)	4592(5)	5603(9)	1	77(2)
Br(7)	3843(4)	2555(11)	8535(19)	1	200(8)
Br(9)	7537(6)	2501(6)	8556(14)	1	78(1)
N(1)	7580(30)	1750(50)	4340(60)	1	131(11)
H(1A)	7796	908	3838	1	157
H(1B)	7061	1535	4615	1	157
H1C()	7874	1969	5209	1	157
C(1)	7590(40)	3190(60)	3210(70)	1	131(11)
H(1D)	8006	3034	2402	1	196
H(1E)	7719	4138	3814	1	196
H(1F)	7062	3308	2716	1	196
N(2)	930(30)	2440(70)	3700(80)	1	177(10)
H(2A)	503	2911	4366	1	212
H(2B)	649	1855	2852	1	212
N(3)	4160(30)	2180(60)	3980(90)	1	177(10)
H(3A)	4582	2600	3432	1	212
H(3B)	4093	1167	3693	1	212
H3C()	4272	2231	5024	1	212
C(2)	1370(30)	1260(70)	4690(80)	1	177(10)
H2C()	1277	200	4246	1	212
H(2D)	1144	1274	5760	1	212
C(3)	2300(30)	1520(70)	4800(70)	1	177(10)
H(3D)	2404	2318	5617	1	212
H(3E)	2556	531	5138	1	212
C(4)	2670(30)	2050(60)	3250(60)	1	177(10)
H(4)	2783	1189	2489	1	212
C(5)	2290(30)	3510(60)	2540(80)	1	177(10)
H(5A)	2347	3449	1389	1	212
H(5B)	2599	4432	2906	1	212
C(6)	1400(30)	3760(60)	2940(90)	1	177(10)
H(6A)	1362	4675	3649	1	212

H(6B)	1116	4041	1958	1	212
C(7)	3400(30)	3090(60)	3640(80)	1	177(10)
H(7A)	3506	3799	2738	1	212
H(7B)	3270	3750	4559	1	212

*U_{eq} is defined as one third of the trace of the orthogonalized U_{ij} tensor.

Table E15. Atomic coordinates ($x10^4$) and equivalent isotropic displacement parameters ($Å^2x10^3$) for $(3AMP)_{0.5}(4AMP)_{0.5}(FA)_{0.5}Pb_2Br_7$ at 297.98 K with estimated standard deviations in parentheses.

Label	x	y	z	Occupancy	U_{eq}*
Pb(1)	5236(1)	2500(2)	5389(1)	1	38(1)
Pb(2)	1407(1)	2499(2)	5388(1)	1	40(1)
Br(3)	5245(5)	4752(9)	8151(10)	1	78(2)
Br(5)	1407(5)	4758(9)	8143(10)	1	78(2)
Br(6)	5243(6)	222(11)	2677(11)	1	86(3)
Br(7)	1414(5)	215(11)	2684(11)	1	87(3)
Br(8)	3294(7)	2511(8)	5316(16)	1	70(1)
Br(9)	7008(5)	2509(9)	5334(18)	1	158(6)
Br(1)	-422(6)	2512(8)	5347(18)	1	157(6)
N(2)	3070(30)	8330(60)	4400(60)	1	172(12)
H2C()	2756	7676	3890	1	206
H(2D)	3178	9243	4002	1	206
N(1)	3180(30)	6490(50)	6220(60)	1	172(12)
H(1A)	2855	5929	5630	1	206
H(1B)	3353	6114	7106	1	206
C(1)	3390(50)	7910(50)	5780(60)	1	172(12)
H(1)	3737	8570	6376	1	206
N(4)	6690(40)	7700(70)	5200(80)	1	245(15)
H(4A)	6816	8200	4304	1	295
H(4B)	6338	8287	5762	1	295
H4C()	6454	6773	4975	1	295
N(3)	9750(40)	8070(70)	4910(70)	1	245(15)
H(3A)	10295	8535	5023	1	295
H(3B)	9700	7661	3839	1	295
C(4)	8180(30)	6970(70)	5080(70)	1	245(15)

H(4)	7951	6268	4274	1	295
C(3)	8420(50)	8450(70)	4240(70)	1	245(15)
H3C()	7941	9127	4126	1	295
H(3D)	8629	8189	3193	1	295
C(5)	8810(40)	6010(50)	5980(80)	1	245(15)
H(5A)	8604	5857	7046	1	295
H(5B)	8848	4976	5484	1	295
C(2)	9100(40)	9320(50)	5160(80)	1	245(15)
H(2A)	9249	10321	4686	1	295
H(2B)	8958	9460	6268	1	295
C(7)	7470(40)	7430(90)	6130(70)	1	245(15)
H(7A)	7369	6594	6899	1	295
H(7B)	7607	8386	6708	1	295
C(6)	9660(40)	6710(70)	6060(90)	1	245(15)
H(6A)	10074	5904	5815	1	295
H(6B)	9769	7086	7128	1	295

*U_{eq} is defined as one third of the trace of the orthogonalized U_{ij} tensor.

Table E16. Atomic coordinates ($x10^4$) and equivalent isotropic displacement parameters ($Å^2x10^3$) for $(3AMP)_{0.5}(4AMP)_{0.5}(MA)_{0.5}Pb_2Br_7$ at 293.0 K with estimated standard deviations in parentheses.

Label	x	y	z	Occupancy	U_{eq}*
Pb(1)	4776(1)	2501(1)	4891(1)	1.000000	34(1)
Pb(2)	6661(1)	2499(1)	6778(1)	1.000000	35(1)
Br(3)	4776(1)	4620(3)	7806(1)	1.000000	73(1)
Br(4)	6651(1)	381(3)	9679(1)	1.000000	76(1)
Br(6)	5730(1)	2497(2)	5832(1)	1.000000	72(1)
Br(8)	4775(1)	-355(3)	7065(1)	1.000000	83(2)
Br(9)	6651(1)	5353(3)	8947(1)	1.000000	86(2)
Br(10)	3875(1)	2516(4)	3922(1)	1.000000	144(2)
Br(12)	7565(1)	2492(5)	7627(1)	1.000000	162(3)
N(1)	3966(6)	2130(30)	8657(14)	1.000000	239(7)
H(1a)	4087(6)	1460(30)	9478(14)	1.000000	287(8)
H(1b)	4163(6)	2460(30)	8167(14)	1.000000	287(8)
C(4)	3094(6)	3120(30)	7828(17)	1.000000	239(7)

H(4)	3165(6)	3860(30)	7036(17)	1.000000	287(8)
C(3)	3197(7)	1440(20)	7450(18)	1.000000	239(7)
H(3a)	3134(7)	730(20)	8267(18)	1.000000	287(8)
H(3b)	3024(7)	1140(20)	6380(18)	1.000000	287(8)
C(5)	3359(7)	3440(30)	9527(16)	1.000000	239(7)
H(5a)	3280(7)	4440(30)	9947(16)	1.000000	287(8)
H(5b)	3330(7)	2590(30)	10273(16)	1.000000	287(8)
C(7)	2642(7)	3300(30)	7831(19)	1.000000	239(7)
H(7a)	2603(7)	3320(30)	8941(19)	1.000000	287(8)
H(7b)	2518(7)	4250(30)	7242(19)	1.000000	287(8)
C(2)	3645(7)	1250(30)	7445(18)	1.000000	239(7)
H(2a)	3671(7)	1550(30)	6357(18)	1.000000	287(8)
H(2b)	3712(7)	130(30)	7584(18)	1.000000	287(8)
C(6)	3802(7)	3530(30)	9372(18)	1.000000	239(7)
H(6a)	3982(7)	3720(30)	10463(18)	1.000000	287(8)
H(6b)	3825(7)	4450(30)	8703(18)	1.000000	287(8)
N(2)	5789(6)	3250(30)	10367(13)	1.000000	168(8)
H(2c)	5680(50)	3760(50)	11090(180)	1.000000	201(9)
H(2d)	6064(7)	3350(30)	10700(200)	1.000000	201(9)
H(2e)	5690(50)	3660(60)	9370(60)	1.000000	201(9)
C(1)	5682(10)	1580(30)	10344(16)	1.000000	168(8)
H(1c)	5387(11)	1460(40)	9900(300)	1.000000	251(11)
H(1d)	5820(60)	1010(60)	9700(200)	1.000000	251(11)
H(1e)	5760(70)	1160(80)	11440(50)	1.000000	251(11)
N(4)	2477(8)	1830(30)	6943(13)	1.000000	271(12)
H(4a)	2450(80)	1960(120)	5870(40)	1.000000	326(14)
H(4b)	2650(40)	1020(70)	7300(200)	1.000000	326(14)
H(4c)	2230(40)	1610(180)	7100(300)	1.000000	326(14)

*U_{eq} is defined as one third of the trace of the orthogonalized U_{ij} tensor.

Table E17. Anisotropic displacement parameters ($Å^2x10^3$) for $(3AMP)(FA)Pb_2Br_7$ at 293(2) K with estimated standard deviations in parentheses.

Label	U_{11}	U_{22}	U_{33}	U_{12}	U_{13}	U_{23}
Pb(1)	44(2)	47(1)	54(2)	0	3(1)	0
Pb(2)	40(1)	39(1)	57(1)	0	-3(1)	0
Br(3)	79(3)	74(2)	108(3)	37(2)	-8(2)	-9(2)
Br(4)	70(2)	71(3)	125(4)	35(2)	3(2)	3(2)
Br(6)	100(4)	110(2)	49(2)	0	6(2)	0
Br(8)	173(10)	184(13)	60(4)	0	-25(5)	0
Br(9)	197(11)	200(13)	49(4)	0	21(5)	0

The anisotropic displacement factor exponent takes the form: $-2\pi^2[h^2a^{*2}U_{11} + ... + 2hka^*b^*U_{12}]$.

Table E18. Anisotropic displacement parameters ($Å^2x10^3$) for $(3AMP)(MA)Pb_2Br_7$ at 293(2) K with estimated standard deviations in parentheses.

Label	U_{11}	U_{22}	U_{33}	U_{12}	U_{13}	U_{23}
Pb(1)	69(2)	50(2)	41(1)	0(1)	3(1)	-1(1)
Pb(2)	73(2)	46(1)	42(1)	-1(1)	-8(1)	-1(1)
Br(5)	56(2)	129(4)	85(6)	-4(3)	17(3)	-13(3)
Br(6)	132(5)	104(4)	86(3)	6(4)	17(3)	-68(3)
Br(7)	147(5)	94(4)	115(5)	-5(4)	-18(4)	84(4)
Br(8)	78(4)	153(8)	150(9)	9(4)	14(5)	67(6)
Br(9)	134(5)	103(4)	84(3)	0(4)	-20(3)	-69(3)
Br(10)	161(6)	88(4)	107(4)	10(4)	21(4)	-78(3)
Br(2)	62(4)	198(10)	135(8)	5(4)	7(4)	71(6)

The anisotropic displacement factor exponent takes the form: $-2\pi^2[h^2a^{*2}U_{11} + ... + 2hka^*b^*U_{12}]$.

Table E19. Anisotropic displacement parameters ($Å^2x10^3$) for $(4AMP)(FA)Pb_2Br_7$ at 293(2) K with estimated standard deviations in parentheses.

Label	U_{11}	U_{22}	U_{33}	U_{12}	U_{13}	U_{23}
Pb(1)	40(2)	35(2)	29(2)	-6(2)	0(2)	-1(2)
Pb(2)	46(2)	42(2)	44(2)	-1(2)	8(2)	-3(2)
Pb(3)	51(2)	45(2)	47(3)	3(2)	-4(2)	11(2)
Pb(4)	51(2)	51(2)	61(2)	-8(2)	2(2)	12(2)

Br(5)	55(9)	240(20)	240(20)	2(13)	-25(11)	-21(17)
Br(6)	32(4)	87(6)	94(7)	7(6)	5(5)	-24(6)
Br(7)	116(11)	26(4)	165(10)	3(5)	14(9)	37(5)
Br(8)	99(8)	124(9)	22(3)	14(8)	4(4)	19(5)
Br(9)	63(8)	196(15)	173(12)	36(10)	-14(8)	76(11)
Br(10)	90(7)	58(4)	34(4)	-12(5)	8(4)	-9(3)
Br(11)	158(14)	29(4)	113(8)	3(5)	19(8)	22(4)
Br(12)	81(7)	45(4)	80(6)	-7(5)	-31(5)	17(4)
Br(13)	52(6)	91(7)	77(7)	-3(6)	-10(6)	-2(5)
Br(14)	6(3)	250(20)	225(17)	20(9)	11(6)	-28(14)
Br(15)	101(8)	50(4)	54(4)	0(5)	20(5)	13(3)
Br(16)	134(13)	148(12)	57(6)	-6(10)	-16(7)	29(7)
Br(17)	119(9)	62(5)	56(5)	-1(6)	-10(5)	-11(4)
Br(18)	43(7)	195(14)	156(10)	-18(8)	23(7)	82(10)

The anisotropic displacement factor exponent takes the form: $-2\pi^2[h^2a^{*2}U_{11} + ... + 2hka^*b^*U_{12}]$.

Table E20. Anisotropic displacement parameters ($Å^2x10^3$) for $(4AMP)(MA)Pb_2Br_7$ at 293(2) K with estimated standard deviations in parentheses.

Label	U_{11}	U_{22}	U_{33}	U_{12}	U_{13}	U_{23}
Pb(1)	76(2)	39(1)	45(2)	10(1)	22(2)	6(2)
Pb(2)	53(1)	58(2)	49(2)	8(1)	7(2)	7(2)
Br(3)	62(3)	107(3)	80(8)	4(5)	16(3)	-2(6)
Br(4)	126(8)	76(6)	75(8)	22(5)	7(6)	-53(6)
Br(6)	112(7)	82(6)	100(10)	0(5)	48(6)	56(6)
Br(8)	53(7)	320(40)	280(40)	-14(10)	11(11)	-60(20)
Br(10)	147(9)	63(5)	53(6)	-21(5)	40(5)	-19(4)
Br(12)	134(8)	66(5)	61(7)	-3(5)	36(6)	8(4)
Br(13)	58(8)	270(30)	250(40)	-33(9)	26(11)	-34(18)

The anisotropic displacement factor exponent takes the form: $-2\pi^2[h^2a^{*2}U_{11} + ... + 2hka^*b^*U_{12}]$.

Table E21. Anisotropic displacement parameters ($Å^2x10^3$) for $(3AMP)_{0.5}(4AMP)_{0.5}(FA)_{0.5}(MA)_{0.5}Pb_2Br_7$ at 292.93 K with estimated standard deviations in parentheses.

Label	U_{11}	U_{22}	U_{33}	U_{12}	U_{13}	U_{23}
Pb(1)	38(1)	29(1)	39(1)	0(1)	0(1)	0(1)
Pb(2)	43(1)	38(1)	28(1)	0(1)	0(1)	0(1)
Br(3)	112(4)	84(4)	85(5)	-6(4)	-1(4)	56(3)
Br(4)	107(4)	87(4)	84(5)	4(4)	8(4)	56(3)
Br(5)	108(4)	66(3)	67(4)	8(3)	-11(3)	-35(2)
Br(6)	115(4)	65(3)	66(4)	-8(3)	4(3)	-36(3)
Br(7)	32(1)	96(2)	100(2)	0(1)	-1(1)	1(1)
Br(10)	37(2)	172(7)	177(8)	2(2)	-3(3)	-14(4)
Br(11)	30(2)	257(9)	246(12)	-4(3)	-3(3)	19(6)

The anisotropic displacement factor exponent takes the form: $-2\pi^2[h^2a^{*2}U_{11} + ... + 2hka^*b^*U_{12}]$.

Table E22. Anisotropic displacement parameters ($Å^2x10^3$) for $(4AMP)(FA)_{0.5}(MA)_{0.5}Pb_2Br_7$ at 293.01 K with estimated standard deviations in parentheses.

Label	U_{11}	U_{22}	U_{33}	U_{12}	U_{13}	U_{23}
Pb(1)	38(1)	42(1)	42(1)	2(1)	0(1)	1(1)
Pb(2)	32(1)	32(1)	34(1)	-2(1)	0(1)	0(1)
Br(1)	59(7)	258(18)	300(20)	-20(5)	3(9)	-25(10)
Br(3)	117(4)	50(2)	56(3)	10(2)	-11(3)	-22(2)
Br(4)	102(4)	60(3)	47(2)	-18(2)	16(2)	-23(2)
Br(5)	123(5)	51(2)	71(3)	2(2)	3(3)	28(2)
Br(6)	106(4)	64(3)	60(3)	-11(3)	-10(3)	30(2)
Br(7)	15(3)	300(17)	285(16)	6(4)	-1(5)	20(9)
Br(9)	31(2)	101(3)	103(3)	0(2)	-2(2)	0(2)

The anisotropic displacement factor exponent takes the form: $-2\pi^2[h^2a^{*2}U_{11} + ... + 2hka^*b^*U_{12}]$.

Table E23. Anisotropic displacement parameters ($Å^2x10^3$) for $(3AMP)_{0.5}(4AMP)_{0.5}(FA)_{0.5}Pb_2Br_7$ at 297.98 K with estimated standard deviations in parentheses.

Label	U_{11}	U_{22}	U_{33}	U_{12}	U_{13}	U_{23}
Pb(1)	42(1)	32(1)	40(1)	0(1)	-5(1)	0(1)
Pb(2)	49(1)	39(1)	32(1)	0(1)	6(1)	0(1)
Br(3)	107(4)	63(4)	65(5)	4(5)	-7(4)	-31(3)
Br(5)	106(4)	68(4)	61(5)	-6(5)	14(4)	-31(4)
Br(6)	106(5)	74(5)	78(6)	-5(5)	-1(5)	-46(4)
Br(7)	110(5)	78(5)	73(6)	10(5)	-6(5)	-45(4)
Br(8)	40(2)	86(2)	85(2)	1(2)	-5(2)	1(2)
Br(9)	34(3)	214(12)	227(13)	1(4)	-21(4)	16(7)
Br(1)	50(3)	213(12)	207(12)	1(4)	18(4)	-14(7)

The anisotropic displacement factor exponent takes the form: $-2\pi^2[h^2a^{*2}U_{11} + ... + 2hka^*b^*U_{12}]$.

Table E24. Anisotropic displacement parameters ($Å^2x10^3$) for $(3AMP)_{0.5}(4AMP)_{0.5}(MA)_{0.5}Pb_2Br_7$ at 293.0 K with estimated standard deviations in parentheses.

Label	U_{11}	U_{22}	U_{33}	U_{12}	U_{13}	U_{23}
Pb(1)	36(1)	26(1)	39(1)	0(1)	9(1)	0(1)
Pb(2)	42(1)	37(1)	27(1)	0(1)	10(1)	0(1)
Br(3)	98(3)	59(2)	69(2)	-13(2)	32(2)	-33(2)
Br(4)	106(3)	62(2)	64(2)	-8(2)	28(2)	31(2)
Br(6)	32(1)	90(2)	90(2)	-5(2)	8(1)	0(2)
Br(8)	100(3)	72(2)	71(3)	-7(2)	12(2)	42(2)
Br(9)	108(3)	76(2)	80(3)	-1(2)	35(2)	-47(2)
Br(10)	29(2)	197(6)	183(5)	4(2)	-14(2)	6(3)
Br(12)	48(2)	209(6)	232(6)	7(2)	43(3)	6(3)

The anisotropic displacement factor exponent takes the form: $-2\pi^2[h^2a^{*2}U_{11} + ... + 2hka^*b^*U_{12}]$.

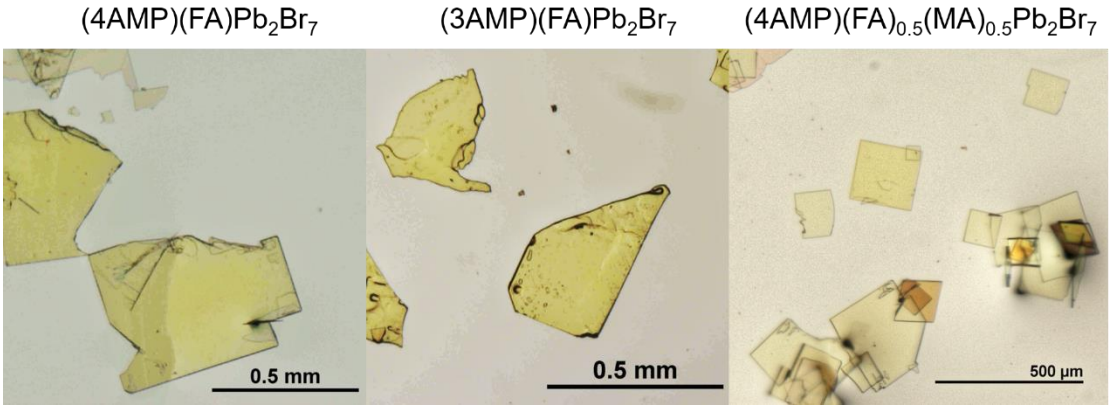

Figure E1. Representative microscopic photos of the (A')(A)Pb_2Br_7 compounds.

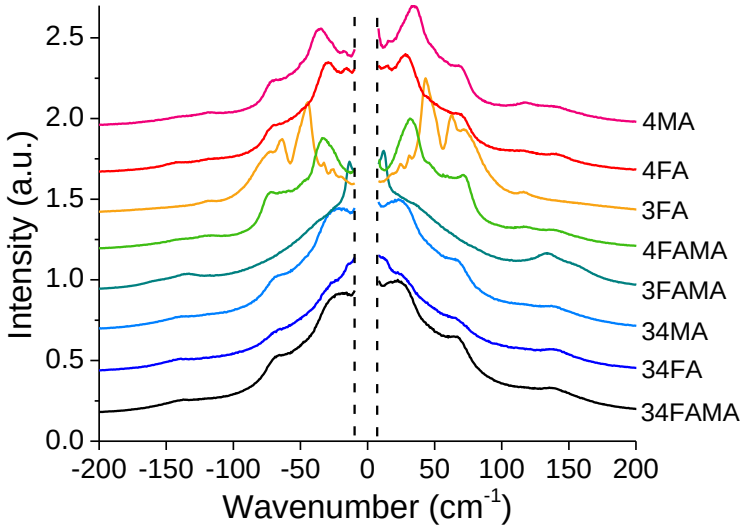

Figure E2. Low-frequency Raman spectra of hybrid lead bromide crystals. The spectral region between ±8 cm^{-1} has been deleted because of the use of notch filter. The spectra were collected using 473 nm laser under ambient condition. The mixing of templating and perovskitizer makes the spectra much less resolved and much broader than the ones with no mixing (4MA, 4FA and 3FA), indicating a more dynamically disorder environment for the mixed ones (4FAMA, 3FAMA, 34MA, 34FA and 34FAMA).

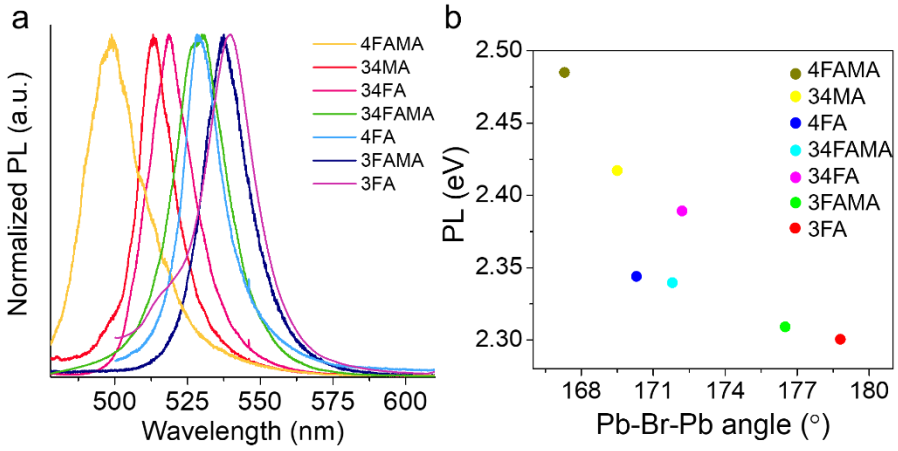

Figure E3. Steady-state PL spectra were collected using HORIBA LabRAM HR Evolution Confocal RAMAN microscope. 473 nm laser (25mW, 0.1% power) was used to excite all samples at 10× or 50× magnification (2μm beam size). The PL emission energy shows a similar trend as the band gap, where with increasing Pb-Br-Pb angle the emission energy decreases. 4FA and 34FAMA are a bit off from the trend, which have lower emission energy than expected.

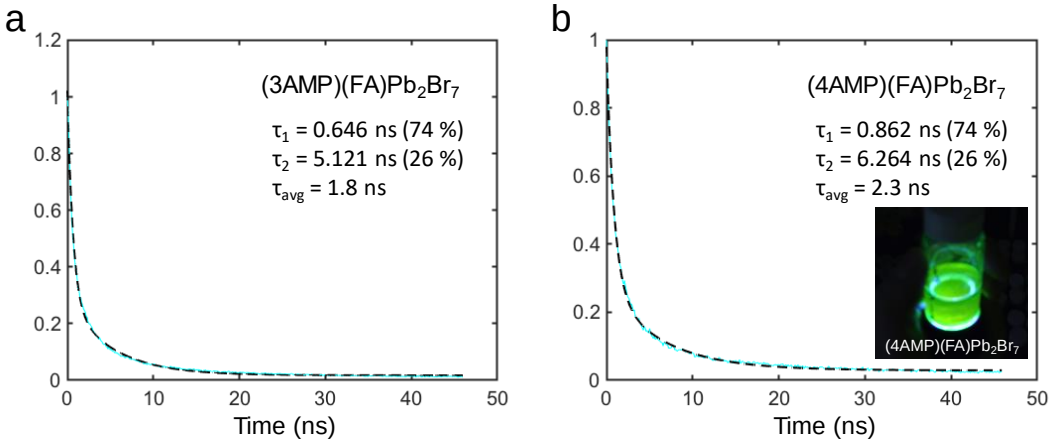

Figure E4. Time-resolved PL decay of (a) (3AMP)(FA)Pb_2Br_7 and (b) (4AMP)(FA)Pb_2Br_7 (inserted shows the compound excited by UV flashlight, exhibiting greenlight emission). Time-resolved PL spectra were captured with a streak camera. During the measurements, the samples were mounted in a vacuum cryostat and maintained under < 10^{-7} Torr pressure (λ_{exc}: 330 nm).

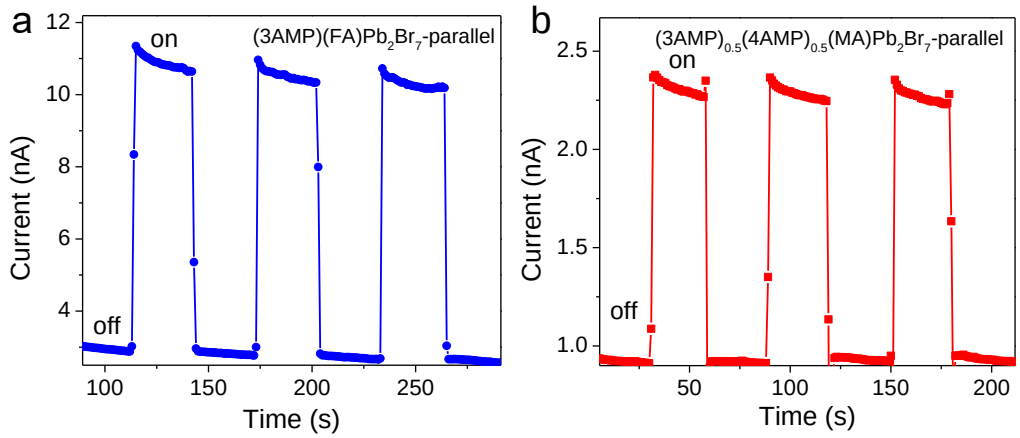

Figure E5. On/off switching cycles of photocurrent responses under 10V bias and ambient light. The electrodes were placed on the same side of the crystal plate. 3FA (on/off ratio ~10) shows better photo-response than the 34MA sample (on/off ratio ~2). The rest of the compounds were not measured due to size limitation.

Lingling Mao

Department of Chemistry, Northwestern University, 2145 Sheridan Road, Evanston, IL
LinglingMao2014@u.northwestern.edu

EDUCATION

Northwestern University· Ph.D.· Chemistry· Evanston, IL Nov. 2018
Sun Yat-sen University· B.S.· Chemistry· Guangzhou, China June 2014

RESEARCH EXPERIENCE

Graduate Research Sept. 2014 – Nov. 2018
Northwestern University, Advisor: Prof. Mercouri G. Kanatzidis
Research topic: Hybrid 2D Halide Perovskite Materials for Optoelectronics.

Undergraduate Research July 2012 – June 2014
Sun Yat-sen University, Advisor: Prof. Ming-liang Tong
Research topic: Construction of d^{10} Metal-Organic Frameworks with 1,2,4,5-Tetra (4-pyridyl)benzene Ligand: Structure and Photoluminescence.
NSF Research Experience for Undergraduates (REU) at University of Southern California
Advisor: Prof. Peter Z. Qin July – Aug. 2013
Research topic: Site-Directed Spin Labeling studies on Human Telomeric DNA.

RESEARCH INTERESTS

- Explore the structure-property relationship in hybrid organic-inorganic halide perovskite materials
- Synthesis and characterization of halide perovskite thin-films and nanocrystals

AWARDS

- 2018 International Institute for Nanotechnology (IIN) Outstanding Research Award
- Outstanding Student Research Award at the Chinese American Chemical Society the Great Lakes Chapter (GLCACS) 22nd Annual Conference in May 2018
- 2017 Chinese Government Award for Outstanding Self-financed Students Abroad
- Kemin Travel Award for 2017 ACS Spring Conference

PUBLICATIONS

1. **Mao, L.**; Stoumpos, C. C.; Kanatzidis, M. G. "Two-dimensional Hybrid Halide Perovskites: Principles and Promises." *J. Am. Chem. Soc., Just Accepted.* DOI: 10.1021/jacs.8b10851

2. **Mao, L.**; Guo, P.; Kepenekian, M.; Hadar, I.; Katan, C.; Even, J.; Schaller, R.; Stoumpos, C. C.; Kanatzidis, M. G. "Structural Diversity in White-light Emitting Hybrid Lead Bromide Perovskites." *J. Am. Chem. Soc.*, **2018**, 140 (40), 13078–13088.

3. **Mao, L.**; Ke, W.; Pedesseau, L.; Wu, Y.; Katan, C.; Even, J.; Wasielewski, M. R.; Stoumpos, C. C.; Kanatzidis, M. G. "Hybrid Dion–Jacobson 2D Lead Iodide Perovskites." *J. Am. Chem. Soc.*, **2018**, 140 (10), 3775–3783.

4. **Mao, L.**; Wu, Y., Stoumpos, C. C.; Traore, B.; Katan, C.; Even, J.; Wasielewski, M. R.; Kanatzidis, M. G. "Tunable White-light Emission in Single Cation Templated Three-layered 2D Perovskites $(CH_3CH_2NH_3)_4Pb_3Br_{10-x}Cl_x$." *J. Am. Chem. Soc.*, **2017**, 139 (34), 11956–11963.

5. **Mao, L.;** Wu, Y.; Stoumpos, C. C.; Wasielewski, M. R.; Kanatzidis, M. G. "White-light Emission and Structural Distortion in New Corrugated 2D Lead Bromide Perovskites." *J. Am. Chem. Soc.*, **2017**, *139* (14), 5210–5215. *-featured in C&EN news and Department of Energy website*

6. **Mao, L.**; Tsai, H.; Nie, W.; Ma, L.; Im, J.; Stoumpos, C. C.; Malliakas, C. D.; Hao, F.; Wasielewski, M. R.; Mohite, A. D.; Kanatzidis, M. G. "Role of Organic Counterion in Lead- and Tin-Based Two-Dimensional Semiconducting Iodide Perovskites and Application in Planar Solar Cells." *Chem. Mater.*, **2016**, *28* (21), 7781–7792.

7. Guo, P.; Huang, W.; Stoumpos, C. C.; **Mao, L.**; Gong, J.; Zeng, L.; Diroll, B.; Xia, Y.; Ma, X.; Gosztola, D.; Xu, T.; Ketterson, J.; Bedzyk, M.; Facchetti, A.; Marks, T.J.; Kanatzidis, M. G.; Schaller, R. "Hyperbolic Dispersion Arising from Anisotropic Excitons in Two-Dimensional Perovskites." *Phys. Rev. Lett.* **2018**, 121(12), 127401.

8. Li, J.; Stoumpos, C. C.; Trimarchi, G. G.; Chung, I.; **Mao, L.**; Chen, M.; Wasielewski, M. R.; Wang, L.; Kanatzidis, M. G." Air-Stable Direct Bandgap Perovskite Semiconductors: All-Inorganic Tin-Based Heteroleptic Halides $A_xSnCl_yI_z$ (A = Cs, Rb)." *Chem. Mater.*, **2018**, *30* (14), 4847-4856

9. Guo, P.; Stoumpos, C. C.; **Mao, L.**; Sadasivam, S.; Ketterson, J.; Darancet, P.; Kanatzidis, M. G.; Schaller, R. "Cross-plane Coherent Acoustic Phonons in Two-dimensional Organic-inorganic Hybrid Perovskites." *Nat. Commun*. **2018**, 9, 2019.

10. Ke, W.; Stoumpos, C. C.; Spanopoulos, I.; **Mao, L.**; Chen, M.; Wasielewski, M. R.; Kanatzidis, M. G. "Efficient Lead-Free Solar Cells Based on Hollow {en}$MASnI_3$ Perovskites." *J. Am. Chem. Soc.*, **2017**, 139 (41), 14800–14806.

11. Ke, W.; Stoumpos, C. C.; Zhu, M.; **Mao, L.**; Spanopoulos, I.; Liu, J.; Kontsevoi, O. Y.; Chen, M.; Sarma, D.; Zhang, Y.; Wasielewski, M. R.; Kanatzidis, M. G. "Enhanced photovoltaic performance and stability with a new type of hollow 3D perovskite {en} $FASnI_3$." *Sci. Adv.*, **2017**, 3 (8), e1701293

12. Stoumpos, C. C.; **Mao, L.**; Malliakas, C. D.; Kanatzidis, M. G. "Structure–Band Gap Relationships in Hexagonal Polytypes and Low-Dimensional Structures of Hybrid Tin Iodide Perovskites." *Inorg. Chem.*, **2017**, *56* (1), 56–73.

13. Zhang, X.; Xu, C. X.; Di Felice, R.; Sponer, J.; Islam, B.; Stadlbauer, P.; Ding, Y.; **Mao, L.**; Mao, Z. W.; Qin, P. Z. "Conformations of Human Telomeric G-quadruplex Studied Using a Nucleotide-Independent Nitroxide Label." *Biochemistry*, **2016**, *55* (2), 360–372.

14. **Mao, L.**; Liu, W.; Li, Q. W.; Jia, J. H.; Tong, M. L. "Controllable Self-Assembly of Two Luminescent Silver (I) Metal–Organic Frameworks Bearing a Tetradentate Ligand." *Cryst. Growth Des.*, **2014**, *14* (9), 4674–4680.

15. Liu, W.; Bao, X.; **Mao, L.**; Tucek, J.; Zboril, R.; Liu, J.L.; Guo, F. S.; Ni, Z. P.; Tong, M. L. "A chiral spin crossover metal–organic framework." *Chem. Comm.*, **2014**, *50* (31), 4059-4061.

16. Guo, F. S.; Chen, Y. C.; **Mao, L.**; Lin, W. Q.; Leng, J. D.; Tarasenko, R.; Orendáč, M.; Prokleška, J.; Sechovský, V.; Tong, M. L. "Anion-Templated Assembly and Magnetocaloric Properties of a Nanoscale {Gd38} Cage versus a {Gd48} Barrel." *Chem. Eur. J.*, **2013**, *19* (44), 14876-14885.

17. Bao, X.; Liu, W.; **Mao, L.**; Jiang, S.D.; Liu, J. L.; Chen, Y. C.; Tong, M. L. "Programmed Self-Assembly of Heterometallic [3×3] Grid [MIICuII4CuI4](M= Fe, Ni, Cu, and Zn)." *Inorg. Chem.*, **2013**, *52* (11), 6233-6235.

SKILLS

Synthesis

- Growth of single crystals using solution, hydrothermal and solid-state synthesis
- Fabrication of thin films by drop casting and spin coating

Instrumentation

- Single-crystal and Powder X-ray diffraction: data collection, structure solution and refinement
- Scanning electron microscopy (SEM)
- Thermal analysis (TGA, DTA, DSC)
- Spectroscopic measurements: FT-IR (diffuse reflectance and transmission setups), FT-Raman and Confocal-Raman spectroscopies, UV/VIS/NIR spectroscopies, Photoluminescence spectroscopy

CONFERENCE PRESENTATIONS

Oral presentations

ACS 256th National Meeting, Boston, Aug. 2018.
"Hybrid 2D Dion–Jacobson Perovskites and Application in Solar Cells."

ACS 253rd National Meeting, San Francisco, Apr. 2017.

"Lead- and Tin-based Two-dimensional Hybrid Organic-inorganic Iodide Perovskites: Structure, Properties and Application in Planar Solar Cells."

TEACHING

General Chemistry Laboratory sessions Fall 2014 – Summer 2015
Teaching Assistant (Chem121, 122, 123, 102), Northwestern University, twelve contact hours per week.

CHEM 350-2 Advanced Laboratory 2 Winter 2016
Teaching Assistant, Perovskite Solar Cells, Northwestern University.

PROFESSIONAL DEVELOPMENT

- Ready, Set, Go (RSG) Research Communication Program Summer 2015
- International Summer Institute (ISI) Program Summer 2014